

# **Coronary Atherosclerosis: Biomechanics and Imaging**

**Coronaire atherosclerose: Biomechanica en beeldvorming**

Eline Hartman

# Coronary Atherosclerosis: Biomechanics and Imaging

Coronaire atherosclerose: Biomechanica en beeldvorming

## Proefschrift

ter verkrijging van de graad van doctor aan de

Erasmus Universiteit Rotterdam

op gezag van de

rector magnificus

Prof. dr. A.L. Bredenoord

en volgens besluit van het College voor Promoties.

De openbare verdediging zal plaatsvinden op

woensdag 25 januari 2023 om 10:30

door

Eline Maria Johanna Hartman

geboren te Haarlem

**Erasmus University Rotterdam**



ISBN: 978-94-6421-972-2

Cover Design: Kwartier M ([www.kwartier-m.nl](http://www.kwartier-m.nl))  
Printing: Ipskamp Printing | [proefschriften.net](http://proefschriften.net)  
Layout and design: Anke Muijsers | [persoonlijkproefschrift.nl](http://persoonlijkproefschrift.nl)

Copyright 2023 © Eline Hartman

The Netherlands. All rights reserved. No parts of this thesis may be reproduced, stored in a retrieval system or transmitted in any form or by any means without prior permission of the author.

The research described in this PhD thesis has received funding from the European Research Council under the European Union's Seventh Framework Programme/ERC Grant Agreement nr. 310457

**Promotiecommissie:****Promotoren:**

prof. dr. ir. A.F.W. van der Steen

dr. ir. J.J. Wentzel

**Overige leden:**

prof. dr. D. Merkus

prof. dr. ir. C.L. de Korte

prof. dr. N. van Royen

**Copromotoren:**

dr. J. Daemen

**Contents**

Chapter 1	Introduction	7
Chapter 2	The definition of low wall shear stress and its effect on plaque progression estimation in human coronary arteries	23
Chapter 3	Invasive coronary imaging in familial hypercholesterolemia pig model	43
Chapter 4	Multidirectional wall shear stress promotes advanced coronary plaque development – comparing five shear stress metrics	63
Chapter 5	Lipid-rich plaques detected by near-infrared spectroscopy are more frequently located in regions of high shear stress	91
Chapter 6	Shear stress related plaque growth of lipid-rich plaques in human coronary arteries: a near-infrared spectroscopy study and OCT-study	109
Chapter 7	Non-invasive coronary imaging as an alternative to invasive imaging to study wall shear stress: A patient-specific computational study	131
Chapter 8	Comparison of swine and human computational hemodynamic models for the study of coronary atherosclerosis	159
Chapter 9	Colocalization of intracoronary lipid-rich plaques and calcifications – an integrated NIRS-IVUS analysis	181
Chapter 10	Near-infrared spectroscopy to predict plaque progression in plaque-free artery regions	193
Chapter 11	Discussion	209
Appendices		227
	Summary	229
	Nederlandse samenvatting	235
	List of publications	240
	PhD-Portfolio	242
	About the author	245



# 1

## Introduction



## Coronary artery disease

Cardiovascular disease has been the leading cause of death over the past decades, and its incidence and prevalence continue to increase<sup>1</sup>. The increasing prevalence of classical risk factors such as hypertension, hypercholesterolemia, and a sedentary lifestyle contribute to the globally growing disease burden dominated by coronary artery disease (CAD). Atherosclerosis is the underlying pathophysiological process of CAD, resulting in significant narrowing of coronary arteries. For three decades, percutaneous coronary intervention (PCI) has emerged as the mainstay for the treatment of coronary stenosis by its ability to restore blood flow by balloon inflation and subsequent stent placement in both stable and unstable settings. Moreover, PCI may facilitate blood flow restoration in patients with myocardial infarction, and myocardial muscle function may be preserved. These interventions significantly improved the prognosis of CAD. Nevertheless, only a minority of the coronary lesions will cause an event<sup>2</sup>. Moreover, uncertainty remains on which lesions will eventually evolve into hemodynamically significant narrowing or plaque rupture. Understanding and unravelling mechanisms that contribute to the development, progression, and destabilization of coronary atherosclerotic lesions is essential for preventing these coronary adverse events.

## Atherosclerosis

Atherosclerosis is an inflammatory, lipid-driven disease. In a healthy artery, the endothelial cell layer is exposed to the bloodstream and maintains homeostasis. Atherosclerosis starts with endothelial cell dysfunction, caused by traditional risk factors such as tobacco use, diabetes mellitus and hypertension<sup>3</sup>. However, it is also influenced by wall shear stress (WSS), the biomechanical force of the blood along the vessel wall<sup>4</sup>. Endothelial dysfunction leads to higher endothelial layer permeability for low-density lipoprotein (LDL), which initiates the inflammatory process<sup>3</sup>. The accumulation of lipids in the intima, the inner layer of the vessel wall, triggers the inflammatory process.

Moreover, endothelial dysfunction leads to leukocyte adhesion allowing monocytes to enter the vessel wall as a reaction to the inflammatory state. After migration into the vessel wall, monocytes differentiate into macrophages and engulf the oxygenized LDL molecules<sup>5</sup>. The impaired efflux of the lipid-filled macrophages (i.e., foam cells) leads to the accumulation of lipids in the vessel wall, stimulating the inflammatory cascade<sup>6</sup>. The death of these foam cells leads to the formation of extracellular lipid-rich debris, the so-called “necrotic core”. Simultaneously, smooth muscle cells from the media layer of the vessel wall start to migrate and proliferate under the influence of growth factors, and cytokines are excreted by the inflammatory cells. The smooth muscle cells excrete extracellular matrix,

encapsulating the necrotic core with a fibrous cap, thereby creating an atheroma with a fibrous cap, the so-called fibroatheroma, covering the necrotic core and the lipid-rich plaque<sup>5</sup>.

Patients with atherosclerotic coronary artery disease typically present with either chronic coronary syndromes (CCS) or acute coronary syndromes (ACS). In patients with CCS, the atherosclerotic plaque grows and intrudes the vessel lumen, obstructs blood flow and may result in a flow-limiting lesion. A subsequent imbalance in myocardial oxygen demand and supply results in the well-known symptom of chest pain, most apparent during exercise when myocardial oxygen demand is increased. Symptoms are typically relieved when provoking factors (stress or exercise) are terminated.

In patients with an ACS, there is a critical moment of onset of the event, often an acute occlusion of the vessel, causing ongoing ischemia with the cardiac muscle in jeopardy, causing acute chest discomfort. From a pathophysiological point of view, this is often caused by a plaque rupture. The fibrous cap covering the fibroatheroma can rupture whenever the cap's stress exceeds the cap's tensile strength. The lipid-rich debris in the fibroatheroma comes in direct contact with the blood, inducing a thrombogenic response, and causing an acute occlusion of the vessel by thrombus<sup>7</sup>.

The atherosclerotic lesions causing an ACS are often non-flow-limiting. Therefore, patients presenting with an acute coronary syndrome often do not have any symptoms before the event<sup>8</sup>. The latter illustrates the importance of the quest for understanding the pathophysiology and mechanisms of how these plaques grow, the importance of plaque composition in plaque vulnerability and which factors stimulate plaque rupture. Several vulnerable plaques' characteristics have been described: a thin fibrous cap, large lipid-rich necrotic core, positive remodelling and inflammation<sup>9</sup>. A complex combination of different pathophysiological processes contributes to plaque vulnerability. For example, the inflammatory state with activated macrophages that produce matrix metalloproteinases (MMPs) affects the tensile strength of the fibrous cap due to weakening the elastin and collagen fibres in the extracellular matrix<sup>10</sup>.

From the initial start of the atherosclerotic process till a plaque rupture that causes the cardiac event, many years pass by in which patients remain asymptomatic. Coronary artery disease is directly linked to ageing, and patients, when presenting themselves, are in a more advanced stage of the atherosclerotic process. Research in patients presenting with CAD and complex pathology does not address the initial process of atherosclerosis. Natural history studies are scarce because of the extended time frame of the development of atherosclerosis. Hence, cardiovascular

research in animal models can contribute to filling this knowledge gap and help understand plaque initiation and progression.

Moreover, animal models better allow plaque assessment at multiple time points to capture the different stages of atherosclerosis development and allow the study of the relationship between imaging, WSS and histology. However, not every animal model is suitable for atherosclerotic research, and human-like coronary artery systems are needed. Porcine models proved to closely resemble the size and geometry of human coronaries and develop atherosclerosis in a human-like manner<sup>11</sup>.

### Imaging techniques for the detection of atherosclerosis

Previous research revealed that not only lumen stenosis but also plaque size and composition are important for future plaque risk assessment<sup>2</sup>. Whereas conventional coronary angiography has been the mainstay for guiding visualization and treatment in patients with CAD, the technology is limited in its ability to visualize specific plaque components. Conversely, due to their improved resolution, invasive coronary imaging techniques allow the visualization of (dynamic) changes in atherosclerotic plaque composition and size, which is essential for further understanding the pathophysiology of atherosclerosis. However, the majority of the atherosclerotic lesions are stable and never cause an event such as a plaque rupture. Therefore, one of the key questions since the introduction of invasive imaging techniques is which imaging marker predicts plaque vulnerability. This started the search for the crucial imaging plaque characteristic that predicts a future event, with the ultimate ambition to decrease the number of future events. In this paragraph, three different intracoronary imaging modalities that have been commercialized will be presented and discussed.

#### IVUS

With the introduction of intravascular ultrasound, it became possible to visualize vessel dimensions. A catheter-based ultrasound probe generates cross-sectional images of the artery during an automatic pulled back with high rotational spiral speed. The technology allows full visualization of the coronary artery, including an accurate assessment of luminal stenosis and identification of plaque burden by allowing visualization of the external elastic lamina (the “outer” wall of the vessel) (Figure 1A). Ultrasound has a large penetration depth and is currently the golden standard for volumetric assessment of coronary plaques. Due to its relatively low spatial and parametric resolution, plaque components are not easily distinguishable in IVUS images. However, calcifications are a major plaque component that can be easily detected using IVUS. Due to high density, calcifications in the plaque reflect the ultrasound beam, precluding penetration to

deeper tissue layers<sup>12</sup>. On IVUS images, calcium visualizes as high intensity (white) signal with a sudden drop and low-intensity backscatter (black shadow) behind it (Figure 1B). Thereby, calcifications hamper the visualization of the outer vessel wall. In regions with extensive calcifications (>90 degrees), no correct volumetric assessment of the wall can be performed, but the presence of calcium as a plaque component can be detected<sup>13</sup>. The PROSPECT study has been one of the cornerstone research projects using intravascular ultrasound to relate plaque characteristics to future events. This prospective study with almost 700 patients with a median follow-up of 3.4 years identified IVUS-derived plaque burden (>70%) and minimal lumen area (<4.0mm<sup>2</sup>) as independent predictors of future clinical events.

#### OCT

OCT was first used in ophthalmology diagnostics in the early 1990s, after which it took almost another two decades before a contemporary coronary OCT catheter became available<sup>14,15</sup>. Similar to IVUS, optical coherence tomography (OCT) is a catheter-based technique that creates cross-sectional images but uses near-infrared light to create images<sup>16</sup>. OCT uses the differences in light absorption by the different plaque components to create an image. OCT has a higher spatial resolution than IVUS and can better distinguish the various plaque components, such as lipid-rich plaques and fibrous tissue (Figure 1D), and allows accurate visualization of plaque ruptures. Even microstructures, such as the thickness of a fibrous cap covering a fibro-atheroma, can be visible<sup>17</sup>. The high resolution of OCT comes at the expense of the penetration depth. Moreover, plaques with a high lipid content cause attenuation of the light signal, resulting in a loss of outer wall visibility (Figure 1C). So, although OCT has a higher resolution, it is less suitable for volumetric assessment of the coronary plaques.

#### NIRS

Similar to OCT, near-infrared spectroscopy (NIRS) uses near-infrared light. NIRS looks at differences in the absorption spectrum between plaque components to detect lipid-rich regions. NIRS was optimized to detect fibroatheromas larger than 60°, more than 200 µm thick, and a mean fibrous cap <450 µm<sup>18</sup>. The second-generation catheters combined the NIRS imaging technique with an IVUS catheter<sup>19,20</sup>. This combined catheter made the simultaneous volumetric assessment of plaque and detection of lipids possible with exact colocalization. NIRS presents the lipid quantity within a vessel as the so-called lipid core burden index (LCBI), representing the fraction of the segment of the artery containing lipid-rich plaques. Recently, large clinical studies showed that lipid-rich plaques (LRPs), as detected by NIRS-IVUS, have a higher vulnerability and are more prone to cause adverse clinical events<sup>21,22</sup>. The evolution of these LRPs, and why some LRPs do and some do not progress remains unclear.

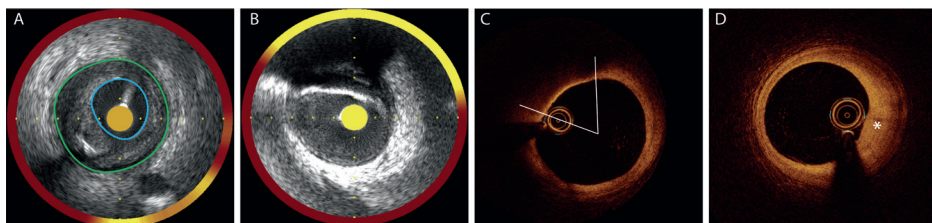


**Figure 1. Example cross-sectional images of NIRS-IVUS and OCT.**

**A-B)** Near-infrared spectroscopy-intravascular ultrasound (NIRS-IVUS) images: The grey-scale ultrasounds images, with the NIRS colour-coded ring around the IVUS image. The colour-coded ring represents the probability of lipids (Yellow = high probability of lipids, red = low probability of lipids) A) IVUS image of concentric non-calcified plaque with the segmented lumen (blue ellipse) and external elastic membrane (EEM) (i.e., outer vessel wall) (green ellipse). B) Calcified plaque with the bright reflection of the ultrasound signal resulting in a dark shadow behind it, hampering the outer vessel wall from view. **C-D)** Optical coherence tomography (OCT) Eccentric plaque with a lipid pool with signal-rich fibrous cap overlying the fibroatheroma (white angle) and healthy vessel wall opposite of the plaque. D) fibrous detected tissue in OCT (\*) with visibility of the EEM.

To follow the natural history of atherosclerotic disease progression, serial imaging studies are needed to capture and understand the process of atherosclerosis progression. Not only to capture the process of atherosclerosis development but also to keep trying to differentiate stable from vulnerable plaques.

## Wall shear stress and atherosclerosis

Coronary atherosclerosis is not equally distributed throughout the coronary artery tree, and some regions are more prone to develop atherosclerosis than others. For example, the inner curvature of the vessel or the vessel wall near a bifurcation is more likely to develop atherosclerotic plaque. Wall shear stress (WSS), the frictional force of the bloodstream along the vessel wall, plays a pivotal role in the patched pattern of atherosclerosis distribution<sup>23,24</sup>. Low WSS causes endothelial cell dysfunction, and those regions, including the inner curvature and bifurcations, are more susceptible to the atherosclerosis process of lipids entering the vessel wall<sup>25</sup>.

Low WSS has been related to plaque initiation and development, causing an increase in plaque size and thus vessel wall volume. Initial plaque growth will lead to minimal local lumen narrowing, which leads to increased WSS sensed by endothelial cells with mechanoreceptors. This increase in WSS initiates the compensatory response of outward remodelling of the vessel wall, preserving the lumen diameter in the earlier stages of atherosclerosis. The outer vessel diameter “grows”. Studies from the late 80s demonstrated that when the plaque burden extends beyond 40%, this compensatory mechanism preventing lumen narrowing is no longer sufficient<sup>26</sup>. Consequently, the lumen will become smaller, resulting

in lumen narrowing and a subsequent increase in local WSS. As low WSS has been related to atherosclerosis development, plaque-free wall exposed to high WSS is protected from atherosclerosis development<sup>27</sup>. However, a higher magnitude of WSS is caused by a lumen intruding plaque, and high WSS has been related to increasing plaque vulnerability<sup>28</sup>. High WSS is suggested to influence thinning of the fibrous cap that overlays a fibroatheroma through apoptosis of smooth muscle cells in the fibrous cap and is related to plaque rupture<sup>29,30</sup>.

## Wall shear stress calculation

Since it is not feasible to measure WSS directly in human coronary arteries with conventional clinical imaging modalities, computational approaches are used to estimate WSS. One of the most accurate methods of calculating WSS is computational fluid dynamics (CFD). This numerical method simulates the coronary artery's blood flow by solving the Navier-Stokes equations. To simulate the coronary blood flow and calculate the WSS using CFD, a 3D reconstruction of the vessel resembling the real-life geometry of the 3D coronary lumen is necessary. Furthermore, the flow at the inlet and outlet of the artery representative of the physiological flow needs to be fed into the simulations, the so-called boundary conditions. Finally, assumptions on the blood viscosity and fluid behaviour are essential in solving the computational model.

### 3D vessel reconstruction

Although biplane angiography and coronary computer tomography angiography (CCTA) both have luminal and 3D spatial information, most studies use a fusion of lumen extracted from the intravascular imaging data and the 3D-centerline information of bi-plane angiography or CCTA<sup>31–33</sup> (Figure 2). One of the most important reasons for choosing this fusion technique is that WSS is susceptible to luminal shape. Therefore, imaging techniques with a relatively high spatial resolution are desirable when extracting lumen shape and size for assessing WSS<sup>34</sup>. To compensate for cardiac motion artefacts, images acquired at the end-diastolic phase are preferred<sup>34</sup>. Since IVUS images are acquired with a low pullback speed and high sampling rate, images can be gated, resulting in one frame per cardiac cycle. OCT has a 36mm/sec pullback speed, ensuring fast vessel imaging in seconds and in only a few cardiac cycles. Unfortunately, luminal size differences are embedded in the OCT data and, therefore, are less preferable for using lumen contours for WSS analysis<sup>34</sup>.

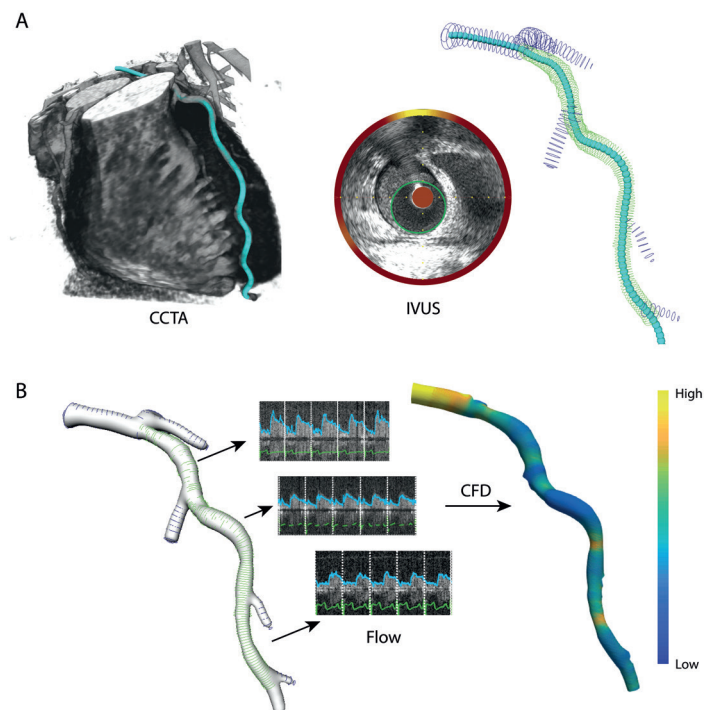


**Figure 2. Overview of 3D reconstruction.**

**A:** A coronary computed tomography angiography (CCTA) derived centerline of the left anterior descending coronary artery (turquoise) combined with intravascular ultrasound (IVUS) derived coronary lumen (green) in a 3D reconstruction, matched on side branches visible in both imaging modalities. Side branches derived from the CCTA are scaled and added to the 3D reconstruction. **B:** A luminal surface was created to make the 3D model of the coronary artery, and Doppler flow was measured at different locations in the coronary vessel. Using the 3D reconstruction and flow measurements in computational fluid dynamics (CFD), we could calculate the coronary artery's wall shear stress (WSS). (yellow = high WSS, blue = low WSS).

To achieve a 3D reconstruction, lumen contours are placed perpendicular to the 3D vessel centreline derived from biplane angiography or CCTA, and a luminal surface between the contours is generated (Figure 2). Most of the studies do not take side branches into account in their 3D reconstruction<sup>32,35,36</sup>. Even though it is known that side branches influence the local flow patterns and bifurcation regions are more exposed to low WSS<sup>37</sup>. Incorporating side branches into the model using biplane angiography is challenging because the exact location of the bifurcation is not always clearly visible due to the foreshortening of the angiogram. The fusion of IVUS with CT segmented side branches has been proven to be an accurate way to model the geometry and reconstruct detailed bifurcation regions<sup>38</sup>.

This type of multimodality imaging research is labour-intensive; a potentially more straightforward approach would be to create a 3D reconstruction solely based on CCTA. This would expand the accessibility of WSS analysis in patients and thereby has a higher potential to be used in the clinic for risk assessment in the future. However, before proceeding with large CCTA outcome studies relating WSS to events, it is vital to know if the WSS patterns in a 3D geometry based on CCTA imaging alone are similar to those obtained using the fusion of IVUS with CCTA<sup>34</sup>.

### Boundary conditions for CFD

In addition to a 3D model resembling real-life geometry, the boundary conditions applied in the CFD model need to be chosen precisely. Due to the pulsatile nature of the blood flow, there is high variability in flow rate over the cardiac cycle. This causes not only variation in shear stress magnitude, but the pulsatility can also cause variations in the local flow direction. Furthermore, the flow waveform measured in the left and the right coronary arteries is different<sup>37,39,40</sup>. One of the most precise ways to capture the local flow velocity in coronary arteries is a catheter-based Doppler flow measurement<sup>39,41</sup>. Recently, multidirectional shear stress metrics have been introduced to study the influence of these time-dependent phenomena on plaque progression<sup>40,42-44</sup>. Different multidirectional shear stress metrics have been previously described and were found to be related to plaque progression. However, a comprehensive study that compares the different metrics within one dataset is still lacking.

To relate WSS to plaque progression and atherosclerosis development, cut-off values of shear stress have been used to categorize WSS into "low" and "high" WSS. In the past years, different methods have been proposed to define low and high WSS<sup>35,45-47</sup>. Some studies use absolute thresholds, while other research groups categorize WSS values based on the observed range per vessel or study (relative thresholds). Care should therefore be taken when comparing WSS-based findings among different studies. As of to date, it remains unclear what the effect is of the use of relative or absolute thresholds determining low and high WSS on the relationship between WSS and plaque progression.

### Thesis outline

The aim of this thesis is to elucidate coronary atherosclerotic disease development further using invasive and non-invasive imaging techniques. Furthermore, we investigated the relationship between multidirectional hemodynamic parameters such as WSS and atherosclerotic plaque composition and progression.



In previous studies on WSS-related plaque progression, both absolute as well as relative WSS thresholds were used to define low WSS. In **Chapter 2**, the effect of these different definitions of low WSS and the impact thereof on the prediction of atherosclerotic plaque progression is described.

**Chapter 3** describes atherogenesis in a full-grown porcine model with familial hypercholesterolemia. Using different serial intravascular imaging techniques and histological analysis of the coronary plaques, a detailed analysis of the development of coronary atherosclerosis was performed.

In **Chapter 4**, the effect of multidirectional WSS metrics on coronary atherosclerosis development using imaging and histological data from the animal model is described in Chapter 3. Serial imaging allowed the investigation of plaque size and WSS change over time, and the subsequent effect of WSS on plaque development was measured.

Lipid-rich plaques have been related to future events. Since high WSS might play a role in thinning of the fibrous cap, high WSS is potentially involved in the evolution from a lipid-rich plaque to an event-causing lesion. For that reason, in **Chapter 5**, a cross-sectional study is described in which the colocalization of lipid-rich plaques with high WSS was investigated. Therefore, NIRS-IVUS imaging and CCTA were fused to obtain 3D reconstructions of human coronary arteries. Using these 3D geometries, WSS was calculated and co-localized with lipid-rich plaque locations, and volumetric plaque measurements were performed. Using the colocalization of plaque components, WSS, and one-year follow-up data, we describe in **Chapter 6** the WSS-related plaque growth of lipid-rich plaques. Near-infrared spectroscopy (NIRS) and optical coherence tomography (OCT) imaging detected lipid-rich plaque.

In the previous chapter, invasive imaging was used as the backbone for the WSS assessment. However, there might be potential to use non-invasive imaging alone to assess WSS. In **Chapter 7**, we investigated the sole use of non-invasive imaging for WSS assessment against the often-used invasive imaging in a feasibility study comparing local WSS patterns and absolute values.

In **Chapter 8**, a detailed analysis compares hemodynamical parameters obtained of atherosclerotic porcine and patient coronary arteries. This analysis includes WSS and intravascular flow quantities and vessel morphology.

With the introduction of a multimodality NIRS-IVUS catheter, calcium and lipid-rich plaques can be assessed simultaneously. While large calcifications have been associated with local plaque stabilization, lipid-rich plaques have been related to

increased risk for events. **Chapter 9** describes an observational retrospective study on the colocalization of calcifications and lipid-rich plaques.

NIRS-IVUS image acquisition is useful in detecting vessel wall regions infiltrated with lipids. However, sometimes the NIRS signal is positive in regions with hardly any vessel wall thickness, which can be misinterpreted as artefacts. In **Chapter 10**, we used a detailed sector analysis to evaluate these thin-wall lipid-rich regions detected by the NIRS-IVUS catheter. The presence of lipids was confirmed with OCT. Furthermore, these thin wall lipid-rich regions were compared to regions without lipid infiltration for differences in plaque progression after one-year follow-up.

Finally, in **Chapter 11**, the main findings of this thesis are summarized and discussed. The clinical implications and future perspectives are presented.

## References

1. Roth GA, Abate D, Abate KH, et al. Global, regional, and national age-sex-specific mortality for 282 causes of death in 195 countries and territories, 1980–2017: a systematic analysis for the Global Burden of Disease Study 2017. *Lancet* 2018;392:1736–88.
2. Stone GW, Maehara A, Lansky AJ, et al. A Prospective Natural-History Study of Coronary Atherosclerosis. *N Engl J Med* 2011;364:226–35.
3. Gimbrone MA, García-Cardena G. Endothelial Cell Dysfunction and the Pathobiology of Atherosclerosis. *Circ Res* 2016;118:620–36.
4. Caro GG. Discovery of the role of wall shear in atherosclerosis. *Arterioscler Thromb Vasc Biol* 2009;29:158–61.
5. Libby P, Buring JE, Badimon L, et al. Atherosclerosis. *Nat Rev Dis Prim* 2019;5:56.
6. Ouimet M, Barrett TJ, Fisher EA. HDL and reverse cholesterol transport: Basic mechanisms and their roles in vascular health and disease. *Circ Res* 2019;124:1505–18.
7. Crea F, Libby P. Acute coronary syndromes: The way forward from mechanisms to precision treatment. *Circulation* 2017;136:1155–66.
8. Fishbein MC, Siegel RJ. How Big Are Coronary Atherosclerotic Plaques That Rupture? *Circulation* 1996;94:2662–6.
9. Schaar JA, Muller JE, Falk E, et al. Terminology for high-risk and vulnerable coronary artery plaques. Report of a meeting on the vulnerable plaque, June 17 and 18, 2003, Santorini, Greece. *Eur Heart J* 2004;25:1077–82.
10. Ikeda U, Shimada K. Matrix metalloproteinases in vascular remodeling. *Connect Tissue* 2002;34:343–50.
11. Getz GS, Reardon CA. Animal models of atherosclerosis. *Arterioscler Thromb Vasc Biol* 2012;32:1104–15.
12. Mintz GS. Intravascular Imaging of Coronary Calcification and its Clinical Implications. *JACC Cardiovasc Imaging* 2015;8:461–71.
13. Mintz GS, Nissen SE, Anderson WD, et al. American College of Cardiology clinical expert consensus document on standards for acquisition, measurement and reporting of intravascular ultrasound studies (ivus): A report of the american college of cardiology task force on clinical expert consensus do. *J Am Coll Cardiol* 2001;37:1478–92.
14. Yabushita H, Bouma BE, Houser SL, et al. Characterization of human atherosclerosis by optical coherence tomography. *Circulation* 2002;106:1640–5.
15. Jang IK, Bouma BE, Kang DH, et al. Visualization of coronary atherosclerotic plaques in patients using optical coherence tomography: Comparison with intravascular ultrasound. *J Am Coll Cardiol* 2002;39:604–9.
16. Bouma BE, Villiger M, Otsuka K, et al. Intravascular optical coherence tomography [Invited]. *Biomed Opt Express* 2017;8:2660.
17. Tearney GJ, Regar E, Akasaka T, et al. Consensus standards for acquisition, measurement, and reporting of intravascular optical coherence tomography studies: A report from the International Working Group for Intravascular Optical Coherence Tomography Standardization and Validation. *J Am Coll Cardiol* 2012;59:1058–72.
18. Gardner CM, Tan H, Hull EL, et al. Detection of Lipid Core Coronary Plaques in Autopsy Specimens With a Novel Catheter-Based Near-Infrared Spectroscopy System. *JACC Cardiovasc Imaging* 2008;1:638–48.
19. Madder RD, Goldstein JA, Madden SP, et al. Detection by Near-Infrared Spectroscopy of Large Lipid Core Plaques at Culprit Sites in Patients With Acute ST-Segment Elevation Myocardial Infarction. *JACC Cardiovasc Interv* 2013;6:838–46.
20. Schultz CJ, Serruys PW, van der Ent M, et al. First-in-man clinical use of combined near-infrared spectroscopy and intravascular ultrasound: a potential key to predict distal embolization and no-reflow? *J Am Coll Cardiol* 2010;56:314.
21. Schuurman A-S, Vroegindewey M, Kardys I, et al. Near-infrared spectroscopy-derived lipid core burden index predicts adverse cardiovascular outcome in patients with coronary artery disease during long-term follow-up. *Eur Heart J* 2018;39:295–302.
22. Waksman R, Di Mario C, Torguson R, et al. Identification of patients and plaques vulnerable to future coronary events with near-infrared spectroscopy intravascular ultrasound imaging: a prospective, cohort study. *Lancet* 2019;394:1629–37.
23. Warboys CM, Amini N, De Luca A, et al. The role of blood flow in determining the sites of atherosclerotic plaques. *F1000 Med Rep* 2011;3.
24. Davies PF, Fang Y, Fleming I. The atherosusceptible endothelium: endothelial phenotypes in complex haemodynamic shear stress regions in vivo n.d.
25. Malek AM, Alper SL, Izumo S. Hemodynamic shear stress and its role in atherosclerosis. *JAMA* 1999;282:2035–42.
26. Glagov S, Weisenberg E, Zarins CK, et al. Compensatory Enlargement of Human Atherosclerotic Coronary Arteries. *N Engl J Med* 1987;316:1371–5.
27. Kwak BR, Bäck M, Bochaton-Piallat M-L, et al. Biomechanical factors in atherosclerosis: mechanisms and clinical implications†. *Eur Heart J* 2014;35:3013–20.
28. Eshtehardi P, Brown AJ, Bhargava A, et al. High wall shear stress and high-risk plaque: an emerging concept. *Int J Cardiovasc Imaging* 2017;33.
29. Fitzgerald TN, Shepherd BR, Asada H, et al. Laminar shear stress stimulates vascular smooth muscle cell apoptosis via the Akt pathway. *J Cell Physiol* 2008;216:389–95.
30. Eshtehardi P, Brown AJ, Bhargava A, et al. High wall shear stress and high-risk plaque: an emerging concept. *Int J Cardiovasc Imaging* 2017;33:1089–99.
31. Bourantas C V, Räber L, Sakellarios A, et al. Utility of Multimodality Intravascular Imaging and the Local Hemodynamic Forces to Predict Atherosclerotic Disease Progression. *JACC Cardiovasc Imaging* 2020;13:1021–32.
32. Stone PH, Saito S, Takahashi S, et al. Prediction of progression of coronary artery disease and clinical outcomes using vascular profiling of endothelial shear stress and arterial plaque characteristics: the PREDICTION Study. *Circulation* 2012;126:172–81.
33. Samady H, Eshtehardi P, McDaniel MC, et al. Coronary Artery Wall Shear Stress Is Associated With Progression and Transformation of Atherosclerotic Plaque and Arterial Remodeling in Patients With Coronary Artery Disease. *Circulation* 2011;124:779–88.
34. Gijzen F, Katagiri Y, Barlis P, et al. Expert recommendations on the assessment of wall shear stress in human coronary arteries: existing methodologies, technical considerations, and clinical applications. *Eur Heart J* 2019;40:3421–33.
35. Bourantas C V, Zanchin T, Sakellarios A, et al. Implications of the local haemodynamic forces on the phenotype of coronary plaques. *Heart* 2019;105:1078–86.
36. Costopoulos C, Timmins LH, Huang Y, et al. Impact of combined plaque structural stress and wall shear stress on coronary plaque progression, regression, and changes in composition. *Eur Heart J* 2019;40:1411–22.
37. Morbiducci U, Kok AM, Kwak BR, et al. Atherosclerosis at arterial bifurcations: Evidence for the role of haemodynamics and geometry. *Thromb Haemost* 2016;115:484–92.
38. Gijzen FJH, Schuurbiers JCH, van de Giessen AG, et al. 3D reconstruction techniques of human coronary bifurcations for shear stress computations. *J Biomech* 2014;47:39–43.
39. Doucette JW, Corl PD, Payne HM, et al. Validation of a Doppler guide wire for intravascular measurement of coronary artery flow velocity. *Circulation* 1992;85:1899–911.
40. Kok AM, Molony DS, Timmins LH, et al. The Influence of Multidirectional Shear Stress on Plaque Progression and Composition Changes in Human Coronary Arteries. *EuroIntervention* 2019.

41. Tanedo JS, Kelly RF, Marquez M, et al. Assessing coronary blood flow dynamics with the TIMI frame count method: Comparison with simultaneous intracoronary Doppler and ultrasound. *Catheter Cardiovasc Interv* 2001;53:459–63.
42. Peiffer V, Sherwin SJ, Weinberg PD. Computation in the rabbit aorta of a new metric – the transverse wall shear stress – to quantify the multidirectional character of disturbed blood flow. *J Biomech* 2013;46:2651–8.
43. Rikhtegar F, Knight JA, Olgac U, et al. Choosing the optimal wall shear parameter for the prediction of plaque location-A patient-specific computational study in human left coronary arteries. *Atherosclerosis* 2012;221:432–7.
44. Mohamied Y, Sherwin SJ, Weinberg PD. Understanding the fluid mechanics behind transverse wall shear stress. *J Biomech* 2017;50:102–9.
45. Stone PH, Coskun AU, Kinlay S, et al. Effect of Endothelial Shear Stress on the Progression of Coronary Artery Disease, Vascular Remodeling, and In-Stent Restenosis in Humans. *Circulation* 2003;108:438–44.
46. Giannopoulos AA, Chatzizisis YS, Maurovich-Horvat P, et al. Quantifying the effect of side branches in endothelial shear stress estimates. *Atherosclerosis* 2016;251:213–8.
47. Timmins LH, Molony DS, Eshtehardi P, et al. Focal Association Between Wall Shear Stress and Clinical Coronary Artery Disease Progression. *Ann Biomed Eng* 2014;43:94–106.



# 2

## **The definition of low wall shear stress and its effect on plaque progression estimation in human coronary arteries**

This chapter is based on:

**The definition of low wall shear stress and its effect on plaque progression estimation in human coronary arteries**

**Eline M.J. Hartman, Giuseppe De Nisco, Frank J.H. Gijzen, Suze-Anne Korteland, Anton F.W. van der Steen, Joost Daemen, Jolanda J. Wentzel**

*Nature: Scientific reports, 2021*



## Abstract

Wall shear stress (WSS), the frictional force of the blood on the vessel wall, plays a crucial role in atherosclerotic plaque development. Low WSS has been associated with plaque growth, however previous research used different approaches to define low WSS to investigate its effect on plaque progression. In this study, we used four methodologies to allocate low, mid and high WSS in one dataset of human coronary arteries and investigated the predictive power of low WSS for plaque progression. Coronary reconstructions were based on multimodality imaging, using intravascular ultrasound and CT-imaging. Vessel-specific flow was measured using Doppler wire and computational fluid dynamics was performed to calculate WSS. The absolute WSS range varied greatly between the coronary arteries. On the population level, the established pattern of most plaque progression at low WSS was apparent in all methodologies defining the WSS categories. However, for the individual patient, when using measured flow to determine WSS, the absolute WSS values range so widely, that the use of absolute thresholds to determine low WSS was not appropriate to identify regions at high risk for plaque progression.

## Introduction

Wall shear stress (WSS), the frictional force of the blood flow exciding on the vessel wall, plays a vital role in the natural history of atherosclerosis. Fusion of multimodality imaging and computational fluid dynamics allowed comprehensive detailed research on WSS related plaque progression in coronary arteries. Using this methodology, multiple studies have shown the relationship between low WSS and atherosclerosis initiation and plaque progression in coronary arteries of humans and animal models of atherosclerosis<sup>1-6</sup>. These WSS patterns mostly explained the patched distribution of plaques throughout the arteries<sup>7</sup>. Therefore, identifying low, mid and high WSS in the coronary system contributes to understanding of the pathophysiology of plaque progression and plaque rupture.

Previous research used different methodologies to define WSS categories. Thereby different approaches were used to divide WSS into three groups: low, mid, and high WSS regions at the vessel wall<sup>2,3,8</sup>. To further explore the effect of WSS on plaque progression in clinical studies and to place the previous WSS research in context, it is crucial to understand the impact of the different approaches of dividing WSS into categories on this process. One of methodologies to determine low WSS regions used *vessel-specific* tertiles to acknowledge the observed heterogeneity in WSS and the patched distribution of plaques within one vessel. Thereby, one-third of the sectors within one vessel allocates as low WSS. When using this method, all vessels will have individual thresholds of low and high WSS<sup>4,6,8</sup>.

A second methodology often used to determine low, mid and high WSS thresholds based on *study-specific* tertiles, allocating one-third of all the sectors of all vessels in the study as being exposed to low WSS and one-third exposed to mid and one-third to high WSS<sup>2,9,10</sup>. A large study used this study-specific threshold methodology deducting low and high WSS thresholds based on their study. Later, these thresholds deducted from this previous study served as an absolute threshold in many studies that followed. Therefore, we classify this third methodology as *literature-based* thresholds<sup>1,11-13</sup>.

As WSS is determined by blood flow, vessel diameter, and curvature, and since we know that the three coronary arteries are located at different parts of the heart surface, this potentially can lead to differences in specific flow rates between the studied coronary artery type. Furthermore, some studies report on WSS and plaque progression in the LADs only<sup>3</sup>. Therefore, a fourth methodology defining *vessel type-specific* thresholds, using tertiles per vessel type. For example, the one-third of sectors with the lowest absolute WSS of all the LADs are used to determine low WSS for the LADs. Similarly, low and high WSS thresholds can be determined for the LAD, LCX and RCA.

It is still unclear how the definition of low, mid and high WSS impacts the predictive power of WSS for plaque progression. Therefore, in this current study, we used four different approaches to determine WSS thresholds within one existing dataset and investigated the WSS-related plaque progression and the predictive power of low WSS for plaque progression. The following four methods to determine WSS thresholds were compared: A) subdivision of the WSS data into tertiles per vessel (*vessel-specific*), B) subdivision of the WSS data into tertiles including all arteries with in the study (*study-specific*), C) absolute thresholds based on the literature (*literature-based*) thresholds, D) Three different thresholds per vessel type, i.e. dividing the sectors of each vessel type separately in tertiles (*vessel-type-specific*).

Furthermore, using these different methodologies to define WSS thresholds, in this study, the data were stratified according to three major coronary artery types to investigate the differences in the WSS-related plaque progression between the vessel types.

Methods

Patient population

This single-centre study was designed to evaluate the association between biomechanical parameters and natural history of atherosclerotic disease in non-stented coronary arteries. Patients presented with an acute coronary syndrome (ASC), with at least one non-stented non-culprit coronary vessel, were eligible for enrolment. The most important clinical exclusion criteria were: previous coronary artery bypass graft surgery, 3-vessel disease, atrial fibrillation, left ventricular ejection fraction <30%, and renal insufficiency (creatinine clearing <50ml/min). Written informed consent was obtained from all patients. The local medical ethical committee of the Erasmus MC (MED 2015-535, NL54519.078.15) approved the study protocol and was registered (ISCRTN:43170100). The study was conducted in accordance with the World Medical Association Declaration of Helsinki (64th WMA General Assembly, Fortaleza, Brazil, October 2013) and Medical Research Involving Human Subject Act (WMO).

Clinical data acquisition

After successful percutaneous coronary intervention, a study segment with a length of at least 30mm and two visible side branches (diameter>1.5mm) was selected. Intravascular imaging of the study segment was performed using intravascular-ultrasound (IVUS) (TVC Insight Coronary Imaging Catheter, InfraRedX, Burlington, MA, USA) (0.5mm/sec) at baseline and repeated at 12 months follow-up. Furthermore, invasive local flow measurements at multiple locations between the side branches in the study segment were preformed to assess patient-specific blood flow at each location of interest using a ComboWire

(Phillips Volcano, Zaventem, Belgium). One month after the index procedure, an ECG-triggered coronary computed tomography angiography (CCTA) was performed. (SOMATOM Force (192 slice 3rd generation dual-source CT scanner), Siemens Healthineers, Germany).

Table 1. Patient characteristics.

Clinical characteristics	N = 40 patients
Age, years	60 ± 8.6
Men, n (%)	37 (93%)
Body Mass Index (kg/m <sup>2</sup> )	27 ± 4.8
Diabetes Mellitus, n (%)	8 (20%)
Hypertension, n (%)	10 (25%)
Dyslipidemia, n (%)	18 (45%)
Current smoking, n (%)	10 (25%)
Positive family history, n (%)	13 (33%)
Previous MI, n (%)	8 (20%)
Previous PCI, n (%)	11 (28%)
LDL (mmol/L)	2.6 (2.1-3.2)
Imaged study vessel	N = 41 vessels
LAD, n (%)	15 (37%)
LCX, n (%)	10 (24%)
RCA, n (%)	16 (39%)

MI = myocardial infarction, PCI = percutaneous coronary intervention, LDL = low dense lipid protein, LAD = left anterior descending, LCX = left coronary circumflex, RCA = right coronary artery

Image analysis and the 3D reconstructions

The methodology used to create the three-dimensional (3D) vessel reconstructions, as well as the computational fluid dynamic (CFD) analysis were previously described in great detail<sup>4,14</sup>. In brief, by fusing the 3D spatial information of the coronary vessel centreline segmented from the CCTA and the lumen contours extracted from the IVUS, a 3D-reconstruction was made in MeVisLab (MeVis Medical Solutions AG, Bremen, Germany) (Figure 1). The CCTA scan was reconstructed at diastole to ensure maximal filling of the coronary arteries, including all the side branches.

In the IVUS analysis, to remove diameter variations as observed in the images obtained by a continuous IVUS pullback due to cardiac contraction, the images were gated by using an in-house developed MATLAB (v 2017B, Mathworks Inc,

USA) algorithm. The gated frames corresponded with the end-diastolic phase of the cardiac cycle. To evaluate plaque progression, both lumen and the external elastic membrane (EEM) contours were segmented in the gated IVUS frames of the study segment. IVUS lumen was used for the 3D-reconstruction, where lumen and EEM were used to evaluate plaque size and plaque progression. An intra-observer analysis was performed in a random sample of 5 IVUS pullbacks (748 frames) with at least two months interval between the segmentations. A good reproducibility of EEM area, lumen area and plaque area was found (0.996 [95%CI 0.996-0.997], 0.983 [95%CI 0.963-0.990] and 0.958 [95%CI 0.939-0.970]). In IVUS images, calcium is defined as a bright signal with a dark shadow behind it. Calcium was identified as angles in the frames, and regions with extensive calcifications (>90 degrees) were excluded from plaque progression analysis.

Matching of IVUS contours and CCTA was done using side branches visible in both modalities, and corrected for longitudinal and circumferential orientation as previously described and validated by Giessen et al.<sup>15</sup>. The IVUS lumen was placed perpendicular to the centreline. For subsequent computational fluid dynamics (CFD), reliable inlet and outlets were needed. Therefore, to create a model that reassembles real-life anatomy in detail, the side branches (>1.5mm) as well as the regions proximal and distal of the IVUS-derived region of interest (ROI) were segmented in the CCTA, scaled to the IVUS lumen contours and fused with the 3D-reconstruction. To finalize the model, a surface was generated by interpolating the contours of the 3D-reconstruction. In each 3D-reconstructed geometry, a time-dependent CFD simulation was performed, assuming blood as an incompressible fluid (Fluent, v.17.1, ANSYS Inc.). Each 3D-reconstruction was converted to a tetrahedral mesh in ICEM CFD (V.17.1 ANSYS INC) with a 5-layer prism layer at the boundary to accurately assess the wall shear stress. The mesh size was determined by a mesh independence study (only errors within 1% of shear stress were allowed), which resulted in a minimum element size of 0.064 mm and a maximum element size of 0.16mm. Additionally, blood was assumed to behave as shear-thinning fluid non-Newtonian fluid and the Carreau model ( $\mu_0$ : 0.25 Pa·s,  $\mu_\infty$ : 0.0035 Pa·s,  $n$ : 0.25 and  $\lambda$ : 25 s) was used in the simulations<sup>16,17</sup>. The most proximal invasive flow measurement of good quality was used to prescribe time-varying inlet boundary condition in the CFD simulation. Furthermore, for the outlet boundary conditions, the flow distribution through the side branches was calculated based on the flow measurements at different locations in the coronary artery. For the regions with no reliable flow measures, a previously described scaling law was used to determine the flow ratio between the mother and her side branches. Additionally, the vessel lumen was considered as rigid and subjected to no-slip condition. Each To obtain the time-averaged WSS, the computed shear stresses were averaged over a cardiac cycle.

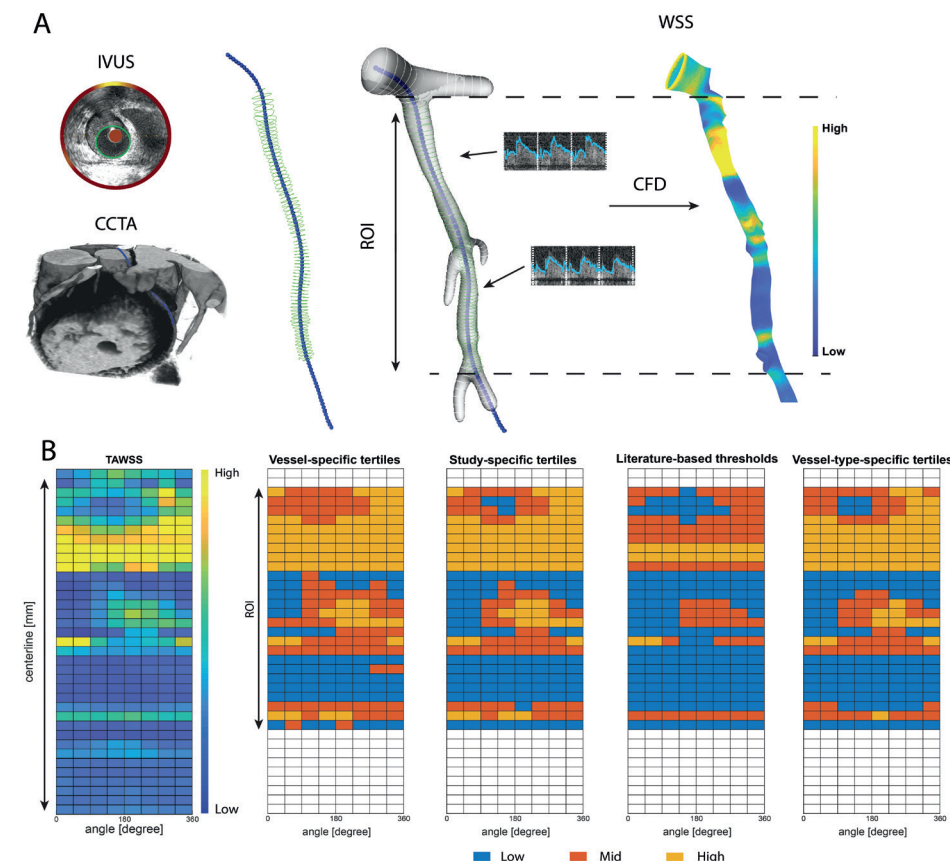


**Figure 1. Example of an LCX showing the methodology of 3D-reconstruction of coronary and wall shear stress (WSS) calculations.**

**A:** Lumen (green) and EEM contours (red) were delineated in intravascular ultrasound (IVUS) images and merged with the centreline (blue markers) segmented from the coronary computer tomography angiography (CCTA) to create a 3D reconstruction. WSS calculations were performed using local flow measurements and computational fluid dynamics, resulting in local WSS. **B:** The 3D reconstruction was converted in a 2D-map by folding the vessel open in the longitudinal direction. Creating a 2D map, dividing the vessel into sectors of 45 degrees/1.5mm thick, WSS was averaged for each sector. For each methodology (vessel-specific tertiles, study-specific tertiles, literature-based thresholds (low WSS < 1.0 Pa) and vessel-type-specific tertiles) a 2D map was created and depicting the distribution of WSS in low (blue), mid (orange) and high (yellow) WSS. Images were generated by MeVis Medical Solutions AG, Bremen, Germany) and MATLAB (v 2017B, Mathworks Inc, USA)

### Data analysis

All IVUS-derived data, such as calcification, wall thickness based on the EEM (baseline and follow-up), were mapped on the 3D geometry of the coronary vessel using VMTK (Orobix, Bergamo, Italy) and MATLAB (v2017b, Mathworks Inc, Natick, MA, USA). To perform statistical analysis, the 3D reconstruction was converted

into a 2D-map by folding the vessel open in the longitudinal direction. In this 2D map configuration, the arteries were divided into cross-sectional segments of 1.5mm thick. Subsequently, these segments were divided into 8 sectors of 45° with the lumen centre as intersection. The WSS was averaged for each sector and categorized by using the three different methodologies to define low, mid and high WSS. First, for *vessel-specific* thresholds, the sectors of one vessel were equally divided into three groups based on the WSS, creating *vessel-specific* tertiles. Second, for the *study-specific* thresholds, the sectors of all vessels combined were equally divided into three groups, allocating low, mid and high WSS to one third of all the sectors. Third, all sectors of all vessels were categorized using absolute WSS thresholds based on literature-based values. All sectors below 1 Pa were categorized as low WSS, between 1pa and 2.5Pa as mid WSS and above 2.5Pa as high WSS<sup>3</sup>. Finally, all sectors of all LAD vessels were equally divided into three groups, allocating low, mid, and high WSS to one-third of the sectors. Similarly, thresholds were extracted for the LCX and the RCA. Furthermore, analysis on plaque progression was done by mapping the IVUS-based vessel area (based on the EEM) and lumen area and the derived wall thickness on these 2D-maps. Both baseline and follow-up plaque burden (PB) were calculated by sectorial plaque area/sectorial vessel area\*100% and subtracted to obtain the plaque progression over time.

Statistics

IBM SPSS statistics (version 25.0) software was used for the statistical analysis. Normally distributed data was presented as mean±standard deviation, statistical differences was determined with a student t-test or ANOVA with *post hoc* testing (Bonferroni). Non-normally distributed data were displayed as median (interquartile range) and significance was tested using a Mann-Whitney U test. All statistical analysis of change in PB (follow-up-baseline) was done with a mixed model. The WSS category (low, mid and high) and vessel type (LAD, LCX or RCA) as a fixed factor and the individual vessel as a random factor to take the within-subject-correlation into account. Furthermore, per vessel, a random sample of 25% of the sectors was used in the mixed model to minimize possible dependencies in the dataset. The mixed model analyses were performed with and without correction for baseline plaque burden. The results showing the relationship between WSS and plaque progression are presented as estimated means of the PB change and the 95% confidence interval (95%CI) and significance between the groups was determined after *post hoc* testing (Bonferroni). To investigate the predictive value of low WSS, a generalized linear mixed-effect model was used, with the individual vessel as a random factor. Plaque growth was defined as delta PB of 15% and is based on the 90<sup>th</sup> percentile of delta PB of all available sectors of all patients. P<0.05 was considered significant in all tests.

Results

For 41 vessels (40 patients), a complete dataset with IVUS at baseline and follow-up, doppler data and the CT-scan was available. The patient characteristics are presented in table 1. The mean age was 60±9 years and 92.5% of the studied population was male. The median length of the ROI was 54 mm (39-62). After excluding regions with extensive calcification, a total of 10205 45°x1.5 mm sectors were used in the final plaque progression analysis. The median baseline plaque burden (PB) was 29% (16-46). In total, 15 LAD's, 10 LCX's and 16 RCA's were present in the study. The characteristics of the three major vessels are presented in table 2.

Table 2. Vessel characteristics.

	LAD	LCX	RCA	p
Length ROI	53 mm [48-62]	38 mm [25-60]	55 mm [40-58]	NS
Baseline PB	27% [16-42]	29% [17-46]	30% [15-47]	*<0.05
Absolute WSS ROI	0.56 Pa [0.35-1.07]	0.87 Pa [0.56-1.46]	0.92 Pa [0.57-1.60]	<0.05
% sectors (no calcification) < 1Pa	72%	59%	54%	<0.05
% sectors showing progression (>90 <sup>th</sup> percentile delta PB)	7.9%	15%	11%	<0.05

ROI = Region of Interest, PB = Plaque Burden, WSS = Wall shear stress, LAD = left anterior descending, LCX = left coronary circumflex, RCA = right coronary artery. \* only significant for LAD vs LCX & LAD vs RCA.

The average WSS in the ROI was 0.77 Pa (0.46-1.37). In Figure 1, for each individual vessel and each methodology to identify the WSS categories, the distribution of sectors exposed to low, mid and high WSS is presented. For the study-specific methodology, the absolute threshold for low WSS was <0.60 Pa and high WSS >1.14 Pa. Using this method, nearly half of LAD sectors (48%) was identified as low WSS, whereas that percentage was much lower for the LCX and RCA, being 28% and 23.5% respectively. Using the thresholds based on literature (low <1 Pa, high> 2.5 Pa), 62% of the sectors were characterized as low WSS; having 73% of the LAD, 56% of the LCX and 54% of the RCA being exposed to low WSS. The average thresholds per vessel type for low and high WSS was for the LAD 0.43 and 0.86, for the LCX 0.67 and 1.27 and RCA 0.68 and 1.30.



Interestingly, even though the LAD presented with significantly lower average absolute WSS (Table 2), a wide range in WSS per vessel was observed. Therefore, the thresholds to demarcate low and high WSS in the LAD using the vessel-specific method were overlapping with the thresholds of the LCX and RCA. Plaque growth of more than 15% PB, i.e. the 90<sup>th</sup> percentile of plaque progression of all sectors, was observed in 8% of the LAD, 15% of the LCX, and 11% of the RCA.

WSS-related plaque progression

The use of different WSS thresholds to define low, mid and high WSS will have an effect on the predictive power of WSS for plaque progression. First, we report the estimated PB progression for sectors exposed to low, mid and high WSS. For vessel-specific WSS tertiles, the plaque progression of the sectors exposed to low WSS was significantly higher compared to the sectors exposed to mid and high WSS (Figure 3A). (low: 3.9% 95%CI (2.5-5.2), mid: 2.0% 95%CI (0.7-3.3) high: 0.8% 95%CI (-0.5-2.2), all  $p<0.024$ . When analyzing the WSS related plaque growth of the different coronary vessels separately, this pattern was also visible in the LAD and RCA, showing significant difference between low WSS and mid/high WSS. The LCX did not show any differences in plaque progression between the three WSS groups (Figure 3A).

When using all sectors within the study to define three equal groups of low, mid and high WSS (*study-specific*), also significant differences in plaque growth were found between sectors exposed to the low, mid and high WSS sectors (Figure 3B). (low: 3.5% 95%CI (2.1-4.9), mid: 2.4% 95%CI (1.0-3.8) high: 0.8% 95%CI (-0.6-2.3), all  $p<0.05$ . Interestingly, after splitting the sectors based on vessel type, only the RCAs in our study demonstrated a similar pattern, which was fully disappeared for the LCX and LAD (Figure 4B).

When defining the WSS categories using *literature-based* absolute thresholds, also significant differences were found between the three different WSS categories with the highest plaque growth for the low WSS sectors (Figure 3C). ((low: 2.9% 95%CI (1.5-4.2), mid:1.7% 95%CI (0.2-3.1) high:0.9% 95%CI (-1.6 – 2.1)  $p<0.05$ . However, for the high WSS sectors no significant plaque growth was observed. For the different vessel types, hardly any plaque growth or differences in plaque growth for the sectors exposed to low, mid and high WSS could be demonstrated (Figure 4C).

Using the *vessel-type-specific* methodology to define the WSS categories, significant differences were found in plaque growth between the three different WSS categories (Figure 3D) ((low: 3.8% 95%CI (2.4-5.1), mid:2.1% 95%CI (0.8-3.5) high:0.9% 95%CI (-0.5-2.3))  $p<0.05$ . In a sub-analysis, the LAD and RCA showed significant differences in plaque growth between WSS categories, whereas no significant differences in plaque growth was observed in the LCX. (Figure 4D).

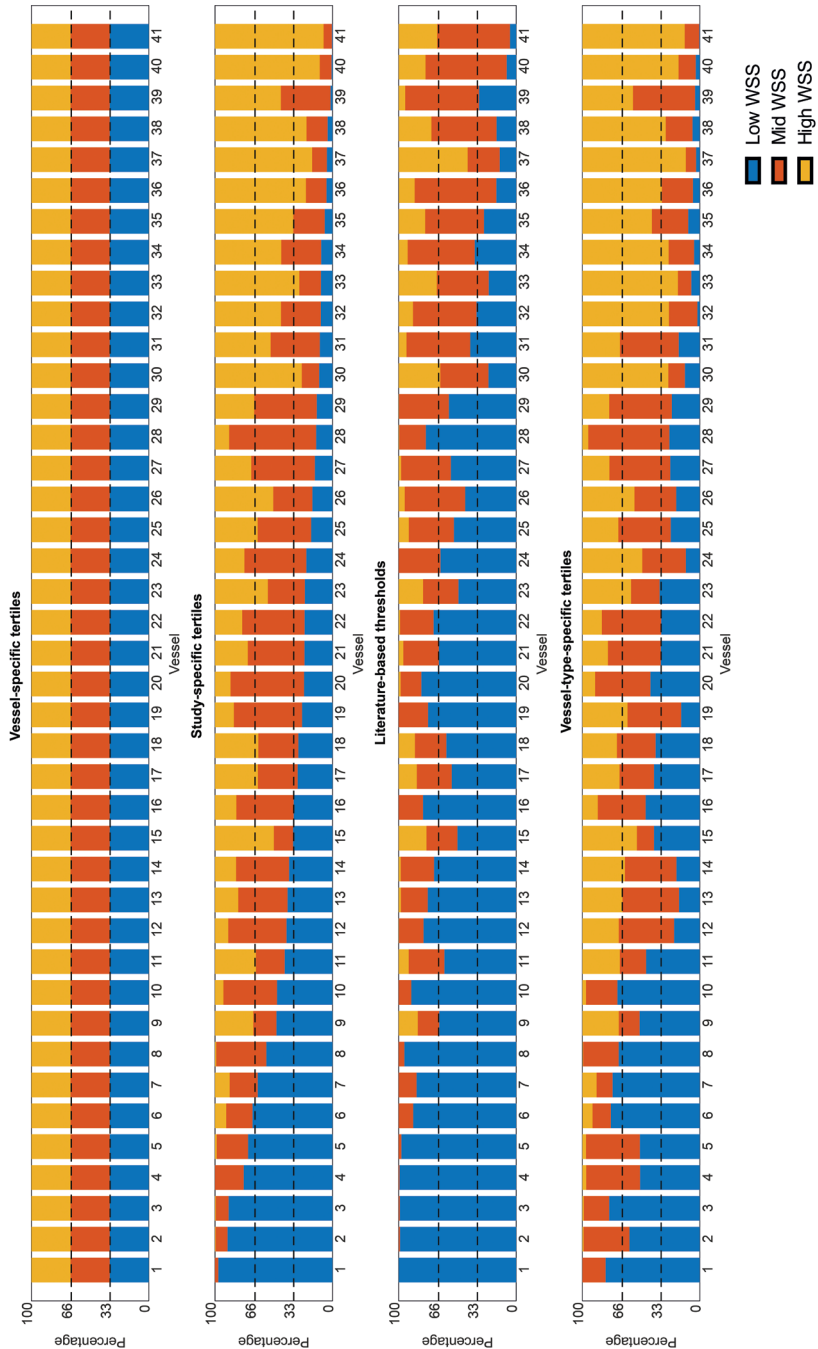


Figure 2. Overview of all individual study vessels (1-41) showing the WSS distribution for each vessel using the four different methodologies of WSS allocation. Sorted from left to right based percentage of low WSS in study-specific thresholds. Low WSS = blue, Mid WSS = orange, High WSS = yellow.

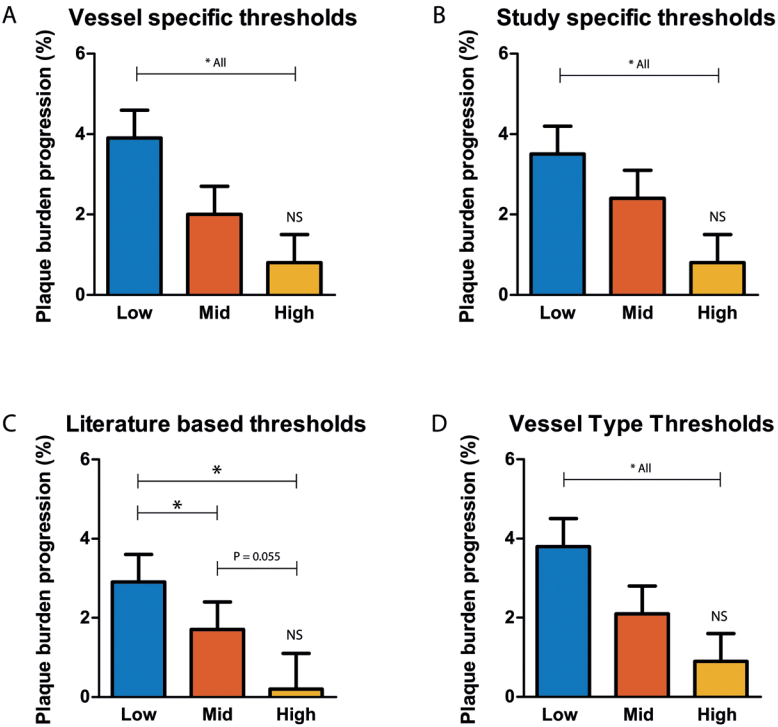


Figure 3. Wall shear stress distribution and plaque progression for the four different thresholding methodologies. \* p<0.05.

Previous WSS studies did not correct for baseline plaque burden, however, today we recognize that regression to the mean, caused by the semi-automated analysis of the atherosclerotic plaque should be considered as a potential explanation for the findings of plaque changes over time. Interestingly, only the vessel-specific method, with WSS categorized into low, mid and high per vessel, showed significant plaque growth for the sectors exposed to low WSS, compared to mid and high WSS (low-mid p=0.025; low-high p=0.024)

To gain extra insight in the predictive value of low WSS for plaque progression applying the different methodologies, the odds ratio for plaque growth of 15% PB in sectors exposed to low WSS was determined. When using the *vessel-specific* tertiles, sectors exposed to low WSS had an odds ratio (OR) of 1.6 (1.3-2.1) for plaque growth. For the *study-specific* tertiles, the OR was 1.5 (1.1-2.0), and for the *literature-based* thresholding, low WSS did not show a significant association between the exposure to low WSS and plaque growth (OR: 1.4 (1.0-2.0)) Using the *vessel-type-specific* tertiles, the OR was 1.6 (1.2-2.2) (Figure 5).

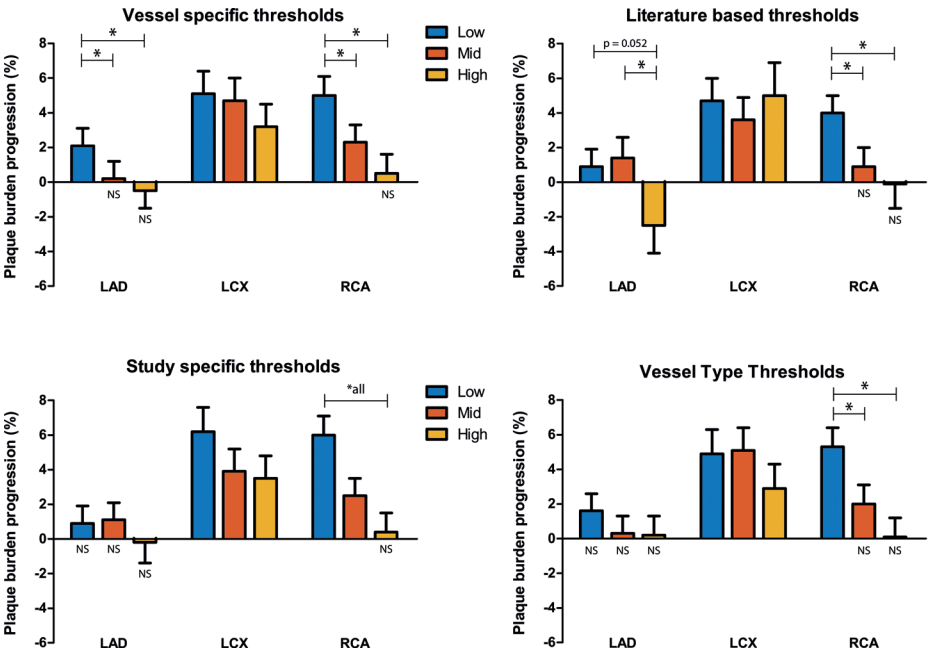


Figure 4. Wall shear stress distribution and plaque progression for the four different thresholding methodologies split up in the three coronary artery types. \* p<0.05.

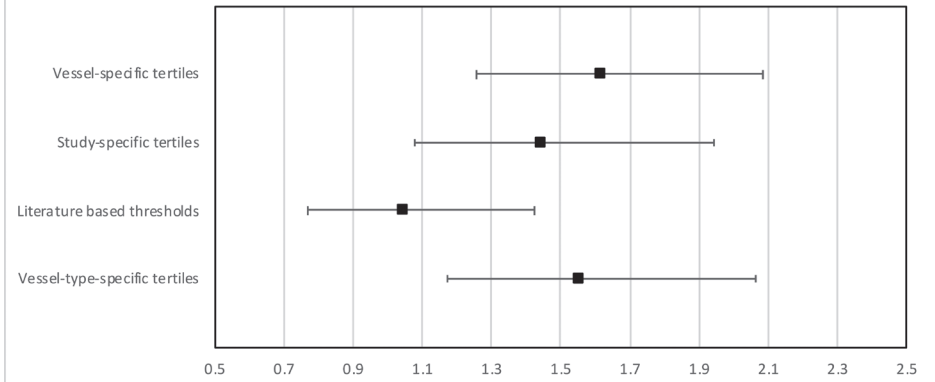


Figure 5. The predictive value of low WSS as predictor for plaque progression for the four different thresholding methodologies.

## Discussion

Wall shear stress of the blood flow at the vessel wall has been proven to impact the natural history of atherosclerotic plaque initiation, progression and destabilization. With data from recent clinical trials and current technical advances, WSS will potentially identify regions at risk of future plaque progression and cardiovascular events. However, different definitions of low and high WSS have been used across studies. Until now it is unclear how these differences impact the final outcome and should be considered when comparing the results. For the use of WSS in future clinical applications, it is essential to line up matters. Therefore, we evaluated the different definitions of low, mid and high WSS within one dataset for their impact on the estimation of plaque progression and the predictive power.

The most important findings of this study were: 1) The absolute WSS distribution majorly varies between the vessels, causing unevenly distributed low, mid and high WSS sectors between the vessels if *study-specific*, *literature-based*, or *vessel-type-specific* thresholds were used. 2) For all methodologies, sectors of low WSS showed significant plaque progression compared to mid and high WSS. However, after correcting for baseline plaque burden, only *vessel-specific* tertiles showed significantly more plaque progression at low compared to mid and high WSS. 3) The predictive power of low WSS for plaque progression compared to all the other sectors was significant using all different thresholds, except for the *literature-based* thresholds. The predictive power was most pronounced applying *vessel-specific* or *vessel-type-specific* tertiles for the definition of low WSS. 4) The effect of the definition of the WSS categories on the estimation of plaque progression varies among the different vessel types.

WSS is a continuous variable, varying in magnitude at the endothelial layer of the vessel wall with low WSS often observed close to side branches or in the inner curvature of the artery. These patched differences in wall shear stress have been related to plaque distribution and progression<sup>18</sup>. This study is the first showing heterogeneity in absolute WSS values among coronary arteries of different patients. Using absolute thresholds, some vessels will completely be characterized as low or high WSS. Knowing the patched pattern of atherosclerosis, these definitions might need more nuances, especially for the identification of regions that are at risk of future plaque progression. Interestingly, and similar to the earlier studies, we found independent of the definition of low WSS, low WSS always showed significant plaque progression. This explains why the different research groups, using different definitions of low WSS, still find similar results for low WSS regions being more susceptible to plaque progression<sup>2,19,20</sup>. Interestingly, after correction for baseline plaque burden only vessel-specific tertiles showed significant plaque progression for the sectors exposed to low WSS compared to

high WSS. Furthermore, analysing the predictive power of low WSS for plaque progression (the highest 90<sup>th</sup> percentile PB change), all but *literature-based* WSS distribution showed a significant OR, although no large differences were seen in OR between the methodologies. Whereas the absolute, *literature based*, thresholds did not show significant predictive power. The heterogeneity of the absolute WSS values might be the cause of loss in predictive power.

The absolute WSS distribution observed in the coronary arteries largely depends on the different assumptions regarding the flow and the 3D-reconstruction of the coronary arteries applied for the calculations. The used methodologies and assumptions of calculating WSS vary considerably among the different studies. Some studies use flow as derived from angiography<sup>2,12</sup>, while others use Doppler flow measurements<sup>3,21</sup>. Also, studies differ in the use of stationary flow versus pulsatile flow and multiple different flow patterns were applied as input for computational fluid dynamics. Furthermore, the 3D-reconstructions of the coronary arteries vary with respect to the presence of side branches and the used invasive imaging modalities to assess detailed information on the lumen shape (IVUS or OCT)<sup>19,22</sup>. If side branches are not included in the CFD model, all flow will remain in the main coronary branch and the smaller artery naturally present more distal in the vascular tree will be incorrectly classified as high WSS. Both the integration of side branches in the 3D geometry as well as patient-specific flow measurements will highly affect the calculated absolute WSS values.

In our study we used patient-tailored CFD models including side branches, with the use of patient-specific flow measurements at each single side branch. The *study-specific* thresholds that we found (low WSS: <0.6Pa and high WSS: >1.14Pa) were much lower than the literature based WSS thresholds. This might be related to the side branches that we included in our models. Interestingly, Samady et al. did include side branches in their models, however their WSS obtained in LADs were much higher than the values we found in the LAD. Speculating on the cause of this difference, one of the reasons might be the use of different inlet profiles. Samady et al. used a plug profile with velocity equal to 80% of the peak velocity measured. In this current study, a parabolic profile with a mean velocity of the peak velocity was used<sup>7</sup>. Both methods have been previously used, and are part of the assumptions necessary for the CFD, however could explain the overall higher WSS found in their coronary models with side branches.

If we applied the *literature-based* thresholds (low WSS: <1 and high WSS >2.5 Pa) to define the WSS categories, we could not demonstrate the often-observed inverse relationship between plaque progression and WSS<sup>2,11</sup>. So, it is advisable that if absolute thresholds are used from literature to define the WSS categories, the applied methodology for WSS calculation and the patient population is similar to

the study that provides the absolute thresholds to find comparable WSS-related plaque progression.

Due to the observed considerable heterogeneity in WSS among the patients, we noticed that by applying absolute *literature-based* thresholds or *study-specific* tertiles to categorize the WSS, some vessels in this dataset qualified almost entirely as low WSS (Figure 2). To further investigate the WSS-related heterogeneous patched distribution of plaques in those vessels, a sub-analysis of the 10 vessels with the highest number of sectors exposed to absolute low WSS ( $<1\text{Pa}$ , *literature-based* threshold) was performed. Interestingly, we observed that the sectors exposed to the lowest WSS in those vessels (thus *vessel-specific* low WSS), demonstrate significantly higher plaque progression than the sectors exposed to mid and high WSS. This implies that in a vessel mainly exposed to absolute low WSS, there is still a significant variation in plaque progression between the sectors exposed to relatively low and high WSS within the vessel.

It is known that the three main coronary arteries have geometrical and hemodynamical differences<sup>23</sup>. Therefore, we hypothesized that the definition of low and high WSS to predict plaque progression and destabilization could be different among the different vessel types. Indeed, both the WSS-related plaque progression and the predictive power of low WSS for plaque progression differed considerably among the different vessel types. The absolute WSS values differed significantly between the three vessels, with the LAD having the lowest absolute WSS values and the LCX the highest absolute shear stress values. These differences are of substantial influence when dividing the sectors according to *study-specific* thresholds or *literature-based* thresholds, especially for the association of low WSS with plaque progression. Although the LCX showed the highest absolute WSS, sectors showed more plaque progression than the LAD, being exposed to lower absolute WSS. The variations in absolute plaque growth and WSS-related plaque growth in these different vessel types might be attributed to differences in local hemodynamics<sup>23–25</sup>, geometrical differences concerning curvature and number of side branches<sup>26</sup>. Unfortunately, the number of coronary arteries investigated in this study was too small to allow a detailed analysis of these differences.

As described above, the absolute WSS is affected by the flow and therefore patient-specific flow measurements are often used in the CFD simulations to obtain accurate absolute WSS values. However, flow measurements are labour-intensive and challenging in clinical practice. With the use of *vessel-specific* thresholds, the lowest one-third WSS at the vessel wall will always be allocated as low WSS, regardless of the magnitude of the WSS, with the benefit that invasive flow measurements become redundant. The absolute measured velocity might become subordinate to the lumen geometry of the reconstructed vessel, for the

allocation of low and high WSS. This is attractive in case the flow measurements are not available, for instance, in retrospective studies. Since this study showed that WSS-related plaque progression as based on vessel-specific WSS thresholds was not inferior to *study-specific* WSS thresholds, future research might adopt this approach to identify regions at risk. However, when using assumptions for the flow, the absolute WSS values among the patients cannot be compared which in future studies with other objectives could be required

## Conclusion

In this study different methodologies were applied to define low, mid and high WSS in human coronary arteries of acute coronary syndrome patients. We studied the predictive power of low WSS using the different definitions of low WSS for plaque progression within one patient group. On population level, the established patterns of most plaque progression at regions exposed to low WSS are visible in all the methodologies. However, on an individual basis with measured vessel-specific flow, WSS values vary too widely to use absolute thresholds for determining low WSS when used to identify regions at risk of plaque progression. Depending on the research question, using a relative measure by dividing coronary arteries in *vessel-specific* tertiles is a robust methodology to predict local plaque progression.



## References

1. Bourantas C V, Zanchin T, Sakellarios A, Karagiannis A, Ramasamy A, Yamaji K, et al. Implications of the local haemodynamic forces on the phenotype of coronary plaques. *Heart* 2019;105:1078–86.
2. Stone PH, Saito S, Takahashi S, Makita Y, Nakamura SS, Kawasaki T, et al. Prediction of progression of coronary artery disease and clinical outcomes using vascular profiling of endothelial shear stress and arterial plaque characteristics: the PREDICTION Study. *Circulation* 2012;126:172–81.
3. Samady H, Eshtehardi P, McDaniel MC, Suo J, Dhawan SS, Maynard C, et al. Coronary Artery Wall Shear Stress Is Associated With Progression and Transformation of Atherosclerotic Plaque and Arterial Remodeling in Patients With Coronary Artery Disease. *Circulation* 2011;124:779–88.
4. Hoogendoorn A, Kok AM, Hartman EMJ, de Nisco G, Casadonte L, Chiastra C, et al. Multidirectional wall shear stress promotes advanced coronary plaque development: comparing five shear stress metrics. *Cardiovasc Res* 2020;116:1136–46.
5. Chatzizisis YS, Coskun AU, Jonas M, Edelman ER, Feldman CL, Stone PH. Role of Endothelial Shear Stress in the Natural History of Coronary Atherosclerosis and Vascular Remodeling. Molecular, Cellular, and Vascular Behavior. *J Am Coll Cardiol* 2007;49:2379–93.
6. De Nisco G, Hoogendoorn A, Chiastra C, Gallo D, Kok AM, Morbiducci U, et al. The impact of helical flow on coronary atherosclerotic plaque development. *Atherosclerosis* 2020;300:39–46.
7. Asakura T, Karino T. Flow patterns and spatial distributions of atherosclerotic lesions in human coronary arteries. *Circ Res* 1990;66:1045–66.
8. Chatzizisis YS, Toutouzias K, Giannopoulos AA, Riga M, Antoniadis AP, Fujinomi Y, et al. Association of global and local low endothelial shear stress with high-risk plaque using intracoronary 3D optical coherence tomography: Introduction of “shear stress score.” *Eur Heart J Cardiovascular Imaging* 2017;18:888–97.
9. Stone PH, Maehara A, Coskun AU, Maynard CC, Zaromytidou M, Siasos G, et al. Role of Low Endothelial Shear Stress and Plaque Characteristics in the Prediction of Nonculprit Major Adverse Cardiac Events. *JACC Cardiovasc Imaging* 2018;11:462–71.
10. De Nisco G, Kok AM, Chiastra C, Gallo D, Hoogendoorn A, Migliavacca F, et al. The Atheroprotective Nature of Helical Flow in Coronary Arteries. *Ann Biomed Eng* n.d.;47.
11. Kok AM, Molony DS, Timmins LH, Ko Y-A, Boersma E, Eshtehardi P, et al. The Influence of Multidirectional Shear Stress on Plaque Progression and Composition Changes in Human Coronary Arteries. *EuroIntervention* 2019.
12. Kumar A, Hung OY, Piccinelli M, Eshtehardi P, Corban MT, Sternheim D, et al. Low Coronary Wall Shear Stress Is Associated With Severe Endothelial Dysfunction in Patients With Nonobstructive Coronary Artery Disease 2018.
13. Costopoulos C, Timmins LH, Huang Y, Hung OY, Molony DS, Brown AJ, et al. Impact of combined plaque structural stress and wall shear stress on coronary plaque progression, regression, and changes in composition. *Eur Heart J* 2019;40:1411–22.
14. Hartman EMJ, De Nisco G, Kok AM, Hoogendoorn A, Coenen A, Mastik F, et al. Lipid-rich Plaques Detected by Near-infrared Spectroscopy Are More Frequently Exposed to High Shear Stress. *J Cardiovasc Transl Res* 2020.
15. van der Giessen AG, Schaap M, Gijzen FJH, Groen HC, van Walsum T, Mollet NR, et al. 3D fusion of intravascular ultrasound and coronary computed tomography for in-vivo wall shear stress analysis: a feasibility study. *Int J Cardiovasc Imaging* 2010;26:781–96.
16. Gijzen F, Katagiri Y, Barlis P, Bourantas C, Collet C, Coskun U, et al. Expert recommendations on the assessment of wall shear stress in human coronary arteries: existing methodologies, technical considerations, and clinical applications. *Eur Heart J* 2019;40:3421–33.
17. Seo T, Schachter LG, Barakat AI. Computational study of fluid mechanical disturbance induced by endovascular stents. *Ann Biomed Eng* 2005;33:444–56.
18. Caro GG. Discovery of the role of wall shear in atherosclerosis. *Arterioscler Thromb Vasc Biol* 2009;29:158–61.
19. Wentzel JJ, Chatzizisis YS, Gijzen FJHH, Giannoglou GD, Feldman CL, Stone PH. Endothelial shear stress in the evolution of coronary atherosclerotic plaque and vascular remodelling: current understanding and remaining questions. *Cardiovasc Res* 2012;96:234–43.
20. Bourantas C V, Räber L, Sakellarios A, Ueki Y, Zanchin T, Koskinas KC, et al. Utility of Multimodality Intravascular Imaging and the Local Hemodynamic Forces to Predict Atherosclerotic Disease Progression. *JACC Cardiovasc Imaging* 2020;13:1021–32.
21. Shishikura D, Sidharta SL, Honda S, Takata K, Kim SW, Andrews J, et al. The relationship between segmental wall shear stress and lipid core plaque derived from near-infrared spectroscopy. *Atherosclerosis* 2018;275:68–73.
22. Vergallo R, Papafakis MI, Yonetsu T, Bourantas C V, Andreou I, Wang Z, et al. Endothelial Shear Stress and Coronary Plaque Characteristics in Humans. *Circ Cardiovasc Imaging* 2014;7:905–11.
23. Chatzizisis YS, Giannoglou GD, Parcharidis GE, Louridas GE. Is left coronary system more susceptible to atherosclerosis than right? *Int J Cardiol* 2007;116:7–13.
24. Rikhtegar F, Knight JA, Olgac U, Saur SC, Poulikakos D, Marshall WC, et al. Choosing the optimal wall shear parameter for the prediction of plaque location—A patient-specific computational study in human left coronary arteries. *Atherosclerosis* 2012;221:432–7.
25. Knight J, Olgac U, Saur SC, Poulikakos D, Marshall W, Cattin PC, et al. Choosing the optimal wall shear parameter for the prediction of plaque location—A patient-specific computational study in human right coronary arteries. *Atherosclerosis* 2010;211:445–50.
26. Wentzel JJ, Morbiducci U, Kok AM, Kwak BR, Stone PH, Steinman DA, et al. Atherosclerosis at arterial bifurcations: evidence for the role of haemodynamics and geometry 2016;115:484–92.



# 3

## Invasive coronary imaging in familial hypercholesterolemia pig model

This chapter adapted from:

Variation in coronary atherosclerosis severity related to a distinct LDL profile – findings from a familial hypercholesterolemia pig model

Ayla Hoogendoorn, Sandra den Hoedt, Eline M.J. Hartman, Ilona Krabbendam – Peters, Maaike te Lintel Hekkert, Leonie van der Zee – van Vark, Kim van Gaalen, Karen Th. Witberg, Kristien Dorst, Jurgen M. R. Ligthart, Ludovic Drouet, Kim Van der Heiden, Jeanine Roeters van Lennep, Antonius F.W. van der Steen, Dirk J. Duncker, Monique T. Mulder, Jolanda J. Wentzel

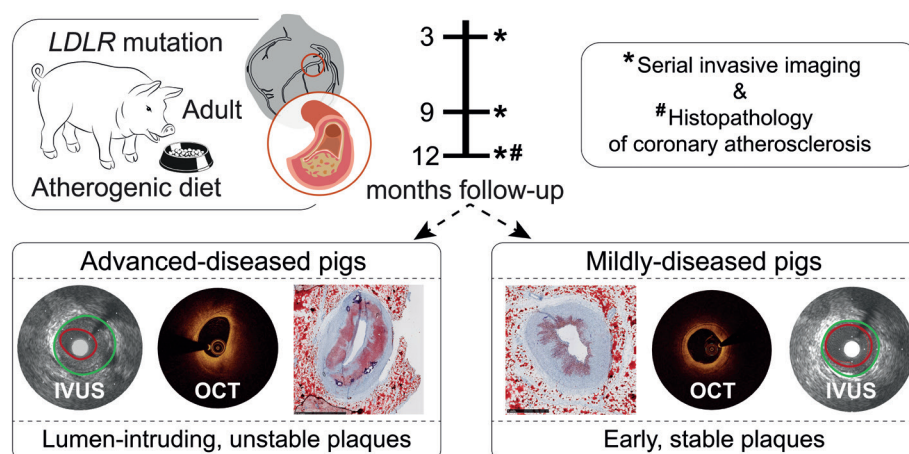
*Published Atherosclerosis vascular biology, 2019*

## Abstract

**Objective** - In an adult porcine model of familial hypercholesterolemia (FH), coronary plaque development was characterised by using serial intravascular multimodality imaging and histology.

**Approach and results** - FH pigs (3 years old, homozygous *LDLR* R84C mutation) received an atherogenic diet for 12 months. Coronary atherosclerosis development was monitored at three timepoints (3, 9 and 10-12 months) by using serial near-infrared spectroscopy-intravascular ultrasound (NIRS-IVUS) and serial optical coherence tomography (OCT). Unexpected, the animals could be divided into two groups; mildly-diseased pigs (MDs)(n=5) and advanced-diseased pigs (ADs) (n=5). The ADs and MDs displayed no differences in conventional risk factors. Nevertheless, this difference was primarily observed using IVUS, where MDs exclusively developed early plaque lesions (maximal plaque burden 25% (23%-34%)) (n=5), and ADs developed more human-like, lumen intruding plaques (maximal plaque burden 69% (57%-77%)). The large majority of the OCT-detected plaques presented as lipid-rich, although fibro cap atheromas (FCA) were scarce. On the other hand, histology showed large necrotic cores, intra-plaque haemorrhage and calcifications in the developed plaques.

**Conclusions** - We describe a new adult FH pig model with differences found based on intravascular imaging and histology.



## Introduction

Coronary atherosclerotic plaque destabilisation and rupture is one of the most important causes of acute coronary events and sudden death<sup>1-3</sup>. Therefore, risk-assessment of atherosclerotic plaques prior to the occurrence of an acute coronary event is an important focus of coronary artery disease (CAD) research. Herein, *in vivo* studies with serial imaging and histopathological analyses are essential to understand the mechanisms and causative factors of plaque growth and destabilisation. Unfortunately, natural history studies in humans are limited by the long time-frame of disease development, by the small number of longitudinal (invasive) imaging time points, and by the very limited possibility to collect tissue. This urges the need for a preclinical animal model that presents with human-like coronary artery disease.

Because of their comparable coronary size, anatomy and diet, pigs are currently the animal model that most closely resembles the human disease pathophysiology and that is most suitable for testing new imaging methods<sup>4-6</sup>. Atherosclerosis development in pig models is often stimulated by a combination of atherogenic diet<sup>7</sup> and/or diabetes<sup>8-14</sup>. Some of the most successful porcine models for non-surgical induced atherosclerosis carry mutations in genes that regulate the lipid metabolism, like in the *LDLR*<sup>15,16</sup> or *PCSK9*<sup>17</sup> genes. These mutations are similar to those found in patients with familial hypercholesterolemia (FH) and result in high plasma cholesterol levels<sup>18</sup>. On an atherogenic diet, these FH pig models do develop (coronary) atherosclerotic disease, but, like in most other pig models, plaque progression is often modest and does not reach human-like advanced disease stages with symptomatic plaques, especially in the coronary arteries.

Previous studies with atherosclerotic pig models assessed plaque development exclusively in young and growing animals. For humans, it is known that lipid profiles, blood pressure, arterial mechanics and inflammatory status are very different between adolescents and older people<sup>19-21</sup>, while these are factors with a major impact on atherosclerotic disease development. These factors may thus also affect atherosclerosis development in young pigs. Therefore, we refined a previously described and promising *LDLR* mutation mini-pig model<sup>15</sup> by using adult animals from the start of the study. Furthermore, in contrast to earlier studies, we followed these animals for up to one year after the start of an atherogenic diet and monitored natural atherosclerotic plaque development and composition in the coronary arteries using multiple invasive imaging techniques and histology. We provide a detailed analysis on plaque size, localisation and composition at three time points during the follow-up period on atherogenic diet as a road-map for future studies with this promising pig model.

## Material and Methods

### FBM pig model, plaque imaging and histology

The animal study protocol was approved by the local animal ethics committee (DEC EMC3318 (109-14-10)) and the study was performed according to the National Institutes of Health guide for the Care and Use of Laboratory animals<sup>22</sup>. Familial Hypercholesterolemia Bretonchelles Meishan minipigs homozygous for the *LDLR* R84C mutation (n=11, castrated male) as described before by Thim *et al.*<sup>15</sup>, were fed a normal laboratory diet (#102243/60, Sanders Ouest, Etrelles, France) until the start of the study. Since female pigs of this breed develop considerably less coronary atherosclerosis (unpublished data by Drouet *et al.*), and since the main aim of this study was to study development of advanced atherosclerosis in this pig model, only castrated males were used. At the age of 34±3 months, an atherogenic diet (10% lard and 0.75% cholesterol, The National Institute of Agronomic Research, France) was started. Plaque development in the coronary arteries was monitored by performing invasive imaging of the left anterior descending (LAD), the left circumflex (LCX) and the right coronary artery (RCA) using intravascular ultrasound (IVUS) and optical coherence tomography (OCT). The imaging protocol was performed at 3 time points (3 (T<sub>1</sub>), 9 (T<sub>2</sub>) and 10-12 (T<sub>3</sub>) months on atherogenic diet) to assess (changes in) plaque size and composition.

The day before the imaging procedure, the pigs were fasted and were given an oral loading dose of 300mg carbasalate calcium. On the day of the procedure, the animals were sedated with a mix of Xylazine (2.25mg/kg, 20 mg/ml) and Zoletil 100 (tiletamine/zolazepam) (6mg/kg, 100 mg/ml) injected intramuscularly, anesthetised with sodium thiopental (4mg/kg, 50mg/ml) administered via an ear vein, intubated and ventilated with oxygen (25-30% v/v) and nitrogen (75-80% v/v) to maintain blood gases within the physiological range. Anaesthesia was maintained by isoflurane inhalation (1–2.5% v/v).

Via a carotid sheath, arterial blood samples were collected, and 250mg acetylsalicylic acid and 10,000 units of heparin were administered to prevent blood clotting. Heparin administration was repeated every hour in a dose of 5,000 units. Subsequently, a guiding catheter (Mach 1, 8F, various types, Boston Scientific, Marlborough, MA, USA) was advanced through the carotid sheath into the ostium of either one of the three main coronary arteries under angiographic guidance to perform a series of imaging procedures. Before imaging, isosorbide mononitrate (0.04mg/kg, 1mg/ml) was administered via the guiding catheter to induce epicardial coronary vasodilation. Starting position of all imaging catheters was registered by serial monoplane angiography under at least 2 angles. First, an optical coherence tomography (OCT) catheter (Dragonfly Optis Imaging Catheter, St. Jude Medical, St. Paul, MN, USA) was advanced into the artery as distal as possible up to

a maximal depth of 75mm. A pullback of 75 mm (36 mm/s) was performed under a constant contrast (Visipaque 320, GE Healthcare, Buckinghamshire, U.K.) flush rate of 4 mL/s (Medrad Injection System, Bayer HealthCare LLC, Whippany, NJ, USA). Subsequently, an intravascular ultrasound (IVUS) catheter (TVC Insight Coronary Imaging Catheter, InfraRedX, Burlington, MA, USA) was positioned at the same anatomical location as the OCT catheter and a pullback (0.5 mm/s) was performed. During the IVUS pullback, the heart rate was closely monitored and registered for later use in IVUS-triggering.

During the imaging procedure at the first time point, one of the pigs died due to an acute cardiac tamponade and was excluded from the study. Furthermore, fast plaque development in two other pigs led to cardiovascular complications and subsequent early sacrifice shortly after T<sub>2</sub>. Of these two latter pigs, the data of T<sub>1</sub> and T<sub>2</sub> were used for analysis. After the final imaging time point, the pigs were sacrificed and the coronary arteries were collected for histology.

### Coronary Histology

Coronary tissue was sampled every 3 mm and was used for histological (Haematoxylin and Eosin (HE), Resorcin-Fuchsin or Miller (collagen and elastin), Oil-red-O (ORO) (lipids) and Martius, Scarlet and Blue (MSB) (fibrin)) and immunohistochemical stainings (CD68 (macrophages), CD31 (endothelial cells)). For the analysis, histological slides taken every 3mm were classified according to the revised AHA classification<sup>23</sup> as no plaque (NP), intimal thickening (IT), intimal xanthoma (IX), pathological intimal thickening (PIT) and fibrous cap atheroma (FA). Quantification of the plaque components was performed by manual or semi-automatic delineation of the lumen, media, outer wall and the respective plaque component on all histological slides using BioPix IQ software (BioPix AB, version 3.4.0).

Analysis of IVUS and OCT data was performed using QCU-CMS software (version 4.69, Leiden University Medical Centre, LKEB, Division of Image Processing/MEDIS medical imaging systems BV, Leiden). ECG-gated IVUS images were analysed approximately every 0.5 mm to assess lumen and outer wall dimensions and thus plaque size. For final analysis, data were averaged over 3mm in longitudinal direction to reduce the influence of manual drawing errors and to reduce statistical dependence amongst the data points. The plaque size was also assessed by classifying the maximal intima-media thickness (IMT) per 3mm-segment into 4 grades (<0.5mm, 0.5-0.7mm, 0.7-1.0mm and >1.0mm) according to the method of Chatzizisis *et al.*<sup>9</sup> The percentage of the segments occupied by the respective grade was quantified per artery and averaged over all arteries.



OCT data were analysed every millimetre (1 out of 5 frames) according to consensus standards as fibrous plaque, lipid-rich plaque or a fibrous cap atheroma (FCA) in pullbacks that showed at least one frame with visible plaque. Angles for individual plaque components were drawn manually.

### Statistics

IBM SPSS Statistics (version 21.0) software was used for statistical analysis. Non-normal distributed data are presented as median (range) and statistical difference was determined with the Mann-Whitney U test. Normally distributed data are shown as mean±standard deviation (SD) and significance was determined using an unpaired student's t-test, a repeated measures ANOVA with post-hoc testing (Bonferroni) or a paired student's t-test. Difference in the frequency distribution of different plaque categories was tested using a Chi-square test or a Fisher's exact test. Absolute values subtracted from imaging and histological data were averaged per artery. For categorical multiple group comparison, z-scores >1.96 were regarded significant. For all other tests  $p < 0.05$  was regarded to indicate statistical significance.

## Results

### General model characteristics

The weight of the pigs remained constant during the follow up period at 86 kg (60-104 kg). After 3 months of atherogenic diet, a significant increase in total cholesterol (from 1.9 mM (1.8-2.2 mM) to 10.4 mM (8.9-22.3 mM)), LDL-cholesterol (LDL-C) (from 1.5 mM (1.4-1.8 mM) to 8.8 mM (6.7-23.3 mM)) and HDL-cholesterol (HDL-C) levels (from 0.3 mM (0.2-0.3 mM) to 2.9 mM (2.1-4.9 mM)) was observed compared the levels before atherogenic diet ( $p < 0.05$ ).

### Advanced and mildly-diseased pigs: general characteristics and in vivo IVUS measurements of plaque size and plaque growth

Five of the 10 pigs displayed development of large, lumen intruding plaques in the coronary arteries (maximal plaque burden 69% (57%-77%)) (advanced-diseased pigs (ADs)) while the other 5 pigs showed limited plaque development (maximal plaque burden 25% (23%-34%)) (mildly-diseased pigs (MDs)) (Figure 1A). Although the animals were run in two subsequent groups, the distribution of the AD/MD animals over both groups appeared random (Group 1: 2/6; Group 2: 3/5 (ADs/total number of animals)), ruling out the effect of factors like housing, diet, seasonal period or birth-year. Since the difference in plaque development between both groups was so pronounced, all subsequent results are presented separately for the MDs and the ADs.

In the ADs, plaque area (PA) was markedly larger and lumen area (LA) was smaller compared to the MDs ( $p < 0.05$ ) (Figure 1B and C). The ADs demonstrated significant increase in PA (Figure 1B) and decrease in LA (Figure 1C) at  $T_2$  and  $T_3$  compared to  $T_1$  ( $p < 0.05$ ). In the MDs, plaque growth (Figure 1B) was limited but still significant ( $p < 0.05$ ), while the LA (Figure 1C) showed a slight increase from  $T_1$  to  $T_2$  ( $p < 0.05$ ) and a decrease at  $T_3$  ( $p < 0.05$ ).

At the last time point, on average 21% of the analysed segments of the ADs was occupied by plaques with a maximal intima-media thickness (IMT) >1.0mm while in the MDs none of the segments demonstrated plaques with this IMT grade (Figure 1D).

### Plaque classification by OCT

The percentage of OCT frames that presented with plaque increased over time in both the MD and AD pigs (Figure 1F). The large majority of the OCT-detected plaques presented as lipid-rich and this distribution did not change over time (Figure 1F). OCT-observed fibrous cap atheroma (FCA) were rare. In ADs, OCT-FCA occurrence increased between  $T_1$  and  $T_2$  from 4.4% (7 frames) to 7.4% (35 frames) of the total number of frames with plaque ( $p = 0.001$ ) and tended to decrease again at  $T_3$  to 3.8% (11 frames) ( $p = 0.07$ ) (Figure 1F). This latter observation is explained by the loss of 2/5 AD pigs before  $T_3$  which demonstrated the majority of OCT-FCAs (57%) at  $T_2$ . In the MDs, OCT-FCA were only observed at  $T_3$  in

2.0% (3 frames) of the total number of frames with plaque. In a more detailed analysis, the ADs displayed an increase in the average total plaque angle between  $T_1$  and  $T_2$  which could mainly be attributed to the increase in both fibrous and lipid-rich angles ( $p < 0.05$ ) (Figure 1G). Furthermore, there was a small, but non-significant increase in the lipid-pool angle. Between  $T_2$  and  $T_3$ , both the average plaque angle and the composition remained constant in the ADs which can again be explained by the loss of 2 AD pigs with the most advanced plaques at  $T_2$ . The MDs displayed a small, but non-significant increase in average plaque angle and no significant changes in plaque composition were observed (Figure 1G). Cap thickness was determined in OCT-FCAs (Figure 1H) and in the ADs respectively 2 ( $T_1$ ), 3 ( $T_2$ ) and 1 ( $T_3$ ) frames presented with a thin-fibrous cap (<65  $\mu$ m). In the MDs, one frame with a thin-fibrous cap atheroma was observed and only at  $T_3$ .

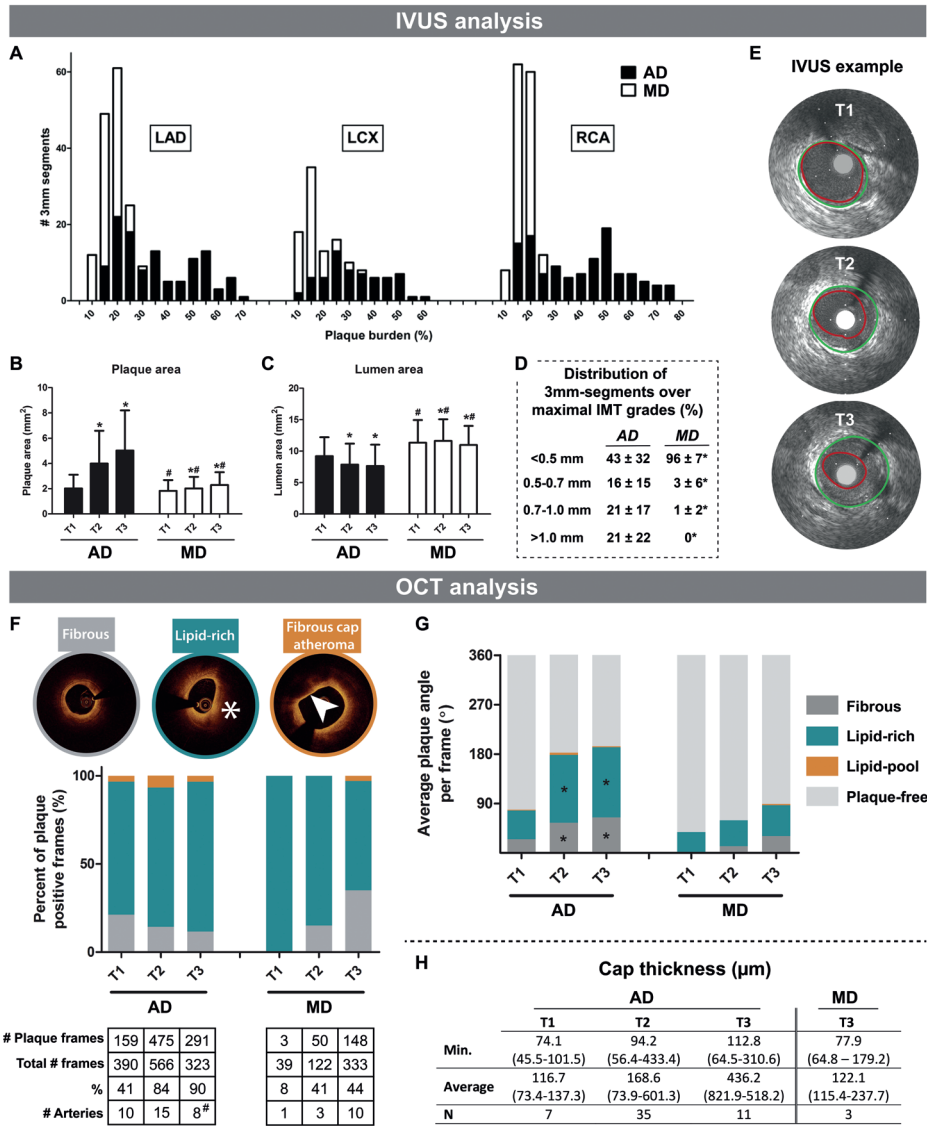


**Figure 1.** In vivo IVUS and OCT analysis of coronary plaque development. IVUS analysis (A-E).

**< Figure 1.** Histogram of the number of 3mm segments (y-axis) with a corresponding PB (%) at the last imaging time point (x-axis) of the advanced-diseased pigs (ADs) (black bars) and mildly-diseased pigs (MDs) (white bars) in the LAD, LCX and RCA. **B-C**) Change of plaque area (PA) (mm<sup>2</sup>) (**B**) and lumen area (LA) (**C**) between T1-T3 (mean±SD). \*p<0.05 compared to T1. #p<0.05 between MDs and ADs at the corresponding time point. **D**) Average percentage (±SD) of the number of 3mm segments per artery that displayed one of the maximal intima-media thickness (IMT) grades at the last imaging time point. \*p<0.05 compared to FRs. **E**) Example IVUS images of plaque growth between T1-T3 at one location in an AD pig. Vessel wall (green) and lumen border (red) are indicated.

**OCT analysis (F-H)** Average percentage of a fibrous, lipid-rich (\*) or fibrous-cap atheroma (FCA; arrowhead points out lipid-pool with overlying fibrous cap) of all plaque positive frames for T1-T3. The total number of plaque positive frames and arteries is depicted under the figure. #Note that at T3, data of 2 highly atherosclerotic AD pigs are missing due to early sacrifice after T2. **G**) The average angle of fibrous plaque, lipid-rich plaque or lipid-pool per frame at T1-T3. **H**) Median (range) cap thickness values derived from the frames presenting with a lipid-pool (i.e. FCA). The minimal (Min.) and average thickness, and the number of fibrous caps are displayed.

**Histological characterisation of the coronary atherosclerotic plaques**

In total, 580 coronary 3 mm segments were analysed by histology: 297 segments from ADs and 283 segments from MDs, with on average 19±6 segments per artery. In the ADs, the presence of a healthy vessel wall or a vessel wall with intimal thickening was rare, while intimal xanthoma, pathological intimal thickening and FCA were each present in approximately one third of all analysed segments (Figure 2A). For the MDs, intimal xanthoma was the most frequently observed plaque type, covering 73.5% of the segments. The frequency of the various plaque classes differed significantly between the ADs and MDs ( $X^2=211.0$ ,  $p<0.0001$ ) (Figure 2A).

The PA of each respective plaque type did not differ between AD and MD pigs (Table 1), while the intima/media ratio for segments with PIT was significantly higher in the AD than the MD pigs.

In the ADs, the anatomical distribution of the various plaque types differed significantly over the coronary arteries with a higher frequency of FCAs in the proximal part of the arteries compared to the distal part ( $\chi^2=39.6$ ,  $p<0.0001$ ). In contrast, the plaque type distribution in the MDs was more homogenous (Figure3A). Mainly for the MDs, the presence of a side branch coincided with a trend towards a more advanced plaque type (Figure 3B). In comparison with the LAD and RCA, the LCX presented with more early-stage plaques which was most apparent in the MDs (Figure 3C).

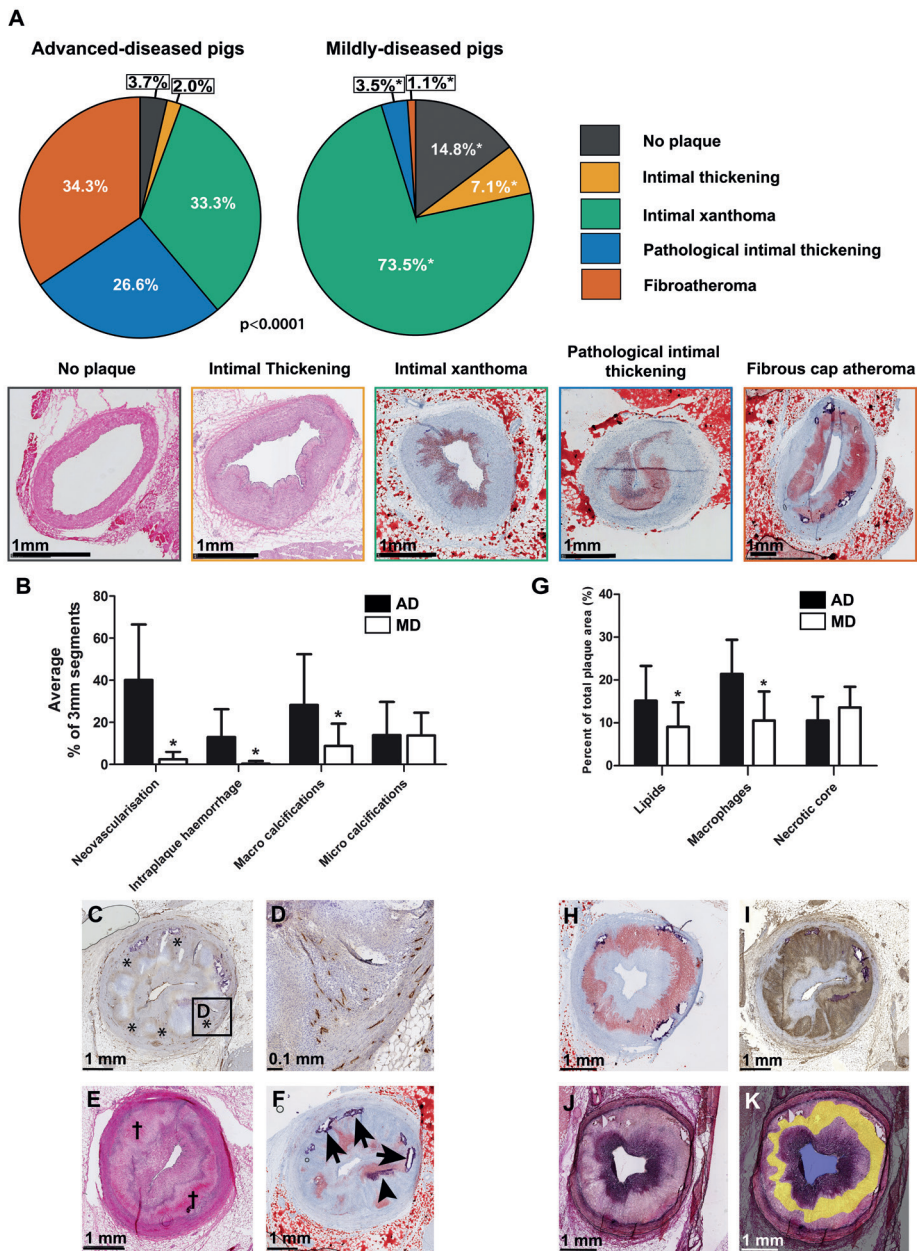


**Figure 2. Histological quantification of coronary plaque classification and components.**  
**A)** Quantification of the frequency of occurrence of the different plaque types. Data are presented as a percentage of the total number of segments, separately for the mildly-diseased pigs (MDs) (283 3mm-segments) and advanced-diseased pigs (AD) pigs (297 3mm-segments). \*z-score>1.96 compared to ADs. Bottom of the figure: example images of the respective plaque types: 'no plaque' and 'intimal

thickening': HE-staining; other plaque types: Oil-red-O staining (red = lipids, purple = calcifications). **B)** Mean ( $\pm$ SD) percentage of 3mm segments per artery that contained the respective plaque component in ADs (black bars) and MDs (white bars). \*p<0.05. **C-F** histological examples of the plaque components quantified in the bar graph. **C)** Neovascularisation (\*, CD31-staining; brown), **D)** Magnification of C). **E)** Intraplaque haemorrhage ( $\dagger$ , HE-staining). **F)** Lipids (Oil-red-O staining: red), microcalcifications (arrowhead) and macrocalcifications (arrows). **G)** Mean ( $\pm$ SD) area percentage per artery of the respective plaque component in ADs (black bars) and MDs (white bars) in segments positive for that plaque component. \*p<0.05 compared to ADs. **H-K)** Example images of: **H)** lipids (Oil-red-O staining (red)); **I)** macrophages (CD68 staining (brown)); **J)** collagen (Miller staining (purple)). The Miller staining was used to delineate the necrotic core (indicated in yellow in **K)**).

**Table 1. Plaque area and intima-media ratio for every plaque type as determined by histology.**

	Advanced-diseased pigs				Mildly-diseased pigs			
	IT	IX	PIT	FCA	IT	IX	PIT	FCA
PA (mm <sup>2</sup> )	0.90 $\pm$ 1.12	0.92 $\pm$ 0.60	2.09 $\pm$ 0.90	4.23 $\pm$ 1.38	0.69 $\pm$ 0.55	0.75 $\pm$ 0.34	1.78 $\pm$ 0.65	3.38 $\pm$ 2.25 <sup>†</sup>
IMR	0.63 $\pm$ 0.68	0.69 $\pm$ 0.35	1.78 $\pm$ 0.48	2.56 $\pm$ 0.70	0.35 $\pm$ 0.23	0.54 $\pm$ 0.36	1.06 $\pm$ 0.38*	1.48 $\pm$ 0.74 <sup>†</sup>

PA=plaque area, IMR=intima/media ratio, IT=intimal thickening, IX=intimal xanthoma, PIT=pathological intimal thickening, FCA= fibrous cap atheroma. \*p<0.05 compared to the same plaque type of the advanced-diseased pigs. <sup>†</sup>FCA in mildly-diseased pigs: n=3, no statistics performed on this category.

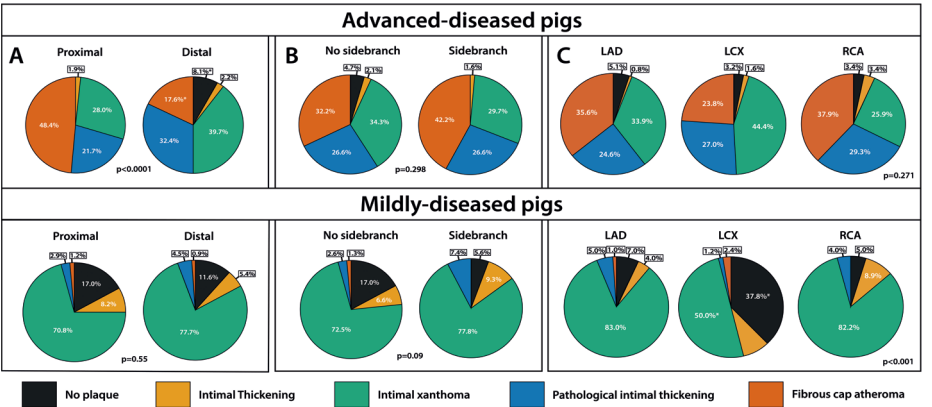


**Figure 3. Association between the anatomical location in the coronary artery and the histological plaque classification.**  
Distribution of plaque in regions **A)** proximal versus the distal, **B)** Side branch (SB) versus no SB, **C)** LAD versus LCX versus RCA. The data are split on advanced diseased pigs (top figures) and mildly diseased pigs (bottom figures). P-values indicate overall significance. \*z-score>1.96 for that respective plaque type compared to the other plaque types.



Neovascularisation, intra-plaque hemorrhage and macro-calcifications were frequently observed in the ADs and were rare in the MDs ( $p < 0.05$ ), while micro-calcifications were equally present (Figure 2B-F). Furthermore, coronary segments obtained from the ADs contained a significantly larger area percentage of lipids and macrophages compared to the MDs (Figure 2G-I) when the component was present. In necrotic core positive segments, the necrotic core area percentage did not differ (Figure 2G, J, K), but necrotic cores were much more frequently present in plaques from ADs (102 segments, 34%) compared to MDs (3 segments, 1%).

## Discussion

Our main findings were that: 1) on an atherogenic diet, plaques in all homozygous FH FBM pigs progressed significantly, but we could distinguish mildly-diseased pigs (MDs) and advanced-diseased pigs (ADs), despite the presence of the same homozygous *LDLR* R84C mutation and similar cholesterol, LDL-C, HDL-C and inflammatory levels. 2) the plaques of the MDs progressed to a stage of intimal xanthoma while in the ADs, large, advanced plaques with vulnerable characteristics including lipid-rich necrotic cores, calcifications, neovascularisation and intraplaque hemorrhage were frequently observed.

### Coronary atherosclerosis development: comparison with other pig models

Although the MD pigs in our study did develop early plaques with a growth rate consistent to humans (on average  $0.05 \text{ mm}^2/\text{month}$  vs.  $0.02 \text{ mm}^2/\text{month}$ ), pigs that develop more advanced, unstable plaques are most useful for cardiovascular studies. Therefore, we compared the results from the AD pigs with data from previously published studies on pig models of non-surgically induced coronary atherosclerosis development (Table 2).

### Coronary plaque size

In comparison with all other porcine models of diet- or genetically-induced hypercholesterolemia with or without diabetes, our AD pigs present with one of the largest histological plaque sizes (Table 2). Only the atherogenic diet-diabetes pig model described by Patel et al.<sup>14</sup> presented with on average larger plaque areas ( $5.0$  vs.  $8.2 \text{ mm}^2$ ). Differences in tissue processing and the lack of perfusion fixation in many studies, including ours, however hampers a direct comparison, especially with the results of three studies which do use this tissue processing technique<sup>15,16,24</sup>.

Although the lack of perfusion fixation of the histological samples could lead to overestimation of the plaque size, invasive imaging confirmed the presence of large plaques in our animals where 21% of the artery was occupied by plaques with a  $\text{maxIMT} > 1.0 \text{ mm}$ . Furthermore, IVUS-derived plaque burden is a measure

that is often applied in the clinic to quantify disease burden, but is unfortunately rarely reported by other porcine model studies. Badin et al.<sup>25</sup> and Tharp et al.<sup>26</sup> observed average plaque burdens of 38% and 50% respectively. We demonstrated a maximal plaque burden of 77% in the ADs, indicating the presence of lumen intruding, clinically relevant plaques<sup>27</sup>.

### Coronary plaque composition

Monitoring changes in plaque composition in animal models by serial invasive imaging is vital to assess the development stage, plaque stability and similarity to human plaques. Our OCT imaging data showed a clear increase of coronary atherosclerosis over time. The large majority of the plaques presented as lipid-rich already from the first time point, whereas lipid-pools, i.e. FCAs, were rare, even at the last imaging time point. This observation is in large contrast to our histological data and might be the result of the main drawback of OCT: the inability to image beyond lipid-rich tissue<sup>28</sup>. According to our histological analysis, one-third of the plaques in the ADs presented as FCAs with lipid-rich necrotic cores. The majority of these FCAs were thick-cap FCAs and lipid-rich tissue, present between the lumen and the lipid-pool, could shield the lipid-pool from detection by OCT, leading to an underestimation of FCA presence by OCT.

The histologically-detected advanced plaque types PIT and FCAs were observed more frequently in the ADs from our study compared to many other models described in literature<sup>9,11-13,17,24,29,30</sup>, except for the atherogenic diet-diabetes model by Patel et al.<sup>14</sup>. (Table 2), confirming that the advanced disease stage observed in our model is very rare.

Besides a generally advanced plaque type, ADs displayed important features of unstable plaques<sup>23</sup>. Several of the previously studied porcine models also present with plaques that display necrotic cores, calcifications and neovascularisation<sup>8,9,11,13,17,31</sup>, although quantification is often not reported. While some papers also report the occurrence of intra plaque hemorrhage<sup>8,15,17,31</sup>, the AD pigs in this study present widespread IPH, known to be an important indicator of fast plaque growth and destabilisation<sup>32</sup>.

While the MD pigs displayed more diffuse disease development, AD pigs developed the largest and most advanced plaques mainly in the proximal coronary regions. This latter observation very well matches the coronary atherosclerosis growth patterns observed in humans<sup>33</sup>.

Taken together, the AD pigs of the adult FBM minipig model from this study develop some of the most advanced plaques so far described in literature and this model is not complicated by the introduction of extra risk-factors like diabetes



mellitus<sup>14</sup>. The development of the large plaques with unstable, human-like features as observed in the AD pigs is likely associated with the advanced age of the animals. Unlike almost all previous studies (Table 2), we used adult pigs instead of juveniles for our experiments. As mentioned in the introduction, the adult age greatly improves the resemblance to human disease pathophysiology, and ageing is known to enhance atherosclerosis development both in pigs<sup>25</sup> and in humans<sup>19-21</sup>. The extensive characterisation of coronary atherosclerosis development in this model forms a road-map for future pathophysiological or imaging studies with this highly relevant model. Future studies will have to provide more information on sex-dependent differences and a possible genetic basis and heredity of the observed inter-individual differences in disease development.

Limitations

The sample size in this study was relatively small. The division of the group of pigs with regard to disease severity was unforeseen and resulted in a low number of animals with advanced disease. Furthermore, while histology was important for determining the plaque composition at a detailed level, the lack of perfusion fixation of the coronary histological samples hampered accurate quantification of plaque size.

Conclusion

The adult, homozygous FH FBM pig model is a large animal model in which half of the pigs allows for assessment of early plaque development while the other half demonstrates development of advanced coronary atherosclerotic plaques when fed an atherogenic diet. This latter group of advanced-diseased pigs presented with widespread development of large, lumen intruding plaques with extensive unstable, human-like features. These features render these pigs very suitable for testing and validating new interventions and (invasive) imaging techniques.

Acknowledgments

We gratefully acknowledge Dennis Akkermans and Vincent Vaes for their help with animal caretaking and for their support during the experimental procedures. We would also like to thank Claire Bal Dit Sollier for her support in arranging the animal logistics.

Table 2. Overview porcine studies of natural coronary atherosclerosis development with histology analysis.

Reference	Breed	Sex	Age at start study (weeks)	Max. FU time (weeks)	Induction of atherosclerosis	Plaque size (PA unless otherwise indicated)	IMR	Plaque classification (% coverage of artery)	Used imaging technique
Prescott 1991 <sup>31</sup>	Rapacz	Unknown	Mature	234	None	Occlusive	-	FCA	-
Neeb 2010 <sup>7</sup>	Ossabaw (O) Yucatan (Y)	Male	Unknown	40	Atherogenic diet	-	-	-	IVUS
Thim 2010 <sup>15</sup>	FBM minipig	Castrated male	39	18	Atherogenic diet	NP/IT/IX: 0.28mm <sup>2</sup> * PIT: 0.93 mm <sup>2</sup> * FCA: 2.53 mm <sup>2</sup> *	NP/IT/IX: 0.19* PIT: 0.42* FCA: 1.26*	-	VH-IVUS
Al-Mashhadi 2013 <sup>17</sup>	Yucatan PCSK9 mutation	Male(m) and female(f)	Unknown	46	Atherogenic diet	Male: 0.29 mm <sup>2</sup> * Female: 0.25 mm <sup>2</sup> * mm <sup>2</sup> +	-	NP: 0%* IX: 0%(m) / 25%(f)* PIT: 100%(m) / 25%(f)* FCA: 0%(m) / 50%(f)*	-
Davis et al. 2014 <sup>16</sup>	Yucatan LDLR <sup>-/-</sup>	Female and castrated male	22	6	Atherogenic diet	0.2 mm <sup>2</sup>	-	-	-
Pedrigi et al. 2015 <sup>29</sup>	Yucatan PCSK9 mutation	Female	Unknown	34	Atherogenic diet	0.2 mm <sup>2</sup>	-	NP:41% IT: 30% IX: 5% PIT: 24%	OCT

Table 2. Continued.

Reference	Breed	Sex	Age at start study (weeks)	Max. FU time (weeks)	Induction of atherosclerosis	Plaque size (PA unless otherwise indicated)	IMR	Plaque classification (% coverage of artery)	Used imaging technique
Poulsen et al. 2016 <sup>24</sup>	FBM minipig	Castrated female	29	38	Atherogenic diet	Average maximal PA*: 1.8 mm <sup>2</sup>	-	NP: 11% IX: 60% PT: 18% FCA: 11% IX: 75%*† PT: 25%*†	-
Shim et al. 2017 <sup>34</sup>	Yucatan ApoE <sup>-/-</sup>	Unknown	8	44	Atherogenic diet	Average maximal PA*†: 0.15 mm <sup>2</sup>	-	-	-
Badin 2018 et al. <sup>25</sup>	Ossabaw	Female	130 (young) or 458 (old)	48	Atherogenic diet	-	Average: 0.3 (young)†; 0.8 (old)†	-	IVUS
Tharp 2019 <sup>26</sup>	Rapacz	Castrated male	60	26	Atherogenic diet	-	-	-	IVUS
Hoogendoorn 2019	FBM minipig	Castrated male	147	52	Atherogenic diet	IT: 0.9 mm <sup>2</sup> ‡ IX: 0.9 mm <sup>2</sup> ‡ PT: 2.1 mm <sup>2</sup> ‡ FCA: 4.2 mm <sup>2</sup> ‡ Average: 2.0 mm <sup>2</sup>	IT: 0.6‡ IX: 0.7‡ PT: 1.8‡ FCA: 2.6‡ Average: 1.4	NP: 4%‡ IT: 2%‡ IX: 33%‡ PT: 27%‡ FCA: 34%‡	IVUS and OCT
Gerrity 2001 <sup>8</sup>	Yorkshire	Male	8-12	48	Atherogenic diet or Atherogenic diet + diabetes	Stenosis degree: 86%†	-	-	-

Table 2. Continued.

Reference	Breed	Sex	Age at start study (weeks)	Max. FU time (weeks)	Induction of atherosclerosis	Plaque size (PA unless otherwise indicated)	IMR	Plaque classification (% coverage of artery)	Used imaging technique
Chatzizisis 2009 <sup>9</sup>	Yorkshire	Male	Unknown	30	Atherogenic diet + diabetes	-	Average: 0.55 – 1.3*†	IT: 18.3%* IX/PT: 39.4%* FCA: 42.3%*	IVUS
Koskinas 2010/2013 <sup>1,30</sup>	Yorkshire	Male	12-14	36	Atherogenic diet + diabetes	Average: 1.6 – 2.7 mm <sup>2</sup> *†	-	IT: 6%* IX/PT: 25%* FCA: 69%*	IVUS
Patel 2013 <sup>14</sup>	Yorkshire	Male	Unknown	39	Atherogenic diet + diabetes	-	-	No plaque: 13% IT/IX: 22% PT: 22% FCA: 43% IX: 33% PT: 33% FCA: 33%	IVUS
Ludvigsen 2015 <sup>12</sup>	Göttingen	Castrated male	11	43	Atherogenic diet + diabetes	0.27 mm <sup>2</sup> †	0.23†	-	-
Ditzhuijzen 2016 <sup>13</sup>	Yorkshire/Landrace	Male	11	65	Atherogenic diet or Atherogenic diet + diabetes	-	-	IT - FCA	OCT

Plaque size and classification are based on histological data. Sizes based on imaging are mentioned in the text if the manuscript. Majority of the numbers are estimated from graphs. NP=no plaque, IT=intimal xanthoma, PT=pathological intimal thickening, FCA=fibrous cap atheroma, IMR=intima-media ratio. \*Only of the largest lesions, †Tissue not pressure fixed, ‡ Of all lesions, not of the whole artery, §Only of the advanced-diseased pigs. ¶No imaging results reported on spontaneous plaque development.

## References

- Farb A, Tang AL, Burke AP, Sessums L, Liang Y, Virmani R. Sudden coronary death. Frequency of active coronary lesions, inactive coronary lesions, and myocardial infarction. *Circulation* 1995;92:1701–9.
- Kolodgie FD, Burke AP, Farb A, Gold HK, Yuan J, Narula J, et al. The thin-cap fibroatheroma: a type of vulnerable plaque: the major precursor lesion to acute coronary syndromes. *Curr Opin Cardiol* 2001;16:285–92.
- Schaar JA, Muller JE, Falk E, Virmani R, Fuster V, Serruys PW, et al. Terminology for high-risk and vulnerable coronary artery plaques. Report of a meeting on the vulnerable plaque, June 17 and 18, 2003, Santorini, Greece. *Eur Heart J* 2004;25:1077–82.
- Getz GS, Reardon CA. Animal models of atherosclerosis. *Arterioscler Thromb Vasc Biol* 2012;32:1104–15.
- Hamamdizic D, Wilensky RL. Porcine models of accelerated coronary atherosclerosis: role of diabetes mellitus and hypercholesterolemia. *J Diabetes Res* 2013;2013:761415.
- Bourantas C V., Jaffer FA, Gijzen FJH, van Soest G, Madden SP, Courtney BK, et al. Hybrid intravascular imaging: recent advances, technical considerations, and current applications in the study of plaque pathophysiology. *Eur Heart J* 2016;38:ehw097.
- Neeb ZP, Edwards JM, Alloosh M, Long X, Mokelke EA, Sturek M. Metabolic syndrome and coronary artery disease in Ossabaw compared with Yucatan swine. *Comp Med* 2010;60:300–15.
- Gerrity RG, Natarajan R, Nadler JL, Kimsey T. Diabetes-induced accelerated atherosclerosis in swine. *Diabetes* 2001;50:1654–65.
- Chatzizisis YS, Jonas M, Coskun AU, Beigel R, Stone B V., Maynard C, et al. Prediction of the localization of high-risk coronary atherosclerotic plaques on the basis of low endothelial shear stress—an intravascular ultrasound and histopathology natural history study. *Circulation* 2008;117:993–1002.
- Koskinas KC, Sukhova GK, Baker AB, Papafaklis MI, Chatzizisis YS, Coskun AU, et al. Thin-capped atheromata with reduced collagen content in pigs develop in coronary arterial regions exposed to persistently low endothelial shear stress. *Arterioscler Thromb Vasc Biol* 2013;33:1494–504.
- Koskinas KC, Feldman CL, Chatzizisis YS, Coskun AU, Jonas M, Maynard C, et al. Natural history of experimental coronary atherosclerosis and vascular remodeling in relation to endothelial shear stress: A serial, in vivo intravascular ultrasound study. *Circulation* 2010;121:2092–101.
- Ludvigsen TP, Kirk RK, Christoffersen BØ, Pedersen HD, Martinussen T, Kildegaard J, et al. Göttingen minipig model of diet-induced atherosclerosis: influence of mild streptozotocin-induced diabetes on lesion severity and markers of inflammation evaluated in obese, obese and diabetic, and lean control animals. *J Transl Med* 2015;13:312.
- van Ditzhuijzen NS, van den Heuvel M, Sorop O, Rossi A, Veldhof T, Bruining N, et al. Serial Coronary Imaging of Early Atherosclerosis Development in Fast-Food-Fed Diabetic and Nondiabetic Swine. *JACC Basic to Transl Sci* 2016;1:449–60.
- Patel DD, Hamamdizic D, Llano R, Patel DD, Cheng L, Fenning RS, et al. Subsequent development of fibroatheromas with inflamed fibrous caps can be predicted by intracoronary near infrared spectroscopy. *Arterioscler Thromb Vasc Biol* 2013;33:347–53.
- Thim T, Hagensen MK, Drouet L, Bal Dit Sollier C, Bonneau M, Granada JF, et al. Familial hypercholesterolaemic downsized pig with human-like coronary atherosclerosis: a model for preclinical studies. *EuroIntervention* 2010;6:261–8.
- Davis BT, Wang X-J, Rohret JA, Struzynski JT, Merricks EP, Bellinger DA, et al. Targeted Disruption of LDLR Causes Hypercholesterolemia and Atherosclerosis in Yucatan Miniature Pigs. *PLoS One* 2014;9:e93457.
- Al-Mashhadi RH, Sorensen CB, Kragh PM, Christoffersen C, Mortensen MB, Tolbod LP, et al. Familial Hypercholesterolemia and Atherosclerosis in Cloned Minipigs Created by DNA Transposition of a Human PCSK9 Gain-of-Function Mutant. *Sci Transl Med* 2013;5:166ra1.
- Sharifi M, Futema M, Nair D, Humphries SE. Genetic Architecture of Familial Hypercholesterolaemia. *Curr Cardiol Rep* 2017;19:44.
- Jani B, Rajkumar C. Ageing and vascular ageing. *Postgrad Med J* 2006;82:357–62.
- Franklin SS, Gustin W, Wong ND, Larson MG, Weber MA, Kannel WB, et al. Hemodynamic patterns of age-related changes in blood pressure. The Framingham Heart Study. *Circulation* 1997;96:308–15.
- Okęcka-Szymańska J, Hübner-Woźniak E, Piątkowska I, Malara M. Effects of age, gender and physical activity on plasma lipid profile. *Biomed Hum Kinet* 2011;3:1–5.
- National Research Council (US) Committee for the Update of the Guide for Care and Use of Laboratory Animals. Guide for the Care and Use of Laboratory Animals. Washington, D.C.: National Academies Press; 2011.
- Virmani R, Kolodgie FD, Burke AP, Farb A, Schwartz SM. Lessons From Sudden Coronary Death. *Arterioscler Thromb Vasc Biol* 2000;20:1262–75.
- Poulsen CB, Al-Mashhadi AL, von Wachenfeldt K, Bentzon JF, Nielsen LB, Al-Mashhadi RH, et al. Treatment with a human recombinant monoclonal IgG antibody against oxidized LDL in atherosclerosis-prone pigs reduces cathepsin S in coronary lesions. *Int J Cardiol* 2016;215:506–15.
- Badin JK, Bruning RS, Sturek M. Effect of metabolic syndrome and aging on Ca<sup>2+</sup> dysfunction in coronary smooth muscle and coronary artery disease severity in Ossabaw miniature swine. *Exp Gerontol* 2018;108:247–55.
- Tharp DL, Masseau I, Ivey J, Laughlin MH, Bowles DK. Endurance exercise training does not limit coronary atherosclerosis in familial hypercholesterolemic swine. *Physiol Rep* 2019;7:e14008.
- Glagov S, Weisenberg E, Zarins CK, Stankunavicius R, Kolettis GJ. Compensatory Enlargement of Human Atherosclerotic Coronary Arteries. *N Engl J Med* 1987;316:1371–5.
- Tearney GJ, Regar E, Akasaka T, Adriaenssens T, Barlis P, Bezerra HG, et al. Consensus standards for acquisition, measurement, and reporting of intravascular optical coherence tomography studies: A report from the International Working Group for Intravascular Optical Coherence Tomography Standardization and Validation. *J Am Coll Cardiol* 2012;59:1058–72.
- Pedrigi RM, Poulsen CB, Mehta V V, Ramsing Holm N, Pareek N, Post AL, et al. Inducing Persistent Flow Disturbances Accelerates Atherogenesis and Promotes Thin Cap Fibroatheroma Development in D374Y-PCSK9 Hypercholesterolemic Minipigs. *Circulation* 2015;132:1003–12.
- Koskinas KC, Chatzizisis YS, Papafaklis MI, Coskun AU, Baker AB, Jarolim P, et al. Synergistic effect of local endothelial shear stress and systemic hypercholesterolemia on coronary atherosclerotic plaque progression and composition in pigs. *Int J Cardiol* 2013;169:394–401.
- Prescott MF, McBride CH, Hasler-Rapacz J, Von Linden J, Rapacz J. Development of complex atherosclerotic lesions in pigs with inherited hyper-LDL cholesterolmia bearing mutant alleles for apolipoprotein B. *Am J Pathol* 1991;139:139–47.
- Kolodgie FD, Gold HK, Burke AP, Fowler DR, Kruth HS, Weber DK, et al. Intraplaque hemorrhage and progression of coronary atheroma. *N Engl J Med* 2003;349:2316–25.
- Vieweg W V, Alpert JS, Johnson AD, Dennish GW, Nelson DP, Warren SE, et al. Distribution and severity of coronary artery disease in 500 patients with angina pectoris. *Cathet Cardiovasc Diagn* 1979;5:319–30.
- Shim J, Poulsen CB, Hagensen MK, Larsen T, Heegaard PMH, Christoffersen C, et al. Apolipoprotein E Deficiency Increases Remnant Lipoproteins and Accelerates Progressive Atherosclerosis, But Not Xanthoma Formation, in Gene-Modified Minipigs. *JACC Basic to Transl Sci* 2017;2:591–600.



# 4

## Multidirectional wall shear stress promotes advanced coronary plaque development – comparing five shear stress metrics

This chapter based on:

Multidirectional wall shear stress promotes advanced coronary plaque development – comparing five shear stress metrics

Ayla Hoogendoorn, Annette M. Kok, Eline M.J. Hartman, Giuseppe de Nisco, Lorena Casadonte, Claudio Chiastra, Adriaan Coenen, Suze-Anne Korteland, Kim van der Heiden, Frank J.H. Gijzen, Dirk J. Duncker, Antonius F.W. van der Steen, Jolanda J. Wentzel

*Published in Cardiovascular Research, 2019*

Abstract

**Aims** - Atherosclerotic plaque development has been associated with wall shear stress (WSS). However, the multidirectionality of blood flow, and thus of WSS, is rarely taken into account. The purpose of this study was to comprehensively compare five metrics that describe (multidirectional) WSS behaviour and assess how WSS multidirectionality affects coronary plaque initiation and progression.

**Methods and results** – Adult familial hypercholesterolemic pigs (n=10) that were fed a high-fat diet, underwent imaging of the three main coronary arteries at three time points [3 (T1), 9 (T2) and 10-12 (T3) months]. A 3D-geometry of the arterial lumen, in combination with local flow velocity measurements, was used to calculate WSS at T1 and T2. For analysis, arteries were divided into 3mm/45° sectors (n=3648). Changes in wall thickness, and final plaque composition were assessed with near-infrared spectroscopy-intravascular ultrasound (NIRS-IVUS) and optical coherence tomography (OCT) imaging, and histology. Both in pigs with advanced and mild disease, the highest plaque progression rate was exclusively found at low TAWSS or high multidirectional WSS regions at both T1 and T2. However, the eventually largest plaque growth was located in regions with initial low time-averaged WSS or high multidirectional WSS, that, over time, became exposed to high time-averaged WSS or low multidirectional WSS at T2. Besides plaque size, also the presence of vulnerable plaque components at the last time point was related to low and multidirectional WSS. Almost all WSS metrics had good predictive values for the development of plaque (47-50%), and for advanced fibrous cap atheroma development (59-61%).

**Conclusions** - This study demonstrates that low and multidirectional WSS promote both initiation and progression of coronary atherosclerotic plaques. The high-predictive values of the multidirectional WSS metrics for FCA development indicate their potential as an additional clinical marker for the vulnerable disease.

Introduction

Ischemic coronary artery disease (CAD), caused by destabilization and subsequent rupture of atherosclerotic plaques, is predicted to remain the leading cause of death<sup>1</sup>. Although the complex process of plaque development is incompletely understood, wall shear stress (WSS) is known to play a key role. WSS is a biomechanical metric that describes the frictional force between blood flow and the endothelial cells covering the arterial wall. Both pre-clinical and clinical studies showed an intricate role of WSS in (advanced) plaque development, since both low and high WSS have been associated with plaque growth and destabilization<sup>2-9</sup>. To further elucidate the role of WSS in coronary atherosclerosis, longitudinal imaging studies are crucial. Moreover, since most studies only use time-averaged WSS (TAWSS) as a descriptor of disturbed blood flow, the multidirectionality of blood flow, induced by its pulsatile nature in combination with the 3D geometry, is not taken into account. Therefore, in recent years, new WSS metrics have been developed to capture this multidirectional flow behaviour: the oscillatory shear index (OSI), relative residence time (RRT), transverse WSS (transWSS) and its normalized version: the cross-flow index (CFI) (Table 1).

Table 1.

Shear stress metric	Description
Time-averaged wall shear stress (TAWSS)	Shear stress averaged over the cardiac cycle
Oscillatory shear index (OSI)	Ratio between back- and forward going shear stress
Relative residence time (RRT)	Relative time that a blood particle resides at a certain location at the vessel wall
Transverse wall shear stress (transWSS)	Shear stress vector in perpendicular direction to the main flow direction
Cross-flow index (CFI)	The transWSS normalized for the time-averaged wall shear stress

The role of TAWSS, RRT and OSI was demonstrated in a number of studies<sup>9-14</sup>. However, transWSS and CFI have not been investigated before in a longitudinal imaging study with histopathology. Since patient studies do not allow for multiple invasive imaging procedures and the collection of coronary tissue, we employed a highly relevant porcine model of familial hypercholesterolemia<sup>15</sup> to study the effect of multidirectional WSS on plaque development. By using adult, full grown pigs, we excluded the influence of growth-related changes in the geometry of the coronaries, important for serial assessment of WSS and plaque size. Serial, multimodality invasive imaging, combined with a detailed histological analysis



enabled us to comprehensively compare five different (multidirectional) WSS metrics to assess how multidirectional WSS affects both plaque initiation and progression.

## Methods

A detailed description of the surgery protocol, anaesthesia and euthanasia, blood and tissue processing, computational modelling and of the histology, imaging, and WSS analysis is provided in Chapter 3.

### Animal model, invasive imaging procedure, and histology analysis

The animal protocol was approved by the local animal ethics committee of the Erasmus MC (DEC EMC109-14-10) and the study was performed according to the National Institutes of Health guide for the care and use of Laboratory animals<sup>16</sup>. At the age of  $34 \pm 3$  months, familial-hypercholesterolemic Bretonchelles Meishan (FBM) pigs<sup>15</sup> ( $n=10$ , castrated males) were put on a high-fat diet (10% lard and 0.75% cholesterol, the National Institute of Agronomic Research, France) that was given in restricted amounts to maintain a constant weight. At three months of high-fat diet ( $T_1$ ), the 3D geometry of the coronary arteries was assessed by CT angiography (CTA). Subsequently, an invasive imaging procedure was conducted in which near-infrared spectroscopy - intravascular ultrasound (NIRS-IVUS), and optical coherence tomography (OCT) imaging were used to assess the coronary plaque size and composition in all three main coronary arteries (i.e., left anterior descending (LAD), left circumflex (LCX) and right coronary artery (RCA)). Furthermore, invasive local Doppler-derived flow velocity measurements were obtained at multiple locations in between the side branches in the coronaries. This imaging procedure was repeated at 9 ( $T_2$ ) and 10-12 months ( $T_3$ ) for all pigs. At the last imaging time point, the animals were sacrificed by an overdose of pentobarbital followed by exsanguination by removal of the heart. The coronary arteries were collected from the heart and used for histological analysis. All 3-mm coronary segments were classified according to the adjusted AHA classification<sup>17</sup> (i.e., no plaque, intimal thickening (IT), intimal xanthoma (IX), pathological intimal thickening (PIT) and fibrous cap atheroma (FCA)). Furthermore, the lipid, macrophage and necrotic core content of each segment was quantified.

### OCT analysis

OCT analysis was performed using QCU-CMS software (version 4.69, LKEB, Division of Image Processing, Leiden University Medical Centre, Leiden, The Netherlands) and plaque composition was assessed every millimetre (1 out of every 5 frames) according to the OCT analysis consensus standards<sup>18</sup>. Lumen contours were delineated semi-automatically. Fibrous tissue, lipid-rich tissue or lipid-pools were indicated manually by drawing angles from the lumen

centre. Fibrous tissue was indicated when a plaque ( $WT > 0.5\text{mm}$ ), presenting as homogeneous and low-attenuation signal with the 3-layered structure still visible was present. A plaque region with an inhomogeneous, slowly attenuating signal and an invisible 3-layered wall structure was classified as lipid-rich. A lipid-pool angle was indicated as a region with a sudden drop in signal with a diffuse border and an overlying signal rich cap structure. Each frame was classified according to its most advanced component as fibrous, lipid-rich or fibrous cap atheroma (FCA). The latter classification was given when a lipid pool was present.

### IVUS analysis

Before analysis, the IVUS pullbacks were gated by selecting the frames that were located 6 frames before the R-peak in the ECG signal using in-house developed software. Hereby, changes in lumen size caused by movement of the catheter or by the contraction of the heart were removed. Analysis of the gated IVUS pullbacks was performed using QCU-CMS software. In every gated IVUS frame, vessel wall and lumen borders were delineated semi-automatically. Interobserver variability was assessed for the manual segmentation of the plaque area. For this analysis, two independent expert observers (AH and EH) both segmented a total of 1192 IVUS frames derived from multiple different pullbacks of different disease stages. The average intraclass correlation coefficient was high: 0.927 (0.805-0.976).

### Shear stress analysis

For the 3D reconstruction of the coronary arteries at  $T_1$  and  $T_2$ , the CTA scan of  $T_1$  was reconstructed over a 300ms time window at diastole to ensure maximal filling of the coronary arteries, including all side branches. Semi-automatic CTA segmentation<sup>19</sup> was performed in Mevislab (Bremen, Germany) whereby the centreline of the coronary artery was determined. The IVUS images were longitudinally and circumferentially registered to the  $T_1$  CTA using the location of side branches. Subsequently, the IVUS lumen and wall contours of  $T_1$  or  $T_2$  were placed at the corresponding location on the centreline. The side branches and the proximal and distal ends of the artery outside of the IVUS region were segmented on CTA. These CTA contours were scaled to match the IVUS lumen contours of the main artery to account for incomplete filling of the artery or for the blooming effect of the contrast in the CTA. The IVUS contours of  $T_1$  and  $T_2$  (main artery and thus region-of-interest) and CTA contours (proximal and distal section outside the IVUS region and the side branches) were fused to reconstruct a 3D geometry of the luminal surface of the whole coronary artery at  $T_1$  and  $T_2$ . The wall thickness (WT) was computed by calculating the distance between the vessel wall and lumen contours.

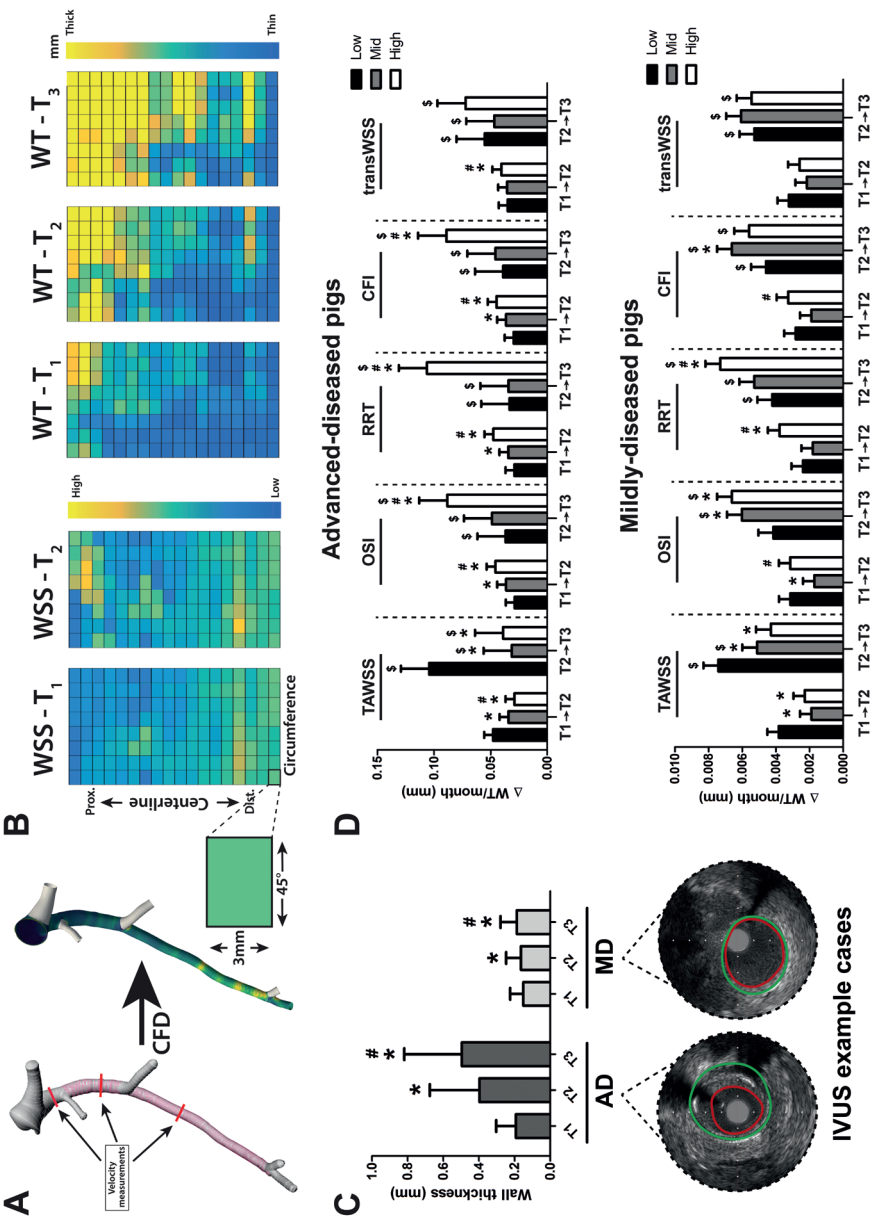


Figure 1. Methodology of wall shear stress (WSS) calculation and analysis, and the relation between local (multidirectional) WSS levels and the subsequent plaque growth rate in both plaque initiation and progression.

< **Figure 1. A)** IVUS (pink) and CT (white) contours were fused to reconstruct the grey lumen surface. This surface, together with local flow measurements between the side branches (three examples shown), was used as input for computational fluid dynamics, resulting in local WSS values (yellow=high; blue=low). **B)** From the 3D reconstructions, a 2D map of the WSS levels at  $T_1$  and  $T_2$ , and of the wall thickness (WT,  $T_1$ - $T_3$ ) was created. For the analysis, the artery was divided in 3mm/45° sectors. **C)** The mean ( $\pm$ SD) WT at  $T_1$ - $T_3$  in advanced-diseased (AD) ( $n=1893$  sectors at  $T_1$  and  $T_2$  and  $n=1240$  sectors at  $T_3$ ) and mildly-diseased (MD) ( $n=1755$  sectors) pigs with two representative IVUS frames from  $T_3$  (red contour=lumen; green contour=vessel wall). \* $p<0.05$  compared to  $T_1$ , # $p<0.05$  compared to  $T_2$  (statistics: two-way repeated-measures anova with Bonferroni post hoc). **D)** The effect of low/mid/high levels of the respective WSS metrics on the subsequent plaque growth rate (estimated mean $\pm$ SEM) in plaque initiation ( $T_1$ - $T_2$ ) and plaque progression ( $T_2$ - $T_3$ ). **Important to note:** for the AD pigs, the  $T_2$ - $T_3$  data are derived from 3 (instead of 5) pigs ( $n=1240$  sectors), which means that the analysis of a difference in the relation between  $T_1$ - $T_2$  and  $T_2$ - $T_3$  (\*) could only be performed in these 3 animals. \* $p<0.05$  compared to the low tertile; # $p<0.05$  compared to the mid tertile; \$ $p<0.05$  compared to  $T_1$ - $T_2$  in the same tertile (statistics: linear mixed effects model). TAWSS=time-averaged WSS; OSI=oscillatory shear index; RRT=relative-residence time; CFI=cross-flow index; transWSS=transverse WSS.

Boundary conditions

For computational fluid dynamics (CFD), information on the inflow and flow distribution through the side branches is required. The flow was derived from intravascular Doppler-derived velocity measurements. Quality of these measurements was assessed by an experienced committee (AH, AK, EH, FG, JW) and only reliable measurements were used to determine the velocity rate. The most proximal good flow measurement was used for a time-dependent velocity waveform that was imposed on the inlet of the artery. Flow distribution was determined based on velocity measurements in the segments between side branches. For regions where no (reliable) flow measurements were available, the Huo-Kassab diameter-based scaling law<sup>20</sup> was applied to determine the flow distribution between the main branch and the side branch. Furthermore, the vessel lumen was considered as rigid and subjected to no-slip boundary condition. Blood was assumed to behave as shear-thinning fluid and was modelled according to the Carreau model<sup>21</sup>.

Meshing and computational fluid dynamics solution procedure

Each 3D geometry of the lumen at  $T_1$  and  $T_2$  was converted to a tetrahedral mesh in ICEM CFD (v.17.1, ANSYS Inc., Canonsburg, PA, USA) which was used for CFD simulations. The mesh size was determined by a mesh independence study (errors <1% of shear stress were allowed), resulting in a typical element size of 0.05 mm. Unsteady CFD simulations were performed using Fluent (v.17.1, ANSYS Inc.). The solution procedure was carried out following previously described methods<sup>22</sup>.

Post processing: matching OCT, NIRS and histology data to WSS

To assess the association between  $T_1$  or  $T_2$  WSS levels and subsequent plaque growth ( $\Delta$ WT/month), all IVUS and WSS data of  $T_2$  and  $T_3$  were matched to the

$T_1$  IVUS pullback. This enabled us to study the relation of  $\Delta WT/month$   $T_1$ - $T_2$  and WSS at  $T_1$ ; and the relation of  $\Delta WT/month$   $T_2$ - $T_3$  and WSS at  $T_2$ . The match was performed both longitudinally and circumferentially based on the location of side branches. For the relation between  $T_1$  WSS levels and plaque composition, OCT and NIRS-IVUS data at  $T_{last}$  were matched to the  $T_1$  IVUS pullback according to the same methods as for the WT analysis to allow a direct coupling to the 3D lumen geometry and thus to the WSS data. Analysis of the OCT-WSS data and of the NIRS-WSS data at  $T_{last}$  was also performed in 3mm/45° sectors. Sectors regarded as 'positive' on OCT (fibrous or lipid-rich) or on NIRS (a 'high probability' (>60%)) were selected. This selection method for NIRS positive sectors is the same analysis method used for standard determination of the lipid-core burden index (LCBI), but applied to sector level instead of total-vessel level. The percentage of all OCT or NIRS-positive sectors that was exposed to low, mid and high WSS was assessed.

To match the histology data with WSS at  $T_1$ , the histological 3mm-segments were matched on the IVUS pullback taken at  $T_{last}$ , which could subsequently be matched to IVUS data of  $T_1$  and thus to WSS at  $T_1$ . Matching was performed in longitudinal direction and was based on the location of side branches and typical plaque components like calcifications. Between the matching points, the histology blocks were linearly distributed. Since the matching between histology and IVUS was not performed in circumferential direction, the WSS data of each matched 3-mm segment was averaged circumferentially.

For the computation of WSS at  $T_1$  and  $T_2$ , the coronary arteries were 3D-reconstructed by fusion of IVUS-derived lumen and wall contours of either  $T_1$  or  $T_2$ , with the 3D CTA-derived centreline. This resulted in a luminal surface and provided information on the local wall thickness (WT) distribution (Figure 1A). The reconstructed lumen surface together with the local velocity measurements served as input to compute the (multidirectional) WSS metrics at both time points, using computational fluid dynamics (CFD).

For analysis, all arteries were divided into 3 mm segments of 45° (sectors) (Fig 1B), a division that was chosen to ensure maximal overlap of the  $T_1$  and  $T_2$  data, even in the presence of small registration errors (max  $\pm 1$  IVUS frame), but to at the same time maximally account for spatial heterogeneity. For each individual artery, the WSS metrics at  $T_1$  and  $T_2$  were divided into artery-specific tertiles (low, mid and high) (Table 2).

IVUS data of  $T_2$  and  $T_3$  were matched based on anatomical landmarks to the IVUS-data at  $T_1$  to assess, at each location, changes in plaque size (i.e. plaque growth). All data on plaque growth ( $\Delta WT$   $T_1 \rightarrow T_2 = WT-T_2 - WT-T_1$ ;  $\Delta WT$   $T_2 \rightarrow T_3 = WT-T_3 - WT-T_2$ ) were expressed as  $\Delta WT$  per month on high-fat diet between the respective time points.

**Table 2. Overview average WSS levels for each tertile of the respective WSS metrics.**

TAWSS (Pa)	$T_1$			$T_2$		
	Low	Mid	High	Low	Mid	High
AD	0.62±0.21	0.85±0.29	1.20±0.57	0.55±0.28 <sup>#</sup>	0.86±0.49	1.32±0.90 <sup>†</sup>
MD	0.70±0.27	0.93±0.40	1.29±0.70	0.48±0.15 <sup>#</sup>	0.60±0.21 <sup>*†</sup>	0.79±0.36 <sup>*†</sup>
OSI ( $\times 10^{-3}$ ) (-)	$T_1$			$T_2$		
	Low	Mid	High	Low	Mid	High
AD	0.52±0.73	2.71±3.54	15.26±23.66	1.06±1.87 <sup>†</sup>	3.65±4.78 <sup>†</sup>	25.60±52.03 <sup>†</sup>
MD	0.79±1.33	2.88±4.07	12.35±22.60	8.03±14.16 <sup>†</sup>	13.75±15.47 <sup>*†</sup>	30.76±24.84 <sup>†</sup>
RRT ( $Pa^{-1}$ )	$T_1$			$T_2$		
	Low	Mid	High	Low	High	
AD	1.04±0.43	1.37±0.47	1.94±0.69	1.06±0.48	1.55±0.65 <sup>†</sup>	2.73±2.97 <sup>†</sup>
MD	1.03±0.51	1.31±0.55	1.75±0.80	1.63±0.79 <sup>*†</sup>	1.99±0.81 <sup>*†</sup>	2.51±0.90 <sup>†</sup>
CFI ( $\times 10^{-2}$ ) (-)	$T_1$			$T_2$		
	Low	Mid	High	Low	Mid	High
AD	3.31±2.22	7.11±3.79	13.93±7.25	2.87±2.03 <sup>†</sup>	6.62±3.85 <sup>†</sup>	14.91±9.68 <sup>†</sup>
MD	3.50±2.24	6.98±3.55	13.84±7.69	4.38±2.21 <sup>*†</sup>	8.79±3.51 <sup>*†</sup>	16.36±7.15 <sup>†</sup>
transWSS ( $\times 10^{-2}$ ) (Pa)	$T_1$			$T_2$		
	Low	Mid	High	Low	Mid	High
AD	2.32±1.97	4.55±3.34	8.14±5.66	1.70±1.37 <sup>†</sup>	3.53±2.47 <sup>†</sup>	6.99±4.81 <sup>†</sup>
MD	2.22±1.40	4.50±2.61	8.82±5.51	1.57±1.09 <sup>†</sup>	3.31±2.07 <sup>†</sup>	6.40±3.99 <sup>†</sup>

AD= advanced-diseased pigs; MD=mildly-diseased pigs. \* $p < 0.05$  compared to AD. <sup>†</sup> $p < 0.05$  compared to  $T_1$

The used matching method enabled projection of  $T_2$  WSS on the  $T_1$  WSS maps, whereby permitting assessment of locations with sustained low WSS or sustained high WSS. Locations were classified as 'sustained' when the WSS remained either 'low' or 'high' at both  $T_1$  and  $T_2$ .

NIRS-IVUS, OCT images and histology data derived at the last imaging time point were also matched to the  $T_1$  IVUS images, again based on anatomical landmarks to establish the relationship between WSS at  $T_1$  and eventual plaque composition at the last imaging time point.



## Statistics

IBM SPSS Statistics (version 24.0) software was used for statistical analysis. Normally distributed data are shown as mean±standard deviation (SD) and statistical difference was determined with a repeated measures ANOVA with Bonferroni post-hoc testing. Statistical differences in frequency distributions were assessed using a Chi-square test. Non-normally distributed data are presented as median (inter-quartile range (IQR)) and statistical difference was determined with a Mann-Whitney U test. Statistical analysis of the WSS data was performed using a linear mixed effects model, with WSS (low, mid, high), as fixed factor and the individual vessel as random factor, adjusting for cholesterol levels. The Bonferroni correction was applied to adjust for multiple comparisons between the WSS tertiles. For comparison of the WSS effect on plaque progression between  $T_1$ - $T_2$  and  $T_2$ - $T_3$ , time was added as a repeated measure factor to this same model. In all figures that display the association between plaque size or composition and the five WSS-metrics, the estimated means and standard errors derived from these models is displayed.  $p < 0.05$  was regarded as significant.

## Results

Of the ten pigs, one pig died during feeding, a day after the invasive imaging procedure at  $T_2$ , due to a presumed myocardial infarction. One pig had to be sacrificed between  $T_2$  and  $T_3$  due to an acute thrombotic occlusion of a femoral artery. Data of these pigs have been included in the analysis, although imaging information at  $T_3$  is missing. For analysis of the relation between  $T_1$  WSS metrics and eventual plaque composition,  $T_2$  was considered as  $T_{last}$  for these two pigs. For the other pigs,  $T_3$  equalled  $T_{last}$ . In total, 30 vessels relating to 3648 3mm/45° sectors were analysed.

### Advanced-diseased and mildly-diseased pigs

Although all pigs had the same mutation and were fed the same diet, 5 of the 10 pigs developed large, lumen intruding coronary plaques (plaque burden (PB) >40%) (advanced-diseased pigs (ADs)) within 9 months, while the other 5 pigs only developed limited atherosclerosis (PB<40%) within 12 months follow-up (mildly-diseased pigs, MDs)).

> **Figure 2.** The plaque growth rate during plaque initiation ( $T_1$ - $T_2$ ) and plaque progression ( $T_2$ - $T_3$ ) in regions with either sustained low (L), low turning to high (H), high turning to low, or sustained high WSS between  $T_1$  and  $T_2$ . Analysis is depicted for all WSS metrics (time-averaged WSS (TAWSS); oscillatory shear index (OSI); relative-residence time (RRT); cross-flow index (CFI); transverse WSS (transWSS)). Number of analysed sectors: for AD pigs  $T_1$ - $T_2$ : n=1893 and  $T_2$ - $T_3$ : n=1240; for MD pigs: n=1755. \* $p < 0.05$  compared to sustained low; # $p < 0.05$  compared to low ( $T_1$ )/high ( $T_2$ ); \$ $p < 0.05$  compared to high ( $T_1$ )/low ( $T_2$ ) (statistics: linear mixed effects model).

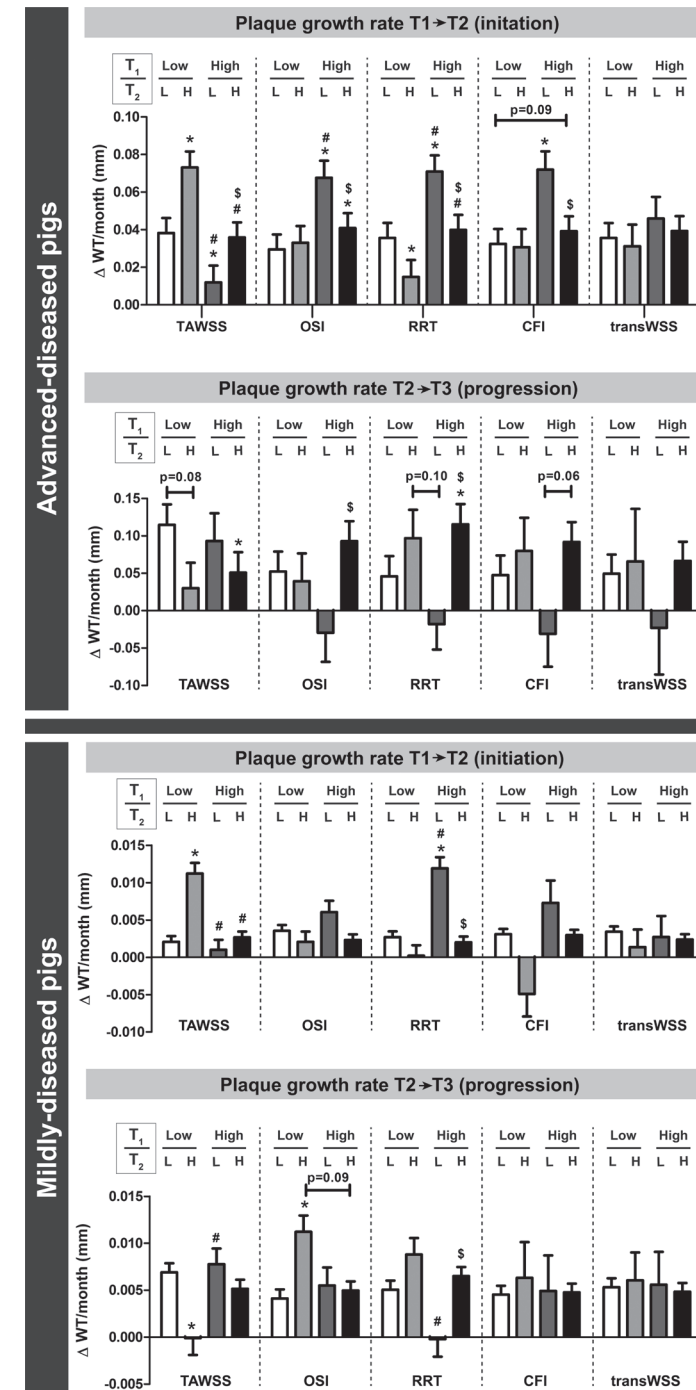


**Figure 2.** The long-term effect of sustained or changed levels of (multidirectional) wall shear stress (WSS) on the plaque growth rate in advanced-diseased and mildly-diseased pigs.

The observed plaque burden at the last imaging time point was 35% (12%-77%) for the ADs and 16% (8%-34%) for the MDs (median (range)). The two groups of pigs showed no difference in weight (MDs: 91 kg (80-94) vs. ADs 82 kg (68-94) ( $p=0.33$ )) and in cholesterol, LDL, HDL levels (10.4 mmol/L (9.2-12.1) vs. 10.5 mmol/L (9.8-18.3) ( $p=0.54$ ); 2.8 mmol/L (2.5-4.2) vs. 3.0 mmol/L (2.3-3.5) ( $p=0.79$ ); 8.5 mmol/L (7.1-9.8) vs. 9.2 mmol/L (8.1-16.6) ( $p=0.33$ ) in MD versus AD respectively). Because of the large difference in plaque development, the subsequent results will be presented separately for both groups.

### Low and multidirectional WSS result in a high coronary plaque growth rate, both in plaque initiation and plaque progression

Overall, the ADs demonstrated a significant increase of the average WT over the three imaging time points ( $T_1$ - $T_3$ ) ( $p<0.001$ ), which was less pronounced, but also significant in the MDs ( $p<0.001$ ) (Figure 1C). There was no difference in absolute WSS values between the AD and MD pigs at  $T_1$ . At  $T_2$ , the OSI, RRT and CFI levels were slightly higher in the MD than in the AD pigs (Table 2). In general, the plaque growth rate was higher between  $T_2$ - $T_3$  than between  $T_1$ - $T_2$  for both AD and MD pigs (Fig. 1D).

In the AD pigs, coronary sectors exposed to low TAWSS or high multidirectional WSS (OSI, RRT, CFI or transWSS) at  $T_1$  exhibited a significantly higher initial plaque growth per month between  $T_1$ - $T_2$  than regions with higher (TAWSS) or lower (multidirectional metrics) WSS levels ( $p<0.05$ ). The same significant relations were seen for the plaque progression rate ( $T_2$ - $T_3$ ), except for the transWSS (Figure 1D). Also in the MDs, low TAWSS and high RRT levels were related to the fastest initial plaque growth ( $T_1$ - $T_2$ ) and plaque progression ( $T_2$ - $T_3$ ). High OSI levels promoted plaque progression, but not initiation in the MDs. For CFI and transWSS, no relation with plaque growth was observed in the MDs (Figure 1D).

Besides the effect of WSS values at a single time point, we also assessed what the relation was between sustained low or high WSS and the plaque growth rate during plaque initiation and progression. In plaque initiation, in the ADs, the plaque growth rate was highest in regions with initial ( $T_1$ ) low TAWSS, that over time changed to high TAWSS (at  $T_2$ ) ( $\Delta$ WT  $T_1$ - $T_2$ :  $0.073\pm0.008$  mm/month;  $n=94$ , 5%), also compared to regions with persistently low TAWSS ( $0.038\pm0.008$  mm/month;  $n=361$ , 19%) (Figure 2). Besides, also regions with initial ( $T_1$ ) high OSI, RRT or CFI and subsequently ( $T_2$ ) low multidirectional WSS presented with the highest plaque growth rate. For the MD pigs, similar results were obtained, but only for the TAWSS and RRT. Subsequently, we assessed in these same regions what the plaque progression was between  $T_2$ - $T_3$ . Both in the ADs and MDs, in regions with initial low and subsequently high TAWSS, the plaque growth rate between  $T_2$ - $T_3$  was lowest (Figure 2).

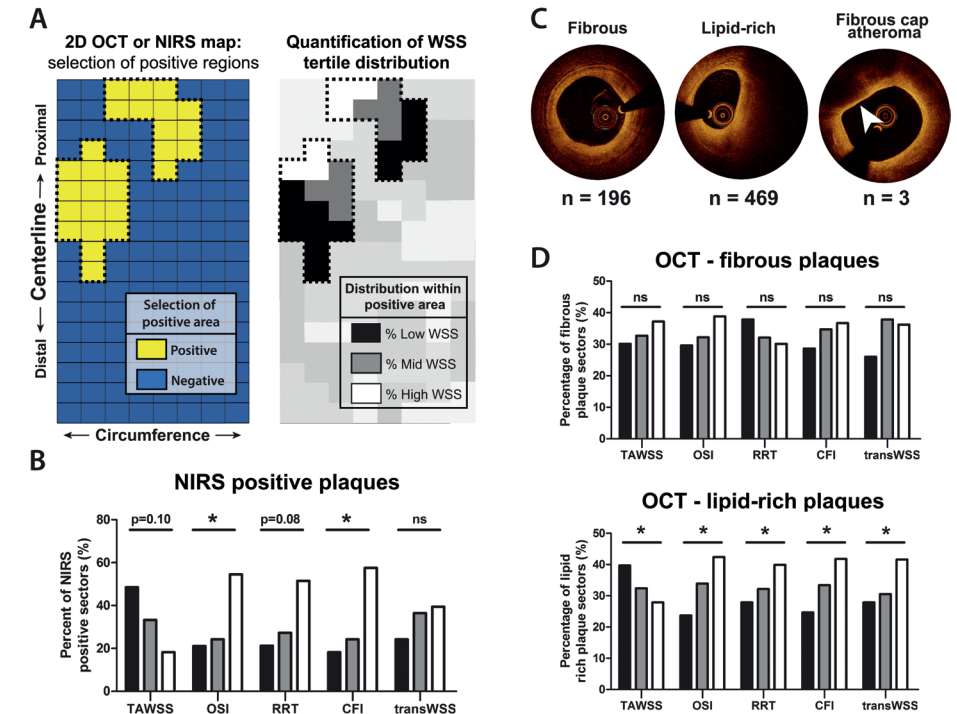


**Figure 3. Association between T1 wall shear stress (WSS) levels and final plaque composition detected by OCT and NIRS in advanced-diseased pigs (ADs) at Tlast.**

**A)** OCT and NIRS analysis method on an imaginary 2D map: all NIRS or OCT 'positive' 3mm/45° sectors were selected. Within these positive regions, the percentage of positive sectors that was preceded by one of the WSS tertiles was quantified. **B)** The percentage of NIRS-positive sectors ( $n=33$ ) that was preceded by low (black bars), mid (grey bars) or high (white bars) levels of the respective  $T_1$  WSS tertiles (time-averaged WSS (TAWSS); oscillatory shear index (OSI); relative-residence time (RRT); cross-flow index (CFI); transverse WSS (transWSS)).  $*p<0.05$  for the overall relations (statistics: chi-square test). **C)** Example images of fibrous, lipid rich and FCA (arrowhead) plaques on OCT.  $n$ =number of sectors of ADs presenting with each respective plaque classification at  $T_{last}$ . **D)** The percentage of sectors presenting with fibrous or lipid rich plaque that was preceded by low (black bars), mid (grey bars) or high (white bars) levels of the respective WSS metrics. Fibrous plaques displayed no significant relation ( $p=ns$ ).  $*p<0.05$  for the overall relations (statistics: chi-square test).

The highest plaque progression rate was observed in regions with low TAWSS at  $T_2$ , independent of the  $T_1$  TAWSS levels, but only in the ADs. For the multidirectional WSS metrics, no clear relations were observed between sustained WSS and the plaque growth rate ( $T_2$ - $T_3$ ), except for low RRT levels at  $T_2$  which appeared leading in very limited plaque growth.

The positive predictive values (PPV) of the  $T_1$  WSS metrics for plaque presence (WT>0.5mm) at  $T_{last}$  in the AD pigs were 48% (low TAWSS), 45% (high OSI), 47%

(high RRT), 45% (high CFI) and 40% (high transWSS). Regions with low TAWSS co-locate with high OSI in 396/624 sectors (63%). Co-localization of low TAWSS and high CFI occurs in 354/624 sectors (57%). Combination of low TAWSS and high OSI resulted in a PPV of 50% for plaque presence. The PPV for low TAWSS and high CFI for plaque presence was 49%. The combination of all three metrics resulted in a PPV of 50%. In the MD pigs, a predictive value analysis could not be applied since only 6 sectors (of the total of 1755 sectors) presented with a WT >0.5 mm at  $T_{last}$ .

#### The development of OCT lipid-rich plaques and NIRS-positive plaques was most often preceded by low and multidirectional WSS

Analysis of the NIRS signal at  $T_{last}$  (Figure 3A) showed that the MDs presented with only 6 NIRS-positive sectors from 3 different arteries, while the ADs demonstrated 33 NIRS-positive sectors derived from 6 arteries. The NIRS positive sectors of the ADs were most frequently preceded by low TAWSS ( $p=0.10$ ), or high OSI ( $p<0.05$ ), RRT ( $p=0.08$ ) or CFI ( $p<0.05$ ) at  $T_1$  (Figure 3B). Only transWSS showed no relation at all with NIRS-positive plaque development in the ADs.

For the OCT analysis (Figure 3A), 2 pullbacks from  $T_{last}$  had to be excluded due to bad image quality or technical problems. From the remaining pullbacks at  $T_{last}$ , 668 sectors from 14 arteries of the ADs and 66 sectors from 10 arteries of the MDs showed plaque presence. In the ADs the plaque positive sectors were characterized as either a fibrous ( $n=196$ ), lipid-rich ( $n=469$ ) or OCT-detected FCA (lipid pool) ( $n=3$ ) plaque (Figure 3C). Since the OCT-FCAs (with lipid-pool) were scarce, no statistical analysis and thus no WSS analysis could be performed on this plaque type. The development of a fibrous plaque showed no relation with  $T_1$  WSS levels in both types of pigs (Figure 3D and Figure 4). In contrast, the development of OCT lipid-rich plaques was most frequently preceded by low and multidirectional WSS in the ADs ( $p<0.05$ ) (Figure 3D). This relation was confirmed for OSI, CFI and transWSS in the MDs, despite the low number of lipid-rich plaques in this group ( $n=45$ ) (Figure 4).

#### Low and multidirectional WSS promoted the development of advanced histological plaque types

For a detailed analysis of the association between histological plaque classification, composition and  $T_1$  WSS levels, 190 3mm-segments (15 arteries) from ADs and 145 3mm-segments (13 arteries) derived from MDs could be reliably matched with the invasive imaging data. In the MDs, of all WSS metrics, only TAWSS showed a significant association with histological plaque type, with relatively the most advanced plaques in regions with low TAWSS compared to regions with mid or high TAWSS ( $p=0.049$ ) (Figure 5). In the ADs, this TAWSS relation was more pronounced ( $p=0.003$ ), and also regions with high OSI and high RRT displayed a more advanced plaque phenotype than regions with lower OSI or RRT levels

( $p<0.05$ ). For transWSS and CFI, no relation with plaque type was observed (Figure 4B). The PPVs of the respective WSS metrics for the presence of an FCA in the ADs were 61% (low TAWSS), 58% (high OSI), 61% (high RRT), 59% (high CFI) and 49% (high transWSS).

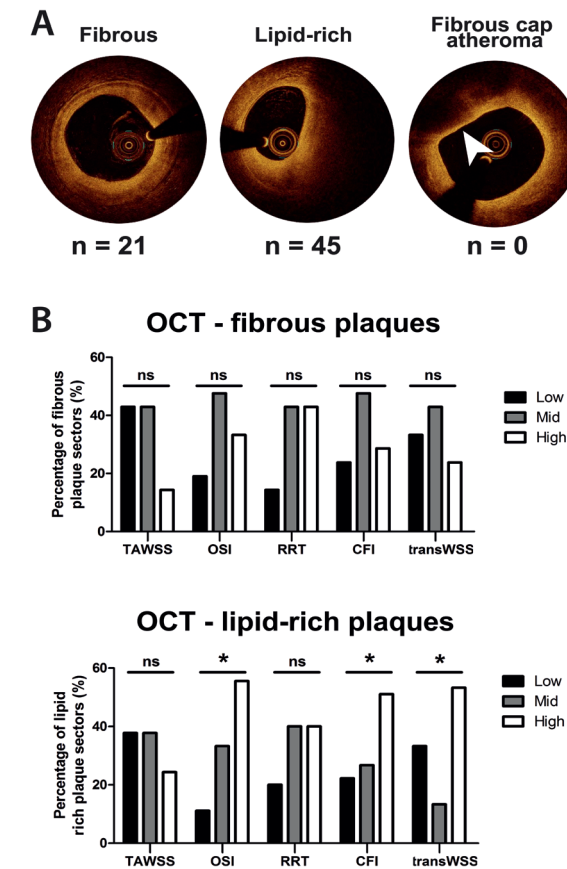


**Figure 4. Association between  $T_1$  wall shear stress (WSS) levels and OCT-detected plaque composition in mildly-diseased pigs (MDs) at  $T_{last}$ .**

**A)** Example images of fibrous, lipid-rich and FCA (arrow) plaques on OCT. N = number of sectors of MDs presenting with each respective plaque classification at  $T_{last}$ . **B)** The percentage of sectors presenting with fibrous or lipid-rich plaque that was preceded by low (black bars), mid (grey bars), or high (white bars) levels the respective WSS metrics. Fibrous plaques displayed no significant relation ( $p=ns$ ). \* $p<0.05$  for the overall relation (statistics: chi-square test). TAWSS = time-average WSS; OSI=oscillatory shear index; RRT=relative-residence time; CFI=cross-flow index; transWSS=transverse WSS.



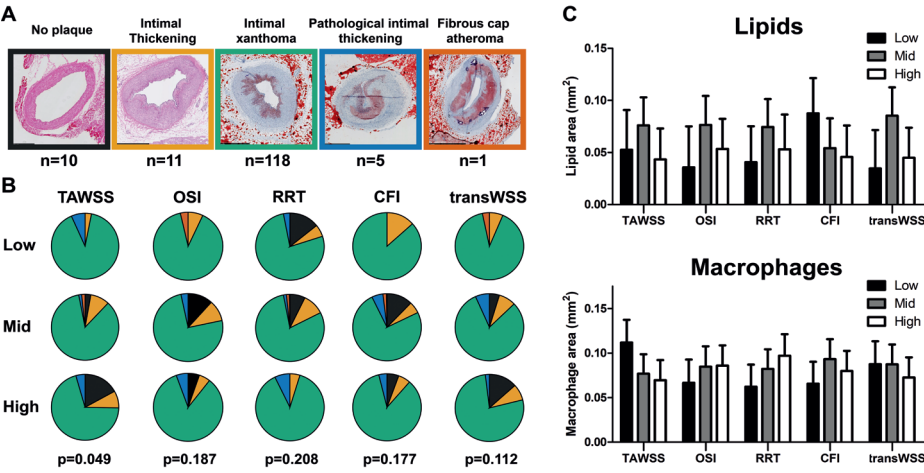


**Figure 5. Histological plaque composition and the relation with WSS metrics in Mildly-diseased pigs.**

**A)** Histological examples of plaques according to the revised AHA plaque classification. **B)** Distribution of the plaque types over regions with preceding low, mid or high levels of the respective WSS metrics (time-averaged WSS (TAWSS); oscillatory shear index (OSI); relative-residence time (RRT); cross-flow index (CFI); transverse WSS (transWSS)). P-value is for the overall relations (statistics: chi-square test). **C)** The absolute lipid or macrophage area observed in regions with either preceding significant relationships were observed (statistics: linear mixed effects model). TAWSS = time-average WSS; OSI=oscillatory shear index; RRT=relative-residence time; CFI=cross-flow index; transWSS=transverse WSS.

A more detailed analysis of the plaque composition in the ADs supported these results. We observed that in regions with low (TAWSS) and multidirectional WSS (RRT and CFI), plaques presented with the largest lipid and macrophage area ( $p<0.05$ ) (Figure 5A and B). High OSI levels showed a positive trend for increased lipid content. For the necrotic core area, low TAWSS and high RRT levels resulted in twice as large necrotic cores compared to regions with higher TAWSS or lower RRT (Figure 5C). TransWSS showed no relation with plaque composition ( $p=NS$ ). For the MDs, no significant relation was observed between any of the WSS metrics and plaque composition (Figure 5C).

## Discussion

In the present study, we used a serial, multimodality imaging protocol in conjunction with histological analyses to assess the influence of (multidirectional) WSS on the natural initiation and progression of coronary atherosclerotic plaques in a unique adult familial hypercholesterolemia pig model. This study design enabled for the first time a comprehensive comparison of five (multidirectional) wall shear stress metrics for their influence on plaque progression and composition changes.

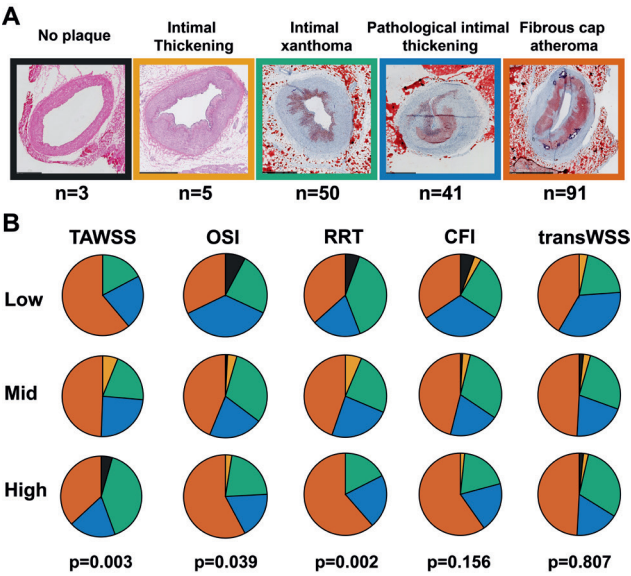


**Figure 6. Relation between histological plaque classification and T1 (multidirectional) WSS levels in the advanced-diseased pigs (ADs).**

**A)** Histological examples of plaques according to the revised AHA plaque classification. **B)** Distribution of the plaque types over regions with preceding low, mid or high levels of the respective WSS metrics (time-averaged WSS (TAWSS); oscillatory shear index (OSI); relative-residence time (RRT); cross-flow index (CFI); transverse WSS (transWSS)). P-value is for the overall relations (statistics: chi-square test).

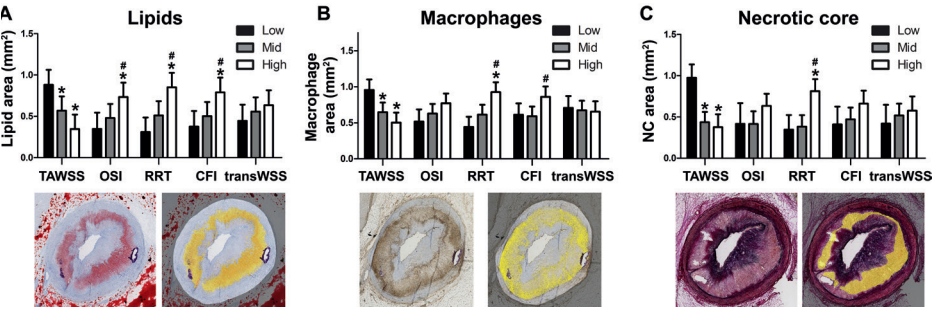


**Figure 7. The effect of T1 (multidirectional) wall shear stress (WSS) levels on final histological plaque composition in advanced-diseased pigs (ADs).**

**A-C)** The absolute lipid (Oil-red-O staining, red=lipid) (A), macrophage (CD68 staining, brown=macrophages) (B) or necrotic core (Miller staining, purple=collagen) (C) area (example positive staining indicated in yellow) preceded by low, mid or high levels of one of the five WSS metrics (mean $\pm$ SD) (time-averaged WSS (TAWSS); oscillatory shear index (OSI); relative-residence time (RRT); cross-flow index (CFI); transverse WSS (transWSS)). \* $p<0.05$  vs. low tertile of the respective WSS metric; # $p<0.05$  vs. mid tertile (statistics: linear mixed effects model).

The results of the study are summarised in Table 2 and demonstrated that: 1) plaque initiation and plaque progression are associated with low TAWSS and high levels of multidirectional WSS, both in mildly-diseased and advanced-diseased pigs, with the most pronounced relations in the latter group; 2) the greatest plaque growth rate was observed in regions with initial low TAWSS, turning into high TAWSS at  $T_2$ , while for multidirectional WSS, no clear differences in plaque growth rate were observed between regions with either sustained or changing WSS levels; 3) plaques with a vulnerable composition, as observed in the AD pigs, most often developed in regions with low TAWSS and high levels of OSI, RRT and CFI, while transWSS was not related to plaque composition; 4) all multidirectional WSS metrics, except transWSS, have a good positive predictive value for development of plaque, and an even better predictive value for the development of fibrous cap atheroma.

#### Relation of low and multidirectional WSS with plaque initiation, progression and composition

In order to discuss our results on the relationship between WSS and plaque initiation and progression, it is vital to recognize the different roles of WSS in the various stages of atherosclerosis<sup>23</sup>. In clinical studies, the presence of larger stenosis degrees leads to local elevation of the WSS. In these advanced disease stages, WSS, in combination with intravascular imaging to detect plaque composition, could serve as a marker for localizing vulnerable plaques, or form a predictor for plaque destabilization as suggested by the studies of Kumar et al.<sup>24</sup> and Slager et al.<sup>25</sup>. Pre-clinical studies, or clinical studies that exclude narrowed arterial regions, are the only way to assess the causal role of WSS in plaque initiation and progression. In this discussion, considering our study design, we focused on the role of (multidirectional) WSS in early disease development.

Absolute WSS levels are highly dependent on the used methodology, which for example results in the, on average, lower TAWSS values in our study compared to most of the previously reported absolute values. This is most likely caused by the fact that side branches were included in our models, which lowers the flow and thus the wall shear stress through the downstream artery. Because of this methodological dependency, a reliable comparison of the relation between different multidirectional WSS metrics and plaque development is only possible within one study. With our current study, we are the first to assess and compare the effect of five different (multidirectional) WSS metrics on plaque initiation and progression. We confirmed the findings from previous studies<sup>9,26,27</sup> which showed that low TAWSS and high levels of OSI and RRT result in the highest initial plaque growth. We also observed that the same relation holds true for plaque progression. Both CFI and transWSS showed similar, but less pronounced relations with plaque initiation and progression.

As already described in a study by Koskinas et al.<sup>28</sup>, WSS levels change over time. We observed that around 48% of the studied segments exhibited changes in local WSS levels. With regard to plaque initiation, the largest plaque growth was found in sectors with  $T_1$  low TAWSS that changed to higher TAWSS at  $T_2$ . This local elevation of TAWSS at  $T_2$  can very well be caused by lumen intrusion of large plaques, which was similarly observed in human advanced disease by Kumar et al.<sup>24</sup>. Interestingly, in these same regions with high TAWSS at  $T_2$ , the plaque growth rate during plaque progression between  $T_2$ - $T_3$  was lowest of all analysed sectors. This could indicate that the growth rate of these large plaques tends to decrease when the TAWSS rises. Despite the relatively short time period between  $T_2$ - $T_3$ , the significantly highest plaque growth rate from  $T_2$ - $T_3$  was observed in regions with low TAWSS at  $T_2$ , independent from the TAWSS levels at  $T_1$ . Apparently, when low WSS is present, it triggers plaque growth, confirming the findings by Koskinas et al.<sup>28</sup>, until the plaque starts to intrude into the lumen and TAWSS levels elevate. For the multidirectional WSS parameters OSI, RRT and CFI, regions with initial ( $T_1$ ) high and subsequently ( $T_2$ ) low levels presented with the highest plaque growth rate. Although never studied before, this could mean that the multidirectionality of WSS reduces upon plaque lumen intrusion. This reduced multidirectionality then results in reduced plaque growth as observed in our plaque progression ( $T_2$ - $T_3$ ) analysis.

Not only plaque size, but also plaque composition is important for risk-assessment of coronary events<sup>29</sup>. In two human studies with advanced disease, a correlation has been shown between (the development of) a positive NIRS signal (i.e. lipid-rich plaques) and high TAWSS<sup>30,31</sup>. Such a relation has never been described for earlier disease stages. In this study, we demonstrated a trend between NIRS-positive plaques and preceding low TAWSS. Multidirectional WSS metrics showed an even stronger effect, with NIRS-positive plaque development significantly more often preceded by high OSI and CFI levels compared to low multidirectional WSS. However, since the number and size of NIRS-positive regions was limited, our results on the correlation between WSS and NIRS should be interpreted with care.

The observed relation between (multidirectional) WSS and lipid-rich plaques derived from NIRS imaging was confirmed by OCT. Important to notice is that the number of OCT-detected FCAs was much lower compared to our histological findings. Reassessment of the accompanying histological data revealed that many lipid-rich necrotic cores are apparently invisible on OCT, hypothetically because they are 'shielded' by a layer of lipids in the cap structure.

Previous pre-clinical studies applied histology to determine the relation between plaque composition and WSS. These studies demonstrated that the development of advanced plaques with lipid and inflammatory cell infiltration was associated



with low TAWSS<sup>13,26,27,32</sup>. Furthermore, Pedrigi et al.<sup>13</sup>, who used a perivascular cuff to induce atherosclerosis formation, concluded that, besides low WSS, also a variant metric of the transWSS was associated with advanced plaques. In our study, we demonstrated with histology that advanced plaques with a higher lipid and inflammatory cell content and larger necrotic cores developed in regions with low WSS, confirming the results from the previous studies<sup>13,26,27,32</sup>. In contrast to the findings by Pedrigi et al.<sup>13</sup>, transWSS was not related to plaque composition. This difference might be related to the use of the perivascular cuff in the study of Pedrigi. The narrowing of the vessel induced by this cuff can result in multidirectional flow patterns that are normally not observed in early disease stages. However, we did show that the multidirectional metric RRT was strongly associated with the development of plaques with an advanced and complex composition. High levels of OSI and CFI mainly colocalized with regions with an overall more advanced plaque phenotype and with a high lipid-content, but could not be related to macrophage abundance or necrotic core size. Following these observations, plaque inflammation might mainly be affected by low WSS resulting in a high particle-residence time (RRT), but not by more complex flow patterns expressed by the OSI and CFI.

Although shear stress is known to influence plaque composition over time and thereby also affects the risk on plaque rupture, analysis of the structural stress in the vessel wall better predict the immediate risk on cardiovascular events. Wall stress can be assessed using computational modelling with the plaque composition and loading conditions as input<sup>33</sup>. Recently, more advanced methodologies have been applied, such as fluid structure interaction, but these methods require input on often unknown boundary conditions<sup>34,35</sup>.

Many of our above-mentioned findings were most pronounced in our advanced-diseased pigs, while in our mildly-diseased pigs, mainly the TAWSS and the RRT were associated with plaque development. The observed differences between MD and AD pigs will be discussed below.

#### **Advanced and mildly-diseased pigs: difference in plaque growth and response to WSS metrics**

We observed clear differences in plaque size and growth, but also in the response to WSS between MD and AD animals, despite similar WSS levels and conventional risk factors. The difference in response to WSS between the ADs and MDs indicates that, as commonly accepted, besides WSS, more factors are (synergistically) involved in determining the sensitivity for plaque development. As discovered in a previous study by our group<sup>36</sup>, a pronounced difference in low-density lipoprotein profile between the ADs and MDs makes the AD pigs much more prone to develop (coronary) atherosclerosis. Recent publications confirm these findings and show

that, also in patients, differences in specific lipoprotein profiles can result in inter-individual differences in cardiovascular outcome<sup>37,38</sup>. Since WSS is mainly a factor that triggers the local influx of inflammatory cells and lipids into the vessel wall in an already high-risk systemic environment, differences in systemic risk-factors like the low-density lipoprotein profile might explain why WSS in the MDs is not as strongly associated with plaque growth as in the ADs. However, despite a systemic predisposition for plaque growth in the AD pigs, plaque development and progression were strongly related to shear stress in both groups of pigs, implying an essential role for shear stress in plaque development.

Unfortunately, comparison of these results with other pre-clinical WSS literature is difficult, since animals that present with limited plaque growth are regarded as 'non-responders' and are often not taken into account for analysis. To make an honest assessment of the role of WSS in plaque development, thereby also better mimicking the large variability in disease development observed in human populations, we retained the MD pigs in the analysis.

#### **The predictive value of multidirectional WSS metrics**

To enable future application of WSS measurements in the clinic, establishing its positive predictive value for plaque progression is important. The PREDICTION study<sup>5</sup> reported a positive predictive value of low TAWSS of 25% in comparison to 50% in our study. The higher positive predictive value in our study could, at least in part, be explained by the fact that, in contrast to all PREDICTION patients, our animals did not receive statin treatment which is known to induce plaque regression. In stable ACS patients, Rikhtegar et al.<sup>11</sup> reported that multidirectional WSS parameters might be a better predictor for plaque localization at one time point than low TAWSS (low TAWSS: 31%; high OSI: 35%; high RRT: 49%). In our study, where the effect of WSS metrics on plaque development *over time* was assessed, we show that low TAWSS and high RRT are the best predictors, partially contrasting the results of Rikhtegar et al.. Finally, while most studies have evaluated the PPV of WSS for plaque size, we are the first to assess the predictive value of WSS for plaque composition. Interestingly, we observed that WSS might be an even better predictor for the development of FCA than for plaque *size* (PPV of 61% (TAWSS and RRT) versus 50% (TAWSS) and 49% (RRT)). With this study we enabled, for the first time, a reliable one-to-one comparison of five different WSS metrics for plaque development. Based on our results, we can now conclude that, although multidirectional WSS is significantly involved in the disease process, low TAWSS remains the strongest driving factor and predictor of both plaque initiation and progression. This finding could offer an advantage with regard to computational times, since TAWSS can reliably be approached by stationary simulations<sup>39</sup>. These stationary simulations are much less time-consuming than full time-dependent simulations that are needed for multidirectional WSS calculation.

### Limitations

The present study has a number of limitations. First, the coronary arteries were modelled as static non-moving arteries. We showed in an earlier study that shear stress in a natural moving and deforming coronary artery is well approximated by modelling steady mean flow in the rigid diastolic geometry of this coronary artery<sup>40</sup>. Second, the number of pigs used in this study was small, and the unexpected split into fast and slow responders further reduced the number of arteries that was available to investigate advanced plaque development. However, multiple sectors within one coronary artery were analysed to capture the local WSS effect. A linear mixed-effects model was applied to correct for remaining dependencies. Using this approach, a statistically significant effect of multidirectional WSS on plaque development could be identified in both types of pigs. Furthermore, since the absolute levels of OSI, CFI and transWSS were low, the division of the WSS tertiles could be considered as somewhat artificial. Still, we did find significant relations between the relative levels of these metrics and both plaque size and composition.

### Conclusion

In the present study we combined detailed invasive imaging and histopathology to demonstrate that the highest plaque growth rate was exclusively found at low TAWSS or high multidirectional WSS at both  $T_1$  (for plaque initiation) and  $T_2$  (for plaque progression). Regions with initial low TAWSS which, over time, turned into regions with high TAWSS, demonstrated the overall largest plaque growth. For multidirectional WSS, the largest plaque growth was found in regions with initial high levels of OSI, RRT and CFI that changed into regions with low levels of these parameters. These elevated TAWSS levels and reduced multidirectional WSS levels at  $T_2$  are probably due to the development of lumen-intruding plaques. The development of plaques with an advanced plaque *composition* was also related to low TAWSS and high OSI, RRT or CFI, but not to transWSS. While the predictive values of the individual multidirectional WSS metrics for plaque growth were high, advanced plaque *composition* was even more reliably predicted by (multidirectional) WSS metrics with the TAWSS and RRT being the strongest predictors. The differences between the AD and MD pigs stress the importance of a synergistic effect of systemic risk factors and local shear stress levels. The overall results highlight that, although multidirectional WSS is significantly involved in coronary plaque initiation and progression, low TAWSS remains the best predictive clinical marker for vulnerable disease development.

### Translational Perspective

Wall shear stress (WSS) plays a key role in coronary atherosclerotic plaque development and destabilization. However, the multidirectionality of WSS is rarely

taken into account. In this pre-clinical study, we demonstrated that both plaque initiation and progression were related to low and multidirectional WSS. Therefore, regions exposed to low and/or multidirectional WSS regions throughout disease development, continue to be at risk for further plaque progression. The high predictive values of almost all multidirectional WSS metrics for plaque progression and advanced plaque composition demonstrated the potential of multidirectional WSS as an additional predictive clinical marker for vulnerable disease.

### Acknowledgements

We gratefully acknowledge Ilona Krabbendam - Peters, Karen Witberg, Maaïke Visser - te Lintel Hekkert, Kim van Gaalen, Jurgen Ligthart and Marcel Dijkshoorn for their expert technical assistance in the animal experiments and data acquisition. Furthermore, we thank Maria Siebes for the lending of the ComboMap device and the accompanying user-advice.

## References

- Mathers CD, Loncar D. Projections of Global Mortality and Burden of Disease from 2002 to 2030. *PLoS Med* 2006;3:e442.
- Chatzizisis YS, Jonas M, Coskun AU, Beigel R, Stone BV, Maynard C, et al. Prediction of the localization of high-risk coronary atherosclerotic plaques on the basis of low endothelial shear stress-an intravascular ultrasound and histopathology natural history study. *Circulation* 2008;117:993–1002.
- Koskinas KC, Chatzizisis YS, Papafaklis MI, Coskun AU, Baker AB, Jarolim P, et al. Synergistic effect of local endothelial shear stress and systemic hypercholesterolemia on coronary atherosclerotic plaque progression and composition in pigs. *Int J Cardiol* 2013;169:394–401.
- Koskinas KC, Chatzizisis YS, Baker AB, Edelman ER, Stone PH, Feldman CL. The role of low endothelial shear stress in the conversion of atherosclerotic lesions from stable to unstable plaque. *Curr Opin Cardiol* 2009;24:580–90.
- Stone PH, Saito S, Takahashi S, Makita Y, Nakamura SS, Kawasaki T, et al. Prediction of progression of coronary artery disease and clinical outcomes using vascular profiling of endothelial shear stress and arterial plaque characteristics: the PREDICTION Study. *Circulation* 2012;126:172–81.
- Stone PH, Maehara A, Coskun AU, Maynard CC, Zaromytidou M, Siasos G, et al. Role of Low Endothelial Shear Stress and Plaque Characteristics in the Prediction of Nonculprit Major Adverse Cardiac Events: The PROSPECT Study. *JACC Cardiovasc Imaging* 2018;11:462–71.
- Corban MT, Eshtehardi P, Suo J, McDaniel MC, Timmins LH, Rassoul-Arzrumly E, et al. Combination of plaque burden, wall shear stress, and plaque phenotype has incremental value for prediction of coronary atherosclerotic plaque progression and vulnerability. *Atherosclerosis* 2014;232:271–6.
- Samady H, Eshtehardi P, McDaniel MC, Suo J, Dhawan SS, Maynard C, et al. Coronary artery wall shear stress is associated with progression and transformation of atherosclerotic plaque and arterial remodeling in patients with coronary artery disease. *Circulation* 2011;124:779–88.
- Peiffer V, Sherwin SJ, Weinberg PD. SPOTLIGHT REVIEW Does low and oscillatory wall shear stress correlate spatially with early atherosclerosis? A systematic review. *Cardiovasc Res* 2013;99:242–50.
- Knight J, Olgac U, Saur SC, Poulikakos D, Marshall W, Cattin PC, et al. Choosing the optimal wall shear parameter for the prediction of plaque location—A patient-specific computational study in human right coronary arteries. *Atherosclerosis* 2010;211:445–50.
- Rikhtegar F, Knight JA, Olgac U, Saur SC, Poulikakos D, Marshall WC, et al. Choosing the optimal wall shear parameter for the prediction of plaque location-A patient-specific computational study in human left coronary arteries. *Atherosclerosis* 2012;221:432–7.
- Timmins LH, Molony DS, Eshtehardi P, McDaniel MC, Oshinski JN, Giddens DP, et al. Oscillatory wall shear stress is a dominant flow characteristic affecting lesion progression patterns and plaque vulnerability in patients with coronary artery disease. *J R Soc Interface* 2017;14:20160972.
- Pedrigi RM, Poulsen CB, Mehta V V, Ramsing Holm N, Pareek N, Post AL, et al. Inducing Persistent Flow Disturbances Accelerates Atherogenesis and Promotes Thin Cap Fibroatheroma Development in D374Y-PCSK9 Hypercholesterolemic Minipigs. *Circulation* 2015;132:1003–12.
- Peiffer V, Sherwin SJ, Weinberg PD. Computation in the rabbit aorta of a new metric – the transverse wall shear stress – to quantify the multidirectional character of disturbed blood flow. *J Biomech* 2013;46:2651–8.
- Thim T, Hagensen MK, Drouet L, Bal Dit Sollier C, Bonneau M, Granada JF, et al. Familial hypercholesterolaemic downsized pig with human-like coronary atherosclerosis: a model for preclinical studies. *EuroIntervention* 2010;6:261–8.
- National Research Council (US) Committee for the Update of the Guide for Care and Use of Laboratory Animals. Guide for the Care and Use of Laboratory Animals. Washington, D.C.: National Academies Press; 2011.
- Virmani R, Kolodgie FD, Burke AP, Farb A, Schwartz SM. Lessons From Sudden Coronary Death : A Comprehensive Morphological Classification Scheme for Atherosclerotic Lesions. *Arterioscler Thromb Vasc Biol* 2000;20:1262–75.
- Tearney GJ, Regar E, Akasaka T, Adriaenssens T, Barlis P, Bezerra HG, et al. Consensus standards for acquisition, measurement, and reporting of intravascular optical coherence tomography studies: A report from the International Working Group for Intravascular Optical Coherence Tomography Standardization and Validation. *J Am Coll Cardiol* 2012;59:1058–72.
- Schaap M, Neefjes L, Metz C, van der Giessen A, Weustink A, Mollet N, et al. Coronary lumen segmentation using graph cuts and robust kernel regression. *InfProcess Med Imaging* 2009;21:528–39.
- Huo Y, Kassab GS. Intraspecific scaling laws of vascular trees. *J R Soc Interface* 2012;9:190–200.
- Seo T, Schachter LG, Barakat AI. Computational study of fluid mechanical disturbance induced by endovascular stents. *Ann Biomed Eng* 2005;33:444–56.
- De Nisco G, Kok AM, Chiastra C, Gallo D, Hoogendoorn A, Migliavacca F, et al. The Atheroprotective Nature of Helical Flow in Coronary Arteries. *Ann Biomed Eng* n.d.;47.
- Wentzel JJ, Chatzizisis YS, Gijzen FJHH, Giannoglou GD, Feldman CL, Stone PH. Endothelial shear stress in the evolution of coronary atherosclerotic plaque and vascular remodelling: current understanding and remaining questions. *Cardiovasc Res* 2012;96:234–43.
- Kumar A, Thompson EW, Lefieux A, Molony DS, Davis EL, Chand N, et al. High Coronary Shear Stress in Patients With Coronary Artery Disease Predicts Myocardial Infarction. *J Am Coll Cardiol* 2018;72:1926–35.
- Slager C, Wentzel J, Gijzen F, Thury A, van der Wal A, Schaap J, et al. The role of shear stress in the destabilization of vulnerable plaques and related therapeutic implications. *Nat Clin Pract Cardiovasc Med* 2005;2:456–64.
- Chatzizisis YS, Jonas M, Coskun AU, Beigel R, Stone BV, Maynard C, et al. Prediction of the Localization of High-Risk Coronary Atherosclerotic Plaques on the Basis of Low Endothelial Shear Stress: An Intravascular Ultrasound and Histopathology Natural History Study. *Circulation* 2008;117:993–1002.
- Koskinas KC, Feldman CL, Chatzizisis YS, Coskun AU, Jonas M, Maynard C, et al. Natural history of experimental coronary atherosclerosis and vascular remodeling in relation to endothelial shear stress: A serial, in vivo intravascular ultrasound study. *Circulation* 2010;121:2092–101.
- Koskinas KC, Sukhova GK, Baker AB, Papafaklis MI, Chatzizisis YS, Coskun AU, et al. Thin-capped atheromata with reduced collagen content in pigs develop in coronary arterial regions exposed to persistently low endothelial shear stress. *Arterioscler Thromb Vasc Biol* 2013;33:1494–504.
- Garcia-Garcia HM, Jang I-K, Serruys PW, Kovacic JC, Narula J, Fayad ZA. Imaging plaques to predict and better manage patients with acute coronary events. *Circ Res* 2014;114:1904–17.
- Wentzel JJ, van der Giessen AG, Garg S, Schultz C, Mastik F, Gijzen FJH, et al. In vivo 3D distribution of lipid-core plaque in human coronary artery as assessed by fusion of near infrared spectroscopy-intravascular ultrasound and multislice computed tomography scan. *Circ Cardiovasc Imaging* 2010;3:e6-7.
- Shishikura D, Sidharta SL, Honda S, Takata K, Kim SW, Andrews J, et al. The relationship between segmental wall shear stress and lipid core plaque derived from near-infrared spectroscopy. *Atherosclerosis* 2018;275:68–73.
- Millon A, Sigovan M, Bousset L, Mathevet J-L, Louzier V, Paquet C, et al. Low WSS Induces Intimal Thickening, while Large WSS Variation and Inflammation Induce Medial Thinning, in an Animal Model of Atherosclerosis. *PLoS One* 2015;10:e0141880.
- Akyildiz AC, Speelman L, Nieuwstadt HA, van Brummelen H, Virmani R, van der Lugt A, et al. The effects of plaque morphology and material properties on peak cap stress in human coronary arteries. *Comput Methods Biomech Biomed Engin* 2015;19:771–9.
- Gao H, Long Q, Graves M, Gillard JH, Li Z-Y. Carotid arterial plaque stress analysis using fluid-structure interactive simulation based on in-vivo magnetic resonance images of four patients. *J Biomech* 2009;42:1416–23.

35. Li Z-Y, Howarth SPS, Tang T, Gillard JH. How Critical Is Fibrous Cap Thickness to Carotid Plaque Stability? *Stroke* 2006;37:1195–9.
36. Hoogendoorn A, den Hoedt S, Hartman EMJ, Krabbendam-Peters I, Te Lintel Hekkert M, van der Zee L, et al. Variation in Coronary Atherosclerosis Severity Related to a Distinct LDL (Low-Density Lipoprotein) Profile. *Arterioscler Thromb Vasc Biol* 2019;39:2338–52.
37. Laaksonen R, Ekroos K, Sysi-Aho M, Hilvo M, Vihervaara T, Kauhanen D, et al. Plasma ceramides predict cardiovascular death in patients with stable coronary artery disease and acute coronary syndromes beyond LDL-cholesterol. *Eur Heart J* 2016;37:1967–76.
38. Anroedh S, Hilvo M, Akkerhuis KM, Kauhanen D, Koistinen K, Oemrawsingh R, et al. Plasma concentrations of molecular lipid species predict long-term clinical outcome in coronary artery disease patients. *J Lipid Res* 2018;59:1729–37.
39. Reuderink PJ. Analysis of the flow in a 3D distensible model of the carotid artery bifurcation. Eindhoven University of Technology, 1991.
40. Wolters BJBM, Slager CJ, Gijzen FJH, Wentzel JJ, Krams R, van de Vossel FN. On the numerical analysis of coronary artery wall shear stress. *Comput. Cardiol.* 2001. Vol.28 (Cat. No.01CH37287), IEEE; n.d., p. 169–72.



# 5

## Lipid-rich plaques detected by near-infrared spectroscopy are more frequently located in regions of high shear stress

This chapter based on:

Lipid-rich plaques detected by near-infrared spectroscopy are more frequently located in regions of high shear stress

Eline M.J. Hartman, Giuseppe De Nisco, Annette M. Kok, Ayla Hoogendoorn, Adriaan Coenen, Frits Mastik, Suze-Anne Korteland, Koen Nieman, Frank J.H. Gijsen, Anton F.W. van der Steen, Joost Daemem, Jolanda J. Wentzel

*Journal of Cardiovascular Translational Research, 2020*

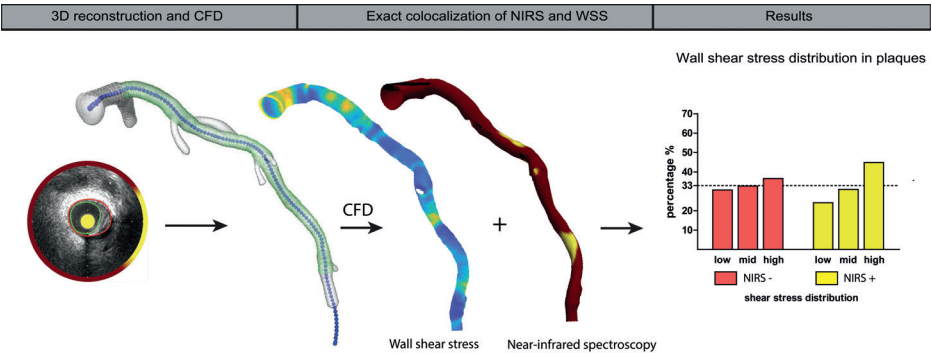


Abstract

High wall shear stress (WSS) and near-infrared spectroscopy (NIRS) detected lipid-rich plaque (LRP) are both known to be associated with plaque destabilization and future adverse cardiovascular events. However, knowledge of spatial colocalization of LRP and high WSS is lacking. This study investigated the colocalization of LRP based on NIRS and high WSS.

Fifty-three patients presenting acute coronary syndrome underwent NIRS-ultrasound (NIRS-IVUS) imaging of a non-culprit coronary artery. WSS was obtained using WSS profiling in 3D-reconstructions of the coronary arteries based on fusion of IVUS-segmented lumen and CT-derived 3D-centerline. 38 vessels were available for final analysis and divided into 0.5mm/45° sectors. LRP sectors, as identified by NIRS, were more often colocalized with high WSS than sectors without LRP. Moreover, there was a dose-dependent relationship between lipid content and high WSS exposure.

This study is a first step in understanding the evolution of LRPs to vulnerable plaques.



Introduction

The underlying cause of most cardiovascular diseases is atherosclerosis, an inflammatory driven disease associated with lipid accumulation in the vessel wall, resulting in plaque formation. The destabilization and rupture of an atherosclerotic plaque remains a leading cause of death. In recent decades, an increasing amount of research has focused on the contribution of local risk factors precipitating future plaque rupture and subsequent cardiovascular events<sup>1-3</sup>.

One of these local risk factors is the composition of the plaque. The presence of a lipid pool inside the plaque has been strongly associated with plaque vulnerability, destabilization, and clinical events<sup>3,4</sup>. Such lipid pools in the vessel wall can currently be detected using the invasive imaging technique near-infrared spectroscopy (NIRS). A combined catheter of NIRS with intravascular ultrasound (IVUS) has been validated for the detection of the local lipid content of coronary plaques<sup>5</sup>. Previous studies using NIRS have shown that the presence of these lipid-rich plaques (LRPs) is independently associated with future major adverse cardiovascular events<sup>3,4</sup>.

A second local factor that is strongly associated with atherosclerosis is wall shear stress (WSS), the frictional force of the bloodstream exerted on the endothelial cells of the vessel wall. Low WSS causes endothelial dysfunction and plays an important role in the development of atherosclerosis<sup>6</sup>. In more advanced stages of atherosclerosis, if plaques intrude into the lumen, WSS will increase. High WSS has been related to apoptosis of smooth muscle cells and consequently, to plaque vulnerability and potentially plaque rupture<sup>7</sup>. Recently, high WSS has been proven to be of added value in the prediction of myocardial infarction<sup>8</sup>.

Although both high lipid content detected by NIRS, and high WSS are associated with plaque destabilization and cardiovascular events, knowledge on colocalization of these two factors is still lacking. We hypothesized that high WSS plays a role in the destabilization of LRPs and thereby contributes to an event. Therefore, in this present study, the co-localization of LRPs and high WSS is investigated in non-culprit segments of patients presenting with an acute coronary syndrome (ACS) as a first step to understand the potential interaction between high WSS and LRPs in plaque destabilization and future events.

## Methods

### Study design

The IMPACT study was a prospective, single-center study designed to evaluate the association between biomechanical parameters and atherosclerotic disease in non-stented coronary arteries. Hemodynamically stable patients with ACS with at least one non-stented non-culprit coronary segment accessible for intracoronary imaging were eligible for enrollment. Exclusion criteria included the presence of previous coronary artery bypass graft surgery, 3-vessel disease, renal insufficiency (creatinine clearing < 50ml/min), left ventricular ejection fraction < 30%, and atrial fibrillation. All patients were treated with percutaneous coronary intervention (PCI) of the culprit lesion(s). After successful treatment, a non-culprit segment was imaged according to the IMPACT acquisition protocol. Written informed consent was obtained from all patients. The study protocol was approved by the local medical ethical committee of the Erasmus MC (MED 2015-535, NL54519.078.15) and the study was conducted in accordance with the World Medical Association Declaration of Helsinki (64<sup>th</sup> WMA General Assembly, Fortaleza, Brazil, October 2013) and Medical Research Involving Human Subject Act (WMO).

### Data acquisition

After successful PCI, a non-culprit coronary segment with a length of at least 30 mm and two readily identifiable side branches (diameter >1.5 mm) was selected as study segment. After angiographic assessment of the non-culprit coronary artery, invasive imaging of the study segment was performed. The images were acquired by an automated pullback (0.5mm/s) with a NIRS-IVUS catheter (TVC Insight Coronary Imaging Catheter, InfraRedX, Burlington, MA, USA) (0.5mm/sec). Subsequently, invasive local flow measurements were performed using a ComboWire (Phillips Volcano, Zaventem, Belgium) at different locations between side branches to assess the local blood flow. One month after the invasive measurements, patients visited the outpatient clinic to undergo coronary computed tomography angiography (CCTA) according to standard prospectively ECG-triggered clinical protocol (SOMATOM Force (192 slice 3<sup>rd</sup> generation dual-source CT scanner), Siemens Healthineers, Germany).

### IVUS-NIRS image analysis.

Data was anonymized and analyzed offline. As a result of a continuous IVUS pullback, variations in coronary lumen and vessel size due to cardiac motion were present. Therefore, the IVUS images were retrospectively gated by selecting the frame that was located 6 frames before the R-peak using an in-house developed MATLAB (v.2017B, Mathworks Inc, USA) algorithm. The gated frames corresponded with the end-diastolic phase of the cardiac cycle. In all gated NIRS-IVUS frames, the lumen and the external elastic membrane were segmented by an experienced reader (EH). An intra-observer analysis was performed in a random sample of

5 IVUS pullbacks (748 frames) with at least two months interval between the segmentations. A good reproducibility of EEM area, lumen area and plaque area was found (0.996 [95%CI 0.996-0.997], 0.983[95%CI 0.963-0.990] and 0.958 [95%CI 0.939-0.970]). In the IVUS images, calcium, defined as a bright signal with a dark shadow behind it, was identified as an angle with the protractor in the center of the lumen. The NIRS signal in the NIRS-IVUS images was analyzed for each degree and labeled as NIRS positive when the signal was >0.6, implying a high probability for the presence of lipids<sup>9</sup>. The Lipid Core Burden Index (LCBI) (area positive for NIRS signal/total area\*1000) was determined for the study segment. Additionally, for each vessel, we identified the 4 mm region with the highest LCBI and thus, the highest lipid content ( $\max\text{LCBI}_{4\text{mm}}$ )<sup>10</sup>.

### 3D vessel reconstruction

By fusing the 3D spatial information of the coronary vessel centerline segmented from the CCTA and the lumen contours extracted from the NIRS-IVUS, a 3D reconstruction was made in MeVisLab (MeVis Medical Solutions AG, Bremen, Germany). The data from the two imaging modalities were matched using large side branches as landmarks, visible in both acquisitions. For subsequent computational fluid dynamics (CFD), reliable inlet and outlets were needed. Therefore, the regions proximal and distal to the IVUS-derived region of interest, as well as side branches (>1.5mm) were segmented on the CCTA and scaled and fused with the 3D reconstruction<sup>11</sup>. Of note, for final analysis, only the IVUS-derived region of interest (ROI) was considered. By using a NIRS-IVUS catheter, we could reliably map information on the vessel wall thickness, as well as the NIRS signal onto the ROI of the 3D reconstruction for colocalization analysis (Figure 1A).

### Computational fluid dynamics

CFD analysis was used to obtain the local according to previously described methodology<sup>12</sup>. In brief, a time-dependent CFD simulation was performed in each reconstructed 3D-geometry, assuming blood as an incompressible, homogeneous, Carreau fluid (Fluent, v.17.1, ANSYS Inc.)<sup>13</sup>. For the CFD simulations, in- and outflow boundary conditions were required. The flow was derived from intravascular Doppler measurements. The quality of those was examined in a consensus meeting of experts (AH, EH, FG, JW) based on the quality, repeatability, and consistency of the flow signal. For the inflow boundary condition, the most proximal flow measurement of good quality was used as a waveform profile for the time-dependent CFD simulation. Furthermore, for the outflow boundary conditions, the flow distribution through the side branches was calculated based on the intravascular flow measurements at different locations in the coronary artery. For the regions with no reliable flow measures, a previously described scaling law was used to determine the flow ratio between the mother and side branches<sup>14</sup>. To obtain the time-averaged WSS, the computed shear stresses were averaged over a cardiac cycle.

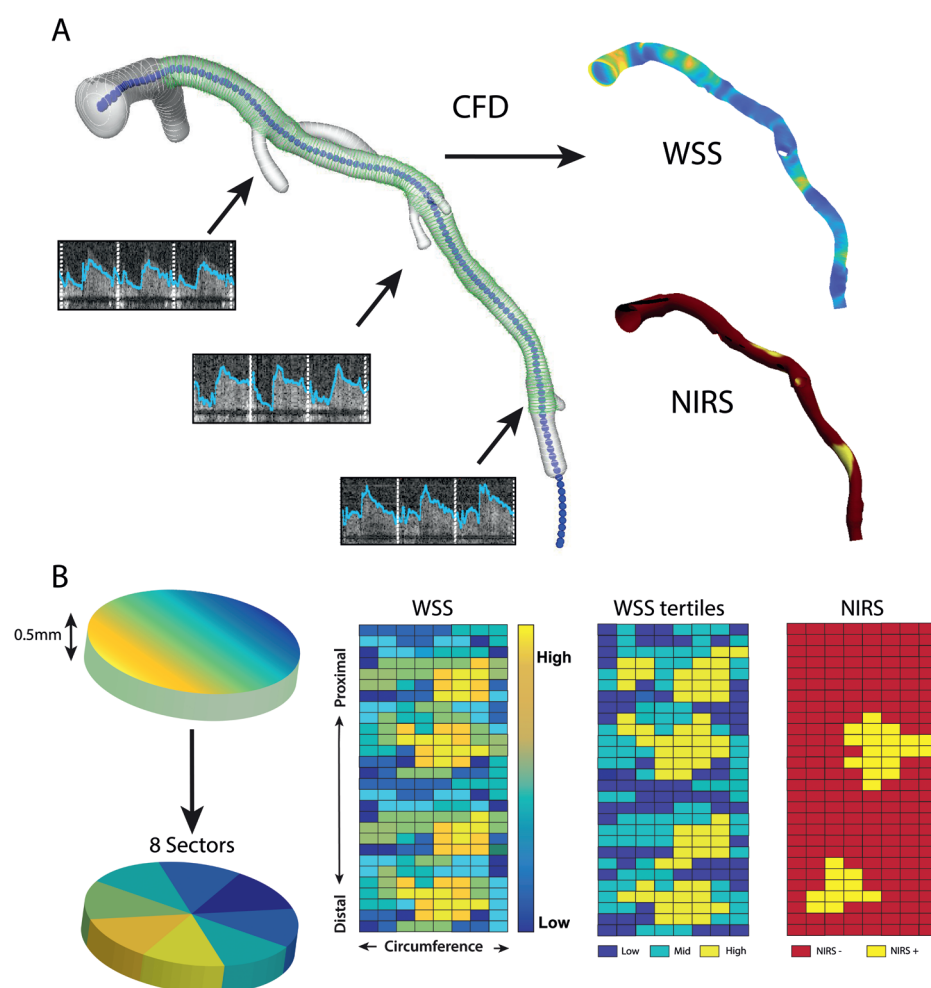


**Figure 1. The methodology of the wall shear stress (WSS) calculations and analysis of near-infrared spectroscopy (NIRS).**

**A:** IVUS contours (green, the region of interest) and CT contours (white) were matched and fused to make a surface of the 3D reconstruction. At different locations along the artery, flow measurements were done (arrows). Combined, these were used as boundary conditions for the computational fluid dynamics (CFD) and resulted in WSS. The NIRS signal was plotted onto the 3D reconstruction for colocalization analysis. **B:** The artery was divided into cross-sectional disks of 0.5mm perpendicular to the centerline of the vessel. These were divided into 8 45° sectors each. A 2D map was created, with on the X-axis, the circumference of the vessel, and on the y-axis, the distance along the centerline. For WSS, the 2D map sectors were divided into low, mid, and high WSS. A similar 2D map was created for binary NIRS data (yellow = NIRS positive, red = NIRS negative).

### Data analysis

All analyzed data was mapped on the 3D geometry of the coronary vessel using VMTK (Orobix, Bergamo, Italy) and MATLAB (v2017b, MathWorks Inc, Natick, MA, USA). For statistical analysis, the 3D reconstruction was converted to a 2D map by folding open the vessel in a longitudinal direction. This type of mapping is comparable to the standard NIRS data display, known as a chemogram. By using this 2D map, all arteries were divided into cross-sectional slices of 0.5 mm thick. All cross-sectional 0.5mm slices were then divided into 8 angular sectors of 45°, and for all different parameters, the averaged value per sector was used (Figure 1B). All sectors covering side branches were excluded from further analysis. Additionally, since calcium hampers the visualization of the outer vessel wall, all sectors that contained extensive calcifications (>90 degrees) were excluded from the analysis. In previous research, a cross-sectional plaque burden was used as a measure for disease burden (Plaque area/vessel area\*100). However, in this study, 8 sectors were used for more detailed colocalization. Therefore, a relative plaque area (sectorial plaque area /sectorial vessel area sector\*100) was calculated (Figure 2). A sector was regarded NIRS(+) when 50% of data in the sector was NIRS positive (>0.6 probability of the presence of lipids). For each vessel, WSS was divided into vessel-specific tertiles (low, mid, and high), allocating one-third of the sectors in the vessel as high WSS.

### Statistical analysis

Normally distributed data were shown as mean  $\pm$  standard deviation. Non-normally distributed data were presented as median (interquartile range (IQR)). For all analyses, sectors with no plaque (wall thickness<0.5mm) were excluded. Firstly, a sector-based analysis was performed in the full ROI comparing NIRS(+) plaques and NIRS(-) plaques for differences in geometrical parameters and exposure to WSS. Secondly, this analysis was repeated for the sectors that were part of the maxLCBI<sub>4mm</sub> region, the 4mm region with the most lipid content. Furthermore, we studied the exposure of high WSS in 3 different groups of the maxLCBI<sub>4mm</sub> based on the LCBI value (<250, 250-400 and >400) to research a dose-dependent relationship between LCBI and exposure to high WSS. These thresholds were based on previously used thresholds for maxLCBI<sub>4mm</sub> in studies that showed that patients with higher maxLCBI<sub>4mm</sub> have a higher risk of future adverse cardiac events<sup>3,4</sup>. All differences in WSS frequency distributions were assessed using a Chi-square test. The differences in wall thickness and relative plaque area were assessed with the Mann Whitney U test. SPSS statistics version 21 for Windows (IBM corp, Armonk, New York) was used for statistical analysis. All tests were 2-tailed, and a p-value <0.05 was considered significant.

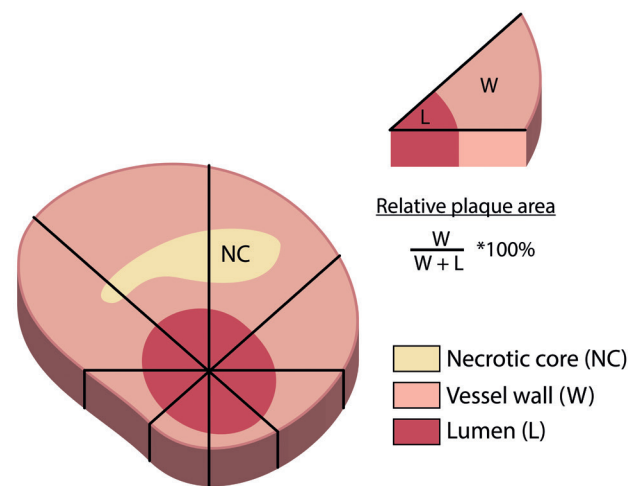


**Figure 2.** Each cross-section divided into 8 sectors of 45 degrees, based in the middle of the lumen. The relative plaque area was calculated for each sector.

Results

Between March 2016 and March 2018, a total of 53 patients were enrolled. Four patients withdrew study consent between the baseline procedure and CTTA. There were no major adverse events related to the study procedure. In one patient, it was not possible to match the CTTA-derived centerline with the NIRS-IVUS due to motion artifacts. In one vessel, no NIRS data was acquired during the NIRS-IVUS pullback, and in twelve vessels, less than one percent of the chemogram contained NIRS(+) data. These were all excluded from the analysis. Consequently, 38 vessels from 37 patients were included in the current analysis. Baseline characteristics are listed in table 1. The mean age of the patients was 62 ± 9 years, 91.9% was male, 24.3% of the patients had a history of previous PCI, and 40.5% of the patients were on statin therapy at the time of inclusion in the study. The studied non-culprit segment was located in the left anterior descending artery in 39% of the cases, in the left circumflex in 29% and in the right coronary artery in 32% of the cases.

Vessel characteristics and relationship to WSS

The median length of the IVUS based ROI in the non-culprit segment was 53 mm (43-64). The average WSS per vessel ranged from 0.31 to 3.00 Pa, and the median WSS over all vessels was 1.16 Pa (0.83-1.61). The median LCBI in the ROI was 54 (35-81), and the maxLCBI<sub>4mm</sub> was 282 (221-385). Out of the 38 vessels, 29% (N=11) had a maxLCBI<sub>4mm</sub> >400.

**Table 1. Baseline characteristics.**

Clinical characteristics	N = 37 patients
Age, years	62 ± 8.9
Men, n (%)	34 (91.8%)
Body Mass Index	27 ± 4.6
Diabetes Mellitus, n (%)	6 (16.2%)
Hypertension, n (%)	13(35.1%)
Dyslipidemia, n (%)	19(51.4%)
Current smoking, n (%)	7(18.9%)
Positive family history, n (%)	16(43.2%)
Previous MI, n (%)	8 (21.6%)
Previous PCI, n (%)	9(24.3%)
LDL (mmol/L)	2.6(2.1-3.2)
Imaged study vessel	N = 38 vessels
LAD, n (%)	15(39%)
LCX, n (%)	11(29%)
RCA, n (%)	12(32%)

Dividing the ROI of each vessel into cross-sections of 0.5mm resulted in a total of 4298 cross-sections. These cross-sections were then divided into 8 sectors of 45 degrees. After removing the sectors with side branches, this resulted in 33323 sectors of 45°. A total of 1925 (5.8%) sectors were excluded due to the presence of extensive calcifications (>90°), 20094 sectors had no plaque (wall thickness <0.5mm), and 431 sectors had no reliable NIRS signal. Therefore, 10873 sectors presenting with plaque, but no extensive calcifications were used for further analysis, and 1272 of these sectors were NIRS(+).

Table 2 summarizes the plaque characteristics of the sectors that were classified according to their NIRS-derived sectorial lipid status. The wall thickness and the relative plaque area were significantly higher in the NIRS(+) plaque sectors than in the NIRS(-) plaque sectors. Furthermore, the WSS distribution between NIRS(+) and NIRS(-) plaque sectors was significantly different. NIRS(-) sectors were for 31% exposed to low, 33% to mid, and 37% to high WSS. NIRS(+) sectors were for 24% exposed to low, 31% to mid, and for 45% exposed to high WSS P<0.001) (Figure 3a). Both for NIRS(-) as for the NIRS(+) sectors, the relative plaque area of the sectors was higher in each subsequent WSS tertile (NIRS(-) 48% vs 52% vs 56% and NIRS(+) 54% vs 58% vs 61% P<0.001).



Table 2. Plaque characteristics of sectors wall thickness >0.5mm.

	NIRS (-)	NIRS (+)	p-value
<b>Whole vessel</b>			
Number of sectors	9601	1272	
Wall thickness	0.70mm [0.59-0.86]	0.84mm[0.67-1.05]	<0.001
Relative plaque area	51% [45-58]	58% [50-66]	<0.001
<b>4mm maxLCBI<sub>4mm</sub></b>			
Number of sectors	652	432	
Wall thickness	0.72mm [0.61-0.90]	0.79mm [0.63-1.03]	<0.001
Relative plaque area	52% [45-59]	55% [47-66]	<0.001

In the maxLCBI<sub>4mm</sub> region, similar to the whole vessel, NIRS(+) sectors were more frequently exposed to high WSS than NIRS(-) sectors (59% vs. 45%) (Figure 3). When assessing the maxLCBI<sub>4mm</sub> regions, there was a dose-dependent relation for exposure of high WSS and the maxLCBI<sub>4mm</sub> value. Between low (<250), mid (250-400), and high (>400) maxLCBI<sub>4mm</sub> thresholds, the exposure to high WSS in this 4mm region increased (44% vs. 53% vs. 58% p<0.001) (Figure 4). The relative plaque area of the sectors was higher each subsequent maxLCBI<sub>4mm</sub> threshold (52% vs. 55% vs. 56% p <0.001).

Discussion

The present study shows for the first time that LRPs co-localize with exposure to high levels of WSS. Additionally, for the most diseased regions in the vessel, as identified by the maxLCBI4mm, a dose-dependent relation was found between LCBI and exposure to high WSS.

LRPs, as detected by NIRS, have been known to be a risk factor for future plaque rupture and major cardiovascular events<sup>3,4</sup>. Since not all LRPs rupture and result in an event, for clinical decision making and invasive treatment strategies, it is of crucial importance to understand the pathophysiology of LRP in its evolution to high-risk vulnerable plaques. Since plaque destabilization has been proven to be associated with high WSS<sup>8</sup>, as a first step in unravelling LRP destabilization, we investigated the exposure of LRP to high WSS. Therefore, we used detailed invasive imaging with NIRS-IVUS and computational fluid dynamics in non-culprit coronary arteries of acute coronary syndrome patients. In order to discuss the relationship between LRP and high WSS, it is essential to understand the interplay between lumen geometry, WSS distribution, and the pathophysiology of atherosclerosis.

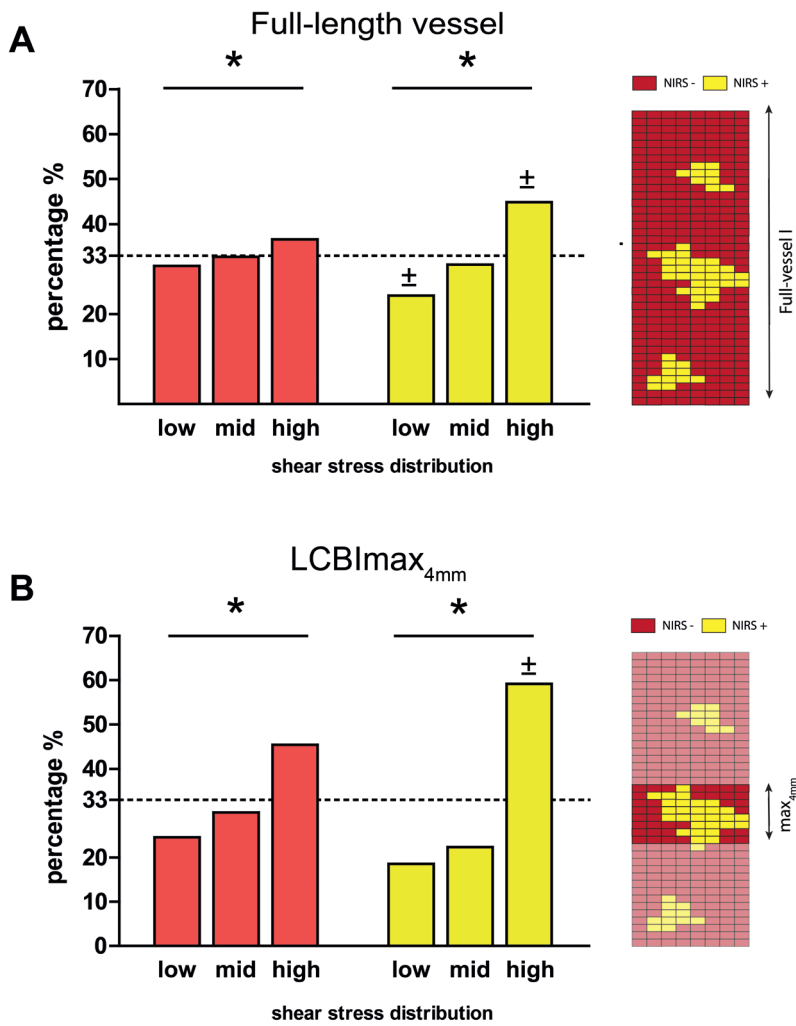


**Figure 3. Wall shear stress distribution in plaques.**  
A: Distribution of the different shear stress tertiles in all sectors with plaque (wall thickness>0.5mm), split into NIRS negative (red) and NIRS positive (yellow) sectors. 2D map showing an exemplary NIRS distribution over the full vessel length. B: Distribution of the different shear stress tertiles in sectors with plaque (wall thickness>0.5mm) in the region with the highest lipid content (maxLCBI4mm) split in NIRS negative (red) and NIRS positive (yellow) sectors. 2D map showing an exemplary a NIRS distribution only in the 4mm with the highest lipid content (maxLCBI4<sub>mm</sub>) (\*p<0.05 for the overall relation, ± p<0.05 compared to the same tertile in NIRS negative sectors (statistics: chi-square test)).



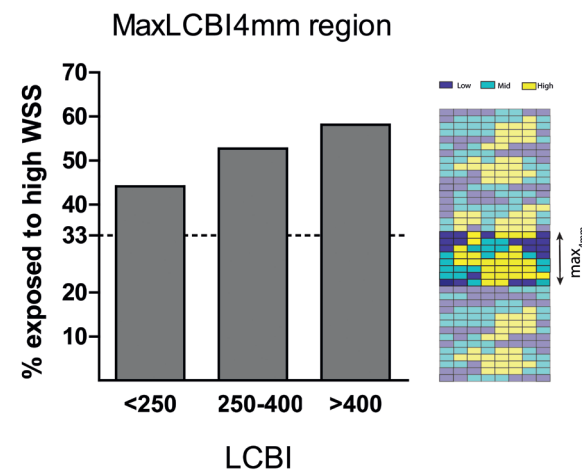


**Figure 4. MaxLCBI<sub>4mm</sub> groups divided into groups to high WSS.**

The percentage exposed to high wall shear stress in the maxLCBI<sub>4mm</sub> regions, split up into 3 groups based on thresholds of maxLCBI<sub>4mm</sub> (<250, 250-400 and >400). 2D map showing an exemplary WSS tertile distribution in the 4mm with the highest lipid content (maxLCBI<sub>4mm</sub>)

The magnitude of WSS is affected by both the flow and the lumen area, such that vessel segments with a smaller lumen but with the same flow are exposed to a higher WSS. Low WSS, mostly observed at inner curves and near side branches, is associated with plaque initiation and progression<sup>15</sup>. If plaque growth leads to minimal local lumen narrowing, this can already result in a local increase in WSS.

This increased WSS is sensed by the endothelial cells with mechanosensors<sup>16</sup> and initiates compensating outward remodeling of the vessel wall, thereby preserving the lumen area and the WSS in the earlier stages of the disease<sup>17</sup>. However, Glagov et al. have shown that if cross-sectional plaque burden (plaque area/vessel area\*100) becomes larger than 40%, lumen narrowing can no longer be prevented, and WSS subsequently remains high in these regions<sup>18</sup>. The relative plaque area used in this study is a local surrogate for the cross-sectional plaque burden. The higher relative plaque area found per subsequent WSS tertile follows the earlier observations by Glagov that cross-sectional plaque burden and lumen narrowing are linked. Therefore, the observed frequent exposure of NIRS(+) sectors to high WSS may be explained by the observed higher relative plaque area of these sectors compared to the NIRS(-) sectors.

Although the higher relative plaque area observed for NIRS(+) sectors might be an obvious explanation for the association between LRP and future events, previous prospective NIRS studies have shown that these relationships were independent of plaque burden, minimal lumen area, or clinical characteristics<sup>3,4</sup>.

Our finding that the majority of regions with high lipid content colocalize with high WSS could therefore be of added value in understanding why LRPs are related to future cardiac events. One of the causes of a coronary event is the rupture of the fibrous cap covering an LRP. High WSS is suggested to play an essential role in the thinning of the fibrous cap through apoptosis of smooth muscle cells, thereby increasing the plaque vulnerability and thereby the likelihood of rupture<sup>19</sup>. This hypothesis is supported by previous data of our research group, showing that indeed, plaque ruptures are located in regions with elevated WSS<sup>20</sup>. To further support this hypothesis, a clinical study by Kumar et al. demonstrated that higher WSS upstream of coronary lesions is predictive for myocardial infarctions, also implying this relationship between high WSS and plaque rupture<sup>8</sup>. The next step in research would be to get more insight into the relationship between high WSS exerted on LRPs and the development of a cardiac event. Potentially, this could be done in a retrospective study using previously collected NIRS and event data such as the LRP study<sup>4</sup>.

A major advantage of this study was the use of the combined NIRS-IVUS catheter. The dual sensor catheter enabled us to simultaneously and precisely detect the NIRS signal, WSS and wall thickness at a high resolution at the same location. This was due to the following three factors: firstly, the 3D model was based on the coronary lumen derived from the IVUS images; secondly, we could precisely map the NIRS signal on top of IVUS images; and thirdly no matching step was needed to add the NIRS signal to the model.

In the present study, we used relative WSS thresholds based on vessel-specific tertile distribution. This method is in contrast to other studies using absolute WSS thresholds<sup>1,21</sup>. The differences in approach are mainly driven by the different methodologies used to determine WSS. Firstly, we used 3D models of all individual coronary arteries, which included all the large side branches of each vessel, whereas other studies used simplified geometrical models without side branches. Although the inclusion of side branches makes the computational model more complex, the side branches are vital to include since they affect the absolute WSS values of the main branch. Also, given their unique disturbed flow patterns, bifurcation regions are more prone to plaque formation and should be taken into account in the analysis<sup>22</sup>. Secondly, we used Doppler-derived velocity measurements at multiple locations throughout the artery to obtain patient-specific boundary conditions for the CFD simulations, whereas other studies made more general assumptions regarding temporal flow patterns and flow magnitude. Both differences in the approach have a major influence on absolute WSS. In our individually tailored model used here, we observed a very large range in WSS among patients. When using absolute thresholds, some patients might present with only sectors labeled as low or high WSS. To answer if LRP vs non-LRPs within a patient have a different

exposure to high WSS, absolute thresholds are not suitable when using our current methodology. Furthermore, we excluded the vessels with no LRPs (LCBI <10, eq of 1% NIRS(+)) to allow the comparison of LRPs and non-LRP coinciding in the same vessel.

### Study limitations

Firstly, we excluded all regions with extensive calcifications. This was done because calcifications hamper the view of the outer vessel wall in IVUS images, which meant that a valid assessment of wall thickness was not possible in these areas. In general, calcified regions are more complex and have thicker plaques, which could have led to an overall underestimation of the colocalization of high WSS and LRP. Secondly, in the CFD simulations, we assumed rigid walls and the absence of motion of coronary arteries because of cardiac contraction. However, their effect on time-averages WSS quantities has been demonstrated to be minor<sup>23</sup>.

### Conclusion

In this study, we used detailed invasive imaging and computational fluid dynamics to demonstrate that lipid-rich plaques, as detected by NIRS, are often co-localized with high WSS. The co-localization of these two features could be of value in understanding why NIRS(+) plaques are more prone to rupture, leading to clinical events. Future studies are needed to demonstrate the influence of high WSS on further lipid-rich plaque development and destabilization.

### Acknowledgments

We thank all the interventional cardiologists and fellows, lab technicians, and nurses and research nurses of the cardiology department of the Erasmus MC for their help and involvement in the IMPACT study.

### References

1. Stone PH, Saito S, Takahashi S, Makita Y, Nakamura SS, Kawasaki T, et al. Prediction of progression of coronary artery disease and clinical outcomes using vascular profiling of endothelial shear stress and arterial plaque characteristics: the PREDICTION Study. *Circulation* 2012;126:172–81.
2. Stone GW, Maehara A, Lansky AJ, de Bruyne B, Cristea E, Mintz GS, et al. A Prospective Natural-History Study of Coronary Atherosclerosis. *N Engl J Med* 2011;364:226–35.
3. Schuurman A-S, Vroegindewey M, Kardys I, Oemrawsingh RM, Cheng JM, de Boer S, et al. Near-infrared spectroscopy-derived lipid core burden index predicts adverse cardiovascular outcome in patients with coronary artery disease during long-term follow-up. *Eur Heart J* 2018;39:295–302.
4. Waksman R, Di Mario C, Torguson R, Ali ZA, Singh V, Skinner WH, et al. Identification of patients and plaques vulnerable to future coronary events with near-infrared spectroscopy intravascular ultrasound imaging: a prospective, cohort study. *Lancet* 2019;394:1629–37.
5. Waxman S, Dixon SR, L'Allier P, Moses JW, Petersen JL, Cutlip D, et al. In Vivo Validation of a Catheter-Based Near-Infrared Spectroscopy System for Detection of Lipid Core Coronary Plaques: Initial Results of the SPECTACL Study. *JACC Cardiovasc Imaging* 2009;2:858–68.
6. Brown AJ, Teng Z, Evans PC, Gillard JH, Samady H, Bennett MR. Role of biomechanical forces in the natural history of coronary atherosclerosis. *Nat Rev Cardiol* 2016;13:210–20.
7. Slager C, Wentzel J, Gijzen F, Schuurbiers J, van der Wal A, van der Steen A, et al. The role of shear stress in the generation of rupture-prone vulnerable plaques. *Nat Clin Pract Cardiovasc Med* 2005;2:401–7.
8. Kumar A, Thompson EW, Lefieux A, Molony DS, Davis EL, Chand N, et al. High Coronary Shear Stress in Patients With Coronary Artery Disease Predicts Myocardial Infarction. *J Am Coll Cardiol* 2018;72:1926–35.
9. Gardner CM, Tan H, Hull EL, Lissauskas JB, Sum ST, Meese TM, et al. Detection of Lipid Core Coronary Plaques in Autopsy Specimens With a Novel Catheter-Based Near-Infrared Spectroscopy System. *JACC Cardiovasc Imaging* 2008;1:638–48.
10. Goldstein JA, Madden SP, Sum ST, Dixon SR, Madder RD, Muller JE. Assessment of Plaque Composition with Near-Infrared Spectroscopy. *Curr Cardiovasc Imaging Rep* 2011;4:298–308.
11. Gijzen F, Katagiri Y, Barlis P, Bourantas C, Collet C, Coskun U, et al. Expert recommendations on the assessment of wall shear stress in human coronary arteries: existing methodologies, technical considerations, and clinical applications. *Eur Heart J* 2019;40:3421–33.
12. De Nisco G, Kok AM, Chiastra C, Gallo D, Hoogendoorn A, Migliavacca F, et al. The Atheroprotective Nature of Helical Flow in Coronary Arteries. *Ann Biomed Eng* n.d.;47.
13. Cutnell JD, Johnson KW. Physics. 4th ed. John Wiley & Sons Inc; 2007.
14. van der Giessen AG, Groen HC, Doriot P-A, de Feyter PJ, van der Steen AFW, van de Vosse FN, et al. The influence of boundary conditions on wall shear stress distribution in patients specific coronary trees. *J Biomech* 2011;44:1089–95.
15. Wentzel JJ, Chatzizisis YS, Gijzen FJHH, Giannoglou GD, Feldman CL, Stone PH. Endothelial shear stress in the evolution of coronary atherosclerotic plaque and vascular remodelling: current understanding and remaining questions. *Cardiovasc Res* 2012;96:234–43.
16. Kwak BR, Bäck M, Bochaton-Piallat M-L, Caligiuri G, Daemen MJ A P, Davies PF, et al. Biomechanical factors in atherosclerosis: mechanisms and clinical implications†. *Eur Heart J* 2014;35:3013–20.
17. Slager C, Wentzel J, Gijzen F, Thury A, van der Wal A, Schaar J, et al. The role of shear stress in the destabilization of vulnerable plaques and related therapeutic implications. *Nat Clin Pract Cardiovasc Med* 2005;2:456–64.
18. Glagov S, Weisenberg E, Zarins CK, Stankunavicius R, Kolettis GJ. Compensatory Enlargement of Human Atherosclerotic Coronary Arteries. *N Engl J Med* 1987;316:1371–5.
19. Fitzgerald TN, Shepherd BR, Asada H, Teso D, Muto A, Fancher T, et al. Laminar shear stress stimulates vascular smooth muscle cell apoptosis via the Akt pathway. *J Cell Physiol* 2008;216:389–95.

20. Gijsen F, van der Giessen A, van der Steen A, Wentzel J. Shear stress and advanced atherosclerosis in human coronary arteries. *J Biomech* 2013;46:240–7.
21. Bourantas C V., Räber L, Sakellarios A, Ueki Y, Zanchin T, Koskinas KC, et al. Utility of Multimodality Intravascular Imaging and the Local Hemodynamic Forces to Predict Atherosclerotic Disease Progression. *JACC Cardiovasc Imaging* 2020;13:1021–32.
22. Gijsen FJH, Wentzel JJ, Thury A, Lamers B, Schuurbiers JCH, Serruys PW, et al. A new imaging technique to study 3-D plaque and shear stress distribution in human coronary artery bifurcations in vivo. *J Biomech* 2007;40:2349–57.
23. Torii R, Keegan J, Wood NB, Dowsey AW, Hughes AD, Yang G-Z, et al. MR image-based geometric and hemodynamic investigation of the right coronary artery with dynamic vessel motion. *Ann Biomed Eng* 2010;38:2606–20.



# 6

## Shear stress related plaque growth of lipid-rich plaques in human coronary arteries: a near-infrared spectroscopy study and OCT-study

This chapter based on:

Wall shear stress related plaque growth of lipid-rich plaques in human coronary arteries: a NIRS and OCT study

Eline M.J. Hartman, Giuseppe De Nisco, Annette M Kok, Mariusz Tomaniak, Fay M.A. Nous, Suze-Anne Korteland, Frank J.H. Gijzen, Wijnand K den Dekker, Roberto Diletti, Nicolas M.D.A. van Mieghem, Jeroen M. Wilschut, Felix Zijlstra, Anton F.W. van der Steen, Ricardo Budde, Joost Daemen, Jolanda J. Wentzel

*Accepted in Cardiovascular Research*

Abstract

**Aim** - Low wall shear stress (WSS) is acknowledged to play a role in plaque development through its influence on local endothelial function. Also, lipid-rich plaques are associated with endothelial dysfunction. However, little is known about the interplay between WSS and the presence of lipids with respect to plaque progression. Therefore, we aimed to study the differences in WSS-related plaque progression between lipid-rich plaque, non-lipid rich plaque or plaque free regions in human coronary arteries.

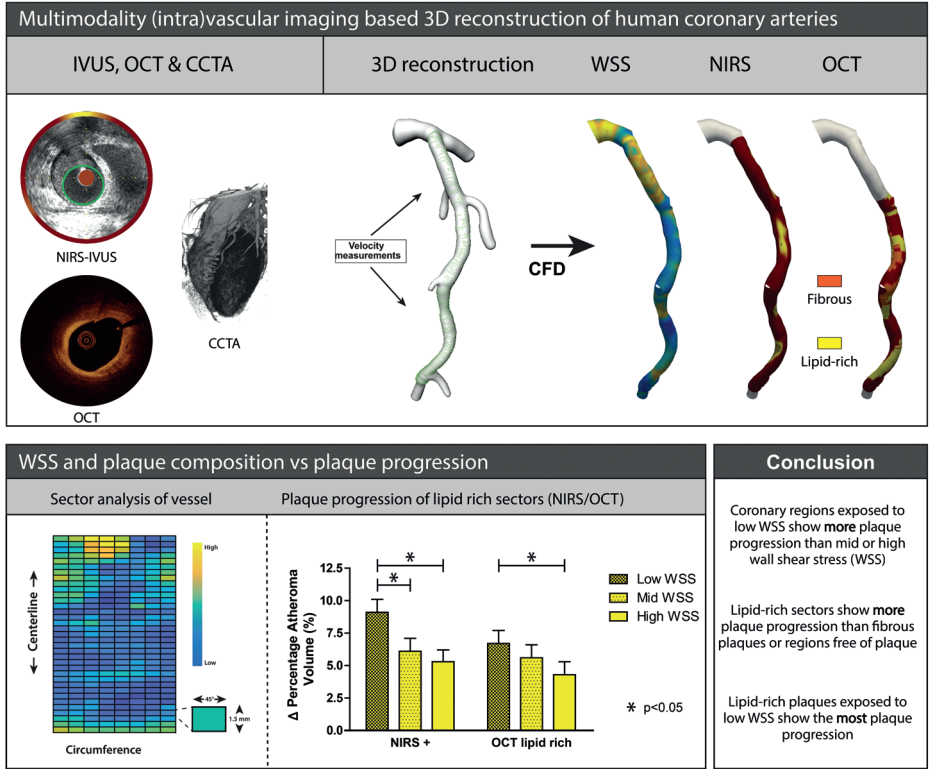
**Methods and results** - In the present single-centre, prospective study, 40 patients presented with an acute coronary syndrome (ACS) underwent successfully near-infrared spectroscopy intravascular ultrasound (NIRS-IVUS) and optical coherence tomography (OCT) of at least one non-culprit vessel at baseline and completed a 1-year follow-up. WSS was computed applying computational fluid dynamics to a 3D reconstruction of the coronary artery based on the fusion of the IVUS-segmented lumen with CT-derived centerline, using invasive flow measurements as boundary conditions. For data analysis, each artery was divided into 1.5mm/45 degrees sectors. Plaque growth based on IVUS-derived percentage atheroma volume change was compared between lipid-rich plaques, non-lipid rich plaques and plaque-free wall segments, as assessed by both OCT and NIRS. Both NIRS- and OCT-detected lipid-rich sectors showed significant higher plaque progression than non-lipid rich plaques or plaque-free regions. Exposure to low WSS was associated with a higher plaque progression than exposure to mid or high WSS, even in the regions classified as plaque-free wall. Furthermore, low WSS and the presence of lipids had a synergistic effect on plaque growth resulting in the highest plaque progression in lipid-rich regions exposed to low shear stress.

**Conclusion** - This study demonstrates that NIRS- and OCT-detected lipid-rich regions exposed to low WSS are subject to enhanced plaque growth over the one year of follow-up. The presence of lipids and low WSS proved to have a synergistic effect on plaque growth.

Translational perspective

The development and location of atherosclerosis is known to be a multifactorial process. Many factors are individually associated with the development of atherosclerosis, such as WSS and lipid-rich plaques. In this current study, we show that there is a synergistic effect between low WSS and lipid-rich plaque on plaque progression. From a translational perspective, regions with endothelial dysfunction because of simultaneous exposure to inflammation due to local lipid infiltration and low WSS are most susceptible to plaque progression. Future studies are needed to demonstrate if these LRPs exposed to low WSS showing plaque progression are related to future cardiovascular events.

Graphical abstract





## Introduction

Coronary atherosclerosis is a lipid-driven inflammatory disease and the most common cause of ischemic heart disease<sup>1</sup>. In the last decades, it has been well established that blood flow-induced wall shear stress (WSS) plays a crucial role in the process of plaque initiation, because low WSS is responsible for local regions of endothelial dysfunction<sup>2-4</sup>. In these regions, lipids infiltrate the vessel wall, eventually resulting in atherosclerotic plaques<sup>5</sup>. In turn, lipids inside the plaque have been proven to influence local inflammation and thereby stimulate further plaque progression<sup>6</sup>. Interestingly, lipids in the vessel wall as detected by NIRS has also been related with endothelial dysfunction in the coronary arteries, independent of the plaque burden<sup>7</sup>. Despite expanding knowledge on the individual roles of WSS and plaque composition (e.g. lipid-rich) on plaque growth, little is known about their interplay and the combined effect on plaque progression. The effect low WSS has on plaque progression via endothelial dysfunction might be enhanced by an inflamed environment of lipid-rich plaque and the related endothelial dysfunction. We hypothesize that regions with endothelial dysfunction both due to low WSS as well as inflammation caused by local lipid infiltration are most susceptible to plaque progression. The latter could be of particular interest since progression has been demonstrated to precede plaque rupture and subsequent events<sup>8</sup>.

At present, several intravascular imaging modalities are available to visualize these lipid-rich plaques (LRP) *in vivo*<sup>9,10</sup>. Currently, there are several devices available in the clinic that can visualize plaque volume and/or plaque components. Among them, optical coherence tomography (OCT) is a high-resolution imaging technique able to visualize different layers of a healthy vessel wall and lipids within the vessel wall. However, it lacks enough penetration depth to assess plaque volumes<sup>11</sup>. The introduction of dual-sensor near-infrared spectroscopy intravascular ultrasound (NIRS-IVUS) allowed simultaneous assessment and thus colocalization of lipids and plaque volume<sup>12</sup>. Combining these intravascular imaging techniques with computational fluid dynamics (CFD) to compute WSS, the interplay between WSS and lipid-rich plaques can be investigated.

The present study uses serial multimodality imaging, 3D-vessel reconstruction, and CFD to investigate the interaction between WSS and intraplaque lipids on plaque progression in human coronary arteries.

## Methods

### Patient inclusion

The IMPACT study was a prospective, single-centre, serial multimodality imaging study designed to evaluate the association between biomechanical parameters and the natural history of atherosclerotic disease in non-stented coronary arteries. Hemodynamically stable patients with an acute coronary syndrome, who had at least one non-stented non-culprit coronary vessel accessible with intracoronary imaging catheters and a Doppler velocity wire, were eligible for enrollment. Patients were treated according to the clinical guidelines and discharged on dual-antiplatelet therapy and high-intensity lipid-lowering therapy (rosuvastatin  $\geq$  20mg, atorvastatin  $\geq$  40mg or PCSK9-inhibitor). The most important exclusion criteria were previous coronary artery bypass graft surgery, three-vessel disease, impaired renal function (creatinine clearing  $<$  50ml/min), left ventricular ejection fraction  $<$  30%, and atrial fibrillation. Written informed consent was obtained from all patients. The study protocol was approved by the local medical ethics committee of the Erasmus MC (MED2015-535, NL54519.078.15) and registered (ISCRTN: 43170100). The IMPACT study was conducted in accordance with the World Medical Association Declaration of Helsinki (64<sup>th</sup> WMA General Assembly, Fortaleza Brazil, October 2013) and Medical Research involving the human subject act (WMO).

### Clinical data acquisition

After successful percutaneous coronary intervention (PCI) of the culprit lesions, a non-culprit artery segment with a minimum of 30mm of length and two readily identifiable side branches (diameter  $>$  1.5mm) was selected as the study segment. A NIRS-IVUS catheter (TVC Insight Coronary Imaging Catheter, InfraRedX, Burlington, MA, USA) was advanced and positioned distally from the distal side branch. An automated pullback (0.5mm/s) was performed. Subsequently, an OCT catheter (Dragonfly Optis Imaging Catheter, St Jude Medical, St Paul, MN, USA) was positioned at the same anatomical location as the NIRS-IVUS catheter, and an automated pullback (36mm/s) was performed. Finally, invasive local flow measurements were performed using a ComboWire (Phillips Volcano, Zaventem, Belgium) at different locations between the side branches throughout the study segment to assess the flow distribution. This invasive imaging protocol was repeated at a one-year follow-up. In addition, one month after the index procedure, patients visited the outpatient clinic to undergo a coronary computed tomography angiogram (CCTA) according to a standard prospectively ECG-triggered clinical protocol (SOMATOM Force (3rd generation dual-source CT scanner), Siemens Healthineers, Germany).

### Invasive imaging analysis.

Data were anonymized and analyzed offline. Analyses of both IVUS and OCT data were performed using QCU-CMS software (version 4.69, LKEB, Division of image processing, LUMC, Leiden, The Netherlands) blinded for the other invasive imaging. IVUS images were gated using an in-house developed MATLAB (V.2017B, Mathworks Inc, USA) algorithm, generating one IVUS frame in every end-diastolic phase of the cardiac cycle to correct for variation in lumen and vessel size due to cardiac contraction. Lumen and external elastic membrane (EEM) contours were semi-automatically delineated and segmented. An intra-observer analysis was performed in a random sample of 5 IVUS pullbacks (748 frames) with at least two months interval. A good reproducibility of EEM area, lumen area and plaque area was found (0.996 [95%CI 0.996-0.997], 0.983 [95%CI 0.963-0.990] and 0.958 [95%CI 0.939-0.970]). In the IVUS frames, calcium was identified as a bright signal with echo lucent shadow. Calcium angles were segmented with the protractor in the centre of the lumen. For each degree in a NIRS-IVUS frame, the NIRS signal was analyzed and was NIRS positive if the signal had a high probability ( $>0.6$ ) for the presence of lipids. The Lipid Core Burden Index (LCBI) (area positive for NIRS signal/total area\*100) was calculated for each vessel. Regions with the highest lipid content per 4mm (maxLCBI4mm) were identified for vessel characterization<sup>13,14</sup>. OCT images were analyzed every millimetre (1 out of 5 frames) according to the consensus standard<sup>11</sup>. Lumen contours were segmented, and plaque components visible on OCT were manually segmented by drawing angles from the centre of the lumen. More in detail, a lipid-rich plaque was defined as an inhomogeneous signal on OCT, with a drop in attenuation and no visible EEM. A lipid pool was identified in case of an overlaying signal rich cap structure with a sudden drop of the signal and classified as a fibrous cap atheroma (FCA). A fibrous plaque was defined as a relatively homogeneous signal on the OCT and identifiable EEM (intima-media thickness  $>0.5$ mm). Plaque-free wall was defined as a healthy wall with a visible three-layered structure with an intima-media thickness  $<0.5$ mm.

### 3D-reconstruction and computational fluid dynamics.

By fusing the 3D spatial information of the coronary vessel centerline segmented from the CCTA and the lumen contours extracted from the IVUS, a 3D reconstruction was made in MeVisLab (MeVis Medical Solutions AG, Bremen, Germany). The two imaging modalities were matched using large side branches as landmarks, both in longitudinal and rotational direction. For subsequent CFD, reliable inlet and outlets were needed. Therefore, the regions proximal and distal to the IVUS-derived region of interest (ROI), as well as side branches ( $>1.5$ mm), were segmented on the CCTA and scaled and fused with the 3D-reconstruction<sup>15,16</sup> (Figure 1A). For the final analysis, only the IVUS-derived ROI was considered CFD analyses were used to obtain the local WSS according to previously described methodology<sup>17</sup>. In brief, a time-dependent CFD simulation was performed in each

reconstructed 3D-geometry, assuming blood as an incompressible, non-Newtonian fluid and modelled using the Carreau fluid model (Fluent, v.17.1, ANSYS Inc). The vessel lumen was considered rigid and subjected to a no-slip condition. For the CFD simulations, in- and outflow boundary conditions were derived from intravascular Doppler measurements. The quality was examined in a consensus meeting of experts (AH, EH, FG, JW) based on the flow signal's quality, repeatability, and consistency. For the inflow boundary condition of the time-dependent CFD simulation, a flat velocity profile was applied with a time-dependent waveform derived from the most proximal flow measurement of good quality. Furthermore, for the outflow boundary conditions, the flow distribution through the side branches was calculated based on the intravascular flow measurements at different locations in the coronary artery. A previously described scaling law was used for regions with no reliable flow measurements to determine the flow ratio between the main and side branches<sup>18</sup>.

### Data analysis

By using side branches as landmarks, both the analyzed OCT data and the segmented IVUS follow-up contours were matched to the IVUS baseline pullback. Matching was performed in both longitudinal and circumferential directions. All matched and analyzed data was mapped and interpolated on the IVUS-based ROI on the 3D-mesh geometry using VMTK (Orobix, Bergamo, Italy) and MATLAB (v2017b, Mathworks Inc, Natick, MA, USA) (Figure 1A). For further analyses, the 3D-ROIs were converted into a 2D-map by folding the vessel open in a longitudinal direction (Figure 1B). The arteries were split into 1.5mm segments and divided into 45 degrees sectors (Figure 1B). All continuous data were averaged per sector. Plaque was expressed as per cent atheroma volume (PAV) (plaque area volume/total vessel area volume\*100). For each vessel, the cardiac-cycle averaged WSS was divided into vessel-specific tertiles (low, mid, and high), assigning one-third of the sectors in the vessel as exposed to low, mid, or high WSS. Furthermore, since calcium hampers visualization of the EEM, in calcium positive locations, any wall thickness and therefore PAV estimation was not possible. All sectors containing an IVUS-derived calcium angle of more than  $90^\circ$  were excluded from all PAV analyses<sup>19</sup>. A sector was considered NIRS positive when at least 50% of a sector was NIRS positive ( $>0.6$  probability of the presence of lipids). NIRS data was divided into three groups: 1. NIRS positive sectors, 2. NIRS negative plaque sectors (wall thickness  $>0.5$ mm), 3. NIRS negative plaque-free wall sectors (wall thickness  $<0.5$ mm), i.e. NIRS-IVUS based plaque-free vessel wall (IVUS-PFW). For the OCT derived plaque classification, a sector was assigned to a group when at least 50% of that sector consisted of that OCT-derived vessel wall feature (FCA, lipid-rich, fibrous, PFW). Since FCA (28/7851 sectors) were scarce, no dedicated statistical analysis was performed, and the sectors classified as FCA have been pooled together with the sectors classified as lipid-rich. As such, based on OCT

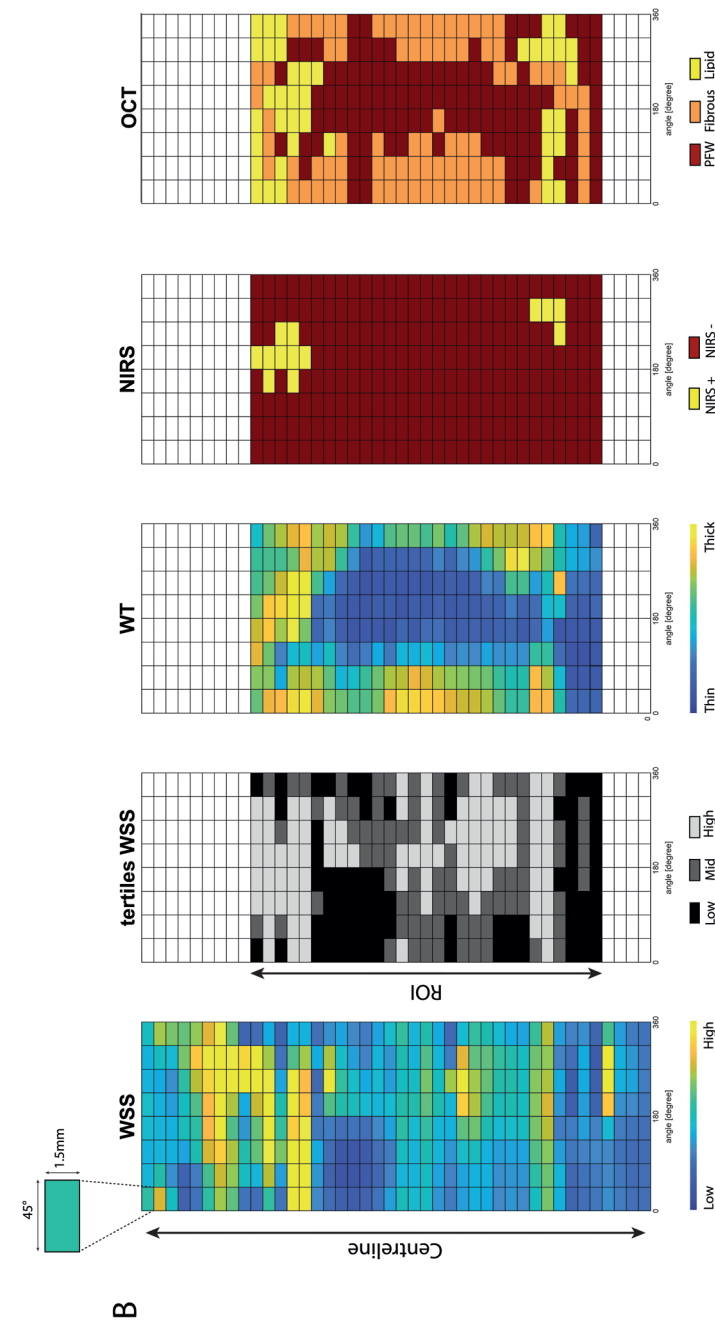
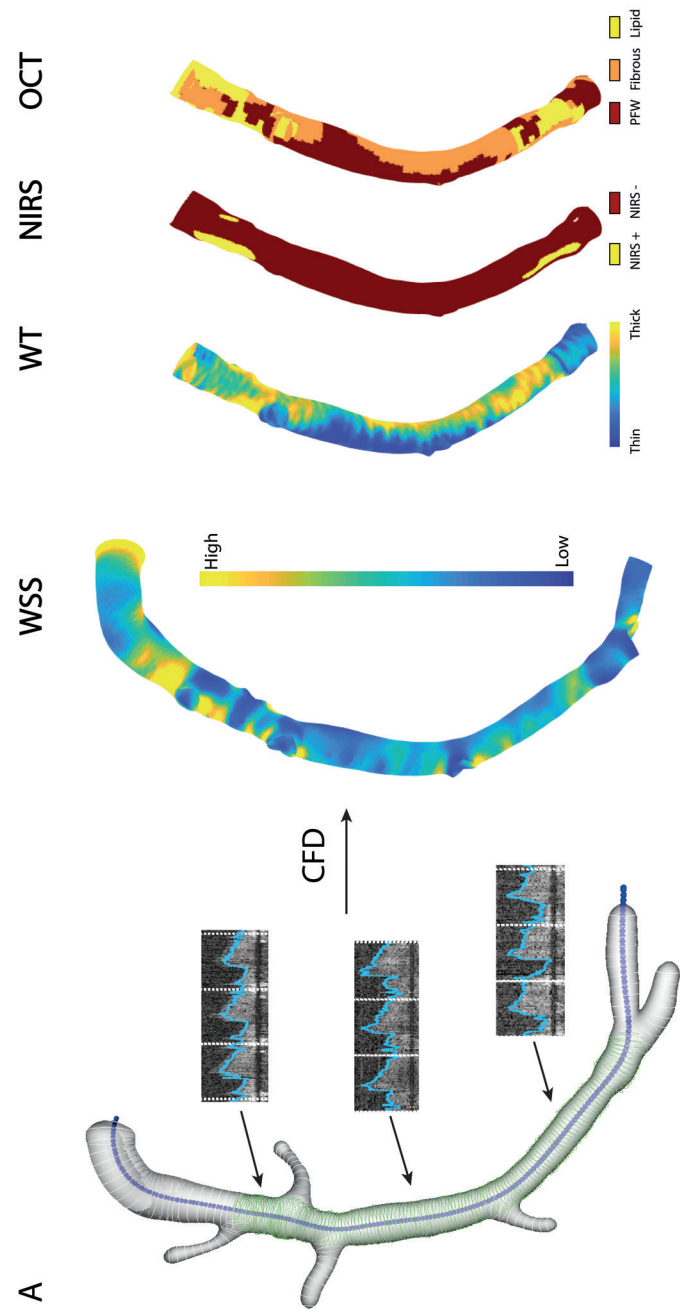


**Figure 1. Methodology overview of 3D reconstruction, wall shear stress (WSS) and data analysis matching with plaque components.**  
A: Example of 3D reconstructed right coronary artery (RCA) IVUS-derived lumen contours (green) were fused with the CT-derived vessel centerline (blue) and CT-derived side branches contours (white). By adding local flow measurements and using computational fluid dynamics (CFD), WSS has been calculated in these reconstructed models. NIRS and OCT derived plaque phenotype were matched and plotted on the IVUS-derived 3D reconstruction, the region of interest (ROI). B: From the 3D-reconstructed vessels, 2D-maps were created by folding open de vessel in longitudinal direction along the vessel centerline. For statistical analysis, the 2D maps were divided into sectors of 1.5mm/45°. Example of 2D maps in this overview are: the continuous WSS, the WSS tertiles (low, mid, high), Wall thickness (WT), NIRS-derived plaque phenotype and OCT-derived phenotype.

imaging, all sectors were stratified using three categories: 1. Lipid-rich plaques, 2. Fibrous plaques, 3. Plaque free wall (OCT-PFW).

Statistical analysis

Normally distributed data are presented as mean standard deviation (SD), and significance was tested using student t-test or ANOVA. Non-normally distributed data are reported as medians (interquartile range, IQR), and the statistical difference was determined with the Mann-Whitney U test.

Statistical analysis of plaque burden changes (follow-up- baseline) was performed using linear mixed-models with WSS tertiles (low, mid, high), OCT and NIRS plaque phenotype of the sectors as fixed factors. The individual vessel was added to the model as a random factor using an unstructured covariance and correlation matrix to take random effects and correlations of the sectors within the individual vessels into account. Since high-intensity lipid-lowering therapy has shown to impact plaque progression and when considering the low compliance of high-intensity lipid-lowering therapy in daily practice<sup>20-22</sup>, we compared the PAV of patients who remained treated with high-intensity lowering therapy after one-year with patients on low or moderate-intensity lipid-lowering therapy. All statistical tests for PAV change were adjusted for baseline PAV since plaques with different phenotypes might present with different plaque sizes at baseline. All the results on plaque progression presented in this study are estimated means of the delta PAV and 95% confidence interval (95%CI). P<0.05 was considered significant.

Results

Between March 2016 and March 2018, a total of 53 patients were enrolled in the study. Four patients withdrew consent at the 1-month follow-up, 8 patients withdrew at the 1-year invasive imaging procedure. In one patient there was no possibility of matching between computed tomography and invasive imaging data. As a result, a total of 40 patients with ACS underwent NIRS-IVUS and OCT assessment of a non-culprit coronary artery after successful treatment of the culprit lesion both at baseline and at 12-month follow-up, and after excluding one patient due to insufficient quality NIRS data and 2 patients due to non-analysable OCT. A complete OCT, serial NIRS-IVUS, and CCTA dataset was available in 37 patients (38 vessels). Consequently, 3D lumen geometries for CFD analyses were created, intravascular imaging data was analyzed and matched for 38 vessels. The patient characteristics are shown in table 1. Mean age was 60±8.8, 92% were male, 46% of the patients were statin naïve at the time of enrollment and 51% were on high-intensity lipid-lowering therapy at one-year follow-up.

Table 1. Baseline characteristics.

Clinical characteristics	N = 37 patients
Age, years	60 ± 8.9
Men, n (%)	34 (91.7%)
Body Mass Index	27 ± 5.0
Diabetes Mellitus, n (%)	8 (21.6%)
Hypertension, n (%)	9 (24.3%)
Dyslipidemia, n (%)	16 (42.2%)
Current smoking, n (%)	8 (21.6%)
Positive family history, n (%)	13 (35.1%)
Previous MI, n (%)	8 (21.6%)
Previous PCI, n (%)	11 (29.7%)
LDL (mmol/L)	2.7 ± 0.9
Imaged study vessel	N = 38 vessels
LAD, n (%)	14 (35.9%)
LCX, n (%)	9 (23.1%)
RCA, n (%)	16 (41.0%)
LCBI4mmMAX	275(167-383)

Baseline imaging characteristics.

The studied non-culprit segment was located in the left anterior descending in 13 vessels, the left circumflex in 10 vessels, and the right coronary artery in 15 vessels. The median length of the IVUS-based ROI was 54 (39-61.5) mm, the time-averaged WSS was 1.10 (0.77-1.73) Pa, and the maxLCBI4mm was 275 (167-338). After exclusion of regions with side branches and dividing the vessels in 1.5mm by 45° - resulted in 9906 sectors. The mean WSS per vessel for the low WSS tertile was 0.47 (0.37-0.69) Pa, for mid WSS tertile 0.87 (0.68-1.23) Pa and for high WSS tertile 2.04 (1.22-2.85) Pa.

Calcifications >90° were found n 739 sectors at baseline and/or follow-up, and these sectors were excluded from all the analysis. Due to guidewire artefacts in the detection of NIRS, 306 sectors at baseline were excluded for the relevant analyses and sub-analyses. In total, 2041 sectors were excluded from the OCT analysis due to matching problems or poor imaging quality (N=1899) or heterogeneity of plaque composition (N=142). In total, 504 sectors were identified as NIRS positive, 2667 sectors as NIRS negative plaque and 5690 sectors as IVUS-PFW. When using OCT for plaque characterization, 1624 sectors were classified as lipid-rich, 1214 sectors were classified as fibrous, and 4288 sectors were classified as OCT-PFW.



### Plaque progression

Firstly, no significant differences were observed in PAV change between patient on high-intensity lipid lowering therapy as compared to patient who were either intolerant or on low-intensity lipid therapy after one-year follow-up. (high: 2.7% 95%CI 0.0-5.4, low/non 2.7% 95%CI -0.09-6.3). Consequently, no sub-analysis of the use of high-lipid lowering therapy was performed.

Secondly, sectors exposed to low WSS, demonstrated significantly more plaque progression, compared to sectors exposed to high WSS (low: 3.7% 95%CI 2.3-5.1, mid: 2.0% 95%CI 1.7-2.4, high: 1.7% 95%CI 1.4-2.1,  $p<0.001$ ). No differences in plaque progression were found comparing sectors exposed to mid vs high WSS ( $p=0.73$ ) (Figure 2).

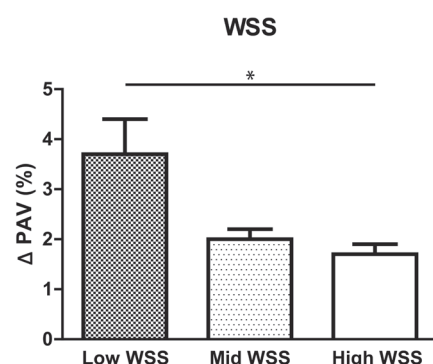


**Figure 2. Plaque progression in different WSS tertiles.**

Change in plaque expressed as Δ percentages atheroma volume (PAV) for low, mid and high wall shear stress (\* $p<0.05$ , linear mixed model)

Thirdly, when analyzing the effect of NIRS-detected local lipids on plaque progression, lipid-rich sectors showed significantly more plaque progression than sectors in which lipids were not present (non-lipid-rich plaques) (*lipid-rich plaque*: 5.2% 95%CI 4.3-6.0 vs *non-lipid-rich plaque*: 3.9% 95%CI 3.3-4.4,  $p=0.010$ ). Furthermore, lipid-rich plaques showed more plaque progression than PFW sectors (*PFW*: 2.2% 95%CI:0.9-3.5%,  $p=0.001$ ) (Figure 3A).

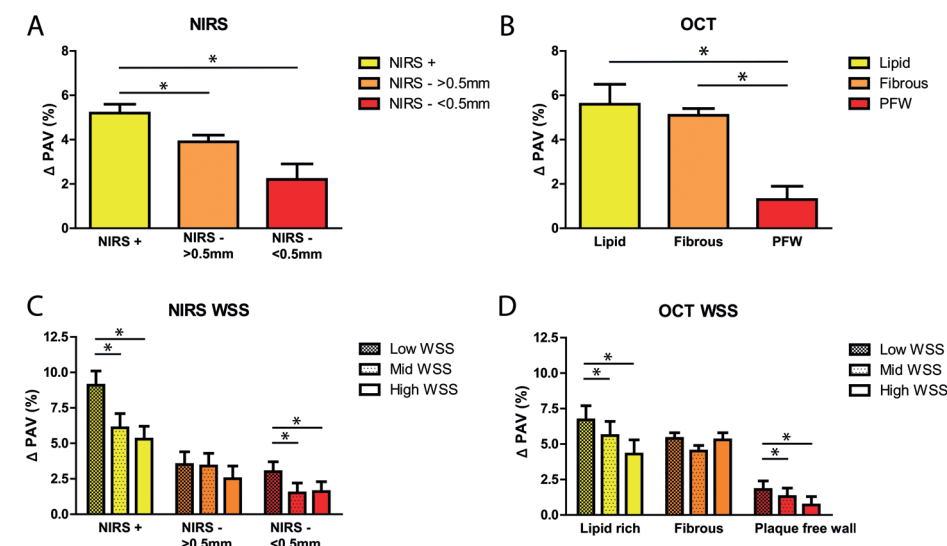


**Figure 3. Plaque progression for different plaque phenotypes and in the different WSS tertiles.**

**A:** Plaque progression for NIRS-IVUS-derived plaque phenotype lipid-rich plaque (yellow), non-lipid-rich plaque (orange) and IVUS-based plaque free wall (red). \* $p<0.05$ . **B:** Plaque progression for OCT-derived plaque phenotype lipid-rich plaque (yellow), fibrous (orange) and OCT-based plaque free wall (red). \* $p<0.05$ . Plaque progression for NIRS-IVUS(**C**) and OCT(**D**) derived plaque phenotypes divided into low (dense pattern), mid (light pattern) and high (no pattern) WSS. \* $p<0.05$ .

Fourthly, when assessing the differences in plaque progression between sectors that demonstrated various OCT-based plaque components, both fibrous and lipid-rich sectors, showed significantly more pronounced plaque progression than the OCT-based PFW sectors. However, no significant differences in plaque progression were found between lipid-rich and fibrous sectors. (lipid: 5.6% (95%CI:3.8-7.4), fibrous: 5.1% (95%CI:4.6-5.6), PFW: 1.3% (95%CI:0.1-2.4),  $p<0.001$ ) (Figure 3B).

Finally, lipid-rich sectors exposed to low WSS showed significantly more plaque progression compared to those exposed to high WSS, both for OCT-based and NIRS-based lipid-rich plaques. In PFW regions (wall thickness  $<0.5$ mm), plaque progression was primarily found in sectors exposed to low WSS and had significantly more plaque progression than PFW sectors exposed to high WSS. (Figure 3C & Figure 3D). In the linear mixed models, the presence of lipids based on NIRS or OCT and WSS showed a significant interaction effect ( $p<0.001$ ), indicating that low WSS had a larger effect on plaque progression in the lipid-rich sectors compared to the non-lipid-rich sectors.



## Discussion

In the present study, we combined serial multimodality imaging with CFD to investigate the influence and interplay of WSS and the presence of NIRS- and OCT-detected lipids on IVUS-based plaque progression over a one-year follow-up period in a dedicated single centre-study. We used a detailed sector-based analysis of NIRS-IVUS derived 3D-CFD models, thereby considering the local heterogeneity in WSS, lipid presence and plaque progression. The most important findings were: 1) Sectors exposed to low WSS displayed more plaque progression than sectors exposed to mid and high WSS. 2) In NIRS-detected lipid-rich sectors, more plaque progression was observed than in non-lipid-rich plaque sectors and PFW sectors. 3) Both lipid-rich and fibrous plaques, as detected by OCT, showed significantly more plaque growth than PFW sectors. 4) When combining WSS and plaque components, lipid-rich sectors exposed to low WSS showed the most plaque progression. 5) In PFW sectors, as determined by either NIRS-IVUS or OCT, plaque progression was most enhanced in sectors exposed to low WSS.

### Plaque progression was most visible in lipid-rich plaques detected by NIRS.

The present study is the first to show that lipid-rich regions, as detected by NIRS, are prone to plaque progression at one-year follow-up compared to sectors that do not contain lipids. Our findings correspond well with the earlier studies showing that lipids cause a pro-inflammatory response inside the vessel wall, leading to the influx of inflammatory cells<sup>5</sup>. Subsequently, the presence of lipids and inflammatory cells stimulates a complex cascade of pathways, finally resulting in plaque progression<sup>5,6</sup>. Earlier, a pre-clinical histological work demonstrated that NIRS positive plaques display greater necrotic cores and more inflammation than NIRS negative plaques supporting the hypothesis of enhancing plaque growth in lipid rich regions<sup>23</sup>.

In the LRP-study, a natural history study, non-culprit vessels with a high lipid content (maxLCBI4mm >400) were at three times higher risk of developing major cardiovascular events than non-culprit vessels with low lipid content<sup>24</sup>. Besides inflammation, plaque progression has also been demonstrated to be one of the precursors of plaque rupture and subsequent events<sup>8</sup>. Therefore, our findings might contribute to the understanding the evolution of an event causing lesion.

It is noteworthy that the analyses stratified according to the OCT-detected plaque phenotypes revealed no significant difference in plaque progression between lipid and fibrous sectors. One of the reasons why differences between lipid and fibrous sectors were not seen in the OCT-lipid analysis, could be the differences in detection and analysis of lipids between the two image modalities. Both NIRS and OCT use a near-infrared light-based imaging technique, however, a number of differences

have to be addressed. First, in this population, OCT-derived FCAs, with potential more vulnerable phenotype, were rare and in total number too few to perform statistical analysis. Therefore, FCA and all other lipid-rich plaques were pooled for the analysis, with a caveat of decreased specificity. Second, OCT-detected lipid was based on an expert observer analysis. In the NIRS-analysis conversely, the presence of lipid was based on an automated analysis of the optical absorption spectrum of different plaque components based on validation algorithm<sup>25</sup>. The discrepancy found between OCT and NIRS on lipid detection has been described before. Previous work demonstrated a modest agreement between NIRS and OCT for lipid detection, partly caused by a 20% false-positive rate of OCT detected lipid compared to NIRS<sup>26</sup>. These data suggest that OCT is more sensitive for lipid detection but less specific for the more vulnerable plaque than NIRS imaging.

### WSS, plaque composition and plaque progression.

Low WSS has been primarily associated with the initiation process of atherosclerosis, resulting from its detrimental effects on endothelial function, promoting increased permeability of the endothelial cells. The subsequent influx of low-density lipoprotein (LDL) into the vessel wall leads to plaque development<sup>27</sup>. In the current study, we investigated the plaque progression using IVUS and found enhanced plaque growth in low WSS regions, in line with the previous studies<sup>28,29</sup>. We found that LRP exposed to *low* WSS displayed the highest plaque progression, and we even showed that low WSS and the presence of lipids have a synergistic effect on plaque progression. Lipid-rich plaques, as well as low WSS, are both independently associated with endothelial dysfunction<sup>3,7</sup>. From a pathophysiological point of view, we hypothesize that the synergistic effect might be related to the combined effect and interaction of low WSS and lipid-rich plaques on endothelial dysfunction, leading to most plaque progression at these lipid-rich locations exposed to low WSS.

At present, little is known about the interplay between LRP and WSS regarding plaque progression. To date, only one study combined serial NIRS-IVUS imaging with WSS and showed that segments with proven *lipid* progression were exposed to *higher* WSS at baseline compared to segments with no lipid progression<sup>30</sup>. In contrast, the present study focused on the role of WSS in plaque volume progression rather than the change in lipid content. Altogether, these results might implicate different roles of WSS for volumetric plaque progression and plaque vulnerability. This dual role of WSS was recognized before by Slager et al.<sup>31</sup>, who envisioned that regions exposed to low WSS are more susceptible to plaque initiation and further plaque progression, while the exposure of plaques to high WSS might affect plaque vulnerability<sup>31</sup>. Although in a previous study we found that lipid-rich plaques are more often exposed to high WSS<sup>15</sup>, there were still lipid-rich regions exposed to low WSS<sup>15</sup>, that showed the most plaque progression. Previous research showed

an association between high risk plaque characteristics being exposed to low WSS at the index procedure with future events after 3 year of follow-up in non-culprit vessels<sup>32</sup>.

Recent research employing multimodality imaging with both OCT and IVUS showed that low WSS and baseline plaque burden could predict disease progression<sup>33,34</sup>. However, those studies did not find a difference in WSS related plaque growth among various plaque phenotypes. The reason for the different results compared to our data could be the level of detail that was used in the analysis. Bourantas et al. used 3 mm sectors in which the minimum predominant WSS, defined as the 90° arc with the minimum averaged WSS, was selected as a representative for the whole segment. Furthermore, each segment's plaque phenotype was defined according to the most vulnerable plaque type located in the segment. To investigate the more local effect of WSS and plaque composition and their interaction in order to unravel the underlying mechanisms, we took this one step further and analyzed every 1.5mm/45° sectors for WSS and plaque composition. One risk of this relatively high sampling rate is the potential interaction effect between sectors within a vessel. Therefore, we used an advanced statistical random-effects model with an unstructured covariance and correlation matrix to take any correlation effects into account. By using this detailed analysis, we did find a synergistic effect of WSS and the presence of lipids with respect to plaque progression. These data suggest that at a very local level WSS and the underlying plaque composition interact in their influence on endothelial dysfunction and thus in the pathophysiology leading to plaque growth.

Furthermore, in contrast to our study, lipid tissue in superficial plaque detected by OCT was not identified as a predictor for disease progression. It is plausible that the difference in the definition of lipid-rich plaques vs lipid tissue in the superficial plaque (<0.5mm depth) underlies this discrepancy. Similar to our study, the number of segments with lipid tissue in the superficial plaque in this study was low. For both NIRS negative plaques (>0.5mm) and OCT detected fibrous plaques, no effect of WSS was visible on plaque progression. Of note, both thin (<0.5mm) NIRS negative sectors, i.e. NIRS-based plaque-free wall, as well as plaque-free wall sectors detected by OCT, showed significant plaque progression in the sectors exposed to low WSS, an indirect confirmation of the role of low WSS specifically in early plaque initiation. Irrespective of the findings above, key differences in the method of WSS computations should be mentioned. As such, in contrast to the vast majority of other studies, we included side branches in our computational model, which profoundly affects the WSS in the main branch<sup>35</sup>. Moreover, Doppler-derived velocity measurements at multiple locations throughout the artery were performed to obtain patient-specific boundary conditions for the CFD simulations. Previous WSS studies used a more simplified geometry and/or made more general

assumptions regarding flow distribution<sup>29,34,36</sup>. A broad between-subjects range in WSS was observed in our more detailed and more individually tailored model. Thus, vessel-specific WSS tertile has been selected in this study to identify the different WSS categories, which in an earlier study proved to be most associated with plaque progression<sup>37</sup>.

### Cross-sectional vs sector-based analysis

The majority of the imaging studies identified lesions and plaques at the cross-sectional or segmental levels, reporting plaque burden, a normalized measure for plaque size. However, coronary atherosclerotic plaques are not equally distributed along the vessel and often have an eccentric shape<sup>38,39</sup>. WSS plays a vital role in atheroprone sites, affecting plaque distribution along the coronary arteries. Most imaging studies do not take the spatial heterogeneity of WSS and its effect on plaque development into account. Timmins et al. showed that dividing the arteries, not only into cross-sectional segments but also into a more detailed sector-based analysis, adds significantly to the granularity of the data aiding in the focal evaluation of the natural history of coronary atherosclerosis<sup>40</sup>. As a consequence of spatial averaging of the plaque and WSS data per cross-sectional segment, local effects of WSS may be averaged out. In contrast, dividing segments into sectors gives more superior insights into the plaque distribution and local WSS effects combined with the opportunity to investigate the WSS effect on a more homogenous type of plaque.

### Limitations

In this study, several limitations need to be addressed. Firstly, we found an unexpectedly low number of sectors meeting the criteria of FCA (i.e. lipid pool); only 28 sectors were identified as per the guideline definitions<sup>11</sup>. Therefore, all sectors containing lipids (both lipid pools and lipid-rich) have been pooled and analyzed as one category. Statistical analysis on FCAs was not feasible due to low numbers. In the present study, the LDL-levels were already relatively low at the index procedure, and only 42% of the patients were statin-naïve at the time of enrollment, this could have contributed to the low number of FCAs observed at baseline. Furthermore, in the current study, no differences were found between patients with and without high-intensity lipid-lowering therapy. In our study, only 50% of the patients remained adherent to high-intensity lipid-lowering therapy after one-year follow-up. Even though the cardiovascular benefits of high-intensity lipid-lowering therapy are known, low adherence is reported in daily clinical practice<sup>20</sup>. In contrast to previous serial invasive imaging studies, designed as large lipid-lowering trials, our study was designed to investigate the natural history of atherosclerosis in non-culprit vessels of patients with an ACS in daily clinical practice, and was not designed as a prospective comparison. Those lipid-lowering trials with a large number of patients showed minimal plaque regression for statin-

naïve patients<sup>21,22</sup>. With the relatively small number of patients investigated in this study, the absence of statistically significant differences in plaque progression of patients treated with high-intensity lipid-lowering therapy vs. low to moderate-intensity lipid-lowering therapy could be anticipated.

Secondly, using multiple imaging modalities in this study, we still needed to co-register NIRS-IVUS and OCT pullbacks. Some minor errors cannot be excluded despite using as many side branches as possible when performing the co-registration. Therefore, the ROI was divided into 1.5 mm segments - on average 3 IVUS frames per segment - to minimize the effect of longitudinal matching errors on the results. The advantage of the NIRS-IVUS derived lipid data was that it was detected and exactly co-localized with the plaque volume data. Finally, the number of patients does not allow to draw any conclusions on the direct link between the interaction of WSS and lipid-rich plaques and clinical events. Future studies or retrospective analyses of NIRS outcome studies may help understand this relationship in more detail.

## Conclusion

In this study, we investigated the WSS-related plaque progression of lipid-rich plaques compared to non-lipid rich plaques and plaque-free wall. By using multimodality imaging techniques as input for our WSS analysis, colocalization of WSS and lipid-rich plaque and volumetric plaque assessment was possible. Lipid-rich plaques as assessed by NIRS showed greater plaque progression than non-lipid rich plaques. Lipid-rich plaques, both identified by NIRS and OCT, exposed to low WSS showed the highest plaque growth after one-year follow-up.

## Acknowledgements

We gratefully acknowledge all the interventional cardiologists and fellows, lab technicians, nurses and research nurses of the cardiology department of the Erasmus Medical University for all their help and involvement in the IMPACT study.

## References

- Mathers CD, Loncar D. Projections of Global Mortality and Burden of Disease from 2002 to 2030. *PLoS Med* 2006;3:e442.
- Peiffer V, Sherwin SJ, Weinberg PD. SPOTLIGHT REVIEW Does low and oscillatory wall shear stress correlate spatially with early atherosclerosis? A systematic review. *Cardiovasc Res* 2013;99:242–50.
- Chiu JJ, Chien S. Effects of disturbed flow on vascular endothelium: Pathophysiological basis and clinical perspectives. *Physiol Rev* 2011;91:327–87.
- Chatzizisis YS, Coskun AU, Jonas M, Edelman ER, Feldman CL, Stone PH. Role of Endothelial Shear Stress in the Natural History of Coronary Atherosclerosis and Vascular Remodeling. *Molecular, Cellular, and Vascular Behavior. J Am Coll Cardiol* 2007;49:2379–93.
- Libby P. Inflammation in atherosclerosis. *Arterioscler Thromb Vasc Biol* 2012;32:2045–51.
- Libby P, Hansson GK. From Focal Lipid Storage to Systemic Inflammation: JACC Review Topic of the Week. *J Am Coll Cardiol* 2019;74:1594–607.
- Choi B-J, Prasad A, Gulati R, Best PJ, Lennon RJ, Barsness GW, et al. Coronary endothelial dysfunction in patients with early coronary artery disease is associated with the increase in intravascular lipid core plaque n.d.
- Ahmadi A, Leipsic J, Blankstein R, Taylor C, Hecht H, Stone GW, et al. Do Plaques Rapidly Progress Prior to Myocardial Infarction?: The Interplay between Plaque Vulnerability and Progression. *Circ Res* 2015;117:99–104.
- Johnson TW, Räber L, Di Mario C, Bourantas C, Jia H, Mattesini A, et al. Clinical use of intracoronary imaging. Part 2: acute coronary syndromes, ambiguous coronary angiography findings, and guiding interventional decision-making: an expert consensus document of the European Association of Percutaneous Cardiovascular Interventions Interventional cardiology. *Eur Heart J* 2019;0:1–19.
- Mintz GS, Maehara A. Serial intravascular ultrasound assessment of atherosclerosis progression and regression. State-of-the-art and limitations. *Circ J* 2009;73:1557–60.
- Tearney GJ, Regar E, Akasaka T, Adriaenssens T, Barlis P, Bezerra HG, et al. Consensus standards for acquisition, measurement, and reporting of intravascular optical coherence tomography studies: A report from the International Working Group for Intravascular Optical Coherence Tomography Standardization and Validation. *J Am Coll Cardiol* 2012;59:1058–72.
- Roleder T, Kovacic JC, Ali Z, Sharma R, Cristea E, Moreno P, et al. Combined NIRS and IVUS imaging detects vulnerable plaque using a single catheter system: A head-to-head comparison with OCT. *EuroIntervention* 2014;10:303–11.
- Goldstein JA, Madden SP, Sum ST, Dixon SR, Maddar RD, Muller JE. Assessment of Plaque Composition with Near-Infrared Spectroscopy. *Curr Cardiovasc Imaging Rep* 2011;4:298–308.
- Schuurman A-S, Vroegindewey M, Kardys I, Oemrawsingh RM, Cheng JM, de Boer S, et al. Near-infrared spectroscopy-derived lipid core burden index predicts adverse cardiovascular outcome in patients with coronary artery disease during long-term follow-up. *Eur Heart J* 2018;39:295–302.
- Hartman EMJ, De Nisco G, Kok AM, Hoogendoorn A, Coenen A, Mastik F, et al. Lipid-rich Plaques Detected by Near-infrared Spectroscopy Are More Frequently Exposed to High Shear Stress. *J Cardiovasc Transl Res* 2020.
- van der Giessen AG, Schaap M, Gijzen FJH, Groen HC, van Walsum T, Mollet NR, et al. 3D fusion of intravascular ultrasound and coronary computed tomography for in-vivo wall shear stress analysis: a feasibility study. *Int J Cardiovasc Imaging* 2010;26:781–96.
- De Nisco G, Kok AM, Chiastra C, Gallo D, Hoogendoorn A, Migliavacca F, et al. The Atheroprotective Nature of Helical Flow in Coronary Arteries. *Ann Biomed Eng* 2019;47:425–38.
- van der Giessen AG, Groen HC, Doriot P-A, de Feyter PJ, van der Steen AFW, van de Vosse FN, et al. The influence of boundary conditions on wall shear stress distribution in patients specific coronary trees. *J Biomech* 2011;44:1089–95.

19. Mintz GS. Intravascular Imaging of Coronary Calcification and its Clinical Implications. *JACC Cardiovasc Imaging* 2015;8:461–71.
20. Vonbank A, Drexel H, Agewall S, Lewis BS, Dopheide JF, Kjeldsen K, et al. Reasons for disparity in statin adherence rates between clinical trials and real-world observations: a review. *Eur Hear J - Cardiovasc Pharmacother* 2018;4:230–6.
21. Nissen SE, Nicholls SJ, Sipahi I, Libby P, Raichlen JS, Ballantyne CM, et al. Effect of very high-intensity statin therapy on regression of coronary atherosclerosis: The ASTEROID trial. *J Am Med Assoc* 2006;295:1556–65.
22. Oemrawsingh RM, Garcia-Garcia HM, Van Geuns RJM, Lenzen MJ, Simsek C, De Boer SPM, et al. Integrated Biomarker and Imaging Study 3 (IBIS-3) to assess the ability of rosuvastatin to decrease necrotic core in coronary arteries. *EuroIntervention* 2016.
23. Patel DD, Hamamdzc D, Llano R, Patel DD, Cheng L, Fenning RS, et al. Subsequent development of fibroatheromas with inflamed fibrous caps can be predicted by intracoronary near infrared spectroscopy. *Arterioscler Thromb Vasc Biol* 2013;33:347–53.
24. Waksman R, Di Mario C, Torguson R, Ali ZA, Singh V, Skinner WH, et al. Identification of patients and plaques vulnerable to future coronary events with near-infrared spectroscopy intravascular ultrasound imaging: a prospective, cohort study. *Lancet* 2019;394:1629–37.
25. Gardner CM, Tan H, Hull EL, Lissauskas JB, Sum ST, Meese TM, et al. Detection of Lipid Core Coronary Plaques in Autopsy Specimens With a Novel Catheter-Based Near-Infrared Spectroscopy System. *JACC Cardiovasc Imaging* 2008;1:638–48.
26. Di Vito L, Imola F, Gatto L, Romagnoli E, Limbruno U, Marco V, et al. Limitations of OCT in identifying and quantifying lipid components: An in vivo comparison study with IVUS-NIRS. *EuroIntervention* 2017;13:303–11.
27. Malek AM, Alper SL, Izumo S. Hemodynamic shear stress and its role in atherosclerosis. *JAMA* 1999;282:2035–42.
28. Samady H, Eshtehardi P, McDaniel MC, Suo J, Dhawan SS, Maynard C, et al. Coronary Artery Wall Shear Stress Is Associated With Progression and Transformation of Atherosclerotic Plaque and Arterial Remodeling in Patients With Coronary Artery Disease. *Circulation* 2011;124:779–88.
29. Stone PH, Saito S, Takahashi S, Makita Y, Nakamura SS, Kawasaki T, et al. Prediction of progression of coronary artery disease and clinical outcomes using vascular profiling of endothelial shear stress and arterial plaque characteristics: the PREDICTION Study. *Circulation* 2012;126:172–81.
30. Shishikura D, Sidharta SL, Honda S, Takata K, Kim SW, Andrews J, et al. The relationship between segmental wall shear stress and lipid core plaque derived from near-infrared spectroscopy. *Atherosclerosis* 2018;275:68–73.
31. Slager C, Wentzel J, Gijzen F, Thury A, van der Wal A, Schaar J, et al. The role of shear stress in the destabilization of vulnerable plaques and related therapeutic implications. *Nat Clin Pract Cardiovasc Med* 2005;2:456–64.
32. Stone PH, Maehara A, Coskun AU, Maynard CC, Zaromytidou M, Siasos G, et al. Role of Low Endothelial Shear Stress and Plaque Characteristics in the Prediction of Nonculprit Major Adverse Cardiac Events: The PROSPECT Study. *JACC Cardiovasc Imaging* 2018;11:462–71.
33. Bourantas C V, Räber L, Sakellarios A, Ueki Y, Zanchin T, Koskinas KC, et al. Utility of Multimodality Intravascular Imaging and the Local Hemodynamic Forces to Predict Atherosclerotic Disease Progression. *JACC Cardiovasc Imaging* 2020;13:1021–32.
34. Bourantas C V, Zanchin T, Sakellarios A, Karagiannis A, Ramasamy A, Yamaji K, et al. Implications of the local haemodynamic forces on the phenotype of coronary plaques. *Heart* 2019;105:1078–86.
35. Li Y, Gutiérrez-Chico JL, Holm NR, Yang W, Hebsgaard L, Christiansen EH, et al. Impact of Side Branch Modeling on Computation of Endothelial Shear Stress in Coronary Artery Disease. *J Am Coll Cardiol* 2015;66:125–35.
36. Yamamoto E, Siasos G, Zaromytidou M, Coskun AU, Xing L, Bryniarski K, et al. Low Endothelial Shear Stress Predicts Evolution to High-Risk Coronary Plaque Phenotype in the Future. *Circ Cardiovasc Interv* 2017;10:e005455.
37. Hartman EMJ, De Nisco G, Gijzen FJH, Korteland S-A, van der Steen AFW, Daemen J, et al. The definition of low wall shear stress and its effect on plaque progression estimation in human coronary arteries. *Sci Rep* 2021;11:22086.
38. Caro GG. Discovery of the role of wall shear in atherosclerosis. *Arterioscler Thromb Vasc Biol* 2009;29:158–61.
39. Fox B, James K, Morgan B, Seed A. Distribution of fatty and fibrous plaques in young human coronary arteries. *Atherosclerosis* 1982;41:337–47.
40. Timmins LH, Molony DS, Eshtehardi P, McDaniel MC, Oshinski JN, Samady H, et al. Focal Association Between Wall Shear Stress and Clinical Coronary Artery Disease Progression. *Ann Biomed Eng* 2014;43:94–106.



# 7

## **Non-invasive coronary imaging as an alternative to invasive imaging to study wall shear stress: A patient-specific computational study**

This chapter adapted from:

Validation of Wall Shear Stress Assessment in Non-invasive Coronary CTA  
versus Invasive Imaging: A Patient-specific Computational Study

Parastou Eslami, Eline M.J. Hartman, Mazen Albaghadai, Julia Karady, Zexi Jin,  
Vikas Thondapu, Nicholas V. Cefalo, Michael T. Lu, Ahmet Coskun, Peter Stone,  
Alison Marsden, Udo Hoffmann, Jolanda J. Wentzel

*Ann Biomec Eng, 2021*



## Abstract

Endothelial shear stress (ESS) identifies coronary plaques at high risk for rapid progression and/or rupture leading to a future acute coronary syndrome. In this study an optimized methodology was developed to derive ESS, pressure drop and oscillatory shear index using computational fluid dynamics (CFD) in 3D models of coronary arteries derived from non-invasive coronary computed tomography angiography (CTA). These CTA-based ESS calculations were compared to the ESS calculations using the gold standard with fusion of invasive imaging and CTA.

In a total of 14 patients, paired patient-specific CFD models of the left anterior descending (LAD) coronary arteries were created. Ten patients were used to optimize the methodology, and four patients to test this methodology. Time-averaged ESS (TAESS) was calculated for both coronary models applying patient-specific physiological data available at the time of imaging. For data analysis, each 3D reconstructed coronary artery was divided into 2mm segments and each segment was subdivided into 8 arcs (45°). TAESS and other hemodynamic parameters were averaged per segment as well as per arc. Furthermore, the paired segment- and arc-averaged TAESS were categorized into patient-specific tertiles (low, medium and high).

In ten LADs, used for optimization of the methodology, we found a high correlation between invasively-derived and non-invasively-derived TAESS averaged over segments ( $n=263$ ,  $r=0.86$ ) as well as arcs ( $n=2104$ ,  $r=0.85$ ,  $p<0.001$ ). The correlation was also strong in the four testing-patients with  $r=0.95$  ( $n=117$  segments,  $p=0.001$ ) and  $r=0.93$  ( $n=936$  arcs,  $p=0.001$ ). There was an overall high concordance of 78% of the three TAESS categories comparing both methodologies using the segment-based and 76% for the arc-averages in the first ten patients. This concordance lower in the four testing patients (64% and 64% in segment- and arc-averaged TAESS). Although the correlation and concordance were high for both patient groups, the absolute TAESS values averaged per segment and arc were overestimated using non-invasive vs. invasive imaging [testing patients: TAESS segment: 30.1[17.1–83.8] vs. 15.8[8.8–63.4] and TAESS arc: 29.4[16.2–74.7] vs 15.0[8.9–57.4]  $p<0.001$ ]. We showed that our methodology can accurately assess the TAESS distribution non-invasively from CTA and demonstrated a good correlation with TAESS calculated using IVUS/OCT 3D reconstructed models.

## Introduction

Coronary artery disease (CAD) continues to be the leading cause of deaths in the US<sup>1</sup>. Prevention of ischemic coronary artery disease is challenging as over 50% of patients with acute coronary syndrome have no prior symptoms of myocardial ischemia or manifestations of CAD<sup>2</sup>. The development coronary events in patients without prior symptoms is commonly caused by the progression and/or disruption of non-calcified plaques and locations with previously no significant obstructive CAD<sup>3</sup>.

Local hemodynamic factors, such as wall shear stress (ESS), defined as tangential force acting on the endothelial cells, play a major role in the development and progression of atherosclerosis<sup>4</sup>. These ESS-related pathophysiological concepts, as investigated using computational fluid dynamics (CFD), have been validated in clinical studies applying invasive intravascular coronary imaging modalities such as intravascular ultrasound (IVUS) and optical coherence tomography (OCT)<sup>5–7</sup>. IVUS and OCT are high-spatial resolution intracoronary modalities (200  $\mu\text{m}$  and 10  $\mu\text{m}$ , respectively) that allow accurate in vivo characterization of atherosclerotic plaque and lumen shape in human coronary arteries. The ability to perform similar ESS analyses based on non-invasive imaging, such as coronary computed tomography angiography (CTA), has the potential to include a much larger number of individuals who can readily undergo non-invasive testing for CAD. In the current standard of care, patients that present with non-acute symptoms of CAD undergo diagnostic non-invasive testing by CTA to decide for either the need of percutaneous coronary intervention or medical treatment. CTA allows for non-invasive evaluation of the entire coronary artery tree including the lumen and vessel wall, and thereby the presence, extent and characteristics of atherosclerotic plaque. Despite a lower CTA resolution of  $\sim 500 \mu\text{m}$ , recent studies show that CFD modeling based on CTA images for the assessment of hemodynamic significance of coronary artery stenosis is as accurate as invasive coronary angiography<sup>8–10</sup>. For example, fractional flow reserve (FFR) defined as the ratio of distal to proximal pressure across the plaque has been shown to be accurately calculated non-invasively based on CTA<sup>11,12</sup>.

Therefore, the overall goal of this study was to develop and validate a methodology to study ESS calculated by CFD using non-invasive CTA. Hence, the objectives of this study were to 1) establish a methodology to create 3D CFD models based on invasive and non-invasive imaging of the same arteries and compare the final geometries, and 2) compare and validate ESS calculation based on coronary CTA against calculations based on fusion of CTA with invasive imaging of coronary arteries. Since we showed a high correlation and similar ESS patterns using the two imaging methods, we hereby provide a clinically relevant, non-invasive

methodological approach to assess a valuable hemodynamic factor that is applicable, and potentially readily available, for a large group of patients at risk of development and progression of CAD.

## METHODOLOGY

### Patient Population

For this study a combination of two existing datasets was used. The first part of the dataset consisted of patient data ( $n=8$ ) that were acquired during a standard patient screening for stable chest pain and percutaneous coronary intervention procedure from the research patient data repository of Massachusetts General Hospital (MGH). Patients that were selected for the current study underwent CTA not more than 90 days before the invasive imaging (IVUS or OCT) and did not have prior coronary interventions, revascularizations or were scheduled for valve replacement. All patients provided written informed consent. This retrospective study was approved by the institutional review board of MGH (Figure 1).

The second part of the dataset ( $n=6$ ) comes from a study repository from the Erasmus MC, Rotterdam (EMC). Hemodynamically stable patients with an acute coronary syndrome (ACS) with at least one non-stented non-culprit coronary vessel were invasively imaged using IVUS. Patients were excluded with a history of previous coronary artery bypass graft surgery, 3-vessel disease, renal insufficiency, ejection fraction  $<30\%$  and atrial fibrillation. Patients included in this study underwent invasive coronary imaging (IVUS) of the non-stented non-culprit coronary vessel and CTA one month after the invasive procedure. All patients provided written informed consent. The study protocol was approved by the local medical ethical committee of the EMC (Figure 1).

Collectively, we selected a total of fourteen patients, eight from MGH, six from EMC. Of these, ten (6 from MGH and 4 from EMC) were used for the training and optimizing the methodology during an iterative development phase (referred to as training dataset) and an additional four patients (2 from MGH and 2 from EMC) were used to test the methodology (referred to as the testing dataset). Only the left anterior descending coronary artery (LAD) was studied, so that all patients had a similar branching pattern.

### Coronary CTA Imaging Data Acquisition

For the MGH cases, coronary CTA were performed as the standard clinical protocol where patients were prospectively ECG gated scanned with automatic exposure control (tube potential and tube current modulation). CTA was performed using Isovue 370 (iopamidol). Images were reconstructed using 0.6 mm thickness using iterative reconstruction methods.

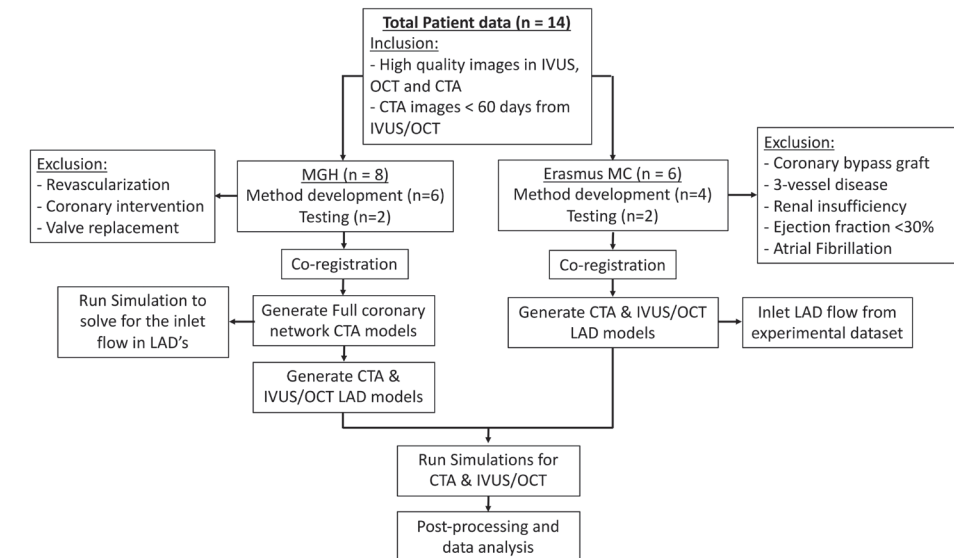


**Figure 1.**

Workflow of the study with 14 total number of patients where 10 is used for methodology development and 4 are used to test the methodology developed. Specifications for each cohort as well as the exclusion criteria are also included.

Similarly, in the patients from EMC, the CT scans were acquired through a prospectively gated protocol with 70-80kV and the tube current was set for automatic exposure control (SOMATOM Force- 192 slice 3<sup>rd</sup> generation dual-source CT scanner, Siemens AG, Germany). Kernel Bv40, Slice thickness 3mm increment 1.5mm, Admire 5 setting was used for reconstruction of the images.

### IVUS and OCT Imaging Data Acquisition

Coronary angiograms were recorded with full contrast injection before the insertion of a guidewire that is used to advance an IVUS/OCT catheter into the coronary artery. From the MGH data repository, patients were selected who underwent IVUS imaging of their coronary arteries using a Boston Scientific Opticross IVUS catheter with automatic pullback rate of 1 mm/sec or OCT imaging using a frequency-domain (FD)-OCT system (St. Jude Medical, St. Paul, MN). Automated pullback was initiated at a speed of 36/54 mm/sec in concordance with blood clearance.

EMC patients went through a similar protocol as MGH IVUS imaging. However, the images were acquired by an automated pullback (0.5mm/s) with a NIRS-IVUS catheter (TVC Insight Coronary Imaging Catheter, InfraRedX, Burlington, MA, USA). Subsequently, local flow measurements were performed in between side

branches in the segment of interest using Doppler velocimetry. All of the IVUS and OCT images were anonymized, digitally stored.

### Co-registration of Invasive and Noninvasive Imaging

To obtain the correct longitudinal location and circumferential orientation of the IVUS/OCT images while fusing them with CTA, anatomic landmarks such as side branches and bifurcations were used (Figure 2A). Further, we used coronary angiograms at the time of IVUS/OCT to keep track of location of branches relative to each other. We also used coronary angiogram to ensure the general shape of the vessel matched the 3D shape reconstructed from CTA. For the training patients, this process was performed and optimized iteratively to ensure that the frames consisting the landmarks in invasive imaging corresponds to the same slice in CTA multiplane reconstruction cross-sections of the LAD. We further established a method to include the vessel of interest such that it all starts and end immediately after the location where the branch leaves the main artery in all imaging modalities. This allowed for a clearly marked proximal and distal end of the vessel. In addition, in the case of IVUS co-registration, there may be branches censored due to gating. Therefore, we closely looked at both gated and un-gated IVUS images to ensure that there are no branches miscounted in the process of co-registration.

### 3D reconstruction of coronary artery tree and coronary vessel of interest: CT based image segmentation

In order to create a 3D reconstruction of a full coronary tree, the lumen of each major coronary artery and the ascending aorta was semi-automatically segmented using a commercially available software package (Medis QAngioCT and 3DWorkbench, Leiden, Netherlands). Corrections were made when necessary by an expert reader to ensure accurate segmentation. After anatomical 3D reconstruction of the coronary arteries and the ascending aorta, the vessels were imported into Simvascular<sup>13</sup> to merge the three major arteries with a coronary network (Figure 2B). With this approach the flow information in the vessel of interest could be computed, in case that information was not available. The methods that were applied to solve the hemodynamics in a coronary network was described in detail before<sup>14</sup>.

Subsequently, the segment of interest from the LAD was isolated (Figure 2C). To select the segment of interest, co-registration of CTA with invasive imaging (as described in details below) was of key importance to ensure that also invasive imaging acquisition was performed on the selected segment. After isolation of the segment of interest the side branches were removed from the CTA segmentation, since the models based on IVUS/OCT do not contain side branches. Therefore, following the conservation of mass law, the total mass flowrate was calculated,

adding all the downstream side branches flowrate on to the main vessel. The final 3D reconstruction of the coronary artery was smoothed using a Laplacian smoothing algorithm with 3 iterations and weighing factor of 0.01. We found 3 iterations of smoothing to be an optimum number to preserve the shape and anatomy of the vessel while sharp edges and skewed surfaces are eliminated. Furthermore, 3D centerlines were extracted for the vessel of interest.

### Invasive Imaging Lumen Segmentations

IVUS images were gated at the same cardiac phase, so that diameter variation as a result of the cardiac contraction were removed. For the dataset acquired at MGH, IVUS/OCT segmentations of the lumen were manually conducted using an in-house segmentation software at the Vascular Profiling Laboratory similar to previous protocol<sup>15,16</sup>. We extracted the segmented lumens at each cross-section as point clouds at each gated frame for IVUS and all the OCT frames. We adapted this methodology which enabled us to fuse the contours segmented based on invasive imaging to be fused with the 3D centerline extracted from CT<sup>17</sup>. The IVUS images for the testing patients acquired at EMC were blindly segmented applying QCU-CMS software (version 4.69, LKEB, Division of image processing, Leiden, The Netherlands) and also exported as point clouds.

### 3D-Reconstruction of coronary artery: CT fused with IVUS/OCT

In order to create a 3D coronary reconstruction based on the 2D-lumen segmentations from IVUS/OCT, we fused the 2D point clouds extracted in the previous step with the 3D-centerline extracted from CT (Figure 2C-E). As a first step in the fusion process, we interpolated the centerline points such that the number of centerline points were the same as the number of 2D-cross sectional lumen segmentations. Then, the obtained point clouds were isotopically transformed such that the lumen centroid coincided with the CT-based centerline points and the normal to the cross sections were aligned with the local curvature tangent of the centerline. In addition, to ensure correct orientation as well as the rotation of each cross-section we used the landmarks in the co-registration process (as described below) and compared each consecutive cross-section's normal to ensure their dot-products are positive. In previous studies, the 3D reconstruction of IVUS/OCT-based geometries were performed fusing the centerline extracted from 2D orthogonal coronary angiograms.

However, in this study we adapted a more recent hybrid methodology fusing the 2D cross-sections based on IVUS/OCT with the 3D centerline extracted from coronary CTA. This methodology have been shown to be as accurate as the former methodology in calculating shear stress and been used other shear stress based studies<sup>18,19</sup>. In addition, this methodology was used partly because in our retrospective MGH patients, not all had orthogonal 2D coronary angiograms for

the centerline to be readily extracted. Lastly, we used MeshLab, an open sources software to create a surface mesh from the point-clouds using a ball-pivoting methodology by Bernardini et al.<sup>20</sup>. Similar to CTA models, the final 3D coronary artery was smoothed using a Laplacian smoothing algorithm with 3 iterations.

It is important to note that ten patients (6 MGH and 4 EMC) were used to optimize the methodology. Therefore, segmentations and model creations were performed iteratively and not fully blinded between the imaging modalities in the process of methodology development. Therefore, segmentations and 3D reconstructions of coronary arteries may have been performed multiple times communicating between the imaging modalities until a consistent method was established through all patients. Hence, addressing imaging artifacts in each imaging modality and methods of co-registration concluded in an iterative process in the training phase. Therefore, we also analyzed a testing data set of four patients (2 EMC, 2 MGH) for which segmentations were done only once and fully blindly where IVUS/OCT segmentations were performed by one reader and CTA segmentations were done by a different reader and the landmarks were communicated only once.

### Simulations

In order to calculate the ESS and other hemodynamic parameters, three-dimensional pulsatile CFD simulations of blood flow were performed using patient-specific coronary artery meshes in Simvascular<sup>13</sup>. This software uses a novel second order preconditioning implicit method<sup>21</sup> and is optimized to solve the 3D incompressible Navier-Stokes equations (Eq1a and 1b) in vascular systems reconstructed from image data; where  $\mathbf{u}$ ,  $\rho$ ,  $w$ ,  $\nu$  and  $\mathbf{g}$  stand for flow velocity, blood density, internal sources, kinematic viscosity and external source, respectively. Blood was treated as Newtonian fluid with a density and kinematic viscosity of 1060 kg/m<sup>3</sup> and 3.8x10<sup>-6</sup> m<sup>2</sup>/s, respectively. We assumed blood as a Newtonian fluid as this is valid assumption in arteries larger than capillaries where the shear rate is relatively low for blood to behave as a Newtonian fluid<sup>22</sup>. Reynolds number were in the laminar region in the coronaries. Mean Reynolds number was defined as  $Re = \frac{U_{avg}D}{\nu}$  where  $U_{avg}$  is the average velocity in the vessel of interest. Therefore, there was no turbulence modeling as the mean ESS was calculated in the 3D reconstruction of coronary based on a) CT only and b) in their counterparts based on the fusion of CT and invasive imaging (IVUS, OCT). The inflow boundary conditions, in case they were not measured, were calculated using a full coronary network (see above).

$$\frac{\partial \rho}{\partial t} + \nabla \cdot (\rho \mathbf{u}) = 0 \quad (\text{Eq 1a})$$

$$\frac{\partial \mathbf{u}}{\partial t} + (\mathbf{u} \cdot \nabla) \mathbf{u} - \nu \nabla^2 \mathbf{u} = -\nabla w + \mathbf{g}; \quad (\text{Eq 1b})$$

### Mesh generation

The 3D-reconstructed coronary anatomy was meshed using TetGen (an open source tetrahedral mesh generator that uses 3D Delaunay Triangulation with 2 layers of boundary layer mesh). To ensure a fully resolved flow, the Courant-Friedrichs-Lewy number was set to be <1 and a maximum allowable edge size for a given element was specified for the entire mesh not to exceed half of the smallest outflow diameter. At the aortic level, the mesh size was adjusted to be larger to avoid having an unnecessary large number of elements. Local refinements were further performed at locations of bifurcations and stenosis. A mesh converge test was performed to determine the threshold of element size for each simulation to ensure no more than 1% change in TAESS at locations with luminal narrowing.

### Boundary conditions

For patient-specific boundary condition assignment, depending on the cohort, two different methodologies were applied to impose the inlet flowrate (Q) waveform. For the MGH dataset, the flow was solved using the 3D-coronary network, by providing the inlet flowrate waveform at the aortic valve level. The waveform used was obtained from measurements in a healthy person in the Vascular Model Repository<sup>23</sup>. However, conserving the shape of the waveform, its period was adjusted for the heart rate of the patient and the area under the curve of the waveform was adjusted using the patient specific stroke volume as an input in the coronary network simulations. The stroke volume was calculated by multiplying the end-diastolic left ventricle volume from the coronary CTA scans (using Syngo. via - Siemens Medical Solutions, USA) with the ejection fraction obtained from a recent Echocardiogram (obtained no longer than 30 days from CTA).

The downstream hemodynamics and circulation that were not included in the 3D model were modeled using lumped parameter networks that use electric circuit analogs to prescribe the relationship between flow and pressure in these vessels. These boundary conditions were based on a previously tested algorithms implemented in Simvascular<sup>13</sup>. To ensure we are using the correct flow rate information, the diastolic, systolic, mean pressure, and cardiac output were checked to match the patient-specific measurements at the time of the scan. In addition, other metrics such as percent total coronary outflow with respect to cardiac output and the shape of the right and left coronary waveforms were checked against reported literature data<sup>24-26</sup>. In the event of more than 10% difference between the clinical measurement and calculated pressure and flowrates, the simulation was repeated by changing the lump network element of resistance and capacitance until a good agreement was reached.



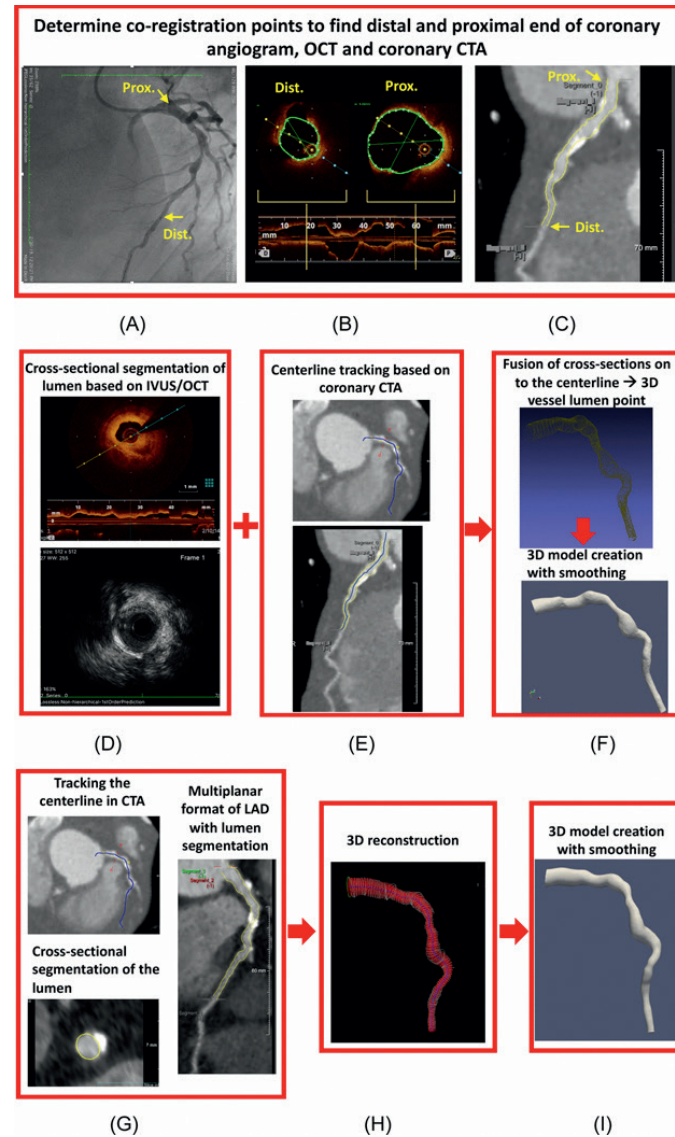


**Figure 2. Illustration for methodology workflow in co-registration of the invasive and noninvasive imaging based on**

(A) coronary angiogram, (B) intravascular imaging (in this case OCT) (C) and coronary CTA on the multiplanar reconstruction view. Steps involved in 3D model for invasive-based models where first (D) cross-sectional segmentation for the lumen is performed (E) second the centerline based on CTA is extracted (F) cross-sectional lumen cloud points are fused with centerline to create 3D shape and lastly the smoothed 3D LAD model is reconstructed. Steps involved in 3D reconstruction based on coronary CTA where first (G) the centerline is first tracked and coronary lumen is segmented and (H) 3D shape of the vessel is crated based on the segmented contours and (I) the final smoothed 3D reconstructed model is created.

Once the flow was solved through the whole coronary network, the flowrate waveform at the vessel of interest (LAD) was retrospectively calculated as the summation of all the downstream branches flowrates. The calculated total LAD flowrate was thereafter used as an input for a second set of CFD calculations in the models of the isolated LAD arteries (Figure 2H). These latter CFD calculations were performed to assess the detailed hemodynamics parameters for the CTA- and IVUS/OCT-based models. To enable a 1:1 comparison between IVUS/OCT and coronary CTA based ESS calculations, the inlet boundary conditions were kept the same between the models. However, the distal lumped element model resistances for the CTA-based models were scaled according to the outlet cross-sectional area of the IVUS/OCT-based models. With this approach, the differences in ESS between the two models is fully based on the local geometry.

For the EMC patient cohort, the average flowrate was calculated by multiplying the time averaged measured velocity and the cross-sectional area of measurement location. Furthermore, the same general waveform used for MGH patients was scaled and adjusted for the patient-specific average flowrate and heart rate measured at the time of imaging acquisition.

For all the simulations, the shape of the inlet velocity profile was assumed to be parabolic and no-slip boundary conditions were imposed at the walls. The arterial wall was assumed to be rigid as it has been previously shown that wall elasticity in calculation of ESS has a negligible effect for the calculation of ESS in the coronary network<sup>27</sup>. Each patient's hemodynamics were solved for 6 cardiac cycles to reach full convergence and the final results were reported based on the results of the last cardiac cycle calculations. The convergence criteria was set to reach a nonlinear residual  $<1\text{E-}4$  and peak flowrate at outlet difference of  $<1\%$  from the 5th to 6th cardiac cycle.

### Data Analysis and Hemodynamic Computations

ESS was calculated as a continuous variable at the wall of the coronary segment as the product of viscosity and the gradient of blood velocity at the wall (Table 1). An in-house python-based code using the "vtk package" was used to extract 1) time averaged ESS (TAESS) at each degree arc angle in each cross-section along the for creation of 2D map of TAESS during the cardiac cycle and 2) cross-sectional diameter and area along the centerline of the vessel. For final data analysis, the constructed coronary models were divided into consecutive 2 mm segments and each segment was divided into  $45^\circ$  arcs along the centerline (Figure 3B). The TAESS was averaged per segment ( $\overline{TAWSS_{seg}}$ ) and per  $45^\circ$  arc ( $\overline{TAWSS_{arc}}$ ) (see Table 1 for definitions). Previous studies used 3 mm segments to summarize the local hemodynamic characteristics to minimize the variation and noise in calculations<sup>4,6</sup>. However, for this study, we chose to compare the TAESS using the 2 mm segments



rather than 3 mm segments for a more detailed comparison of the two imaging modalities. Subsequently, the segments and 45° arcs were categorized into low, medium and high TAESS according to the TAESS using patient-specific tertiles following previously reported studies<sup>6,17,28</sup>. Furthermore, in each 2 mm segment the local minimum  $TAESS_{min}$  and max  $TAESS_{max}$  were as the 90° arc with the lowest and the highest TAESS within the segment, examining these 90° arcs per 1° around the circumference of the segment following previous studies<sup>5,29,30</sup> (Figure 3B).

Segment averaged oscillatory shear index ( $\overline{OSI_{seg}}$ ) —characterizing the degree of shear stress reversal in a pulsatile flow— was calculated as the averaged OSI

values over the 2-mm segment where  $OSI = 0.5 \left( 1 - \frac{\left| \int_0^T \vec{\tau}_w dt \right|}{\int_0^T |\vec{\tau}_w| dt} \right)$ .

Similarly, time averaged pressure was averaged over each 2-mm segment. All the time-averaged values reported here were averaged over the last cycle of the simulations.

Table 1. Hemodynamic factors calculated in this study.

Eq #	Term	Meaning
2	$\tau_w$	Blood velocity gradient at vessel wall
3	$\overline{TAWSS_{seg}}$	Area averaged TAESS
4	$\overline{TAWSS_{arc}}$	45° arc averaged TAESS
5	$OSI$	Oscillatory shear index
6	$\overline{OSI_{seg}}$	Area averaged oscillatory shear index
7	$\overline{P_{seg}}$	Time-averaged area-averaged pressure

Statistical Analysis

Continuous parameters were reported in mean ± standard deviation or median (interquartile range [IQR]) and the categorical variables were reported as counts and percentages and compared in a paired analysis. The mean for normally distributed data were tested to be significantly different with a paired t-test and Wilcoxon rank sum test was used for the median in non-normal distributed data. Pearson linear coefficient, r, was calculated to report the correlation between the (hemodynamic) parameters derived between the two imaging modalities. Standard

errors of the correlation coefficient were corrected for the fact that the multiple arterial segments within patients were not independent using the “Huber-White” sandwich estimator<sup>31</sup>. Bland-Altman plots were created to evaluate agreement between the ESS calculations based on CTA and IVUS/OCT. All calculations were two-tailed with p<0.05 considered statistically significant.

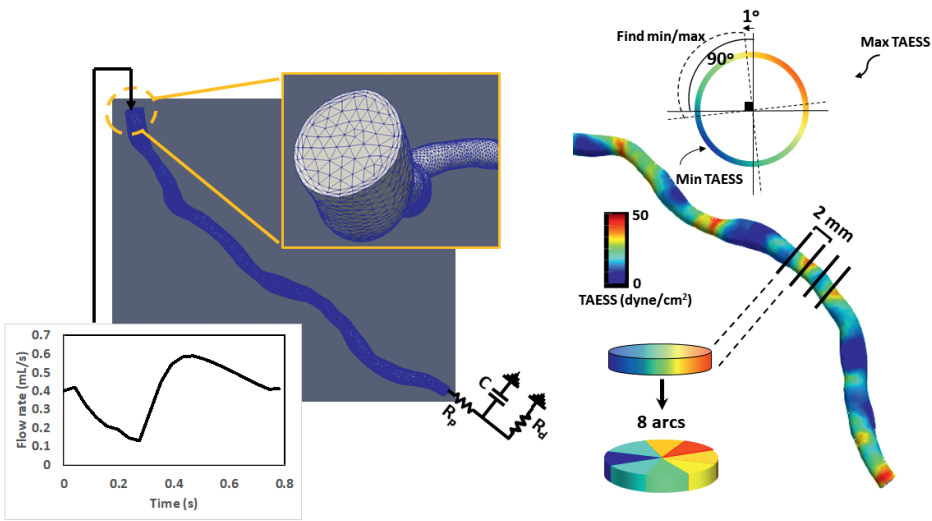


**Figure 3.** **A:** Boundary conditions used for the left anterior descending 3D reconstructed models where the input flow rate is a waveform adapted from a healthy person in the Vascular Model Repository<sup>21</sup> such that the waveform is adjusted for the patient-specific mean flow rate as well as the heart rate at the time of patient scans. The distal boundary condition is an RCR lumped element model where the proximal ( $R_p$ ) and distal ( $R_d$ ) resistance are adjusted by the mean flow rate and pressure measurements. C stands for capacitance and is kept as the constant value of  $4.16 \times 10^{-6}$ . The mesh generated for each coronary artery included 2 boundary layers with maximum of 0.5 portion of edge size. **B:** Schematics illustrating methods used to calculate segment- and arc-averaged and minimum/maximum TAESS along the artery’s centerline. The minimum and maximum TAESS is determined by finding the minimum/maximum of TAESS in each 90° arc and in the entire cross-section rotating at 1° increments at a time.

Results

Patient Population

The patients selected were  $60.0 \pm 10.2$  of age and 93% were male.

Continuous TAESS

The overall TAESS pattern (in 3D and 2D maps) as obtained using the models based on invasive and non-invasive imaging were very similar. Figure 4 displays

a case with a very high correlation. The training dataset consisted of 263 paired segments and the median  $\overline{TAESS}_{seg}$  was significantly higher as assessed with the non-invasive models compared to the invasive models (50.1 [25.8-90.1], 31.7 [19.3-62.4] dyne/cm<sup>2</sup>,  $p < 0.001$ ). Similarly, in a total of 2104 arcs, the arc-averaged TAESS values were 47.7 [24.1-90.0] and 29.9 [18.1-62.4] dyne/cm<sup>2</sup> ( $p < 0.001$ ) based on non-invasive and invasive models, respectively. The values for the other hemodynamic parameters for both the training and validation dataset are reported in Table 2 with non-significant differences in OSI and significant differences in pressure. There was a strong and significant Pearson correlation found between the two methodologies for  $\overline{TAESS}_{seg}$  and  $\overline{TAESS}_{arc}$  [ $r = 0.86$  and  $r = 0.85$  ( $p < 0.001$ )], (Figure 5). Similarly, in the testing patients (117 segments and 936 45° arcs) a high correlation between the two imaging modalities was found for  $\overline{TAESS}_{seg}$  and  $\overline{TAESS}_{arc}$  ( $r = 0.95$  and  $0.93$ ;  $p = 0.001$ ), and similarly, as the training patients, the absolute  $\overline{TAESS}_{seg}$  and  $\overline{TAESS}_{arc}$  were overestimated using non-invasive imaging (Table 2).

The Bland-Altman plots (Figure 6) showed that apart from the observed absolute differences in the TAESS values for both segment- (mean difference:  $-21.3 \pm 36.3$  dyne/cm<sup>2</sup>) and arc-averaged (mean difference:  $-21.3 \pm 38.2$  dyne/cm<sup>2</sup>) TAESS, the differences were also dependent on the higher values of the TAESS. Similar differences and trends were observed for the testing patients (Figure 6 C-D) TAESS values were not normally distributed (and skewed towards lower values) and thus we reported median values in this study. However, the mean differences between the TAESS values based on two imaging modalities had a normal distribution and hence we reported means and standard deviations in Bland-Altman plots.

For the training patients, medians of  $TAESS_{min}$  were significantly different in invasive and non-invasive imaging with values of 10.3[4.4-19.5] and 16.2[6.7-34.7] dynes/cm<sup>2</sup>, respectively.  $TAESS_{max}$  values were also significantly different in the invasive and non-invasive models (55.3[34.0-117.3] vs. 90.3[42.8-167.6] dynes/cm<sup>2</sup>). In addition, minimum and maximum TAESS had a correlation of 0.82 and 0.86 respectively ( $p < 0.001$ ) between the two models based on invasive and non-invasive imaging. A similar tendency was observed in the testing patients along the entire vessel with significant difference in absolute values of  $TAESS_{min}$  and  $TAESS_{max}$  with a high correlation between the two imaging modalities ( $r = 0.85$  and  $0.89$  for,  $TAESS_{min}$  and  $TAESS_{max}$ , respectively)

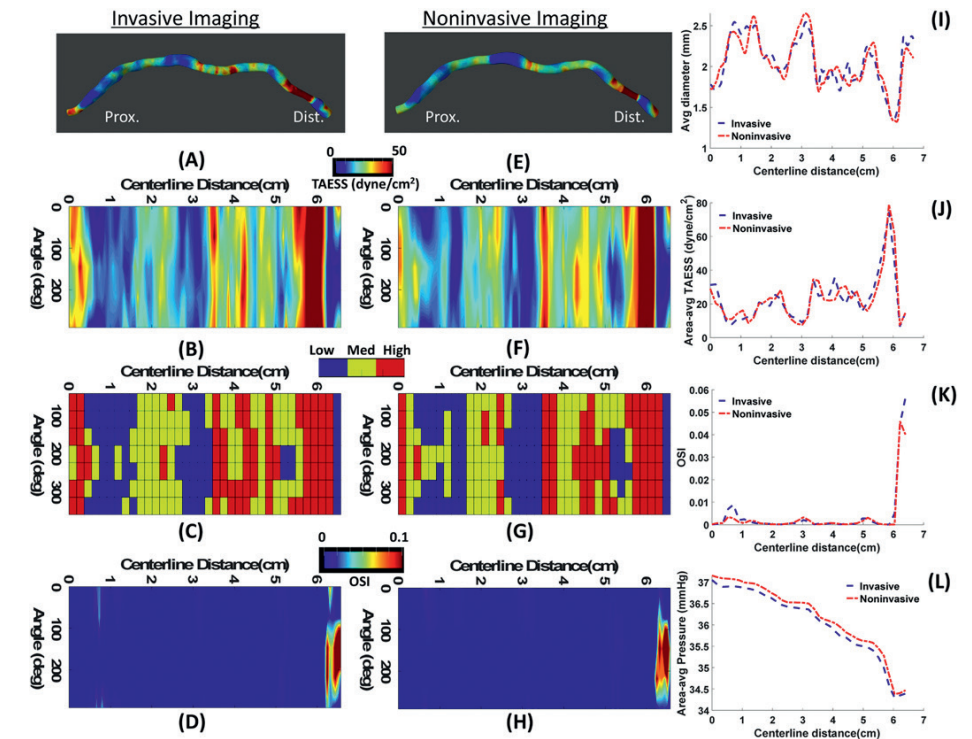


**Figure 4.**

A representative case (Patient 3) with high agreement between the hemodynamics calculation based on invasive IVUS (A-D) and noninvasive CTA (E-H). 3D map of ESS representations (A,D) where the proximal and distal ends of the vessels are aligned with the 2D map of ESS (B,F) along the centerline of the vessel. Categorical values of ESS (C,G) show low, medium and high at each 45° arc and 2D map of OSI (D,H) values along the centerline are shown. Comparisons of average diameter (I), area averaged TAESS (J), area averaged OSI (K) and area-averaged pressure (L) show a high agreement between IVUS and CTA calculated parameters.

### Categorical TAESS

After categorizing the TAESS in three patient-specific tertiles (low, mid, high) for each 2mm-segment and 45°-arc, we found a high agreement between invasive and non-invasive imaging (Figure 7). The confusion matrices shows an overall accuracy of 78.3% for the categorical  $\overline{TAESS}_{seg}$  values where low, medium and high categories had 82.2%, 77.2% and 76.5% concordance between the two imaging modalities. Similarly, in categorical  $\overline{TAESS}_{arc}$  values had an overall accuracy of 76.2% where the low, medium and high categories had an agreement of 78.8%, 69.5% and 81.4%, respectively. The same trend was observed in the testing dataset with a lower overall accuracy of 64.1% and 63.8% in for the segment-averaged and arc-averaged concordance.

In both training and testing datasets, the majority of disagreements were observed in the arcs and areas where the non-invasive-based TAESS was labeled as medium (77.1% in training, 55% in testing) and the invasive model labeled as low (17.8% in training, 32.4% in validation) or high (23.5% in training, 28.0% in validation).

### Other Hemodynamic Calculations

The median [IQR] values for OSI and pressure are reported in Table 2.  $\overline{OSI}_{seg}$  based on non-invasive imaging had a significant moderate Pearson correlation with invasive imaging in the training dataset ( $r=0.64$ ,  $p<0.001$ ) and validation dataset ( $r=0.70$ ,  $p<0.001$ ).  $\overline{P}_{seg}$  had a high correlation of ( $r=0.91$ ,  $p<0.001$ ) in the training dataset and  $r=0.85$ ,  $p<0.001$ ) in the testing dataset.

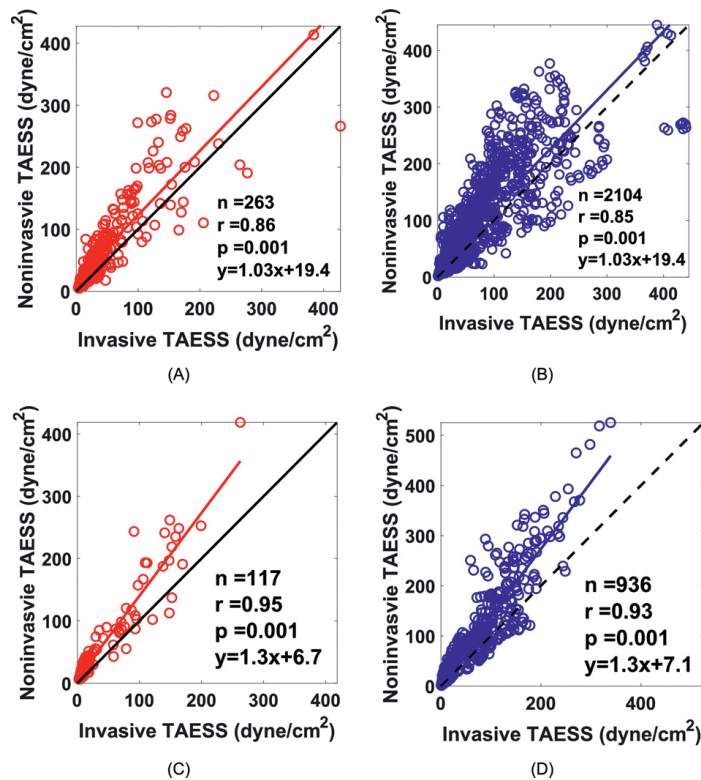


**Figure 5.**

Correlation plots between on TAESS calculations based on invasive and noninvasive imaging for the training dataset showing a high (A) Pearson correlation ( $r=0.86$ ) for area-averaged TAESS and (B)  $r=0.85$  for arc-averaged TAESS. The linear fit curve has a slope of 1.03 and a y-intercept of 19.4 showing a slightly higher TAESS values for the noninvasive imaging modality. The independent and testing patients show very high correlation between the invasive and noninvasive models for (C) area averaged and (D) arc-averaged TAESS with a higher TAESS estimation in noninvasive TAESS.

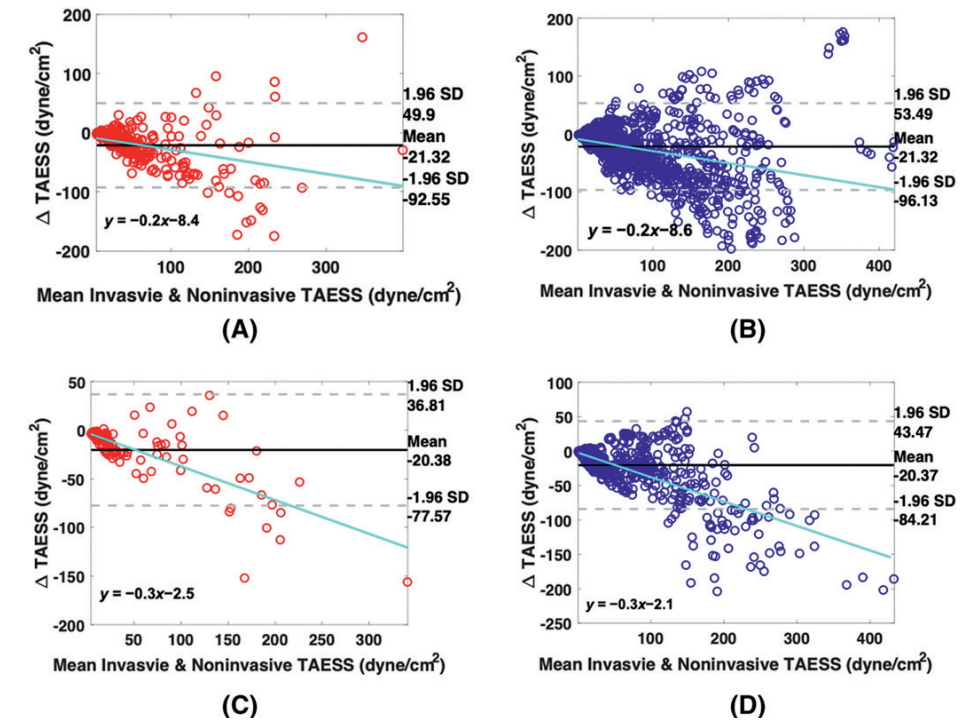


**Figure 6.**

Bland-Altman plots to compare the TAESS calculated based on noninvasive-based models versus the gold standard invasive-based models for (A) the area averaged TAESS (B) arc-averaged TAESS in the training cohort and (C) the area-averaged and (D) arc-averaged in the four independent testing patients.  $\Delta TAESS = TAESS_{invasive} - TAESS_{non-invasive}$



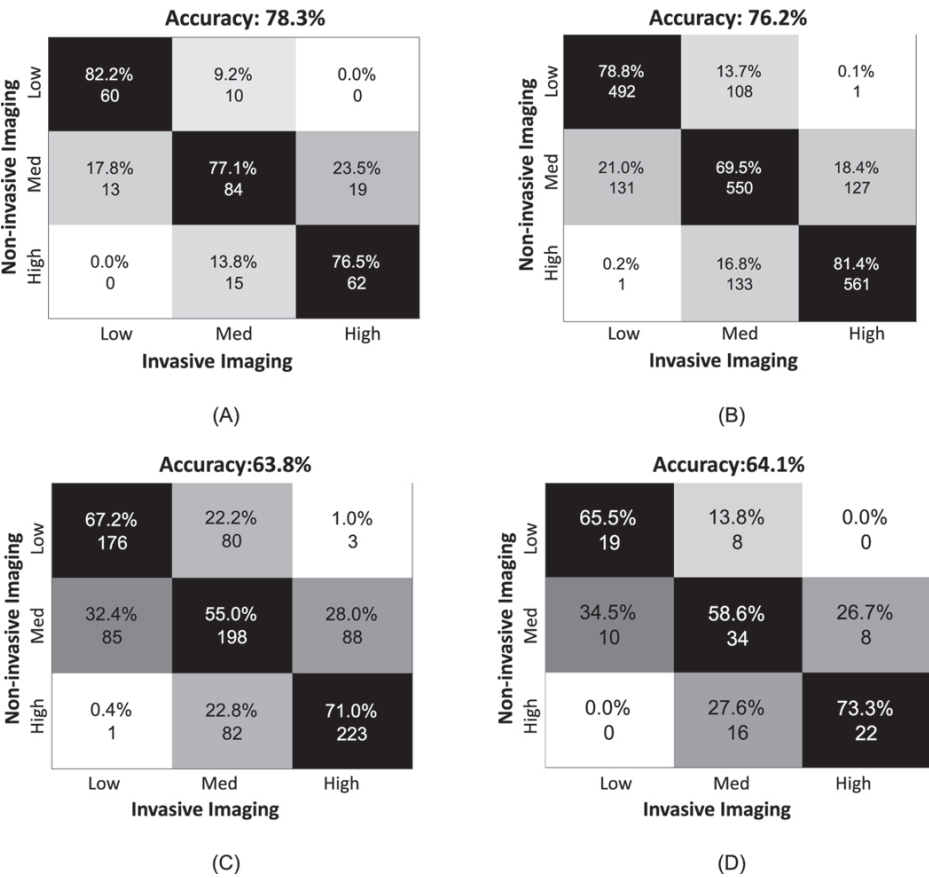


**Figure 7.** Confusion matrices to demonstrate the agreement between categorical TAESS based in invasive- and no- invasive-based models based on patient-specific tertiles for **A:** area-averaged and **B:** arc-averaged calculation in the training cohort and **C:** area-averaged and **D:** arc-averaged calculations in the testing cohort. The testing cohort accuracy is relatively lower than the training cohort models when matching categorical TAESS, however the trend is similar where there is higher accuracy in the low and high categories and the medium category is mis-categorized in the noninvasive-based models.

**Lumen diameter**

The median lumen diameter of the LAD arteries as assessed with invasive imaging was 2.4[2.0-3.1]mm and significantly larger than the lumen diameter as measured with coronary CTA (2.2[1.8-2.7]mm ( $p<0.001$ )). In the linear regression analysis, we found that also diameter as derived for both imaging methods are highly correlated with a significant correlation of 0.93 ( $p<0.001$ ). The high correlation trend remained very similar for the testing dataset.

**Table 2.** Median[IQR] values for hemodynamics calculated in the training and testing dataset based on invasive (IVUS/OCT) and noninvasive (CTA) imaging.

	Training Data			Testing Data		
	CTA Median [IQR]	OCT/IVUS Median [IQR]	p-value	CTA Median [IQR]	OCT/IVUS Median [IQR]	p-value
TAESS <sub>seg</sub> (dyne/cm <sup>2</sup> )	50.1 [25.8–90.1]	31.7 [19.3–62.4]	<0.001	30.1 [17.1–83.8]	15.8 [8.8–63.4]	<0.001
TAESS <sub>arc</sub> (dyne/cm <sup>2</sup> )	47.7 [24.1–90.0]	29.9 [18.1–62.4]	<0.001	29.4 [16.2–74.7]	15.0 [8.9–57.4]	<0.001
TAESS <sub>min</sub> (dyne/cm <sup>2</sup> )	16.2 [6.7–34.7]	10.3 [4.4–19.5]	0.006	13.4 [6.1–25.9]	6.0 [4.1–17.1]	<0.001
TAESS <sub>max</sub> (dyne/cm <sup>2</sup> )	90.3 [42.8–167.6]	55.3 [34.0–117.3]	0.007	51.8 [27.4–128.4]	25.6 [18.0–120.9]	<0.001
OSI <sub>seg</sub> (x10 <sup>-4</sup> )	6.3 [2.0–34.0]	1.1 [2.0–51.0]	0.15	8.5 [3.0–24.0]	23.0 [7.0–57.0]	<0.001
P <sub>seg</sub> (mmHg)	84.8 [52.5–100.5]	69.2 [43.1–87.6]	<0.001	96.3 [70.9–98.9]	78.8 [78.5–90.3]	<0.001
Diameter (mm)	2.2 [1.8–2.7]	2.4 [2.0–3.1]	<0.001	2.5 [1.9–3.0]	3.1 [2.2–3.6]	<0.001

**Discussion**

In this study a robust methodology was developed and validated to assess TAESS non-invasively using CTA. Therefore, TAESS as assessed with CTA was compared and validated against invasive imaging data from both clinically routine imaging as well as a dataset from a controlled clinical trial. With correct co-registration, accurate segmentation, adjusted boundary conditions as well as optimized smoothing of both imaging modalities, the methodology developed here demonstrates the ability to perform a detailed hemodynamic assessment based on non-invasive CTA. Although the absolute TAESS values were overestimated using CTA-based calculations, the observed patterns had a high concordance, which allows for providing non-invasively derived ESS information as a potential biomarker available for a new group of patients at high risk of plaque progression and future events.

There are a few studies that based ESS calculations solely on coronary CTA imaging with no comparison of invasive imaging. Lee et al<sup>9</sup> studied an adverse hemodynamic characteristic including FFRCT, ESS and axial plaque stress to assess the presence of adverse plaque characteristics resulting in future ACS. In Han

et al.<sup>28</sup> high categorical ESS was associated with adverse plaque characteristics independent of stenosis severity. However, in both of these studies, ESS was not studied in detail and was averaged over the length of the lesion discarding the heterogeneity of the local ESS over the stenosis.

Since CTA-based ESS calculations have shown a great potential to serve as a non-invasive method for risk prediction of ACS<sup>9,28</sup>, it is of crucial importance to have access to accurate TAESS measurements. Therefore, we aimed at developing a robust methodology to assess CTA-based TAESS and validated it against IVUS/OCT TAESS in human coronary arteries. A previous study performed by Bulant et al.<sup>32</sup> showed that the CFD models based on CTA estimated higher ESS compared to IVUS, similar to our observations. Although we showed a high correlation ( $r$ ) TAESS calculated between the two imaging modalities, this over estimation of TAESS based on non-invasive imaging is visualized more clearly in Bland-Altman plots (Figure 6) where the systematic bias of on  $\sim -20$  dyne/cm<sup>2</sup> can be observed on the mean differences in both training and testing patients as well as a proportional difference when a linear regression is performed with a slope of  $\sim -0.2$  to  $-0.3$  in the training and testing patients, respectively.

In our study, geometry difference is the main contributor to calculation of different TAESS values between the two geometries. One of the reasons for a higher estimation of TAESS in the CT-based models is the observed difference in measured diameters. CT-based diameters were smaller than invasive imaging and were undermeasured by 30%. Our data is consistent with previous studies that compared minimal lumen area where Collet et al.<sup>33</sup> and Veselka et al.<sup>34</sup> reported a 25 or 28% of undermeasurement of CTA lumen diameter as compared to IVUS imaging. In addition, in the FIGURE-OUT (Functional Imaging criteria for GUIding REview of invasive coronary angiOgraphy, intravascular Ultrasound, and coronary computed Tomographic angiography) trial, Doh et al.<sup>35</sup> showed a consistent underestimation of minimal luminal diameter and minimal luminal area based on coronary CTA compared to IVUS regardless of vessel size, lesion severity, lesion location, and the presence of calcification. This underestimation of luminal diameter is particularly clinically relevant when the severity of coronary artery disease in patients is assessed using different imaging modalities. Therefore, in our study when calculating the shear stress, this disagreement of luminal measurement becomes clinically relevant. Although lumen size has a major influence in determining TAESS values, it is not the only determinant factor. For example, the shape of the lumen is another important contributing factor. We assume that the cross-sections are circular, however, in some segments, due to the presence of disease, cardiac phase and the curvature of the artery, the lumen shape takes a different form and is not a perfect circular shape. As IVUS/OCT has a higher resolution in capturing these variations, the diameter can be measured accounting

for those changes while coronary CTA is not capable of capturing those details. Therefore, shear stress is highly dependent on local geometry such as curvature and presence of plaque resulting in a complex 3D flow structure where TAESS will have a different pattern as compared to a straight cylinder. A list of sources that contribute to the differences in 3D geometry reconstruction and therefore calculation of shear stress is discussed further in this section.

Although Bulant *et al.* compared TAESS based on non-invasive and invasive imaging, they did not study the local heterogeneity in ESS in great detail. Furthermore, they did not check the agreement between the two-imaging modality for categorizing TAESS. We showed detailed agreement of segment-averaged as well as arc-averaged between the two-imaging modality using standard coronary CTA and IVUS/OCT and showed that our methods can be robustly used in four additional patients. In addition, for clinical implication of CTA, we studied categories of low, medium and high ESS values and demonstrated that there is a high agreement between the relative TAESS values as well. Lastly, it should be mentioned that although our analysis was done for a 2mm segment which shows a more detailed comparison, we saw a very similar, slightly higher, correlation between the TAESS values for 3mm segments calculated in both the training and testing patients

We found a large range in absolute TAESS values in our study (Table 2). Compared to the reported values based on IVUS/OCT in our study were generally in the same range as other studies. For example in Stone et al.<sup>36</sup> values from the PREDICTION trial for the lowest and highest values of local ESS based on IVUS imaging were reported as  $6.1 \pm 3.4$  and  $60.2 \pm 2.9$  dyne/cm<sup>2</sup>. In another IVUS-based study, Samady et al.<sup>37</sup> reported values for TAESS with low categorical ESS as  $5.7 \pm 2.3$  dyne/cm<sup>2</sup> and high ESS as  $43.9 \pm 21.4$  dyne/cm<sup>2</sup>. Our results may have higher absolute TAESS values due to removal of side branches which are consistent with the observations in other studies, however the wide range in TAESS values did not allow us to conclude clear differences with other studies<sup>4,16,38</sup>. It should be noted that each patient-specific physiologic conditions are different from one another resulting in a variability of TAESS values. Therefore, to categorize the shear stress values, the thresholds were chosen based on each patient-specific range. However, we repeated the categorical analysis, this time with predefined thresholds based on previous studies<sup>6,39</sup> where low, medium and high categories were defined as TAESS  $< 10$ ,  $10 \leq \text{TAESS} < 25$  and TAESS  $\geq 25$  dynes/cm<sup>2</sup>, respectively, and found that low TAESS is categorized very accurately (75% in training and 100% testing patients) based on invasive vs. noninvasive imaging while medium and high categories are less accurately categorized (66% and 85%, respectively in training patients) compared to the patient-specific tertiles.



In the process of creating computational models using two approaches applying CTA and IVUS/OCT we have discovered a few issues that may introduce errors in anatomical model creation. The first and most important source of error was a mismatch in co-registration of images between modalities. For example, in gated IVUS images, there may be branches that are not visible on the gated views and this issue could cause a miscount and therefore mismatch of branches.

The second source of error was the imaging artifacts that influenced the lumen segmentation. As expected, the contrast between lumen and vessel wall was most clear in OCT images. However, the following imaging artifacts could influence our ability to segment the lumen properly: incomplete blood displacement/residual blood artifact- resulting in light attenuation, sew-up<sup>40</sup> artifacts resulting from rapid wire or vessel movement along one frame and misalignment of the lumen border. We also observed signal-poor regions at sites with oblique incidence of OCT beam with introduced an asymmetric oval cross-sectional area as opposed to a circular cross-section<sup>41</sup>. For IVUS, similar to OCT, sew-up artifacts may cause uncertainty in lumen border segmentation especially at locations with side branches. In coronary CTA, one of the major segmentation challenges were regions with calcium where the blooming effects artificially causes the lumen to look smaller. Therefore, we segmented the lumen to the best of our ability such that it represents the true lumen size.

The third source of error is the lower image resolution of CTA. This is especially important for distal segments where the lumen in some cases was not clearly visible. We followed the current clinical and research protocols to exclude the vessels that are <1.5 mm in diameter in distal segments<sup>8</sup>. Indeed, the minimum reported CTA-based lumen diameter in one of the distal segments was 1.53 mm.

### Study Limitations and Future Work

The underlying hypothesis of this work was that coronary CTA, although with 3-10 fold lower resolution than IVUS and OCT imaging can capture the local hemodynamics and detailed flow structures to estimate endothelial shear stress. We selectively included patients with high image quality and excluded patients with large amount of calcified plaques or previous stent placement in the CTA images. Including sub-optimal dataset would conclude a result where CTA may not perform as well as invasive imaging. A future study should be implemented including sub-optimal images to have a more comprehensive analysis of all types of CTA images. Although the time between the imaging acquisitions was up to 90 days, we assumed that the patient-specific cardiovascular hemodynamics and anatomy did not majorly change between the two imaging modalities acquisitions. Since IVUS/OCT are single vessel imaging modalities, our study included no side branches. In addition, this study includes only LAD arteries that contain

a high number of branches. Since side branches were majorly important in our methodology as landmarks to match the invasive with non-invasive imaging, a study including right coronary arteries with less side branches should be also implemented to ensure the results can be replicated for this vessel as well. We used a general input waveform and tailored it specific to each patient's cardiac output and heart rate which introduces a limitation to the patient-specific waveform effect in calculation of ESS. Previous studies based on invasive imaging have shown the association of ESS with future events as well as atherosclerosis progression<sup>5,6,42,43</sup>. With the results of this proof of concept study, we showed that non-invasive CTA based 3D models have similar ESS patterns compared to the golden standard of intravascular invasive imaging-based models. A future study or retrospective analysis of studies with serial coronary CTA scans should be conducted to assess the ability of coronary CTA CFD models in predicting plaque progression on CTA and the relationship with future events.

### Conclusion

In this methodology development study, we demonstrated that our CTA-based models can assess TAESS in great detail. These TAESS have a high correlation with TAESS derived from golden standard of IVUS/OCT based 3D reconstructions. Although CTA-based calculation over-estimated the absolute TAESS, the found patterns of relative TAESS were very similar to the ones based on invasive imaging. Therefore, CTA-based studies may be an alternative noninvasive imaging modality to capture the same relationship between ESS and plaque morphology as the invasive imaging-based calculations.

## References

- Benjamin EJ, Blaha MJ, Chiuve SE, Cushman M. Heart Disease and Stroke Statistics—2017 Update. vol. 135. 2017.
- Bech GJW, De Bruyne B, Pijls NHJ, De Muinck ED, Hoorntje JCA, Escaned J, et al. Fractional flow reserve to determine the appropriateness of angioplasty in moderate coronary stenosis: A randomized trial. *Circulation* 2001;103:2928–34.
- Parikh NI, Gona P, Larson MG, Fox CS, Vasan RS, Levy D. Long-Term Trends in Myocardial Infarction Incidence and Case- Fatality in the National Heart, Lung, and Blood Institute's Framingham Heart Study 2010;119:1203–10.
- Chatzizisis YS, Jonas M, Beigel R, Coskun AU, Baker AB, Stone B V., et al. Attenuation of inflammation and expansive remodeling by Valsartan alone or in combination with Simvastatin in high-risk coronary atherosclerotic plaques. *Atherosclerosis* 2009;203:387–94.
- Stone PH, Maehara A, Coskun AU, Maynard CC, Zaromytidou M, Siasos G, et al. Role of Low Endothelial Shear Stress and Plaque Characteristics in the Prediction of Nonculprit Major Adverse Cardiac Events: The PROSPECT Study. *JACC Cardiovasc Imaging* 2018;11:462–71.
- Costopoulos C, Timmins LH, Huang Y, Hung OY, Molony DS, Brown AJ, et al. Impact of combined plaque structural stress and wall shear stress on coronary plaque progression, regression, and changes in composition. *Eur Heart J* 2019;40:1411–22.
- Kumar A, Hung OY, Piccinelli M, Eshtehardi P, Corban MT, Sternheim D, et al. Low Coronary Wall Shear Stress Is Associated With Severe Endothelial Dysfunction in Patients With Nonobstructive Coronary Artery Disease. *JACC Cardiovasc Interv* 2018;11.
- Choi G, Lee JM, Kim HJ, Park JB, Sankaran S, Otake H, et al. Coronary artery axial plaque stress and its relationship with lesion geometry application of computational fluid dynamics to coronary CT angiography. *JACC Cardiovasc Imaging* 2015;8:1156–66.
- Lee JM, Choi G, Koo BK, Hwang D, Park J, Zhang J, et al. Identification of High-Risk Plaques Destined to Cause Acute Coronary Syndrome Using Coronary Computed Tomographic Angiography and Computational Fluid Dynamics. *JACC Cardiovasc Imaging* 2019;12:1032–43.
- Barbato E, Toth GG, Johnson NP, Pijls NHJ, Fearon WF, Tonino PAL, et al. A Prospective Natural History Study of Coronary Atherosclerosis Using Fractional Flow Reserve. *J Am Coll Cardiol* 2016;68:2247–55.
- Nakazato R, Park HB, Berman DS, Gransar H, Koo BK, Erglis A, et al. Noninvasive fractional flow reserve derived from computed tomography angiography for coronary lesions of intermediate stenosis severity results from the DeFACTO study. *Circ Cardiovasc Imaging* 2013;6:881–9.
- Lu MT, Ferencik M, Roberts RS, Lee KL, Ivanov A, Adami E, et al. Noninvasive FFR Derived From Coronary CT Angiography. Management and Outcomes in the PROMISE Trial. *JACC Cardiovasc Imaging* 2016.
- Updegrove A, Wilson NM, Merkow J, Lan H, Marsden AL, Shadden SC. SimVascular: An Open Source Pipeline for Cardiovascular Simulation. *Ann Biomed Eng* 2017;45:525–41.
- Tran JS, Schiavazzi DE, Kahn AM, Marsden AL. Uncertainty quantification of simulated biomechanical stimuli in coronary artery bypass grafts. *Comput Methods Appl Mech Eng* 2019;345:402–28.
- Chatzizisis YS, Jonas M, Coskun AU, Beigel R, Stone B V., Maynard C, et al. Prediction of the localization of high-risk coronary atherosclerotic plaques on the basis of low endothelial shear stress-an intravascular ultrasound and histopathology natural history study. *Circulation* 2008;117:993–1002.
- Stone PH, Coskun AU, Kinlay S, Clark ME, Sonka M, Wahle A, et al. Effect of Endothelial Shear Stress on the Progression of Coronary Artery Disease, Vascular Remodeling, and In-Stent Restenosis in Humans. *Circulation* 2003;108:438–44.
- Hoogendoorn A, Kok AM, Hartman EMJ, de Nisco G, Casadonte L, Chiastra C, et al. Multidirectional wall shear stress promotes advanced coronary plaque development: comparing five shear stress metrics. *Cardiovasc Res* 2020;116:1136–46.
- van der Giessen AG, Schaap M, Gijsen FJH, Groen HC, van Walsum T, Mollet NR, et al. 3D fusion of intravascular ultrasound and coronary computed tomography for in-vivo wall shear stress analysis: a feasibility study. *Int J Cardiovasc Imaging* 2010;26:781–96.
- Gijsen F, Katagiri Y, Barlis P, Bourantas C, Collet C, Coskun U, et al. Expert recommendations on the assessment of wall shear stress in human coronary arteries: existing methodologies, technical considerations, and clinical applications. *Eur Heart J* 2019;40:3421–33.
- Bernardini F, Mittleman J, Rushmeier H, Silva C, Tuabin G. The Ball-Pivoting Algorithm for Surface Reconstruction. *IEEE Trans Vis Comput Graph* 1999;5:349–59.
- Esmaily-Moghadam M, Bazilevs Y, Marsden AL. A new preconditioning technique for implicitly coupled multidomain simulations with applications to hemodynamics. *Comput Mech* 2013;52:1141–52.
- SA berger, W. Goldsmith E lewis. Introduction to bioengineering. 1996.
- Wilson NM, Ortiz AK, Johnson AB. The Vascular Model Repository: A Public Resource of Medical Imaging Data and Blood Flow Simulation Results. *J Med Device* 2013;7:040923.
- Burattini R, Sipkema P, van Huis GA, Westerhof N. Identification of canine coronary resistance and intramyocardial compliance on the basis of the waterfall model. *Ann Biomed Eng* 1985;13:385–404.
- Kim HJ, Vignon-Clementel IE, Coogan JS, Figueroa CA, Jansen KE, Taylor CA. Patient-specific modeling of blood flow and pressure in human coronary arteries. *Ann Biomed Eng* 2010;38:3195–209.
- Johnson K, Sharma P, Oshinski J. Coronary artery flow measurement using navigator echo gated phase contrast magnetic resonance velocity mapping at 3.0 T. *J Biomech Eng* 2008;41:595–602.
- Eslami P, Tran J, Jin Z, Karady J, Sotoodeh R, Lu MT, et al. Effect of Wall Elasticity on Hemodynamics and Wall Shear Stress in Patient-Specific Simulations in the Coronary Arteries. *J Biomech Eng* 2019.
- Han D, Starikov A, Hartaigh B, Gransar H, Kolli KK, Lee JH, et al. Relationship between endothelial wall shear stress and high-risk atherosclerotic plaque characteristics for identification of coronary lesions that cause ischemia: A direct comparison with fractional flow reserve. *J Am Heart Assoc* 2016;5:1–9.
- Vergallo R, Papafaklis MI, Yonetsu T, Bourantas C V., Andreou I, Wang Z, et al. Endothelial shear stress and coronary plaque characteristics in humans combined frequency-domain optical coherence tomography and computational fluid dynamics study. *Circ Cardiovasc Imaging* 2014;7:905–11.
- Bourantas C V., Räber L, Sakellarios A, Ueki Y, Zanchin T, Koskinas KC, et al. Utility of Multimodality Intravascular Imaging and the Local Hemodynamic Forces to Predict Atherosclerotic Disease Progression. *JACC Cardiovasc Imaging* 2020;13:1021–32.
- Holland PW, Welsh RE. Robust Regression Using Iteratively Reweighted Least-Squares. *Commun Stat Theory Methods* 1977;6:813–827.
- Bulant CA, Blanco PJ, Maso Talou GD, Bezerra CG, Lemos PA, Feijóo RA. A head-to-head comparison between CT- and IVUS-derived coronary blood flow models. *J Biomech* 2017;51:65–76.
- Collet C, Chevalier B, Cequier A, Fajadet J, Dominici M, Helqvist S, et al. Diagnostic Accuracy of Coronary CT Angiography for the Evaluation of Bioresorbable Vascular Scaffolds. *JACC Cardiovasc Imaging* 2018;11:722–32.
- Veselka J, Cadova P, Tomasov P, Theodor A, Zemanek D. Dual-source CT angiography for detection and quantification of in-stent restenosis in the left main coronary artery: Comparison with intracoronary ultrasound and coronary angiography. *J Invasive Cardiol* 2011;23:460–4.
- Doh J-H, Koo B-K, Nam C-W, Kim J-H, Min JK, Nakazato R, et al. Diagnostic value of coronary CT angiography in comparison with invasive coronary angiography and intravascular ultrasound in patients with intermediate coronary artery stenosis: results from the prospective multicentre FIGURE-OUT (Functional Imaging crite. *Eur Hear Journal Cardiovasc Imaging* 2014;15:870–7.
- Stone PH, Saito S, Takahashi S, Makita Y, Nakamura SS, Kawasaki T, et al. Prediction of progression of coronary artery disease and clinical outcomes using vascular profiling of endothelial shear stress and arterial plaque characteristics: the PREDICTION Study. *Circulation* 2012;126:172–81.
- Samady H, Eshtehardi P, McDaniel MC, Suo J, Dhawan SS, Maynard C, et al. Coronary artery wall shear stress is associated with progression and transformation of atherosclerotic plaque and arterial remodeling in patients with coronary artery disease. *Circulation* 2011;124:779–88.

38. Koskinas K, Chatzizisis YS, Papafaklis MI, Coskun AU, Baker AB, Jarolim P, et al. Synergistic Effect of Local Endothelial Shear Stress and Systemic Hypercholesterolemia on Coronary Atherosclerotic Plaque Progression and Composition in Pigs *Konstantinos* 2010;119:5124–36.
39. Kumar A, Thompson EW, Lefieux A, Molony DS, Davis EL, Chand N, et al. High Coronary Shear Stress in Patients With Coronary Artery Disease Predicts Myocardial Infarction. *J Am Coll Cardiol* 2018;72:1926–35.
40. Bezerra HG, Costa MA, Guagliumi G, Rollins AM, Simon DI. Intracoronary Optical Coherence Tomography: A Comprehensive Review: Clinical and Research Applications. *JACC Cardiovasc Interv* 2009;2:1035–1046.
41. van Soest G, Regar E, Goderie TPM, Gonzalo N, Koljenović S, van Leenders GJLH, et al. Pitfalls in plaque characterization by OCT: image artifacts in native coronary arteries. *JACC Cardiovasc Imaging* 2011;4:810–3.
42. Papafaklis MI, Takahashi S, Antoniadis AP, Coskun AU, Tsuda M, Mizuno S, et al. Effect of the local hemodynamic environment on the de novo development and progression of eccentric coronary atherosclerosis in humans: Insights from PREDICTION. *Atherosclerosis* 2015;240:205–11.
43. Eshtehardi P, McDaniel MC, Suo J, Dhawan SS, Timmins LH, Binongo JNG, et al. Association of Coronary Wall Shear Stress With Atherosclerotic Plaque Burden, Composition, and Distribution in Patients With Coronary Artery Disease. *J Am Heart Assoc* 2012;1:e002543–e002543.



# 8

## Comparison of swine and human computational hemodynamics models for the study of coronary atherosclerosis.

This chapter based on:

Comparison of swine and human computational hemodynamics models for the study of coronary atherosclerosis

Giuseppe De Nisco, Claudio Chiastra, Eline M.J. Hartman, Ayla Hoogendoorn, Joost Daemen, Karol Calò, Diego Gallo, Umberto Morbiducci, Jolanda J. Wentzel

*Frontiers in Bioengineering and Biotechnology, 2021*

## Abstract

Coronary atherosclerosis is a leading cause of illness and death in Western World and its mechanisms are still not completely understood. Several animal models have been used to 1) study coronary atherosclerosis natural history and 2) propose predictive tools for this disease, that is asymptomatic for a long time, aiming for a direct translation of their findings to human coronary arteries. Among them, swine models are largely used due to the observed anatomical and pathophysiological similarities to humans. However, a direct comparison between swine and human models in terms of coronary hemodynamics, known to influence atherosclerotic onset/development, is still lacking. In this context, we performed a detailed comparative analysis between swine- and human-specific computational hemodynamic models of coronary arteries. The analysis involved several near-wall and intravascular flow descriptors, previously emerged as markers of coronary atherosclerosis initiation/progression, as well as anatomical features.

To do that, non-culprit coronary arteries (18 right – RCA, 18 left anterior descending – LAD, 13 left circumflex – LCX coronary artery) from patients presenting with acute coronary syndrome were imaged by intravascular ultrasound and coronary computed tomography angiography. Similarly, the three main coronary arteries of ten adult mini-pigs were also imaged (10 RCA, 10 LAD, 10 LCX). The geometries of the imaged coronary arteries were reconstructed (49 human, 30 swine), and computational fluid dynamic simulations were performed by imposing individualized boundary conditions.

Overall, no relevant differences in 1) wall shear stress-based quantities, 2) intravascular hemodynamics (in terms of helical flow features), and 3) anatomical features emerged between human- and swine-specific models.

The findings of this study strongly support the use of swine-specific computational models to study and characterize the hemodynamic features linked to coronary atherosclerosis, sustaining the reliability of their translation to human vascular disease.

## Introduction

Coronary atherosclerosis is a major cause of morbidity and mortality in Western World<sup>1</sup>, consisting of the build-up of an atherosclerotic plaque in the wall of coronary arteries, possibly leading to severe stenosis and/or thrombus formation, with vascular lumen occlusion and death<sup>2</sup>.

The natural history of the coronary atherosclerotic disease is driven by a complex interplay of several local biological, systemic and biomechanical factors, with a still uncomplete understanding of the underlying mechanisms<sup>3-7</sup>. Although several large *in vivo* human studies have provided valuable insights into the initiation and progression of coronary atherosclerosis<sup>8,9</sup>, these studies remain often limited to short durations and limited number of imaging moments, mainly due to ethical reasons<sup>10</sup>. Therefore, they lack the time scales necessary for the development of this pathology and might not capture all phenomena present during this complex, multifactorial disease<sup>11</sup>. Such limitations may affect the *in vivo* investigation of innovative clinical strategies for coronary atherosclerotic treatment in humans<sup>10-12</sup>.

Animal models of coronary atherosclerosis have the potential to overcome many of these inherent restrictions of human studies<sup>10-12</sup>, facilitating the analysis of the coronary atherosclerotic disease at different stages<sup>11</sup>. For this reason, several large animal models based on the use of rabbits, pigs, or non-human primates, have been adopted to e.g.: (1) study coronary atherosclerosis natural history<sup>11,13</sup>; (2) evaluate the efficacy of clinical treatment procedures<sup>14</sup>; (3) identify predictive tools for the evolution of the disease, which most of the time is asymptomatic<sup>15-17</sup>. Most of the animal model-based studies on atherosclerosis onset and progression imply that their findings reliably inform human studies, sometimes suggesting a direct translation to humans. However, the value of animal models in identifying hemodynamic factors involved in the atherosclerotic disease or in predicting the effectiveness of treatment strategies in clinical trials has remained not fully clarified.

In relation to coronary atherosclerotic disease, the capability of an animal model to mimic the complexity of the human coronary pathophysiology plays a critical role<sup>11,14</sup>. In this regard, due to their similarities to humans in terms of anatomy (i.e., size and distribution)<sup>18,19</sup>, pathophysiology<sup>19,20</sup>, lipoprotein profile<sup>21</sup>, and site of lesion formation<sup>20</sup>, swine models are massively applied to study coronary atherosclerosis<sup>11,12</sup>. In particular, swine models of familial hypercholesterolemia with a mutation in genes coding for apolipoproteins and low-density lipoproteins receptor allows studying sustained atherosclerotic plaques onset/progression because of their capability to develop advanced atherosclerotic lesions within 12-18 months when fed a high fat diet<sup>11,22</sup>.



Besides the already investigated differences/similarities between human and swine models, a direct comparison in terms of coronary hemodynamics, a well-established biomechanical factor influencing atherosclerotic onset/development<sup>4,7</sup>, is still lacking. This may limit the translation to human models of previous findings suggesting the role of near-wall and intravascular hemodynamic descriptors as markers of coronary atherosclerosis initiation/progression in swine-specific models<sup>15,16,23,24</sup>

Aiming to bridge this gap of knowledge, in this study we perform, for the first time, a detailed comparative analysis between swine- and human-specific computational hemodynamic models of the three main coronary arteries, in terms of several descriptors of (1) near wall and (2) intravascular flow quantities, and (3) vessel morphology, that have been already identified as biomechanical risk factors in the initiation/progression of coronary atherosclerotic plaques<sup>7,8</sup>.

Materials and Methods

Human population

Forty-eight hemodynamically stable patients from the IMPACT study data set<sup>25</sup> were involved in the analysis. Clinical characteristics are listed in Table 1. The IMPACT study enrolled patients with acute coronary syndrome and with at least one non-stented non-culprit coronary segment accessible for intracoronary imaging study. The presence of previous coronary artery bypass graft surgery, 3-vessel disease, renal insufficiency (creatinine clearing < 50 ml/min), left ventricular ejection fraction < 30%, and atrial fibrillation, were considered as exclusion criteria. All patients underwent percutaneous coronary intervention of the culprit coronary vessel. After successful treatment, a non-culprit coronary segment (right – RCA, left anterior descending – LAD, or left circumflex – LCX coronary artery) was imaged and used for the study.

All patients gave their informed consent. The study was approved by the local medical ethical committee of the Erasmus MC (MEC 2015-535, NL54519.078.15), was registered (ISCRTN:43170100) and conducted in accordance with the World Medical Association Declaration of Helsinki (64<sup>th</sup> WMA General Assembly, Fortaleza, Brazil, October 2013) and Medical Research Involving Human Subject Act (WMO).

Animal model

Ten adult familial hypercholesterolemia Bretoncelles Meishan mini-pigs with a low-density lipoprotein receptor mutation were enrolled in the analysis. The study involved the three main coronary arteries (i.e., RCA, LAD, and LCX) of each

animal at 3 months after the start of a high fat diet. At this stage, the animals were considered ostensibly healthy.

Table 1. Baseline characteristics.

Clinical characteristics	N = 48 patients
Age (years)	61.3 ± 9
Men (%)	43 (90%)
Body mass index	27.0± 4.5
Diabetes mellitus, n (%)	8 (17%)
Hypertension, n (%)	14 (29%)
Dyslipidemia, n (%)	23 (48%)
Smokers, n (%)	36 (75%)
Positive family history, n (%)	19 (40%)
Previous MI, n (%)	9 (19%)
Previous PCI, n (%)	11 (23%)
LDL (mmol/L)	2.84±1.02

MI: myocardial infarction; PCI: percutaneous coronary intervention; LDL: low-density lipoproteins.

The study was approved by the local animal ethics committee of the Erasmus MC (EMC nr. 109-14-10) and performed according to the National Institute of Health guide for the Care and Use of Laboratory animals<sup>26</sup>.

Medical Imaging and geometry reconstruction

An overview of the methods is provided in Figure 1. The same imaging protocol was applied to human- and swine-specific coronary segments. Each coronary artery was imaged by computed coronary tomography angiography (CCTA) (SOMATOM Force, Siemens Healthineers, Germany) and intravascular ultrasound (IVUS) (InfraRedX, Burlington, MA, USA), as detailed elsewhere<sup>15,16,23,25</sup>. Coronary lumen contours were segmented on IVUS images (QCU-CMS, Medis Medical Imaging, Leiden) and aligned along the 3D CCTA centerline in order to reconstruct the 3D vessel geometry. Additional luminal regions proximally (up to the aorta) and at least two diameters distally to the IVUS-imaged segment were reconstructed using CCTA images<sup>15,16,23,25</sup>. The 79 reconstructed luminal surfaces of the coronary arteries (49 human-specific models: 18 RCA, 18 LAD, and 13 LCX; 30 swine-specific models: 10 RCA, 10 LAD, and 10 LCX) are presented in Figure 2 and Figure 3 for humans and animal models, respectively. The 3D geometries were reconstructed including the side branches.

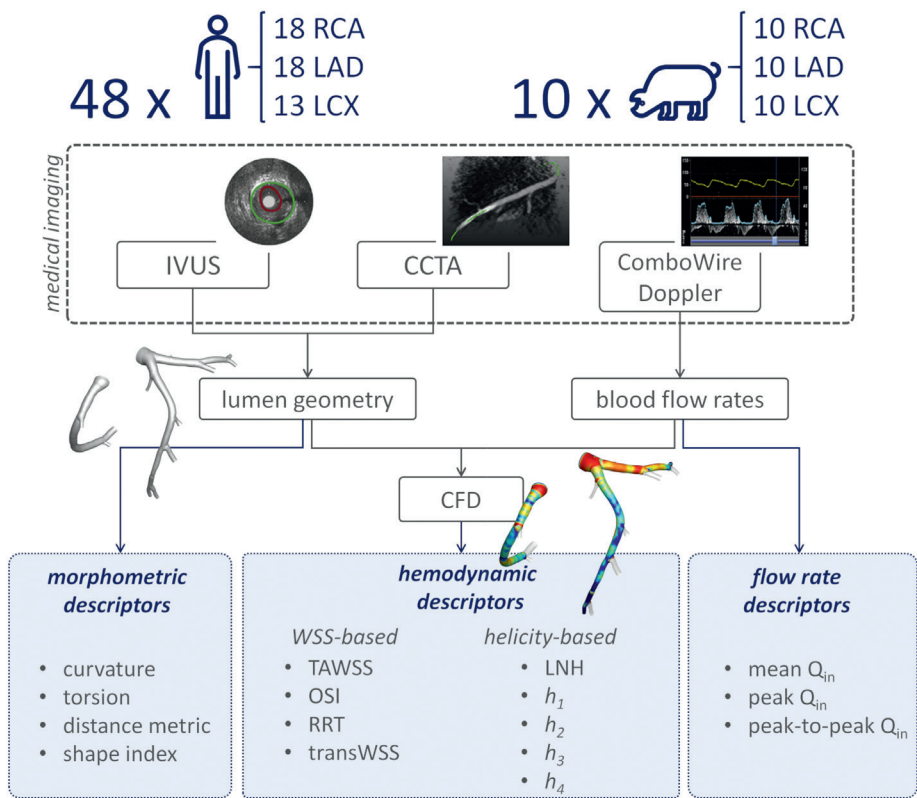


**Figure 1. Schematic diagram of the study design, showing how imaging data contribute to define vessel geometry and hemodynamic, morphometric, and flow variables.**  
RCA, LAD, and LCX denote right, left anterior descending, and left circumflex coronary artery, respectively. IVUS: intravascular ultrasound; CCTA: coronary computed tomography angiography; CFD: computational fluid dynamics; TAWSS: time-averaged wall shear stress; OSI: oscillatory shear index; RRT: relative residence time; transWSS: transverse wall shear stress; LNH: local normalized helicity;  $h_1$ : average helicity;  $h_2$ : average helicity intensity;  $h_3$ : signed balance of counter rotating helical flow structures;  $h_4$ : unsigned balance of counter rotating helical flow structures;  $Q_{in}$ : inflow rate.

Combwire Doppler (Phillips Volcano, Zaventem, Belgium) flow velocity measurements were acquired in each coronary artery at the inflow section and immediately upstream and downstream of each side branch, as extensively detailed elsewhere<sup>15,16,23,25</sup>.

### Computational hemodynamics

The reconstructed vessel geometries were discretized, and unsteady-state computational fluid dynamics (CFD) simulations were performed to characterize coronary hemodynamics (Figure 1).

The governing equations of fluid motion were numerically solved in Fluent environment (ANSYS Inc., Canonsburg, PA, USA), by using the finite volume method. All the CFD settings are extensively detailed elsewhere<sup>15,16,23,25</sup>. Briefly, blood was assumed as an incompressible, homogeneous, non-Newtonian fluid<sup>27</sup>. No-slip condition was assumed at the arterial wall. *In vivo* ComboWire Doppler velocity measurements were used to derive individualized (specific for each

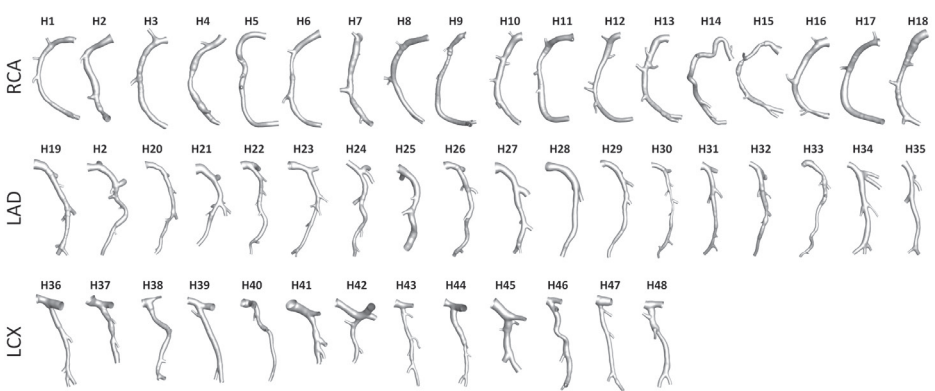


**Figure 2. Geometry of the 49 human coronary artery models.**  
Labels from H1 to H48 identify the single patients. Right (RCA), left anterior descending (LAD) and left circumflex (LCX) coronary artery geometries are grouped.

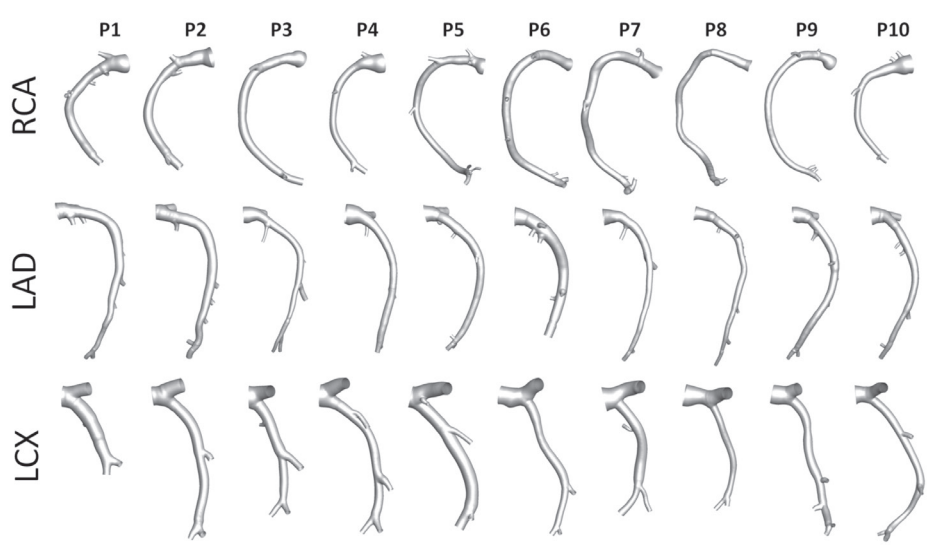


**Figure 3. Geometry of the 30 swine coronary artery models.**  
Labels from P1 to P10 identify the single pig. Right (RCA), left anterior descending (LAD) and left circumflex (LCX) coronary artery geometries are grouped.

human and swine model, as reported elsewhere<sup>15,16,23,25</sup>) boundary conditions (BCs) as follows: (1) the inlet flow rate was estimated from the most proximal Doppler velocity measurement, and prescribed as inlet boundary condition in terms of time-dependent flat velocity profile; (2) side branches perfusion was quantified as the difference between upstream and downstream Doppler velocity-based flow rate measurements and applied as outflow condition in terms of measured flow ratio. If velocity-based flow measurements were inaccurate or not available, a generalized flow rate<sup>28</sup> was prescribed as inflow BC, while a proper diameter-based scaling law for human<sup>28</sup> and swine-specific<sup>29</sup> models was applied to estimate the flow ratio at the outflow section<sup>15,16,23,25</sup>.

### Hemodynamic descriptors

Near-wall and intravascular hemodynamics was analyzed by computing the hemodynamic quantities listed in Table 2.

Near-wall hemodynamics was characterized in terms of the three canonical WSS-based descriptors, namely time-averaged wall shear stress (TAWSS), oscillatory shear index (OSI)<sup>30</sup>, and relative residence time (RRT)<sup>31</sup>. Additionally, the transversal WSS (transWSS)<sup>32</sup>, a descriptor of WSS multidirectionality, was also considered. The transWSS represents the average WSS component acting orthogonal to the time-average WSS vector direction (Table 2).

Based on the recently emerged atheroprotective role of physiological helical-shaped blood flow structures in coronary arteries<sup>15,23</sup>, intravascular hemodynamics was investigated in terms of helical flow, quantified through the quantities summarized in Table 2. In detail, the local normalized helicity (LNH)<sup>33</sup>, representing the cosine of the angle between local velocity ( $\mathbf{v}$ ) and vorticity ( $\boldsymbol{\omega}$ ) vectors (Table 2), was used to visualize right- and left-handed helical blood flow patterns (positive and negative LNH values, respectively)<sup>34,35</sup> inside the coronary artery models. Furthermore, four additional helicity-based descriptors<sup>34,35</sup> were applied to characterize the strength, size and relative rotational direction of helical flow in the 79 coronary artery models (Table 2): cycle-average helicity ( $h_1$ ) and helicity intensity ( $h_2$ ), indicating the net amount and the intensity of helical flow, respectively; signed ( $h_3$ ) and unsigned helical rotation balance ( $h_4$ ), measuring the prevalence (identified by the sign of descriptor  $h_3$ ) or only the strength of relative rotations of helical flow patterns, respectively.

The hemodynamics of each coronary vessel was characterized also in terms of inflow rate ( $Q_{in}$ ), as given by its mean, peak, and peak-to-peak values (Figure 1). Peak-to-peak  $Q_{in}$  was defined as the difference between the maximum and the minimum values of the inflow rate.

**Table 2. Definition of hemodynamic descriptors involved in the analysis.**

WSS-based descriptors	
Time-Averaged WSS (TAWSS)	$TAWSS = \frac{1}{T} \int_0^T  \mathbf{WSS}  dt$
Oscillatory Shear Index (OSI)	$OSI = 0.5 \left[ 1 - \frac{\left  \int_0^T \mathbf{WSS} dt \right }{\int_0^T  \mathbf{WSS}  dt} \right]$
Relative Residence Time (RRT)	$RRT = \frac{1}{TAWSS \cdot (1 - 2 \cdot OSI)} = \frac{1}{\frac{1}{T} \left  \int_0^T \mathbf{WSS} dt \right }$
Transverse WSS (transWSS)	$transWSS = \frac{1}{T} \int_0^T \left  \mathbf{WSS} \cdot \left( \mathbf{n} \times \frac{\int_0^T \mathbf{WSS} dt}{\left  \int_0^T \mathbf{WSS} dt \right } \right) \right  dt$
Helicity-based descriptors	
Local Normalized Helicity (LNH)	$LNH = \frac{\mathbf{v} \cdot \boldsymbol{\omega}}{ \mathbf{v}  \cdot  \boldsymbol{\omega} } = \cos \gamma$
Average helicity ( $h_1$ )	$h_1 = \frac{1}{TV} \int \int \mathbf{v} \cdot \boldsymbol{\omega} dV dt$
Average helicity intensity ( $h_2$ )	$h_2 = \frac{1}{TV} \int \int  \mathbf{v} \cdot \boldsymbol{\omega}  dV dt$
Signed balance of counter-rotating helical flow structures ( $h_3$ )	$h_3 = \frac{h_1}{h_2} \quad -1 \leq h_3 \leq 1$
Unsigned balance of counter-rotating helical flow structures ( $h_4$ )	$h_4 = \frac{ h_1 }{h_2} \quad 0 \leq h_4 \leq 1$

**WSS** is the WSS vector;  $T$  is the period of the cardiac cycle;  $\mathbf{n}$  is the unit vector normal to the arterial surface at each element;  $\mathbf{v}$  is the velocity vector;  $\boldsymbol{\omega}$  is the vorticity vector;  $\gamma$  is the angle between velocity and vorticity vectors;  $V$  is the arterial volume.

### Morphometry

The geometric quantities summarized in Table 3 were adopted for characterizing coronary vessel morphometry. In detail, a robust centerline-based analysis was performed, where vessel curvature ( $\kappa$ ) and torsion ( $\tau$ ) were assessed according to an approach proposed elsewhere<sup>36</sup>. Briefly, after extracting the main vessel

centerline (defined as the geometrical locus of the centers of maximum inscribed spheres) in the Vascular Modeling Toolkit (VMTK, Orobix, Bergamo, Italy) environment, its continuous, noise free analytical formulation ( $C$ ) was obtained by adopting free-knots regression splines<sup>37</sup>. Coronary curvature and torsion were then calculated by differentiation of the free-knots regression, spline centerline representation (Table 3). Here the average values of curvature ( $\bar{\kappa}$ ) and torsion ( $\bar{\tau}$ ) along the main vessel were considered, which are known to have an influence on arterial hemodynamics<sup>36</sup>. Additionally, the degree of tortuosity of coronary vessels was assessed by computing the standard Distance Metric index (DM, Table 3)<sup>38,39</sup>. DM, computed as the ratio between the curvilinear ( $L$ ) and Euclidean ( $l$ ) distance between the centerline curve endpoints (Figure 4a), quantifies the “lengthening effect” of coronary tortuosity.

Finally, coronary cross-section eccentricity along the main vessel centerline was measured by computing the Shape Index (SI), as the ratio between the local cross-section minimum ( $d$ ) and the maximum ( $D$ ) diameter<sup>40</sup>. To calculate the SI, the opensource Vascular Modelling Toolkit software (VMTK, Orobix, Bergamo, Italy) was used. SI ranges between 0 and 1, where 1 indicates a perfectly circular cross-sectional shape (Figure 4b). As for  $\kappa$  and  $\tau$ , the average value of Shape Index ( $\bar{SI}$ ) along the main vessel was considered for the analysis.

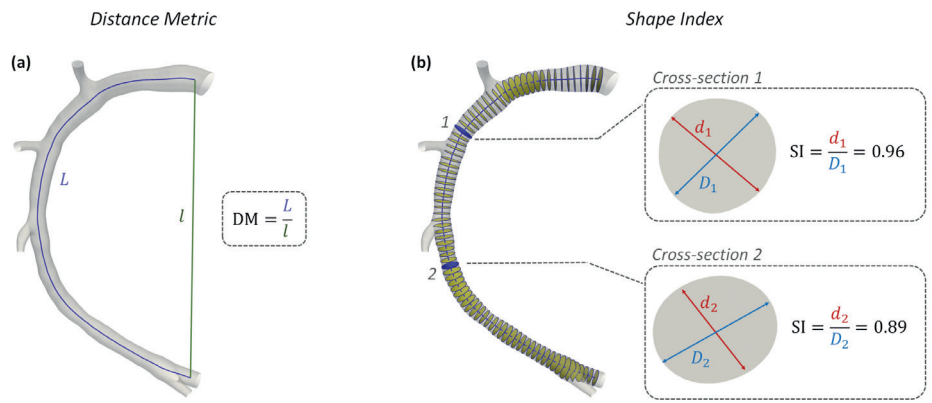


**Figure 4. Methodology of Distance Metric (DM) and Shape Index (SI) assessment.** Model H1 was taken as explanatory example. **A:** DM computing:  $L$  and  $l$  are the curvilinear (blue) and Euclidean (green) distance between the centerline curve endpoints; **B:** SI computing at 2 explanatory coronary cross-sections along the vessel centerline:  $d$  and  $D$  are the minimum and maximum diameter of arterial cross-section, respectively.

**Table 3. Definition of the geometric quantities adopted for characterizing coronary vessels morphometry.**

Morphometric descriptors	
Curvature ( $\kappa$ )	$\kappa(s) = \frac{ \mathbf{C}'(s) \times \mathbf{C}''(s) }{ \mathbf{C}'(s) ^3}$
Torsion ( $\tau$ )	$\tau(s) = \frac{[\mathbf{C}'(s) \times \mathbf{C}''(s)] \cdot \mathbf{C}'''(s)}{ \mathbf{C}'(s) \times \mathbf{C}''(s) ^2}$
Distance Metric (DM)	$DM = \frac{L}{l} \quad DM \geq 1$
Shape Index (SI)	$SI(s) = \frac{d(s)}{D(s)} \quad 0 \leq SI \leq 1$

$\mathbf{C}'$ ,  $\mathbf{C}''$ , and  $\mathbf{C}'''$  are the first, second, and third derivative of the centerline curve  $\mathbf{C}$ , respectively;  $s$  is the curvilinear abscissa;  $L$  and  $l$  are the curvilinear and Euclidean distance between the centerline curve endpoints, respectively;  $d$  and  $D$  are the minimum and maximum diameter of arterial cross-section, respectively.

Statistical analysis

Data analysis was performed in the main branch of the RCA, LAD and LCX segments only, by removing coronary side branches in the post-processing step using VMTK. Hemodynamic and morphometric data were grouped according to the population (humans vs. animals) and the coronary vessel type (i.e., RCA, LAD, or LCX). Differences between the two populations were investigated in Matlab environment (MathWorks Inc., USA) by the Mann-Whitney U-test. Statistical significance was assumed for  $p < 0.05$ .

Results

Near-wall and intravascular flow features visualization

Helical blood flow patterns developing in human and swine coronary models were visualized in Figure 5 and Figure 6, respectively, using the cycle-average LNH isosurface values (blue and red colors indicate left-handed and right-handed helical flow patterns, respectively). Despite intra- and inter-species variations, the intravascular hemodynamics of both human and swine coronary arteries were markedly characterized by the presence of two distinguishable counter-rotating helical flow patterns.

Intra- and inter-species differences were analyzed by visual inspection also in terms of TAWSS luminal distribution, presented in Figure 7 and Figure 8 for human and swine models, respectively. In detail, the luminal surface of some of the human coronary arteries were largely exposed to low TAWSS values (red color in figure, e.g., cases H2-RCA, H21-LAD, and H38-LCX), whereas other human arteries were not (e.g., cases H5-RCA, H28-LAD, and H39-LCX).



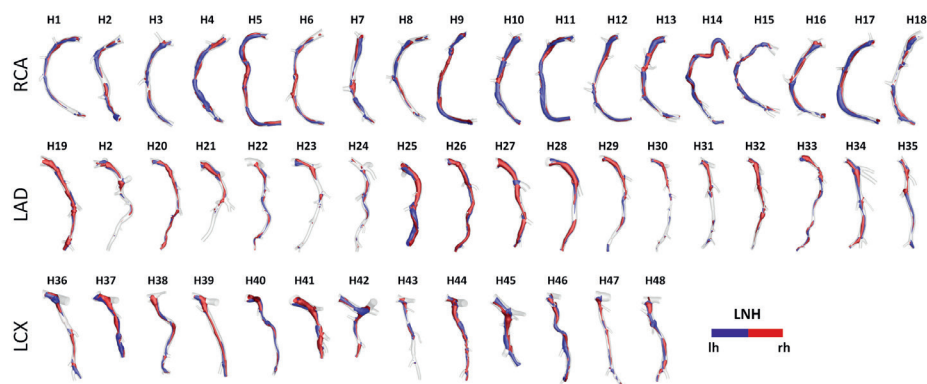


**Figure 5. Intravascular fluid structures in the 49 human coronary arteries.** For each case, isosurfaces of cycle-average LNH are presented. Distinguishable left-handed (lh -  $LNH < 0$ ) and right-handed (rh -  $LNH > 0$ ) helical flow structures can be observed in all coronary arteries. Labels from H1 to H48 identify the single patient. Right (RCA), left anterior descending (LAD), and left circumflex (LCX) coronary artery geometries are grouped.

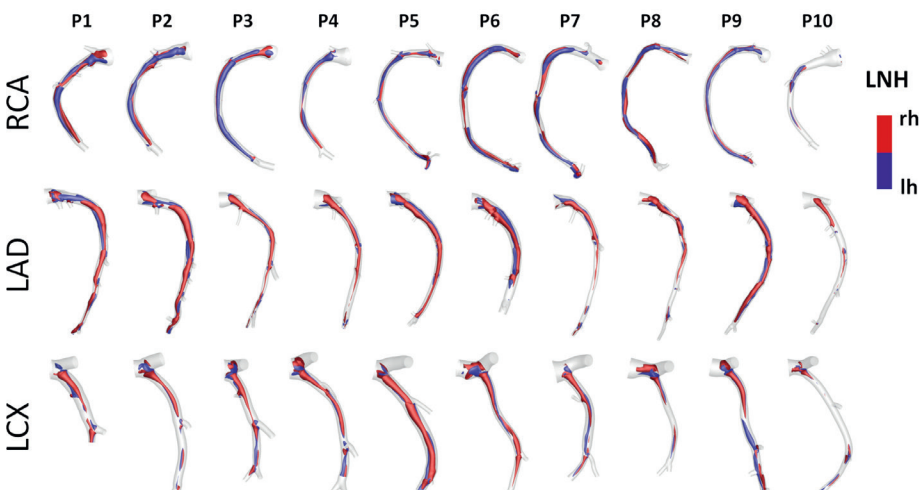


**Figure 6. Intravascular fluid structures in the 30 swine coronary arteries.** For each case, isosurfaces of cycle-average LNH are presented. Distinguishable left-handed (lh -  $LNH < 0$ ) and right-handed (rh -  $LNH > 0$ ) helical flow structures can be observed in all coronary arteries. Labels from P1 to P10 identify the single pig. Right (RCA), left anterior descending (LAD), and left circumflex (LCX) coronary artery geometries are grouped.

The same observations on intra-species variability can be extended to swine models also (Figure 8), with some individual cases exposed to low TAWSS values over most of the luminal surface (e.g., cases P5-RCA, P10-LAD, and P7-LCX) and other ones presenting with low TAWSS luminal regions of moderate extension (e.g., cases P8-RCA, P9-LAD, and P4-LCX).

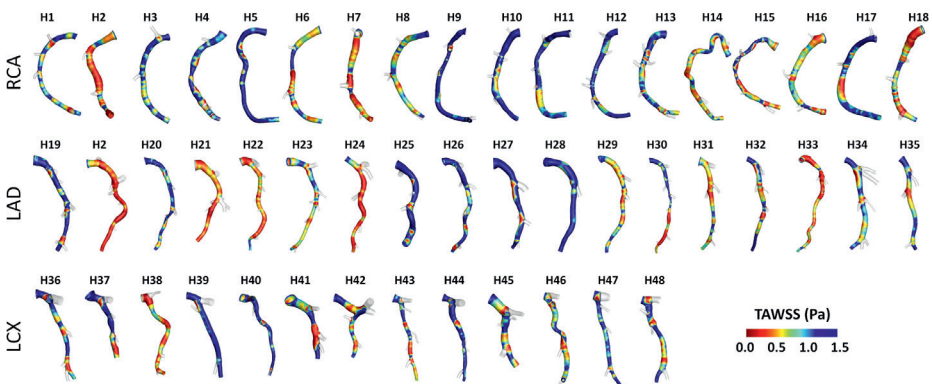


**Figure 7. TAWSS distribution at the luminal surface of the 49 human coronary arteries.** Red color highlights luminal regions exposed to low TAWSS values. Labels from H1 to H48 identify the single patient. Right (RCA), left anterior descending (LAD), and left circumflex (LCX) coronary artery geometries are grouped.

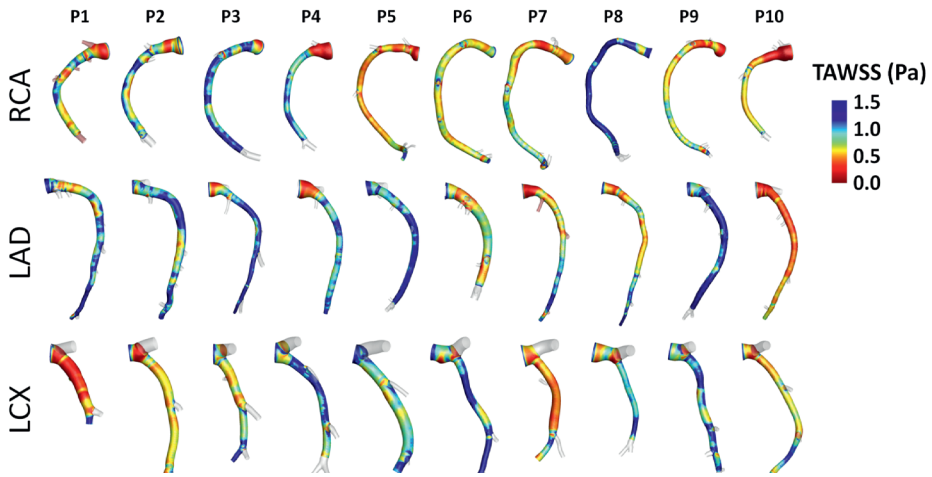


**Figure 8. TAWSS distribution at the luminal surface of the 30 swine coronary arteries.** Red color highlights luminal regions exposed to low TAWSS values. Labels from P1 to P10 identify the single pig. Right (RCA), left anterior descending (LAD), and left circumflex (LCX) coronary artery geometries are grouped.

### Hemodynamics: quantitative analysis

A detailed quantitative comparison between human and swine models is presented in Figure 9 in terms of hemodynamics and morphometry. Human and swine models were grouped per species and per coronary vessel. Among the WSS-based descriptors, no significant difference emerged between the two species (WSS column in Figure 9) in terms of TAWSS (confirming the qualitative results



presented in Figures 7 and 8), RRT, and transWSS. Contrarily, a significant inter-species difference emerged for OSI but only for the LADs ( $p<0.001$ ), with swine LADs characterized by higher median value and larger interquartile range than human LADs (0.0005 [0.0004, 0.0007] and 0.0023 [0.0013, 0.0057] for human and swine models, respectively). Interestingly, an overall poor WSS multidirectionality emerged in both species, with OSI values lower than 0.08 (0.0005 [0.0003, 0.0009] and 0.0009 [0.0006, 0.0022] for human and swine models, respectively), and transWSS values lower than 0.10 Pa (0.03 [0.02, 0.05] and 0.03 [0.02, 0.04] Pa for human and swine models, respectively).

The quantitative analysis of the intravascular flow patterns, based on helicity-based descriptors (*Helicity* column in Figure 9), highlighted a significant inter-species difference for helical flow intensity in RCA ( $p<0.05$ ) and LCX ( $p<0.01$ ). In detail, human RCA and LCX vessels (2.53 [0.83, 3.76] and 2.33 [1.73, 4.63]  $\text{m/s}^2$  for human RCA and LCX, respectively) exhibited higher  $h_2$  values compared to the respective swine vessels (0.71 [0.35, 1.33] and 0.46 [0.20, 1.40]  $\text{m/s}^2$  for swine RCA and LCX, respectively), and larger intra-species variability. Of note, no significant inter-species difference emerged for topological quantities  $h_3$  and  $h_4$ , suggesting an overall similar configuration of the counter-rotating helical flow patterns developing in human and swine coronary arteries, presented in Figures 5 and 6.

The analysis of the hemodynamics is completed by the *Flow* column in Figure 9. Overall, human and swine coronary vessels were characterized by similar mean, peak, and peak-to-peak values of measured inflow rate, except for the LAD, where swine models presented significantly higher  $Q_{in}$  maximum values ( $2.52 \cdot 10^{-5}$  [ $1.95 \cdot 10^{-5}$ ,  $3.87 \cdot 10^{-5}$ ] and  $5.20 \cdot 10^{-5}$  [ $3.36 \cdot 10^{-5}$ ,  $7.95 \cdot 10^{-5}$ ]  $\text{m}^3/\text{s}$  for human and swine models, respectively;  $p<0.05$ ) and larger dynamics ( $1.86 \cdot 10^{-6}$  [ $1.48 \cdot 10^{-6}$ ,  $3.09 \cdot 10^{-6}$ ] and  $4.97 \cdot 10^{-6}$  [ $3.01 \cdot 10^{-6}$ ,  $7.09 \cdot 10^{-6}$ ]  $\text{m}^3/\text{s}$  for human and swine models, respectively;  $p<0.01$ ) than human models.

### Morphometry: quantitative analysis

No significant inter-species difference emerged in vessel curvature, torsion, and tortuosity (*Morphometry* column in Figure 9). In both populations, RCA models were characterized by higher DM values and larger intra-species variability, compared to LAD and LCX vessels. Conversely, a significant inter-species difference emerged in coronary vessels eccentricity, as measured by the shape index ( $p<0.01$ ). In detail, the cross-section of human coronary arteries presented with a more elliptical shape than swine arteries (Figure 4b and Figure 9), as highlighted by the lower ( $\bar{S}_I$ ) values.

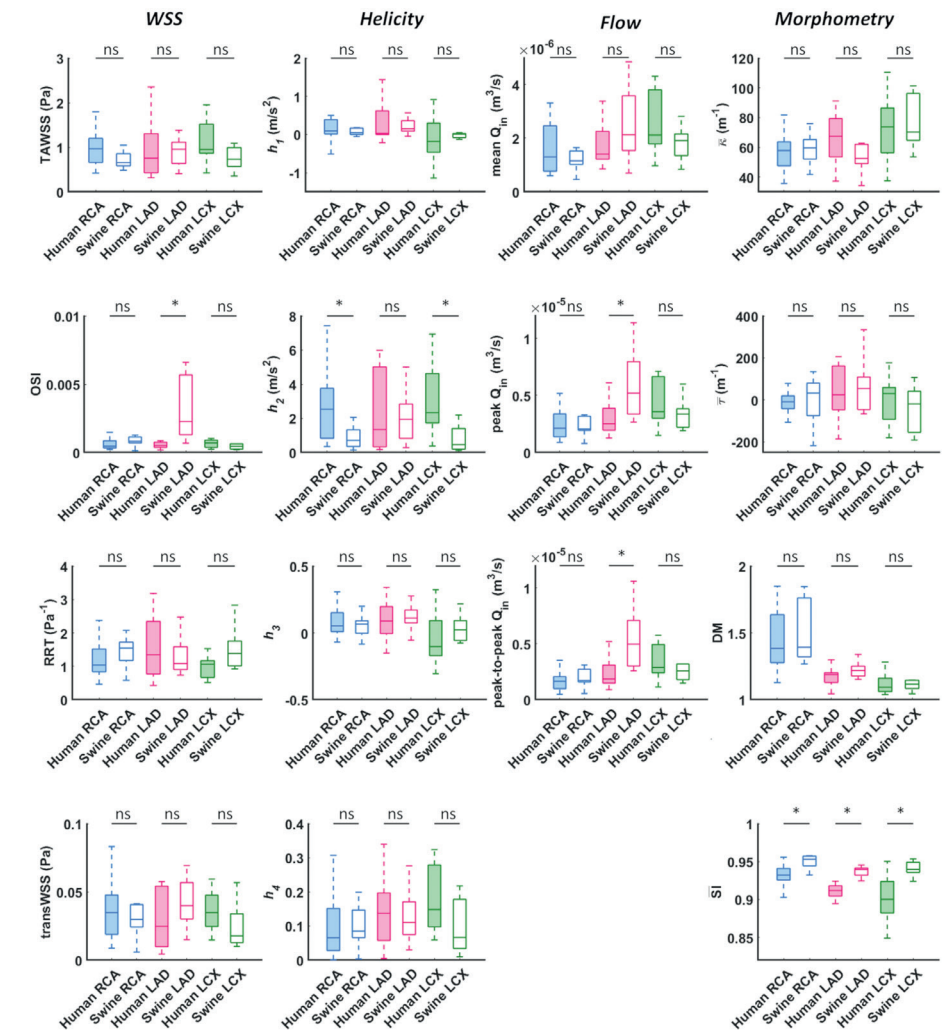


**Figure 9.** Box plot comparing WSS, helicity, flow rate, and morphometry in human and swine coronary arteries.

For each population, right (RCA), left anterior descending (LAD), and left circumflex (LCX) coronary artery geometries are grouped and distinguished by box color (blue, magenta, and green, respectively). WSS column: TAWSS - time-average wall shear stress, OSI - oscillatory shear index, RRT - relative residence time, transWSS - transverse wall shear stress; *Helicity* column:  $h_1$  - average helicity,  $h_2$  - average helicity intensity,  $h_3$  - signed balance of counter rotating helical flow structures,  $h_4$  - unsigned balance of counter rotating helical flow structures; *Flow* column:  $Q_{in}$  - inflow rate; *Morphometry* column:  $\kappa$  - curvature,  $\tau$  - torsion, DM - distance metric, SI - similarity index. Median and interquartile range are displayed for each descriptor. \*  $p<0.05$ .

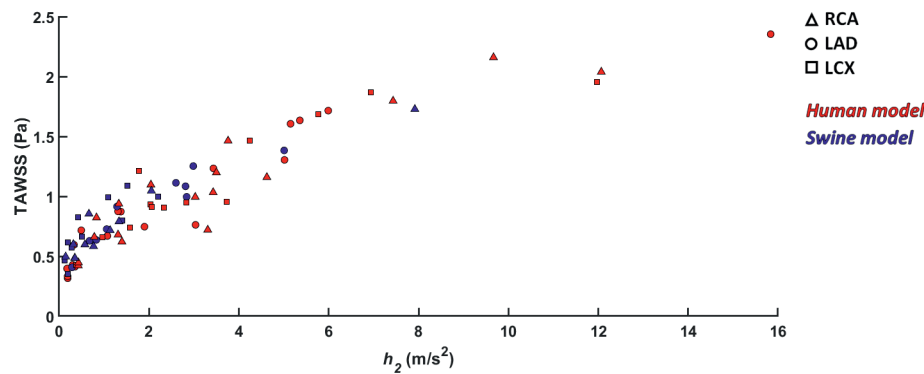


**Figure 10. Scatter plots of helicity intensity  $h_2$  vs. TAWSS.**

Red color indicates human models; blue color indicates swine models. Right (RCA), left anterior descending (LAD), and left circumflex (LCX) coronary artery geometries are distinguished by marker shape.

## Discussion

Swine models have contributed to a deeper understanding of the natural history of coronary atherosclerosis, with a valuable application to multiple research fields, such as the study of novel clinical treatment procedures efficacy<sup>11,13,14</sup>. The translation of results obtained in swine models to the patient situation is mainly based on intra-species comparisons of the coronary anatomy<sup>18,19</sup>, pathophysiology<sup>19,20</sup>, cholesterol levels<sup>21</sup> and sites of lesion formation<sup>20</sup>. However, a direct comparison in terms of coronary local hemodynamics, a recognized risk factor of atherosclerosis<sup>3-7</sup>, is still lacking.

Here a detailed comparative analysis between 49 human- and 30 swine-specific computational hemodynamic models of coronary arteries is presented in terms of coronary near-wall and intravascular hemodynamics, and morphometry. The study highlighted that overall human and swine coronary models present equivalent near-wall and intravascular hemodynamics, as well as equivalent geometrical features, with some minor exceptions, as discussed below.

### Hemodynamics

No significant inter-species difference emerged in terms of TAWSS, RRT, and transWSS in the three main coronary arteries. The two populations differed only in terms of OSI of the LAD coronary segment, with swine vessels presenting with significantly higher OSI median values than the human ones [0.0023 [0.0013, 0.0057] and 0.0005 [0.0004, 0.0007] for swine and human models, respectively,  $p < 0.001$ ). Such inter-species difference can be interpreted as a consequence of the observed inter-species difference in the measured inflow rates at LAD coronary

arteries, presenting with significantly larger peak and peak-to-peak values in swine than human models ( $p < 0.05$  and  $p < 0.01$ , respectively), thus physically precipitating oscillations of the WSS vector along the cardiac cycle<sup>30,41,42</sup>.

As previous research has shown<sup>15,23</sup>, relatively low WSS multidirectionality is present in coronary arteries of both ostensibly healthy swine and human coronary arteries, as reflected by the observed very low OSI and transWSS values (WSS column in Figure 9). Even though low multidirectionality was observed, plaque progression was proven to be significantly related to multidirectional WSS parameters<sup>16</sup>. However, multidirectional WSS seems to be more relevant for atherosclerotic plaque development in later stages of the disease and therefore this inter-species observed difference in OSI in the LAD is of less relevance for studies on atherosclerotic plaque initiation<sup>16,42,43</sup>.

An overall inter-species equivalence emerged also in terms of intravascular hemodynamics, characterized by the presence of distinguishable counter-rotating helical flow patterns (Figures 5 and 6). The evident similarity of helical flow features in human and swine coronary models finds confirmation in average helicity ( $h_1$ ), and in the balance between counter-rotating helical flow patterns ( $h_3$  and  $h_4$ , respectively) in the three main coronary arteries (*Helicity* column in Figure 9). Significant inter-species differences emerged only for the helical flow intensity ( $h_2$ ), being higher in human RCAs ( $p < 0.05$ ) and LCXs ( $p < 0.01$ ) compared to the swine ones (*Helicity* column in Figure 9). However, despite the emerged significant difference in helical flow intensity, the relationship between the latter and WSS in coronary arteries, as previously reported for swine models<sup>23</sup>, was also observed in human coronary arteries. Physiological high values of helical flow intensity keep TAWSS values within a physiological, atheroprotective range (Figure 10), and thereby prevent atherosclerotic plaque progression, which was also demonstrated by a direct association between plaque progression and helical flow intensity<sup>15</sup>. Hence, the emerged inter-species difference in helical flow intensity does not cancel out but confirms previous findings on its physiological significance in swine coronary arteries<sup>15,23</sup>, and remarks upon its possible use as surrogate marker of cardiovascular flow disturbances<sup>34-36,42,44,45</sup>.

### Morphometry

The comparative analysis between human and swine coronary anatomical features confirmed the strong inter-species similarity. In addition to the already observed equivalence in vessel size and distribution<sup>18,19</sup>, human and swine coronary arteries are characterized by comparable values of mean curvature, mean torsion and tortuosity of the three main coronary arteries (*Morphometry* column in Figure 9). Interestingly, the emerged significant inter-species difference in coronary

eccentricity ( $\epsilon$ ), revealed that the luminal section of human coronary arteries is more elliptical than that of swine coronary arteries.

### Limitations

Several limitations could weaken the findings of this study. Computational hemodynamic modelling suffers from assumptions and uncertainties. Among them, the assumption of rigid vascular wall might affect WSS estimation. However, studies applying fluid-structure interaction approaches reported that WSS spatial distribution is preserved when using rigid walls<sup>46,47</sup>. Additionally, the cardiac-induced motion of coronary arteries was neglected. This idealization was based on previous evidences reporting the minor effect of myocardial motion on coronary flow and WSS distribution with respect to the blood pressure pulse<sup>48,49</sup>. Moreover, cardiac-induced motion could markedly affect instantaneous WSS distribution, but it has a minor effect on cycle-average WSS quantities as the ones considered in the present study<sup>50</sup>. Finally, the limitations above affect swine as well as human populations. Hence, even not knowing whether their influence is species-independent, it might be negligible on the outcome of this study.

### Conclusion

Atherosclerosis is a multifactorial disease with hemodynamics as one of the main determinants of atherosclerotic plaque localization and progression. This study demonstrates that individual swine computational hemodynamic models of the three main coronary arteries are representative of the human hemodynamics in the same vessels. In detail, the study points out that swine and human coronary arteries present the same near-wall and intravascular hemodynamic features, as well as demonstrate anatomical similarities. These findings thus support the application of swine-specific computational models to investigate the hemodynamic-related risk of coronary atherosclerosis and have a high potential to translate directly into human coronary artery disease.

### References

1. Virani SS, Alonso A, Aparicio HJ, Benjamin EJ, Bittencourt MS, Callaway CW, et al. Heart Disease and Stroke Statistics-2021 Update: A Report From the American Heart Association. *Circulation* 2021;143:e254–743.
2. Lusis AJ. Atherosclerosis. *Nature* 2000;407:233–41.
3. Kwak BR, Bäck M, Bochaton-Piallat M-L, Caligiuri G, Daemen MJ a P, Davies PF, et al. Biomechanical factors in atherosclerosis: mechanisms and clinical implications†. *Eur Heart J* 2014;35:3013–20.
4. Morbiducci U, Kok AM, Kwak BR, Stone PH, Steinman DA, Wentzel JJ. Atherosclerosis at arterial bifurcations: Evidence for the role of haemodynamics and geometry. *Thromb Haemost* 2016;115:484–92.
5. Zaromytidou M, Siasos G, Coskun AU, Lucier M, Antoniadis AP, Papafakis MI, et al. Intravascular hemodynamics and coronary artery disease: New insights and clinical implications. *Hell J Cardiol* 2016;57:389–400.
6. Chatzizisis YS, Coskun AU, Jonas M, Edelman ER, Feldman CL, Stone PH. Role of Endothelial Shear Stress in the Natural History of Coronary Atherosclerosis and Vascular Remodeling. Molecular, Cellular, and Vascular Behavior. *J Am Coll Cardiol* 2007;49:2379–93.
7. Wentzel JJ, Chatzizisis YS, Gijsen FJHH, Giannoglou GD, Feldman CL, Stone PH. Endothelial shear stress in the evolution of coronary atherosclerotic plaque and vascular remodelling: current understanding and remaining questions. *Cardiovasc Res* 2012;96:234–43.
8. Stone PH, Saito S, Takahashi S, Makita Y, Nakamura SS, Kawasaki T, et al. Prediction of progression of coronary artery disease and clinical outcomes using vascular profiling of endothelial shear stress and arterial plaque characteristics: the PREDICTION Study. *Circulation* 2012;126:172–81.
9. Cheng JM, Garcia-Garcia HM, De Boer SPM, Kardys I, Heo JH, Akkerhuis KM, et al. In vivo detection of high-risk coronary plaques by radiofrequency intravascular ultrasound and cardiovascular outcome: Results of the ATHEROREMO-IVUS study. *Eur Heart J* 2014;35:639–47.
10. Millon A, Canet-Soulas E, Boussel L, Fayad Z, Douek P. Animal models of atherosclerosis and magnetic resonance imaging for monitoring plaque progression. *Vascular* 2014;22:221–37.
11. Daugherty A, Tall AR, Daemen MJAP, Falk E, Fisher EA, García-Cardena G, et al. Recommendation on Design, Execution, and Reporting of Animal Atherosclerosis Studies: A Scientific Statement From the American Heart Association. *Arterioscler Thromb Vasc Biol* 2017;37:e131–57.
12. Xiangdong L, Yuanwu L, Hua Z, Liming R, Qiuyan L, Ning L. Animal models for the atherosclerosis research: a review. *Protein Cell* 2011;2:189–201.
13. Getz GS, Reardon CA. Animal models of atherosclerosis. *Arterioscler Thromb Vasc Biol* 2012;32:1104–15.
14. Shin HS, Shin HH, Shudo Y. Current Status and Limitations of Myocardial Infarction Large Animal Models in Cardiovascular Translational Research. *Front Bioeng Biotechnol* 2021;9:321.
15. De Nisco G, Hoogendoorn A, Chiastra C, Gallo D, Kok AM, Morbiducci U, et al. The impact of helical flow on coronary atherosclerotic plaque development. *Atherosclerosis* 2020;300:39–46.
16. Hoogendoorn A, Kok AM, Hartman EMJ, de Nisco G, Casadonte L, Chiastra C, et al. Multidirectional wall shear stress promotes advanced coronary plaque development: comparing five shear stress metrics. *Cardiovasc Res* 2020;116:1136–46.
17. Mazzi V, De Nisco G, Hoogendoorn A, Calò K, Chiastra C, Gallo D, et al. Early Atherosclerotic Changes in Coronary Arteries are Associated with Endothelium Shear Stress Contraction/Expansion Variability. *Ann Biomed Eng* 2021:in press.
18. Weaver ME, Pantely GA, Bristow JD, Ladley HD. A quantitative study of the anatomy and distribution of coronary arteries in swine in comparison with other animals and man. *Cardiovasc Res* 1986;20:907–17.
19. Lelovas PP, Kostomitsopoulos NG, Xanthos TT. A comparative anatomic and physiologic overview of the porcine heart. *J Am Assoc Lab Anim Sci* 2014;53:432–8.



20. Shim J, Al-Mashhadi RH, Sørensen CB, Bentzon JF. Large animal models of atherosclerosis--new tools for persistent problems in cardiovascular medicine. *J Pathol* 2016;238:257–66.
21. Mahley RW, Weisgraber KH, Innerarity T, Brewer HBJ, Assmann G. Swine lipoproteins and atherosclerosis. Changes in the plasma lipoproteins and apoproteins induced by cholesterol feeding. *Biochemistry* 1975;14:2817–23.
22. Thim T, Hagensen MK, Drouet L, Bal Dit Sollier C, Bonneau M, Granada JF, et al. Familial hypercholesterolaemic downsized pig with human-like coronary atherosclerosis: a model for preclinical studies. *EuroIntervention* 2010;6:261–8.
23. De Nisco G, Kok AM, Chiastra C, Gallo D, Hoogendoorn A, Migliavacca F, et al. The Atheroprotective Nature of Helical Flow in Coronary Arteries. *Ann Biomed Eng* n.d.;47.
24. Chatzizisis YS, Jonas M, Coskun AU, Beigel R, Stone B V., Maynard C, et al. Prediction of the localization of high-risk coronary atherosclerotic plaques on the basis of low endothelial shear stress--an intravascular ultrasound and histopathology natural history study. *Circulation* 2008;117:993–1002.
25. Hartman EMJ, De Nisco G, Kok AM, Hoogendoorn A, Coenen A, Mastik F, et al. Lipid-rich Plaques Detected by Near-infrared Spectroscopy Are More Frequently Exposed to High Shear Stress. *J Cardiovasc Transl Res* 2020.
26. Council NR. Guide for the Care and Use of Laboratory Animals: Eighth Edition. Washington, DC: The National Academies Press; 2011.
27. Chiastra C, Gallo D, Tasso P, Iannaccone F, Migliavacca F, Wentzel JJ, et al. Healthy and diseased coronary bifurcation geometries influence near-wall and intravascular flow: A computational exploration of the hemodynamic risk. *J Biomech* 2017;58:79–88.
28. van der Giessen AG, Groen HC, Doriot P-A, de Feyter PJ, van der Steen AFW, van de Vosse FN, et al. The influence of boundary conditions on wall shear stress distribution in patients specific coronary trees. *J Biomech* 2011;44:1089–95.
29. Huo Y, Kassab GS. Intraspecific scaling laws of vascular trees. *J R Soc Interface* 2012;9:190–200.
30. Ku DN, Giddens DP, Zarins CK, Glagov S. Pulsatile flow and atherosclerosis in the human carotid bifurcation. Positive correlation between plaque location and low oscillating shear stress. *Arteriosclerosis* 1985;5:293–302.
31. Himburg HA, Grzybowski DM, Hazel AL, LaMack JA, Li X-M, Friedman MH. Spatial comparison between wall shear stress measures and porcine arterial endothelial permeability. *Am J Physiol Heart Circ Physiol* 2004;286:H1916–22.
32. Peiffer V, Sherwin SJ, Weinberg PD. Computation in the rabbit aorta of a new metric – the transverse wall shear stress – to quantify the multidirectional character of disturbed blood flow. *J Biomech* 2013;46:2651–8.
33. Morbiducci U, Ponzini R, Grigioni M, Redaelli A. Helical flow as fluid dynamic signature for atherogenesis risk in aortocoronary bypass. A numeric study. *J Biomech* 2007;40:519–34.
34. Gallo D, Steinman DA, Bijari PB, Morbiducci U. Helical flow in carotid bifurcation as surrogate marker of exposure to disturbed shear. *J Biomech* 2012;45:2398–404.
35. Morbiducci U, Ponzini R, Gallo D, Bignardi C, Rizzo G. Inflow boundary conditions for image-based computational hemodynamics: impact of idealized versus measured velocity profiles in the human aorta. *J Biomech* 2013;46:102–9.
36. Gallo D, Steinman DA, Morbiducci U. An insight into the mechanistic role of the common carotid artery on the hemodynamics at the carotid bifurcation. *Ann Biomed Eng* 2015;43:68–81.
37. Sangalli LM, Secchi P, Vantini S, Veneziani A. Efficient estimation of three-dimensional curves and their derivatives by free-knot regression splines, applied to the analysis of inner carotid artery centrelines. *J R Stat Soc Ser C (Applied Stat)* 2009;58:285–306.
38. Vorobtsova N, Chiastra C, Stremler MA, Sane DC, Migliavacca F, Vlachos P. Effects of Vessel Tortuosity on Coronary Hemodynamics: An Idealized and Patient-Specific Computational Study. *Ann Biomed Eng* 2016;44:2228–39.
39. Ciurică S, Lopez-Sublet M, Loeys BL, Radhouani I, Natarajan N, Vikkula M, et al. Arterial Tortuosity. *Hypertens (Dallas, Tex 1979)* 2019;73:951–60.
40. Finotello A, Faggiano E, Conti M, Spinella G, Pane B, Palombo D, et al. Medical image analysis to measure the follow-up geometry of thoraco-abdominal aortic aneurysms treated with multilayer flow modulator stent. *Comput Methods Biomech Biomed Eng Imaging Vis* 2020;8:126–33.
41. Soulis J V, Giannoglou GD, Chatzizisis YS, Farmakis TM, Giannakoulas GA, Parcharidis GE, et al. Spatial and phasic oscillation of non-Newtonian wall shear stress in human left coronary artery bifurcation: an insight to atherogenesis. *Coron Artery Dis* 2006;17:351–8.
42. Gallo D, Bijari PB, Morbiducci U, Qiao Y, Xie Y (Joyce), Etesami M, et al. Segment-specific associations between local haemodynamic and imaging markers of early atherosclerosis at the carotid artery: an in vivo human study. *J R Soc Interface* 2018;15:20180352.
43. Kok AM, Molony DS, Timmins LH, Ko Y-A, Boersma E, Eshtehardi P, et al. The Influence of Multidirectional Shear Stress on Plaque Progression and Composition Changes in Human Coronary Arteries. *EuroIntervention* 2019.
44. Morbiducci U, Ponzini R, Rizzo G, Cadioli M, Esposito A, De Cobelli F, et al. In vivo quantification of helical blood flow in human aorta by time-resolved three-dimensional cine phase contrast magnetic resonance imaging. *Ann Biomed Eng* 2009;37:516–31.
45. Liu X, Sun A, Fan Y, Deng X. Physiological significance of helical flow in the arterial system and its potential clinical applications. *Ann Biomed Eng* 2015;43:3–15.
46. Malvè M, García A, Ohayon J, Martínez MA. Unsteady blood flow and mass transfer of a human left coronary artery bifurcation: FSI vs. CFD. *Int Commun Heat Mass Transf* 2012;39:745–51.
47. Torii R, Wood N, Hadjiloizou N, Dowsey A, Wright A, Hughes A, et al. Fluid-structure interaction analysis of a patient-specific right coronary artery with physiological velocity and pressure waveforms. *Commun Numer Methods Eng* 2009;25:565–80.
48. Theodorakakos A, Gavaises M, Andriotis A, Zifan A, Liatsis P, Pantos I, et al. Simulation of cardiac motion on non-Newtonian, pulsating flow development in the human left anterior descending coronary artery. *Phys Med Biol* 2008;53:4875–92.
49. Zeng D, Ding Z, Friedman MH, Ethier CR. Effects of cardiac motion on right coronary artery hemodynamics. *Ann Biomed Eng* 2003;31:420–9.
50. Torii R, Keegan J, Wood NB, Dowsey AW, Hughes AD, Yang G-Z, et al. MR image-based geometric and hemodynamic investigation of the right coronary artery with dynamic vessel motion. *Ann Biomed Eng* 2010;38:2606–20.





# 9

## **Colocalization of intracoronary lipid-rich plaques and calcifications – an integrated NIRS-IVUS analysis.**

This chapter adapted from:

**Colocalization of intracoronary lipid-rich plaques and calcifications  
– an integrated NIRS-IVUS analysis.**

**Eline M.J. Hartman, Ayla Hoogendoorn, Ali C. Akyildiz, Anne-Sophie Schuurman,  
Anton F.W. van der Steen, Eric Boersma, Jolanda J. Wentzel, Joost Daemen**

*JACC Cardiovascular imaging, 2020*

Introduction

Atherosclerosis is the underlying disease of multiple leading causes of morbidity and mortality worldwide<sup>1</sup>. More specifically, several morphometric plaque features showed to substantially increase the risk of future cardiovascular events. Whereas high lipid content of the plaque has been associated with increased plaque vulnerability<sup>2</sup>, calcifications, depending on their size, have been related to both plaque stabilization, as well as vulnerability<sup>3</sup>. Using near-infrared spectroscopy-intravascular ultrasound (NIRS-IVUS) both plaque components can be detected simultaneously<sup>4</sup>. Where IVUS enables reliable detection of plaque size and has a high sensitivity for detecting coronary calcifications<sup>5</sup>, NIRS is optimized to detect lipid rich plaque (LRP)<sup>6</sup>. At present, little is known about the prevalence of the colocalization of calcifications and lipid-rich plaques (LRPs). Our aim was to investigate the incidence of the colocalization of lipids and calcium in coronary arteries of patients with coronary artery disease.

Methods

In this single-center retrospective study, we included all patients from the prospective IBIS3 study of whom a combined NIRS-IVUS (TVC, InfraRedx, USA) pullback was available. The design of the IBIS3 study has been described in great detail elsewhere<sup>7</sup>. In brief, IBIS3 was a prospective investigator-initiated, single-center study in which NIRS-IVUS assessment of a proximal segment of a non-culprit coronary artery was performed to evaluate the effect of rosuvastatin on necrotic core volume in patients with stable or acute coronary syndrome (ACS). NIRS-IVUS imaging was performed in non-culprit vessels using a motorized pullback at a speed of 0.5 mm/sec. The study was approved by the local institutional review board (METC Erasmus Medical Center), conducted in accordance to the Declaration of Helsinki, and registered in The Netherlands trial register, number NTR2872. All patients provided written informed consent.

One frame per millimeter of each pullback was analyzed. Regions that were previously stented were excluded from the analysis. Frames with non-uniform rotational distortion (NURD) imaging artefacts were excluded from the analysis to avoid matching errors between the IVUS and NIRS signal<sup>8</sup>. Calcium on IVUS was defined as a high intensity signal (bright on the image) with a low intensity region (dark shadow) behind it<sup>9</sup>. The minimal measurable and validated calcium angle on IVUS was set at 15°<sup>5</sup>. Calcium angles were manually indicated using QCU-CMS software (version 4.69, LKEB, Leiden) by two independent expert reviewers (EH and AH), blinded to the NIRS signal during analysis. The protractor originated in the center of the catheter to segment the calcification angles from the same point as the NIRS detection. An interobserver analysis between the two readers

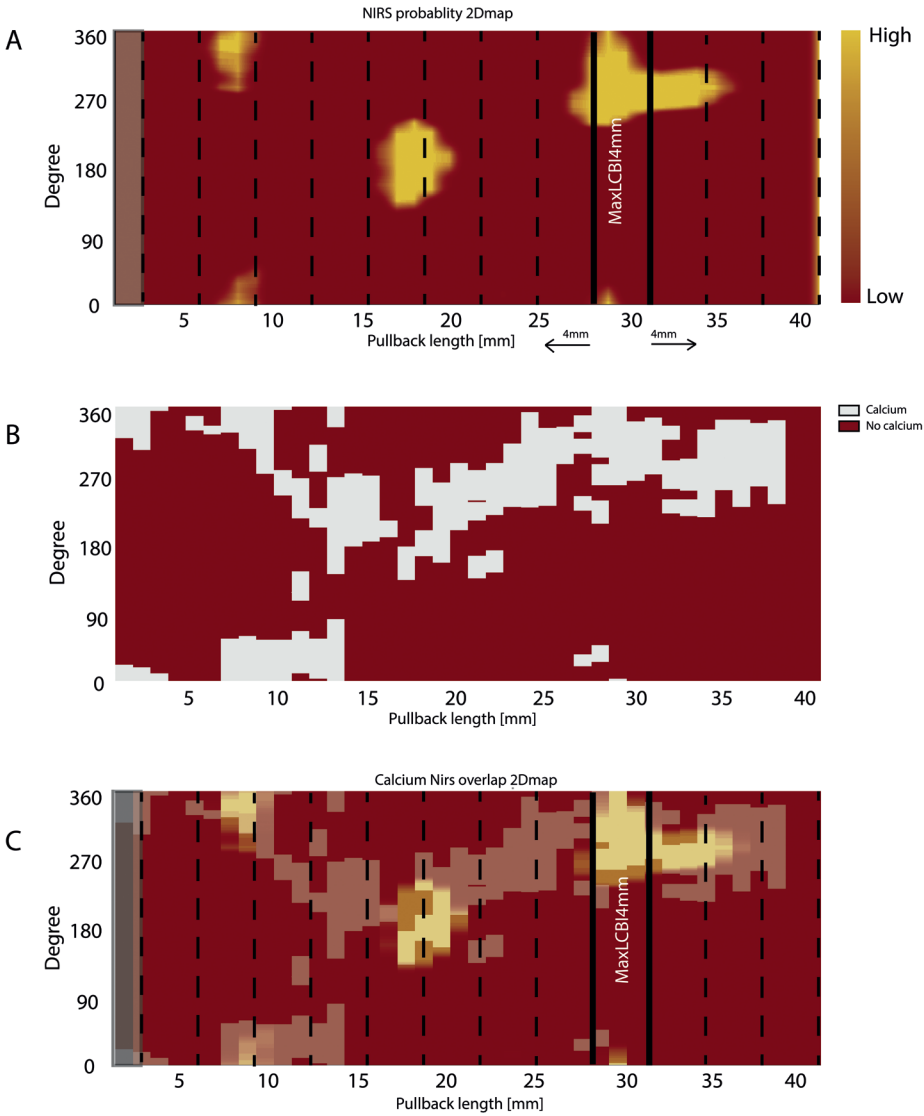


**Figure 1. 2D maps of NIRS, calcium and overlap.** 2D maps of coronary vessel as if the vessel is cut open along the longitudinal axis. The X-axis is the longitudinal length of the pullback with a sample size of 1 frame every millimeter. The Y-axis is the circumference of the vessel. **A:** 2D maps with the NIRS probability (chemogram). Red is low probability, yellow is high probability. MaxLCBI4mm is indicated between continues lines. From this Max LCBI4mm region, the vessel is divided in 4mm segments (dashed lines) in proximal and distal direction (as indicated by the arrows). **B:** 2D map with the presence of calcium. White is calcified, red is non calcified. **C:** Overlay of calcium 2Dmap (A) and NIRS 2D map (B).

was performed on a subset of 10 arteries using interclass correlation coefficient. Values above 0.8 were considered as good agreement. No distinction between deep and superficial calcium was made. The NIRS data was analyzed based on the color-coded ring that is projected around the IVUS image in each frame. The 128-color scale from red to yellow represent the probability of the presence of lipids, with red as the lowest and yellow as the highest probability. With in-house developed software (MATLAB, v. 2017b, MathWorks Inc., Natick, MA, USA) the probability of the NIRS signal for lipid content was assessed for each 1° in circumference and extract as a continuous number for each degree on the NIRS-IVUS image. Every degree with a lipid probability > 0.6 was scored as NIRS positive<sup>6</sup>. For the integrative analyses, 2D-maps for the presence of both calcium and a positive NIRS signal were generated (Figure 1). The latter is comparable to the standard NIRS-data display known as the chemogram<sup>6</sup>. By combining the NIRS data with the segmented calcium angles, we assessed the colocalization of NIRS signal and calcium.

Lipid Core Burden Index (LCBI) was calculated for all frames, 4mm segments and each vessel (the fraction of NIRS positive degrees\*1000)<sup>10</sup>. The 4mm segments with a LCBI >0 were defined as lipid-rich. Previously, 4mm segments with LCBI scores higher than 250 were considered as high-risk plaques, therefore a subsequent analysis was performed using these cut-off values<sup>11</sup>. LCBI scores were subdivided into 3 different groups: lipid-free (LCBI 0), low-lipid (LCBI 1-250) and high-lipid (LCBI >250). Furthermore, the MaxLCBI<sub>4mm</sub> was defined as the 4 mm with the highest LCBI within a pullback of the vessel. From the location of the MaxLCBI<sub>4mm</sub>, the artery was both proximally and distally divided in consecutive segments of 4 mm. The residual proximal and distal segments smaller than 4 mm were discarded (Figure 1). A similar methodology was used to calculate an IVUS based calcium score, resulting in a calcium score per frame and 4mm segment and each vessel. At frame level, calcifications covering less than 90° (score<250) of the frame were classified as 'spotty'. Large calcifications were defined as a calcium score above 250

### Statistical analysis

For continuous variables, mean and standard deviations (mean ± SD) or median and interquartile range (IQR) were calculated. Categorical variables were reported as frequencies (%) and compared with Chi-Square test. Statistical analysis of the colocalization of the different calcium score categories and lipids categories was performed using generalized linear mixed models, with LCBI categories as a fixed factor. To correct for potential clustering effect of multiple frames per vessel, the individual vessel was added as random factor in this statistical model. All tests were 2-tailed and a p-value <0.05 was considered significant. SPSS statistics version 25 for Windows (IBM Corp, New York) was used for statistical analysis.

## Results

A total of 154 vessels from 139 patients (9811 frames) were analyzed with a mean pullback length of 63±19 mm. The baseline characteristics are presented in table 1. Mean age was 61±10 years and 81% of the patients were men. ACS was the presenting symptom in 40% of the patients and a percutaneous coronary intervention was performed in 88% of the patients. The distribution of the analyzed coronary vessels was LAD 43%, LCX 31% and RCA 27%. For the interobserver analysis, 810 IVUS frames derived from multiple pullbacks were analyzed by the two observers. The analysis demonstrated a good agreement between the observers, with an average interclass coefficient of 0.957(95%CI:0.944-0.968).

A number of vessels in this study was not affected by atherosclerosis, no presence of calcium or NIRS detectable lipids, which caused a skewed distribution of calcium and LCBI scores. This resulted in a total vessel calcium score ranging from 0 to 309 with a median value of 30 (IQR: 7-63). The total vessel LCBI ranged from 0 to 175 with a median of 23 (IQR: 6-44). The median MaxLCBI<sub>4mm</sub> was 246 (IQR:92-345). The correlation of the absolute LCBI and calcium score at vessel-level was weak (Spearman's  $\rho=0.215$ ,  $p=0.007$ ).

On a frame level, calcifications and a NIRS positive signal were present in 25.2% and 21.7% of the frames respectively, and 9.3% of the frames showed both lipids and calcium. In frames with a positive NIRS signal, the median frame LCBI score was 164 (IQR: 83-269). The median calcium score in frames with calcification was 150 (IQR: 81-242). In the calcified NIRS positive frames, the calcium angle was significantly larger (197; IQR: 117-278) than the one in the calcified NIRS negative frames (128; IQR: 69-208) ( $p<0.001$ ). Of the calcified NIRS positive frames, 33% presented with large calcifications and 77% with spotty calcifications while of calcified NIRS negative frames, 16% of the frames had large calcifications and 84% spotty calcifications( $p<0.001$ ).

On the 4mm segment level, lipid rich segments had a greater likelihood for the presence of calcification as compared to segments with no lipids (LCBI>250 vs LCBI 0: odds ratio 6; 95%CI 4-10;  $p<0.001$  and LCBI 1-250 vs LCBI 0: odds ratio 4; 95%CI 3-5;  $p<0.001$ ). Segments with a high LCBI score (>250) had a greater likelihood for large calcification (>250) as compared to segments with no lipids (odds ratio 54; 95%CI 23-128;  $p<0.001$ ). For segments with LCBI 1-250, the likelihood for large calcification (>250) remained higher than in segments with no lipids (odds ratio 10; 95%CI 6-19;  $p<0.001$ ) (Figure 2)

Table 1. Baseline characteristics.

Clinical characteristics	N = 139 patients
Age, years	60.9 ± 9.3
Men, n (%)	112 (80.6)
Diabetes Mellitus, n (%)	29 (20.9)
Hypertension, n (%)	95 (68.3)
Dyslipidemia, n (%)	86 (61.9)
Current smoking, n (%)	34 (24.5)
Positive family history, n (%)	67 (48.2)
Previous MI, n (%)	40 (28.8)
Previous PCI, n (%)	50 (36.0)
Previous CABG, n (%)	1 (0.7)
Previous CVA, n (%)	13 (9.4)
History of peripheral artery disease, n (%)	14 (10.1)
History of renal impairment, n (%)	9 (6.5)
Procedural characteristics	
Indication for coronary angiography	
Acute MI, n (%)	15 (10.8)
Unstable angina, n (%)	41 (29.5)
Stable angina, n (%)	83 (59.7)
PCI performed, n (%)	121 (87.1)
Coronary artery disease	
No significant stenosis, n (%)	7 (5.0)
1-vessel disease, n (%)	74 (53.2)
2-vessel disease, n (%)	48 (34.5)
3-vessel disease, n (%)	10 (7.2)
Invasive Imaging characteristics	
Imaged study vessel	
Left anterior descending, n (%)	66(42.8)
Left circumflex, n (%)	47(30.5)
Right coronary artery, n (%)	41(26.7)
Average pullback length, mm(SD)	63±19
total LCBI vessel (IQR)	23(6-44)

Table 1. Continued.

Clinical characteristics	N = 139 patients
total Ca score vessel (IQR)	30(7-63)
MaxLCBI4mm (IQR)	246(92-345)
MaxCa4mm (IQR)	181(60-265)

MI = myocardial infarction, PCI = percutaneous coronary intervention, CABG = coronary artery bypass graft, CVA = cerebral vascular accident, LCBI = lipid core burden index, Ca = Calcium.

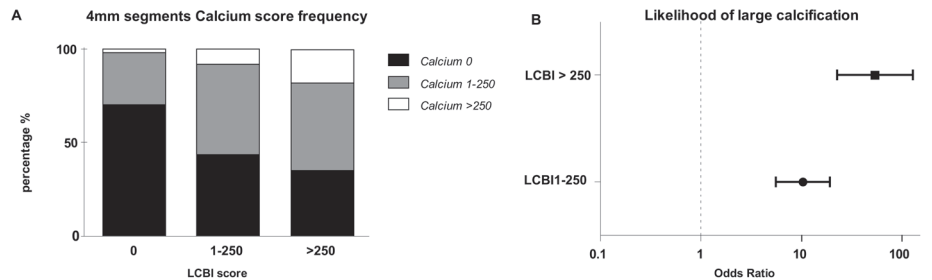


Figure 2. Frequency and median calcium score in subgroups. A: Frequency of calcium score subgroups of all 4 mm segments divided categorized based on an LCBI cut-of-value of 250. B: Forest plot of large calcifications in segments of LCBI subgroups relative to segments with an LCBI of 0.

Discussion

While both calcifications and lipid rich plaques proved to be associated with inferior clinical outcome, little is known about the colocalization of both components and their individual contribution to plaque vulnerability and future adverse clinical events. As calcification is known to originate from inflammation<sup>12</sup>, the colocalization of calcium and a positive NIRS signal could confirm more advanced plaques phenotypes. Histological studies showed that calcifications are often present around inflamed lipid-rich necrotic cores<sup>13</sup>.

In this study of non-culprit vessels, we found a large range in both the calcium and LCBI scores, as well as in colocalization of the two plaque components. However, segments with an LCBI scores >250 had higher calcium scores than segments LCBI scores <250. The discrepancies that were found in colocalization of the two plaque components could be explained by both a biological and a technical phenomenon. From a biological perspective, it could be that the NIRS-positive segments with calcification are in a different stage of atherosclerosis, as compared to NIRS-positive segments without calcification. The occurrence of segments with extensive calcifications but no positive NIRS signal may be explained by the



development of calcifications in necrotic cores<sup>13</sup>, whereby calcifications replace the lipid rich content and reduce the positive NIRS signal.

From a more technical perspective, NIRS uses near-infrared light with the capability to penetrate through calcium<sup>6</sup>. The technique, as validated by Garner et al. in 2008 was optimized to detect lipid-core plaque and was optimized for plaques that are classified as fibro-atheroma, have a larger angle than 60°, are more than 200 µm thick and with a mean fibrous cap thinner than 450 µm<sup>6</sup>. This definition corresponds to an LCBI score of 167 in a single frame. The smallest detectable calcium angle in IVUS is 15 degrees<sup>5</sup>, which corresponds to a calcium score of 24 ( $15^\circ/360^\circ * 1000$ ) in a single frame. The large number of 4mm segments (423) with a low calcium score (1-125) and absence of lipids (low LCBI score), could partially be explained by the fact that the atherosclerotic plaques in these frames did not meet the minimal detection criteria of NIRS and could thus not be detected by the NIRS catheter.

#### **Influence of calcification on image analysis**

A number of NIRS studies focused on the correlation between plaque burden and plaque characteristics<sup>14,15</sup>. They showed that combining NIRS and plaque burden improves the detectability of a fibro-atheroma. Plaque burden calculation (plaque area/vessel area \*100%) requires an accurate assessment of vessel area. However, in case of large calcifications, acoustic shadowing hampers the plaque burden measurement<sup>9</sup>. In the present study, 43% of the NIRS positive frames was partially or completely calcified, hence no analysis with plaque burden was performed in our study.

#### **Risk prediction based on plaque composition**

Both CT-derived coronary artery calcification score (CAC) and LCBI indicators of advanced stages of coronary atherosclerosis and have shown to be significant predictors of future adverse events<sup>2,16</sup>. However, distinguishing the rupture-prone “vulnerable” plaque from the stable plaque has proven to be complex. The impact of calcium on plaque stability is widely debated. Larger and denser calcifications, that can be detected using (invasive) imaging, may have a mechanically stabilizing effect on the plaque<sup>17</sup>.

With regard to the clinical implication of calcifications, Beckman et al.<sup>18</sup> showed in an IVUS study that the total amount of calcium was higher in culprit lesions of stable angina pectoris (SAP) patients than in patients with ACS. Also the arc of the calcification was significantly larger in SAP lesions, confirming that IVUS-detectable calcium could be indicative for a more stable coronary atherosclerotic plaque<sup>18</sup>. Pu et al. showed that in NIRS-detected LRPs, spotty calcifications were more prevalent than extensive calcifications<sup>19</sup>. This is in accordance with the current

study result, in which we found overall more spotty (<90°) calcification than large calcification (>90°). However, we also found that NIRS positive calcified frames had larger calcification angles than the NIRS negative calcified frames. Combining the size of the calcification and a high LCBI score can potentially improve the detection of the vulnerable plaque. Concluding, NIRS-positive segments without calcification might indicate unstable vulnerable plaques and segments with extensive calcifications but no positive NIRS signal might indicate more stable disease as calcifications might have replaced lipid rich content in necrotic cores.

#### **Limitations**

We opted to only use a subpopulation of the IBIS-3 study in which the combined catheter was used instead of two separate catheters to avoid any matching errors between individual IVUS and NIRS acquisitions. In this sub-group of this single-center retrospective study in non-culprit coronary arteries only had 11 imaged vessel related events after 4 years. Future studies with larger patient cohorts that register clinical outcome data at a coronary segment level are needed to establish the added value of the presence and size of calcifications in NIRS positive plaques as a predictor for plaque vulnerability. As a future perspective for clinical practice, when determining treatment strategy of NIRS-positive vessels, one has to be aware of the frequent colocalization with calcium deposits and their potential role in plaque stability. This type of extended image interpretation might further improve the detection of the vulnerable plaques as well as improve risk-assessment for the patient.

#### **Conclusion**

To the best of our knowledge the present study is the first to demonstrate a significant correlation between calcium and LCBI with significantly higher calcium scores in segments and frames with a higher LCBI and suggests that both plaque characteristics should not be seen as separate entities that might independently predict future adverse events. Combining calcium burden with LCBI has the potential to improve the detection of vulnerable plaques as well as individual risk-assessment.

## References

1. Virmani R, Kolodgie FD, Burke AP, Farb A, Schwartz SM. Lessons from sudden coronary death: A comprehensive morphological classification scheme for atherosclerotic lesions. *Arterioscler Thromb Vasc Biol* 2000;20:1262–75.
2. Schuurman A-S, Vroegindewey M, Kardys I, Oemrawsingh RM, Cheng JM, de Boer S, et al. Near-infrared spectroscopy-derived lipid core burden index predicts adverse cardiovascular outcome in patients with coronary artery disease during long-term follow-up. *Eur Heart J* 2018;39:295–302.
3. Barrett HE, Van der Heiden K, Farrell E, Gijzen FJH, Akyildiz AC. Calcifications in atherosclerotic plaques and impact on plaque biomechanics. *J Biomech* 2019;87:1–12.
4. Brugaletta S, Garcia-Garcia HM, Serruys PW, de Boer S, Ligthart J, Gomez-Lara J, et al. NIRS and IVUS for Characterization of Atherosclerosis in Patients Undergoing Coronary Angiography. *JACC Cardiovasc Imaging* 2011;4:647–55.
5. Mintz GS, Nissen SE, Anderson WD, Bailey SR, Erbel R, Fitzgerald PJ, et al. American College of Cardiology clinical expert consensus document on standards for acquisition, measurement and reporting of intravascular ultrasound studies (ivus): A report of the american college of cardiology task force on clinical expert consensus do. *J Am Coll Cardiol* 2001;37:1478–92.
6. Gardner CM, Tan H, Hull EL, Lisauskas JB, Sum ST, Meese TM, et al. Detection of Lipid Core Coronary Plaques in Autopsy Specimens With a Novel Catheter-Based Near-Infrared Spectroscopy System. *JACC Cardiovasc Imaging* 2008;1:638–48.
7. Simsek C, Garcia-Garcia HM, van Geuns R-J, Magro M, Girasis C, van Mieghem N, et al. The ability of high dose rosuvastatin to improve plaque composition in non-intervened coronary arteries: rationale and design of the Integrated Biomarker and Imaging Study-3 (IBIS-3). *EuroIntervention* 2012;8:235–41.
8. Kawase Y, Suzuki Y, Ikeno F, Yoneyama R, Hoshino K, Ly HQ, et al. Comparison of nonuniform rotational distortion between mechanical IVUS and OCT using a phantom model. *Ultrasound Med Biol* 2007;33:67–73.
9. Mintz GS. Intravascular Imaging of Coronary Calcification and its Clinical Implications. *JACC Cardiovasc Imaging* 2015;8:461–71.
10. Kini AS, Baber U, Kovacic JC, Limaye A, Ali ZA, Sweeny J, et al. Changes in Plaque Lipid Content After Short-Term Intensive Versus Standard Statin Therapy: The YELLOW Trial (Reduction in Yellow Plaque by Aggressive Lipid-Lowering Therapy). *J Am Coll Cardiol* 2013;62:21–9.
11. Waksman R, Di Mario C, Torguson R, Ali ZA, Singh V, Skinner WH, et al. Identification of patients and plaques vulnerable to future coronary events with near-infrared spectroscopy intravascular ultrasound imaging: a prospective, cohort study. *Lancet* 2019;394:1629–37.
12. Shanahan CM. Inflammation ushers in calcification: A cycle of damage and protection? *Circulation* 2007;116:2782–5.
13. Nakahara T, Dweck MR, Narula N, Pisapia D, Narula J, Strauss HW. Coronary Artery Calcification: From Mechanism to Molecular Imaging. *JACC Cardiovasc Imaging* 2017;10:582–93.
14. Kang S-J, Mintz GS, Pu J, Sum ST, Madden SP, Burke AP, et al. Combined IVUS and NIRS Detection of Fibroatheromas: Histopathological Validation in Human Coronary Arteries. *JACC Cardiovasc Imaging* 2015;8:184–94.
15. Puri R, Madder RD, Madden SP, Sum ST, Wolski K, Muller JE, et al. Near-Infrared Spectroscopy Enhances Intravascular Ultrasound Assessment of Vulnerable Coronary Plaque: A Combined Pathological and In Vivo Study. *Arterioscler Thromb Vasc Biol* 2015;35:2423–31.
16. Taylor AJ, Bindeman J, Feuerstein I, Cao F, Brazaitis M, O'Malley PG. Coronary calcium independently predicts incident premature coronary heart disease over measured cardiovascular risk factors: Mean three-year outcomes in the Prospective Army Coronary Calcium (PACC) project. *J Am Coll Cardiol* 2005;46:807–14.
17. Criqui MH, Denenberg JO, Ix JH, McClelland RL, Wassel CL, Rifkin DE, et al. Calcium density of coronary artery plaque and risk of incident cardiovascular events. *JAMA - J Am Med Assoc* 2014;311:271–8.
18. Beckman JA, Ganz J, Creager MA, Ganz P, Kinlay S. Relationship of clinical presentation and calcification of culprit coronary artery stenoses. *Arterioscler Thromb Vasc Biol* 2001;21:1618–22.
19. Pu J, Mintz GS, Biro S, Lee J-B, Sum ST, Madden SP, et al. Insights Into Echo-Attenuated Plaques, Echolucent Plaques, and Plaques With Spotty Calcification: Novel Findings From Comparisons Among Intravascular Ultrasound, Near-Infrared Spectroscopy, and Pathological Histology in 2,294 Human Coronary Artery Segment. *J Am Coll Cardiol* 2014;63:2220–33.



# 10

## Near-infrared spectroscopy to predict plaque progression in plaque-free artery regions

This chapter based on:  
Near-infrared spectroscopy to predict plaque progression in plaque-free artery regions

Mariusz Tomaniak, Eline M.J. Hartman, M.N. Tovar Forero, Jeroen Wilschut, Felix Zijlstra, Nicolas M. Van Mieghem, Isabella Kardys, Jolanda J. Wentzel, Joost Daemen

*Eurointervention, 2021*

## Abstract

**Background** - Positive near infrared spectroscopy (NIRS) signals might be encountered in areas without evident artery wall thickening being typically perceived as artefacts.

**Aims** - We aimed to evaluate the utility of NIRS to identify artery wall regions associated with an increase in wall thickness (WT) as assessed by serial IVUS and optical coherence tomography (OCT).

**Methods** - In this prospective, single-centre study, patients presenting with acute coronary syndrome (ACS) underwent NIRS-IVUS and OCT assessment of a non-culprit artery at baseline and 12-month follow-up. For each vessel, 1.5-mm segments were identified, matched and divided into 45° sectors. The relationship between change in IVUS-based WT (DWT), and the presence of NIRS positive signal and OCT-detected lipid was evaluated using linear mixed models.

**Results** - A total of 37 patients (38 vessels, 6936 matched sectors) were analysed at baseline and 12 months. A total of 140/406 (34.5%) NIRS(+) sectors and 513/1575 (32.6%) OCT-lipid(+) sectors were found to be located in thin (WT<0.5mm) wall sectors. In the thin wall sectors, increase in WT was significantly more pronounced in NIRS(+) vs. NIRS(-) sectors: 0.11 mm vs. 0.06 mm,  $p<0.001$ ). In the thick wall sectors, there was a decrease in WT observed, that was less pronounced in the NIRS(+) vs. NIRS(-) sectors (-0.08mm vs. -0.09mm,  $p<0.001$ ). Thin wall NIRS(+) OCT-lipid(+) sectors showed significant wall thickening (DWT = 0.13 mm).

**Conclusion** - NIRS-positive signals in otherwise non-diseased arterial walls as assessed by IVUS could identify vessel wall regions prone for WT increase over 12-month follow-up. Our observations suggest that NIRS positive signals in areas without evident wall thickening by IVUS should no longer be viewed as benign or imaging artefact.

## Introduction

Intravascular ultrasound (IVUS) has emerged as the 'gold standard' modality for assessing the evolution of coronary atherosclerosis<sup>1-8</sup>. Due to its penetration depth IVUS allows for exact quantification of plaque volume and wall thickness (WT). Whereas grayscale IVUS is less sensitive in detecting plaque specific predictors of progression, such as lipids, the combined near-infrared spectroscopy (NIRS)-IVUS catheter allows for accurate detection of lipid content with exact colocalization of volumetric assessment by IVUS. The added clinical value of NIRS was shown by several clinical studies linking lipid rich plaque (LRP) to future cardiovascular events<sup>9-11</sup>.

To date, little is known on the association between LRP as detected by NIRS, baseline WT and change in WT over time. The latter is of particular importance since NIRS positive signals might be routinely recognized in areas without evident vessel wall thickening on IVUS. Such findings are considered benign or perceived as artefacts. However, pathophysiological work has indicated lipid influx as one of the earliest stages of atherosclerosis<sup>12</sup>. While histopathology of the autopsied hearts revealed that non-fibroatheromas with NIRS positive signal (vs. non-fibroatheromas without NIRS positive signal) were mostly pathological intimal thickening (50%) with a greater prevalence of histological lipid pool or calcified nodule,<sup>13</sup> the implications of positive NIRS signals detected in otherwise non-diseased arteries as assessed by IVUS have never been investigated in a prospective intravascular imaging study.

Our aim was to assess the change in WT in regions with NIRS positive and NIRS negative signals with and without underlying plaque as detected by IVUS, using optical coherence tomography (OCT) to confirm the actual lipid presence within the artery wall. We did so in a dedicated longitudinal follow-up study with multimodality imaging of non-culprit arteries of patients presenting with acute coronary syndrome (ACS) and serial (baseline and 12-month) invasive imaging using NIRS-IVUS and OCT.

## Methods

In this prospective, single-centre study, patients presenting with ACS successfully treated with percutaneous coronary intervention (PCI) underwent combined NIRS-IVUS and OCT assessment of a non-culprit coronary artery at baseline and at 12-month follow-up. All patients received guideline-recommended secondary prevention, including dual antiplatelet and lipid-lowering therapy<sup>14</sup>. Major exclusion criteria included: previous coronary artery bypass grafting, three-vessel disease, estimated glomerular filtration rate < 50ml/min, left ventricular ejection fraction



< 30% and atrial fibrillation. All patients provided written informed consent prior to enrolment. The study protocol was approved by the local ethics committee (MEC 2015-535, NL54519.078.15) and is registered (ISCRTN:43170100). The study was conducted in accordance with the Declaration of Helsinki (64th WMA general Assembly, Fortaleza, Brazil, October 2013) and Medical Research Involving Human Subject Act (WMO).

### NIRS-IVUS and OCT acquisition

A near-infrared intravascular ultrasound (NIRS-IVUS) pullback (TVC Insight Coronary Imaging Catheter, InfraRedX, Burlington, MA, USA) (0.5mm/s) and a 75mm OCT acquisition (Dragonfly Optis Imaging Catheter, St. Jude Medical, St. Paul, MN, USA) (36 mm/s) were done in the same non-stented non-culprit coronary segment with a minimum length of 30 mm and two readily identifiable side branches (diameter >1.5mm). The study segment for invasive imaging was selected by the operator based on the availability of optimal identifiable landmarks required for matching of multimodality imaging data, the anticipated segment length and the feasibility of invasive local Doppler flow measurements in this cohort<sup>15</sup>.

### IVUS analysis

First, IVUS-pullbacks were ECG-gated by selecting the frame recorded 6 frames before the R-peak by in-house developed software using in-house developed software (MATLAB (V.2017B, Mathworks Inc, USA)<sup>16</sup>. As a result, changes in lumen size related to the movement of the catheter or pressure changes during the contraction of the heart were removed. The gated pullback had approximately one frame every 0.5 mm. Second, image analysis of the ECG-triggered IVUS pullbacks was performed using QCU-CMS software (Version 4.69, Division of Image Processing, Leiden University Medical Centre, Leiden, The Netherlands), external elastic membrane (EEM) and lumen borders were delineated semi-automatically. Vessel WT was determined as the distance between lumen and EEM contours. An intra-observer analysis was performed in a random sample of 5 IVUS pullbacks (748 frames) with at least two months interval between the segmentations. A good reproducibility of EEM area, lumen area, and plaque area was found with an interclass correlation coefficient of respectively 0.996 (95%CI 0.996– 0.997), 0.983 (95%CI 0.963–0.990), and 0.958 (95%CI 0.939–0.970).

Since WT cannot be reliably quantified in regions with extensive calcification by IVUS<sup>1</sup>, sectors with calcifications > 90° of the vessel circumference were excluded. Likewise, sectors were excluded<sup>17</sup> in case EEM was not reliably visualized by IVUS due to any other reasons (eg. attenuation). Subsequently, all analysed wall sectors were stratified into thin ('plaque-free', WT by IVUS <0.5 mm) or thick ('plaque-containing', WT by <sup>3</sup>0.5mm) wall sectors using the previously described WT cut-off value of 0.5 mm<sup>18</sup>.

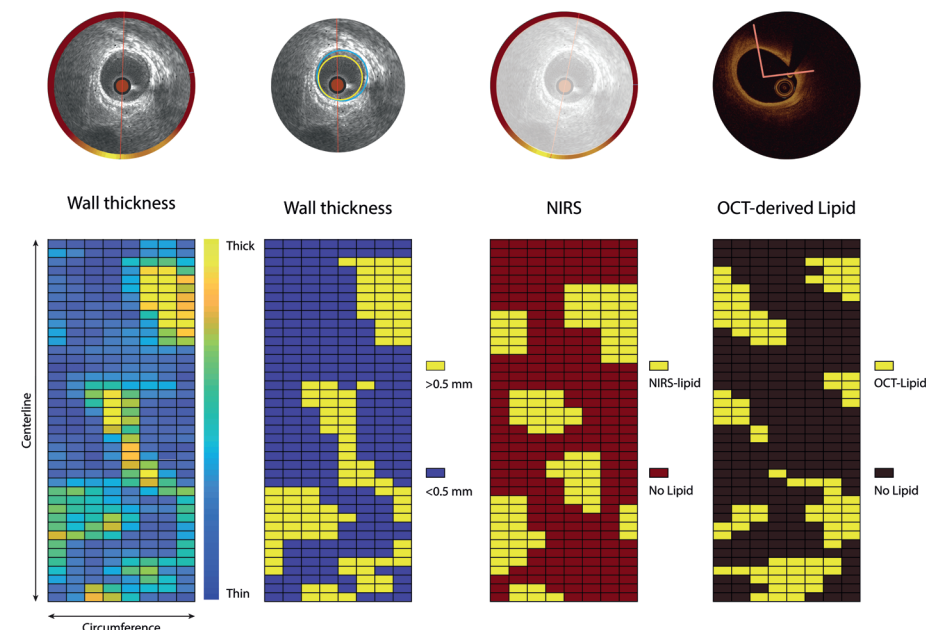


**Figure 1. Methodology of sectorial wall thickness quantification.**

A division into paired 1.5-mm segments of 45° sectors has been selected to ensure maximal overlap of the baseline and follow-up IVUS data, even in the presence of small registration errors (max ±1 IVUS frame), thereby maximally accounting for spatial heterogeneity in wall thickness changes. IVUS: intravascular ultrasound, NIRS: near-infrared spectroscopy, OCT: optical coherence tomography

### OCT analysis

OCT pullbacks were analysed every millimetre (1 out of every 5 frames) using the QCU-CMS software following the previously published OCT analysis consensus standards<sup>19,20</sup>. Lumen contours were delineated semi-automatically. Lipid-rich plaque or lipid-pool were identified manually by indicating the angles with the protractor on the lumen centre.

### NIRS-IVUS and OCT matching and sector-level analyses

Baseline OCT data and segmented IVUS follow-up data were matched to the NIRS-IVUS baseline pullback, based on side branches visible in both modalities, both in longitudinal and axial direction. All matched pullbacks were divided into paired 1.5-mm segments and further divided into 8 circumferential 45° sectors (Figure 1), a division that was selected to ensure maximal overlap of the baseline and follow-up IVUS data, thereby allowing a maximally detailed analysis of spatial heterogeneity of WT changes.

For each degree in circumference, the presence of NIRS positive signal (a probability of 0,6 or higher for the presence of lipids), and the presence of OCT-detected lipid

was determined. The sector was considered NIRS positive or OCT-detected lipid positive, in case the lipid content exceeded 50% of the sector area. Sectorial WT-progression over the 12-month follow-up was defined as the difference between the 12-month and baseline WT.

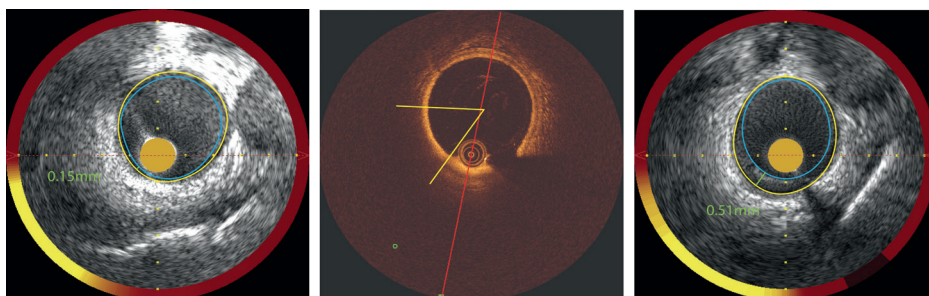


**Figure 2. Example of thin wall NIRS positive regions.**

**A/B:** Matched NIRS-IVUS and OCT cross-sections at baseline. Presence of NIRS signal and lipid plaque by OCT in the plaque free wall regions (wall thickness <0.5mm). **C:** Follow-up IVUS revealed artery wall thickening in the baseline NIRS-positive and OCT-lipid positive sectors. IVUS: intravascular ultrasound, NIRS: near-infrared spectroscopy, OCT: optical coherence tomography

### Statistical analysis

Continuous variables with normal distribution are presented as mean  $\pm$  standard deviation (SD), data with non-normal distribution are presented as median (25<sup>th</sup>-75<sup>th</sup> percentile). Categorical variables were displayed as counts and percentages. Differences in frequency distributions were evaluated using  $\chi^2$  tests. The association between presence of lipid (by either NIRS or OCT) (independent variable) and change in WT or sectorial PA (dependent variable) was analysed using linear mixed models. Presence of lipid was included as a fixed factor. To investigate the difference between plaque and plaque free wall, the variable baseline WT was dichotomized (thin vs thick) and used as a fixed factor. Random effects were included to account for the presence of multiple sectors in each vessel. Moreover, an unstructured covariance and correlation matrix was used for the random effects to account for the covariances and correlations of the sectors. In the figures presenting the association between the baseline NIRS signal or OCT-detected lipid and change in WT ( $\Delta$ WT), the estimated means and confidence intervals derived from these linear mixed models are presented. The Bonferroni correction was applied to adjust for multiple testing (repeating the analysis in above-described subgroups). Specifically, analyses were performed in the overall sectors as well as in the thin and thick wall sectors, as assessed by IVUS at baseline. Statistical analyses were performed using the IBM SPSS Statistics 27.0 software. A two-sided *p*-value of <0.05 was considered as significant.

### Results

Between March 2016 and March 2018, a total of 56 patients with ACS were included in the study and underwent NIRS-IVUS and OCT assessment of a non-culprit coronary artery after successful treatment of the culprit lesion at baseline.

Three patients were excluded during the baseline procedure, 4 patients withdrew consent at the 1-month follow-up, 8 patients refused consent for the 1-year invasive imaging procedure. In one patient there was no possibility of matching between computed tomography and invasive imaging data. As a result, a total of 40 patients with ACS underwent NIRS-IVUS and OCT assessment of a non-culprit coronary artery after successful treatment of the culprit lesion both at baseline and at 12-month follow-up. After excluding one patient due to insufficient quality NIRS data and 2 patients due to non-analysable OCT recordings, a total of 37 patients with 38 vessels were analysed at baseline and 12 months. Mean age was  $60 \pm 8.9$  years, 34 patients (91.7%) were male, 8 had diabetes (21.6%), 16 (43.2%) presented with dyslipidaemia. The median low-density lipoprotein (LDL) level at time of enrolment was  $2.8 [2.1-3.2]$  mmol/l. At baseline, 20 patients (54.1%) were on statin treatment (5 patients (13.5%) were on high intensity lipid-lowering treatment) while at follow-up 33 patients (89.2%) were using lipid lowering therapy (17 patients (45.9%) were on high-intensity lipid-lowering treatment). The baseline characteristics of the analysed population are detailed in Table 1.

Median length of the analysed segment was 50.3mm (36.4 - 58.5). After excluding sectors containing side branches or extensive (>90°) calcifications, 6936 corresponding sectors were analysed at baseline and 12 months. Overall, there were 4552 thin wall and 2384 thick wall sectors identified by IVUS at baseline. Median baseline WT was 0.42mm [0.17-0.61]. NIRS and OCT-lipid positivity was found in 140 (3.1%) and 513 (11.3%) of the 4552 thin wall sectors, respectively.

Conversely, a total of 140/406 (34.5%) NIRS positive sectors and 513/1575 (32.6%) OCT-lipid positive sectors were found to be located in sectors without vessel wall thickening by IVUS at baseline (WT <0.5mm).

Table 1.

Clinical characteristics	N = 37 patients
Age, years	60 ± 8.9
Men, n (%)	34 (91.9%)
Body Mass Index	27 ± 5.0
Diabetes Mellitus, n (%)	8 (21.6%)
Hypertension, n (%)	9(24.3%)
Dyslipidemia, n (%)	16(43.2%)
Current smoking, n (%)	9(24.3%)
Positive family history, n (%)	13(35.1%)
Previous MI, n (%)	8 (21.6%)
Previous PCI, n (%)	11(29.7%)
LDL (mmol/L)	2.8 [2.1-3.2]
Statin therapy	20 (54.1%)
High intensity lipid lowering*	5(13.5%)
Imaged study vessel N = 38 vessels	
LAD, n (%)	13(34%)
LCX, n (%)	10(26%)
RCA, n (%)	15(39%)
Imaged segment length, mm <sup>2</sup>	50.3(36.4-58.5)
Minimal lumen area, mm <sup>2</sup>	3.91(2.77-5.05)
Mean vessel area, mm <sup>2</sup>	1.89(1.62-2.10)
Percent atheroma volume, (%)	37.5(32.2-47.8)
Max LCBI <sub>4mm</sub>	275(166-393)

\* high-intensity lipid-lowering therapy: Rosuvastatin ≥20 mg or Atorvastatin ≥40 mg or PCSK9-inhibitor. LAD: left anterior descending artery; LCBI: lipid core burden index; LCX: left circumflex artery; LDL: low-density lipoprotein cholesterol; MI: myocardial infarction; PCI: percutaneous coronary intervention; RCA: right coronary artery

Changes in wall thickness over 12-month follow-up

A total of 37 patients (38 vessels,6936 matched sectors) were analysed at baseline and 12 months. A total of 140/406 (34.5%) NIRS(+) sectors and 513/1575 (32.6%) OCT-lipid(+) sectors were found to be located in the thin (WT<0.5mm) wall sectors. In the thin wall sectors, increase in WT was significantly more pronounced in NIRS(+) vs. NIRS(-) sectors: 0.11 mm (95%CI: 0.08- 0.13) vs. 0.06 mm (95%CI: 0.05-0.08), p<0.001). In the thick wall sectors, there was a decrease in WT observed, that was less pronounced in NIRS (+) vs. NIRS (-) sectors: -0.08mm (95%CI -0.10 - -0.05) vs. -0.09mm (95%CI -0.10 - -0.07), p<0.001) (Figure 3A).

Similarly, the thin wall sectors with OCT-detected lipids showed significantly greater WT increase than the thin wall sectors with no OCT-detected lipids (0.11 mm (95%CI: 0.7 - 0.14) vs 0.6mm (95%CI:0.04 - 0.08), p<0.001) (Figure 3B).

The thin wall NIRS(+) OCT-lipid(+) sectors showed significant wall thickening (DWT = 0.13 mm (95%CI: 0.08-0.17)) over 12-month follow-up (Figure 4).

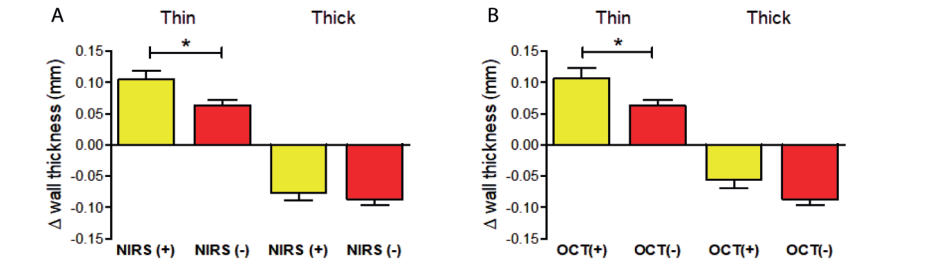


Figure 3. Wall thickness progression in thin and thick wall sectors, as assessed by IVUS at baseline. Yellow: lipid-rich positive sectors, Red: non-lipid rich sectors. A: Lipid content assessed by NIRS, B: Lipid content assessed by OCT. \*p<0.001.

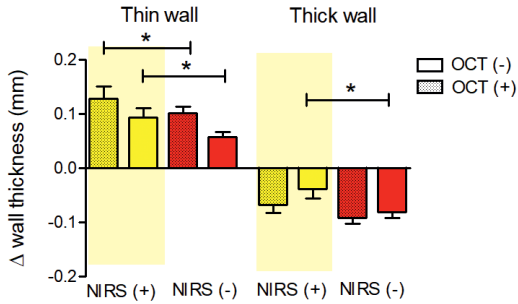


Figure 4. Wall thickness progression in thin and thick wall sectors lipid rich sectors both assessed by NIRS and OCT.

Discussion

The salient findings of this serial multimodality NIRS-IVUS and OCT imaging investigation could be summarized as follows: Surprisingly, nearly one-third of all identified NIRS positive sectors and one third of the overall OCT-detected lipid sectors were found in thin-wall non-culprit coronary artery regions, otherwise considered as ‘plaque-free’ sectors by IVUS, with baseline WT < 0.5 mm. NIRS signal imaged at baseline in thin artery wall regions was consistently associated

with high WT increase over 12-month follow-up, suggesting that NIRS evaluation of non-culprit coronary arteries by IVUS could indicate the regions with ongoing plaque initiation (before any structural plaque features become detectable by IVUS).

To the best of our knowledge, this is the first in-human demonstration of the association between NIRS signal, OCT-confirmed lipid content and subsequent long-term plaque progression. Previously, Patel et al. showed in diabetic and hypercholesterolemic pigs that 88% of NIRS(+) lesions developed into a fibroatheroma at 9 months follow up<sup>21</sup>. In the present study, baseline NIRS positivity proved to be associated with more pronounced WT increase at 12 months in non-culprit segments of patients presenting with ACS. Interestingly, the observed WT increase in NIRS(+) regions was not restricted to regions with clearly visible plaque (WT>0.5mm). Plaque growth was found to be significantly increased in NIRS(+) thin wall regions, to date typically perceived as non-diseased arteries by IVUS. It therefore may be hypothesized that NIRS 'chemically' captures very early stages of plaque growth characterized by intracellular lipid influx and accumulation<sup>12</sup>, even before it translates into the structural changes visible by IVUS. These findings above could have important clinical implications given that NIRS signal in artery regions without IVUS-defined wall thickening is typically considered as 'artefact'.

Considering the anticipated value of further division of the cross-sectional artery wall segments into sectors in the studies of coronary atherosclerosis<sup>22</sup>, we have chosen to evaluate plaque progression at a sector level, analysing the sectorial changes in WT as the outcome measure in this study. By doing so, significant granularity was added to our methods which allowed us to precisely characterize the local heterogeneity in plaque growth, extending the observations from prior studies that described changes in cross sectional plaque burden only<sup>1-5,23,24</sup>.

The risk of major adverse cardiac events proved to increase with higher intraplaque lipid content. Patients with a maximum lipid core burden index in a 4-mm length of artery (maxLCBI4mm)<sup>3</sup> 400, lesions were at a four-fold higher risk of future events as compared to those with a maxLCBI4mm <400<sup>11</sup>. Recently, a cross-sectional *in vivo* analysis of the morphological features of NIRS-detected lipid rich plaques showed that NIRS positive plaque exhibit OCT and IVUS features of presumed plaque vulnerability, correlating positively with increasing lipid content<sup>25</sup>. Yamamoto et al. previously reported that OCT-detected lipid component is a precursor for a rapid plaque progression<sup>24</sup>. Our work extends these observations by demonstrating that NIRS positivity can act as a predictor of plaque growth in non-culprit coronary arteries of ACS patients, even in thin wall artery regions.

In the present study, NIRS+ thin wall regions were apparent despite statin use at baseline in 54% of patients while the plaque growth at 12 months should be interpreted in light of routine high-intensity statin recommendation post ACS in all individuals. The latter might stimulate future research assessing the impact of more aggressive and costlier lipid lowering therapy including novel agents such as PCSK 9 antagonists, even in case the positive NIRS signals are imaged within thin – apparently non-diseased – artery regions, as assessed by IVUS. In the present study, high-intensity statins or PCSK 9 inhibitors were administered in less than half of the patients over the course of the study, indicating a potential for streamlined imaging-based up titration of costly adjunctive lipid lowering therapy. Nevertheless, the clinical benefits of such a therapeutic approach would need to be confirmed in a dedicated randomized trial.

## Limitations

Although the presented study is the largest to date focusing on serial invasive imaging with combined use of NIRS-IVUS and OCT to study plaque progression, our findings warrant confirmation in larger studies. Despite IVUS ability to generate high-resolution imaging of the entire thickness of the coronary artery wall permitting evaluation of the entire burden of atherosclerotic plaque, it has been shown that large calcification may hinder reliable assessment of wall thickness by IVUS<sup>1</sup>. Given the abovementioned considerations, artery wall regions with large calcium deposits (>90° of vessel circumference) have been excluded from the present analysis<sup>17,26</sup>. As a result, our study was not designed to determine the association between presence of calcifications at baseline and plaque progression.

The threshold for division of artery wall regions into 1.5-mm 45° sectors has been chosen to enhance matching accuracy. These matching/postprocessing procedures were internally validated and demonstrated a high reproducibility and accuracy of sector matching; still, some minimal degree mismatch between the regions of interests analysed by the two intravascular imaging modalities as well as the follow-up pullback cannot be excluded.

Arguably lipid lowering therapy in our cohort was subpar per society guidelines that recommend high-dose statins in the context of ACS. Yet, routine clinical follow-up was typically performed outside our tertiary care institution and might reflect real world practice in which more than 50% of patients treated with statins do not achieve their target LDL-C levels or cannot tolerate effective statin doses<sup>27</sup>.



## Conclusions

NIRS positive signal and OCT-detected lipid plaque components at baseline in non-culprit coronary arteries could identify wall regions prone to WT increase over 12-month follow-up. NIRS positive signal and OCT-derived lipid plaque might be detected in otherwise non-diseased vessel wall arteries as assessed by IVUS, having a value as predictors of early plaque growth and plaque progression in non-culprit coronary arteries. Therefore, NIRS positive signal in areas without evident wall thickening by IVUS should no longer be viewed as benign or imaging artefact in clinical practice.

## Impact on daily practice

NIRS positive signals in otherwise non-diseased arterial walls as assessed by IVUS – typically perceived as artefacts – could identify vessel wall regions prone for wall thickness increase over 12-month follow-up. Such positive NIRS signals within the areas without evident artery wall thickening might represent a very early stage of coronary atherosclerosis and thus have a value as predictors of early plaque development in non-culprit coronary arteries. Insights from this dedicated serial multimodality intravascular imaging study improve the understanding of the natural course of coronary atherosclerosis and in this context, especially early stages of atherosclerosis could help to identify potential therapeutic targets. NIRS positive signals in areas without evident wall thickening by IVUS should no longer be viewed as benign or imaging artefact.

## References

1. Mintz GS, Garcia-Garcia HM, Nicholls SJ, Weissman NJ, Bruining N, Crowe T, et al. Clinical expert consensus document on standards for acquisition, measurement and reporting of intravascular ultrasound regression/progression studies. *EuroIntervention* 2011;6:1123–30, 9.
2. Tardif J-C, Grégoire J, L'Allier PL, Anderson TJ, Bertrand O, Reeves F, et al. Effects of the acyl coenzyme A:cholesterol acyltransferase inhibitor avasimibe on human atherosclerotic lesions. *Circulation* 2004;110:3372–7.
3. Nissen SE, Tuzcu EM, Schoenhagen P, Brown BG, Ganz P, Vogel RA, et al. Effect of intensive compared with moderate lipid-lowering therapy on progression of coronary atherosclerosis: a randomized controlled trial. *JAMA* 2004;291:1071–80.
4. Kubo T, Maehara A, Mintz GS, Doi H, Tsujita K, Choi S-Y, et al. The dynamic nature of coronary artery lesion morphology assessed by serial virtual histology intravascular ultrasound tissue characterization. *J Am Coll Cardiol* 2010;55:1590–7.
5. Nissen SE, Nicholls SJ, Sipahi I, Libby P, Raichlen JS, Ballantyne CM, et al. Effect of very high-intensity statin therapy on regression of coronary atherosclerosis: The ASTEROID trial. *J Am Med Assoc* 2006;295:1556–65.
6. Eisen HJ, Tuzcu EM, Dorent R, Kobashigawa J, Mancini D, Valentine-von Kaeppler HA, et al. Everolimus for the prevention of allograft rejection and vasculopathy in cardiac-transplant recipients. *N Engl J Med* 2003;349:847–58.
7. Jensen LO, Thayssen P, Pedersen KE, Stender S, Haghfelt T. Regression of coronary atherosclerosis by simvastatin: a serial intravascular ultrasound study. *Circulation* 2004;110:265–70.
8. Okazaki S, Yokoyama T, Miyauchi K, Shimada K, Kurata T, Sato H, et al. Early statin treatment in patients with acute coronary syndrome: demonstration of the beneficial effect on atherosclerotic lesions by serial volumetric intravascular ultrasound analysis during half a year after coronary event: the ESTABLISH Study. *Circulation* 2004;110:1061–8.
9. Schuurman A-S, Vroegindewey M, Kardys I, Oemrawsingh RM, Cheng JM, de Boer S, et al. Near-infrared spectroscopy-derived lipid core burden index predicts adverse cardiovascular outcome in patients with coronary artery disease during long-term follow-up. *Eur Heart J* 2018;39:295–302.
10. Oemrawsingh RM, Cheng JM, García-García HM, van Geuns R-J, de Boer SPM, Simsek C, et al. Near-Infrared Spectroscopy Predicts Cardiovascular Outcome in Patients With Coronary Artery Disease. *J Am Coll Cardiol* 2014;64:2510–8.
11. Waksman R, Di Mario C, Torguson R, Ali ZA, Singh V, Skinner WH, et al. Identification of patients and plaques vulnerable to future coronary events with near-infrared spectroscopy intravascular ultrasound imaging: a prospective, cohort study. *Lancet* 2019;394:1629–37.
12. Libby P, Hansson GK. From Focal Lipid Storage to Systemic Inflammation: JACC Review Topic of the Week. *J Am Coll Cardiol* 2019;74:1594–607.
13. Kang S-J, Mintz GS, Pu J, Sum ST, Madden SP, Burke AP, et al. Combined IVUS and NIRS Detection of Fibroatheromas: Histopathological Validation in Human Coronary Arteries. *JACC Cardiovasc Imaging* 2015;8:184–94.
14. Roffi M, Patrono C, Collet J-P, Mueller C, Valgimigli M, Andreotti F, et al. 2015 ESC Guidelines for the management of acute coronary syndromes in patients presenting without persistent ST-segment elevation: Task Force for the Management of Acute Coronary Syndromes in Patients Presenting without Persistent ST-Segment Elevation of. *Eur Heart J* 2016;37:267–315.
15. Hartman EMJ, De Nisco G, Kok AM, Hoogendoorn A, Coenen A, Mastik F, et al. Lipid-rich Plaques Detected by Near-infrared Spectroscopy Are More Frequently Exposed to High Shear Stress. *J Cardiovasc Transl Res* 2020.

16. Hoogendoorn A, den Hoedt S, Hartman EMJ, Krabbendam-Peters I, Te Lintel Hekkert M, van der Zee L, et al. Variation in Coronary Atherosclerosis Severity Related to a Distinct LDL (Low-Density Lipoprotein) Profile: Findings From a Familial Hypercholesterolemia Pig Model. *Arterioscler Thromb Vasc Biol* 2019;39.
17. Mintz GS, Nissen SE, Anderson WD, Bailey SR, Erbel R, Fitzgerald PJ, et al. American College of Cardiology clinical expert consensus document on standards for acquisition, measurement and reporting of intravascular ultrasound studies (ivus): A report of the american college of cardiology task force on clinical expert consensus do. *J Am Coll Cardiol* 2001;37:1478–92.
18. Tuzcu EM, Kapadia SR, Tutar E, Ziada KM, Hobbs RE, McCarthy PM, et al. High prevalence of coronary atherosclerosis in asymptomatic teenagers and young adults: evidence from intravascular ultrasound. *Circulation* 2001;103:2705–10.
19. Tearney GJ, Regar E, Akasaka T, Adriaenssens T, Barlis P, Bezerra HG, et al. Consensus standards for acquisition, measurement, and reporting of intravascular optical coherence tomography studies: A report from the International Working Group for Intravascular Optical Coherence Tomography Standardization and Validation. *J Am Coll Cardiol* 2012;59:1058–72.
20. Johnson TW, Räber L, Di Mario C, Bourantas C, Jia H, Mattesini A, et al. Clinical use of intracoronary imaging. Part 2: acute coronary syndromes, ambiguous coronary angiography findings, and guiding interventional decision-making: an expert consensus document of the European Association of Percutaneous Cardiovascular Interventions Interventional cardiology. *Eur Heart J* 2019;0:1–19.
21. Patel DD, Hamamdžić D, Llano R, Patel DD, Cheng L, Fenning RS, et al. Subsequent development of fibroatheromas with inflamed fibrous caps can be predicted by intracoronary near infrared spectroscopy. *Arterioscler Thromb Vasc Biol* 2013;33:347–53.
22. Timmins LH, Molony DS, Eshtehardi P, McDaniel MC, Oshinski JN, Samady H, et al. Focal Association Between Wall Shear Stress and Clinical Coronary Artery Disease Progression. *Ann Biomed Eng* 2014;43:94–106.
23. Nissen SE, Tuzcu EM, Libby P, Thompson PD, Ghali M, Garza D, et al. Effect of antihypertensive agents on cardiovascular events in patients with coronary disease and normal blood pressure: the CAMELOT study: a randomized controlled trial. *JAMA* 2004;292:2217–25.
24. Yamamoto MH, Yamashita K, Matsumura M, Fujino A, Ishida M, Ebara S, et al. Serial 3-Vessel Optical Coherence Tomography and Intravascular Ultrasound Analysis of Changing Morphologies Associated With Lesion Progression in Patients With Stable Angina Pectoris. *Circ Cardiovasc Imaging* 2017;10.
25. Zanchin C, Ueki Y, Losdat S, Fahrni G, Daemen J, Ondracek AS, et al. In vivo relationship between near-infrared spectroscopy-detected lipid-rich plaques and morphological plaque characteristics by optical coherence tomography and intravascular ultrasound: a multimodality intravascular imaging study. *Eur Hear J - Cardiovasc Imaging* 2020;0:1–11.
26. Hartman EMJ, Hoogendoorn A, Akyildiz AC, Schuurman A-S, van der Steen AFW, Boersma E, et al. Colocalization of Intracoronary Lipid-Rich Plaques and Calcifications. *JACC Cardiovasc Imaging* 2020.
27. Koskinas KC, Gencer B, Nanchen D, Branca M, Carballo D, Klingenberg R, et al. Eligibility for PCSK9 inhibitors based on the 2019 ESC/EAS and 2018 ACC/AHA guidelines. *Eur J Prev Cardiol* 2021;28:59–65.



# 11

**General discussion**

Atherosclerosis is a lipid-driven inflammatory disease leading to myocardial infarctions and subsequent morbidity and mortality<sup>1</sup>. In the last decades, much research has been done into atherosclerosis from different working fields' perspectives. Both clinicians and engineers have researched the process of atherosclerosis development. In daily practice, there is still a distance between the clinician and the engineer when studying coronary atherosclerosis. In this thesis, we used clinically available imaging techniques and computational fluid dynamics to analyse biomechanical forces of the bloodstream on the vessel wall, such as wall shear stress (WSS).

We sought to unravel the mystery of atherosclerotic plaque development using state-of-the-art multimodality imaging and computational techniques in a patient study and an animal model of atherosclerosis. The different atherosclerotic plaque components visible with intravascular imaging were correlated with WSS and the multidirectionality of the blood flow to investigate their interaction in the development and progression of plaques. Furthermore, we compared different approaches for WSS distribution to assess the impact of WSS on specific outcome parameters. Finally, the WSS distribution in 3D geometries was compared based on various imaging techniques.

In this thesis, **Chapters 2, 5-8 and 10** were based on data collected in the IMPACT study (**I**maging and **M**odelling to investigate the mutual relationship of plaque growth and biomechanical **P**arameters in human **C**oronary **a**rTeries), a dedicated clinical prospective multimodality imaging study designed to investigate the effect of local WSS and plaque composition on wall thickness progression at 1-year in non-culprit vessels of patients presenting with acute coronary syndrome. In **Chapters 3, 4 and 8**, a new porcine model was used to study atherosclerotic plaque development in a preclinical setting allowing invasive imaging at multiple timepoints and detailed tissue collection. Both studies used intravascular imaging as well as computational fluid dynamics to research the influence of WSS on plaque progression. Finally, in **Chapter 9**, we performed an extensive retrospective analysis of all NIRS-IVUS dual imaging catheter data available in the Erasmus MC to investigate the colocalisation of various plaque components.

In this final chapter, the new insights described in this thesis are discussed concerning the impact and clinical applicability and future perspective in coronary atherosclerosis research.

## WSS in coronary atherosclerotic research

In this thesis, we tried to understand the effect of the biomechanical force of blood flow on the vessel wall, i.e. the impact of WSS on atherogenesis. However, since the introduction of WSS in coronary artery disease research, different definitions and methods for determining "low" and "high" WSS thresholds have been used<sup>2-6</sup>. When defining quantifying WSS, both absolute numbers and relative thresholds (e.g. the lowest tertile of WSS within an exposed vessel wall) have been used. In **Chapter 2**, we review the different methodologies described in the literature to define thresholds for low and high WSS. Subsequently, four different methods were used to determine low and high WSS in our dataset. First, *study-specific tertiles*, allocating one-third of all sectors (1.5mm\*45 degrees) in the study as low WSS<sup>7</sup>. Second, *vessel-specific tertiles*, focussing on the local patched distribution of the vessel, allocating one-third of the sectors in each vessel as low WSS<sup>8</sup>. Third, by allocating one-third of all sectors of a specific coronary (e.g. LAD) as low WSS, *vessel type-specific tertiles*. Finally, an absolute cut-off threshold for low WSS, based on literature, *literature-based thresholds*<sup>4</sup>. The predictive value of the different methods on plaque progression was compared.

Several differences in geometry reconstruction and CFD models between research groups should be considered to understand the differences in defining low and high WSS. For example, we included side branches and patient-specific invasive flow measurements in our study, where some studies removed side branches, and others used a standardised inflow. Using a 3D model without side branches, all flow remains in the main coronary branch. Due to the natural tapering of the coronary artery more distal in the vascular tree, absolute WSS values will increase and might become artificially elevated in distal parts of the studied coronary branch<sup>6</sup>. Despite these differences in 3D reconstruction, most previous studies used the same absolute thresholds for defining low WSS<sup>7,9</sup>. One major finding described in this chapter is the heterogeneity in the absolute WSS distribution between the coronary arteries of different patients. When using the often-applied absolute thresholds based on previous literature, several vessels in this current dataset would almost completely be categorised as being exposed to low WSS. Another method used to determine low WSS is dividing the sectors of each vessel or all the study segments into three equal groups (i.e., tertiles). Thus, low and high WSS are relative to the observed absolute range. Even when dividing the complete dataset into three equal groups (study-specific tertiles), some vessels were almost completely exposed to the study-specific defined low WSS value.

Interestingly, relative vessel-specific thresholds showed the highest absolute plaque progression in the regions exposed to low WSS, indicating that this definition of low WSS has the highest potential in predicting areas at risk of plaque



progression. Applying this methodology, each vessel has, per definition, one-third of the data allocated as low WSS, thereby acknowledging the patchy distribution of plaque progression observed in earlier studies<sup>10</sup>. Since the *distribution* of the WSS over the vessel is entirely determined by the 3D geometry, it is the geometry that identifies regions exposed to low WSS, independent of the flow. The consequence of this finding is that the invasive flow measurements become redundant when using vessel-specific thresholds to determine low WSS.

One remark has to be made when using vessel-specific thresholds: the number of segments per vessel must be sufficient and cover the complete circumference of the coronary artery to capture and include the spatial heterogeneity present in the arteries. Therefore, similar to previous research, we divided vessels into smaller local sectors (1.5mm\*45 degrees) to analyse WSS at a local level<sup>11</sup>. This equals eight circumferential sectors per segment of 1.5mm and comprises the spatial heterogeneity of the WSS better than averaging WSS out over the whole circumference of the vessel<sup>12</sup>.

However, several studies included the heterogeneity of the segment in their study by identifying the lowest WSS averaged over a 90 degrees angle in the segment<sup>4,13</sup>. By doing so, only one data point per segment is analysed compared to the much more detailed analysis in which eight sectors per segment are used as described in this thesis. Using vessel-specific thresholds with a low number of segments will reduce the accuracy of the estimates and thus the applicability of this methodology.

A remarkable finding described in this chapter is the differences found in the relationship between low WSS and plaque progression in the different coronary vessels. Especially the differences in WSS-related plaque progression between the left circumflex (LCX) versus the left anterior descending (LAD) artery and right coronary artery have never been described before. The absolute WSS differed the most between the LAD and the LCX. Although the LCX showed the highest absolute WSS, these sectors showed more plaque progression than LAD sectors, which were exposed to lower absolute WSS. These WSS-related plaque growth differences might be attributed to geometrical variations, the number of side branches, and more local hemodynamics such as multidirectional WSS. Unfortunately, the current analysis did not allow a more detailed geometrical explanation for these differences, although differences between the coronary arteries have been observed before<sup>14</sup>. Future research, potentially using the multidirectional WSS metrics by combining geometry and time-dependent flow differences, might clarify the differences between the three coronary arteries.

In the last decade, several multidirectional shear stress parameters have been introduced to capture the multidirectionality of WSS during the cardiac cycle. The question is whether time-average WSS fully captures the regions at risk of plaque progression since endothelial cells might respond differently to temporal directional changes. In **Chapter 4**, both time-averaged WSS and several multidirectional shear stress metrics were associated with plaque development, composition, and growth. The imaging and histology data acquired from coronary arteries of the atherosclerotic pigs, as described in **Chapter 3**, were used to conduct this comprehensive biomechanical study. The porcine model in this study demonstrated that plaque progression was most enhanced in regions of low time-averaged WSS and high multidirectional WSS. Therefore, the time-averaged WSS and the variation during a cardiac cycle and multidirectionality of the WSS play a role in atherosclerotic disease development. For example, regions with high oscillatory behaviour of the blood flow are prone to plaque development. In contrast to promising findings in earlier research, none of the multidirectional shear stress metrics stood out or performed better than time-averaged WSS to predict plaque progression<sup>15,16</sup>. This might be explained by the fact that we used the relative distribution of WSS in each study vessel for all multidirectional WSS metrics.

### Porcine models versus human studies in coronary atherosclerosis research.

Animal models have a pivotal role in understanding the atherosclerotic disease process<sup>17</sup>. One of the significant advantages of animal research is the possibility of monitoring the initial atherogenesis and progression of atherosclerosis with multiple serial in-vivo imaging analyses and the potential to have final histological confirmation of the observed findings. The new porcine model with a homozygous LDLR-R84C mutation used in **Chapter 3** was introduced to study human-like coronary atherosclerosis development. The minipigs used were of adult age when enrolled in the study, and thus interfering ageing-related vessel growth was ruled out.

In **Chapters 2, 5-6**, the IMPACT study has been described, a patient study with serial imaging of non-culprit arteries of patients presenting with an acute coronary syndrome. In contrast to the animal study with barely any atherosclerosis at baseline presented in **Chapters 3-4**, the patient study showed already atherosclerosis in varying stages at baseline. Furthermore, there was an essential difference between the two study designs. In the animal study, the goal was to visualise plaque development, and stimulation of the atherosclerosis process was desired. The animals had an LDL-receptor mutation and were put on a high-fat diet to stimulate atherosclerotic plaque progression. This was in contrast to the patient

study, where we wanted to minimise the risk of a recurrent event and slow down the natural process of atherosclerosis. The patients were treated according to the latest guidelines, including high-dose cholesterol-lowering treatment and lifestyle advice to slow down the plaque progression or ideally induce plaque regression<sup>18,19</sup>.

The animal study, as conducted with this new porcine model, was a unique opportunity to investigate atherogenesis with multiple invasive imaging techniques and repeated measurements at three-time points and finally using histology to characterise the tissue further. After the high-fat diet, half of the pigs developed large, lumen intruding plaques. Some of these plaques showed unstable and vulnerable features, resembling patient-like plaques. However, the majority of the vessel walls contained lipid-rich fibroatheromas with a thick to very thick fibrous cap. Previous OCT and NIRS research found an inverse relationship between the detected lipid core and the cap thickness<sup>20</sup>. This might suggest that thick to very thick fibrous caps influence the detection capability of a lipid pool when using clinically available intravascular imaging techniques. Optical coherence tomography (OCT) and near-infrared spectroscopy-intravascular ultrasound (NIRS-IVUS) are calibrated and optimised for use in patients and evaluating human plaques. For example, only a few NIRS-positive plaques were found in the pig study, indicating a low number of lipid pools based on NIRS-imaging. However, histology confirmed necrotic cores and thus lipid pools present in these animals. Presumably, the thick caps in the fast-growing animals and the limited penetration depth of the near-infrared light hampered the necrotic cores and thus limited lipid pools from view when using intravascular image modalities, leading to underestimating of the number of detected fibroatheromas imaged *in vivo* in animals<sup>21</sup>. However, from a clinical perspective, these thick fibrous cap fibroatheromas with stable plaque features might be less relevant to research.

Another difference observed between the atherosclerotic plaques of this pig model and the plaques in human coronary arteries is the total amount of calcium burden. The calcifications in the pigs were found at the medial border of the arteries. This is in contrast to the calcifications found in the non-culprit arteries of the patients, having more extensive calcifications and were more often localised towards the luminal side of the vessel wall. Animal models help research atherogenesis and plaque initiation, although obtaining similar and realistic human-like lesions in animal models is still challenging. Nevertheless, when introducing and testing new intravascular imaging methodologies and for the intensive research of pathophysiological processes, as demonstrated in this thesis, large human-size coronary arteries in animal models of atherosclerosis are still crucial to validate the findings with histology<sup>22–24</sup>.

### Differences in WSS analysis between human and porcine study

In **Chapter 4**, multidirectional shear stress metrics and WSS analysis were performed in the porcine model described in **Chapter 3**. The imaging analysis, 3D reconstruction, and computational fluid dynamics methodology were similar to the patient study described in **Chapters 2, 5–6**. However, when investigating the effect of WSS on plaque progression, there are some noticeable differences between the patient and the porcine studies. As mentioned above, there were differences in the disease stage of the atherosclerotic process between the porcine study and the patient study. More advanced atherosclerosis affects the lumen and causes wall irregularities. The local WSS magnitude is affected by flow, lumen area, vessel curvature and side branches<sup>25</sup>. A slight variation in lumen size significantly impacts the calculated WSS<sup>26</sup>. In the porcine model, baseline 3D-reconstructed lumen models were smooth and were barely affected by atherosclerosis. Whereas, in human coronary arteries, the process of plaque development and growth is an ongoing process over decades. Indeed, the patients included in the IMPACT study had advanced atherosclerosis leading to an acute coronary syndrome at the time of inclusion. Since atherosclerosis is a systemic disease affecting all arteries, the studied non-culprit vessel had to some extent, atherosclerosis present. Although these vessels did not have flow-limiting stenosis, some were already severely affected by atherosclerosis. Consecutively, atherosclerosis leads to plaque burden and lumen variation, affecting WSS magnitude. However, with vessel-specific thresholds, one-third of the vessel is always exposed to low WSS, independent of the magnitude of the WSS. Still, both in the patient as well as in the animal study, the association of the lowest one-third WSS with plaque progression was found.

In **Chapter 8**, a comparison of the hemodynamics of the coronary arteries was made between the porcine model and the patient in the IMPACT study. Interestingly, despite different disease stages (human vs porcine) when depicted, no relevant differences were found in WSS-based quantities, intravascular hemodynamics and anatomical features between human and porcine models. Unfortunately, plaque progression was not yet studied in this study. However, the outcomes of **Chapter 4** and **Chapter 6** suggest that the biomechanical and hemodynamic effects on plaque progression are similar in the porcine model and the patient study, despite the different atherosclerotic disease stages. Both chapters show the highest plaque progression at low shear stress.

### Lipid detection using OCT versus NIRS-IVUS

In the last decades, intravascular imaging-derived metrics have been used to identify the so-called “vulnerable plaque”. Characteristics of a vulnerable plaque were based on previous histological data and defined as a large lipid core with a thin fibrous cap(<65mm)<sup>27</sup>. The previous PROSPECT and AtheroRemo-IVUS

study used greyscale and radiofrequency intravascular ultrasound to relate plaque composition to events<sup>28,29</sup>. However, intravascular ultrasound is limited in identifying lipid pools in coronary plaques<sup>30</sup>. In contrast, near-infrared spectroscopy (NIRS) was introduced as an intravascular imaging technique to detect the presence of lipids in the plaque. The IBIS-3 and, recently, the LRP-study related the presence of lipids as detected by NIRS to events<sup>31,32</sup>. As a result of combining NIRS and IVUS, lipids and plaque volume can be detected using a single NIRS-IVUS pullback<sup>33</sup>. Optical coherence tomography (OCT), conversely, is a light-based imaging technique with the capability of imaging the superficial vessel wall in great detail due to a high resolution (10µm) at the cost of a lower penetration depth in high attenuating tissues, such as lipid-rich plaques. The latter precludes volumetric plaque measurements based on OCT<sup>34</sup>. In the IMPACT study, we used NIRS-IVUS and OCT to identify the specific types of plaque. In **Chapters 6 and 10**, both modalities were used to identify lipid-rich sectors and fibrous/non-lipid-rich plaque sectors. The number of detected lipid-rich sectors by OCT was much higher than by NIRS. One of the reasons might be that only the slightest presence of lipid in the plaque can cause absorption and attenuation of the light-based signal on OCT<sup>34</sup>, losing the external elastic membrane in the image for the expert observer, wherein the NIRS analysis, the classification of lipids is based on an automated algorithm based on the probability of the presence of lipids.

Similarly, we encountered NIRS positive regions without visible intima thickening on the greyscale IVUS images. These NIRS-positive regions were initially interpreted as imaging artefacts, the multimodality imaging data from the IMPACT study allowed for further validation of this subset of NIRS-positive lesions (**Chapter 10**). This study was the first to study the morphometric details of these lipid-positive regions with no visible intima thickening on IVUS and thus a thin-wall region and concluded that these plaques developed differently after one-year follow-up compared to thin-wall regions without NIRS-detected lipids. We found that the thin wall lipid-positive regions showed more enhanced plaque progression after one year of follow-up compared to thin wall non-lipid-rich lesions. OCT imaging data confirmed the lipid-positive NIRS signal, ensuring that this phenomenon was not an imaging artefact. These thin regions with NIRS positive signal showed increased plaque progression comparable with NIRS positive regions with intima thickening. Therefore, it may be hypothesised that NIRS' chemically' captures very early stages of plaque growth characterised by intracellular lipid influx and accumulation, even before it translates into the structural changes visible by IVUS. The underlying pathophysiological process for this observation in thin wall regions might be early atherogenesis along with lipid infiltration and macrophages presence before wall thickness increases by extracellular fibrous tissue<sup>35</sup>. Thus, we potentially visualised an early phase in the plaque development process.

## Lipids, inflammation, WSS and plaque progression.

In **Chapter 6**, both NIRS-IVUS and OCT imaging were used to investigate the interaction between WSS and plaque composition on plaque growth. Lipid-rich plaque showed most plaque progression after a one-year follow-up. It demonstrated that the effect of low WSS on plaque progression was still apparent in these already developed atherosclerotic regions. There was a synergistic effect between the presence of lipids and WSS, suggesting a potential combined effect on plaque progression. Interestingly, this effect was not present in the lipid-negative plaque regions, identified by NIRS-negative regions with a wall thickness > 0.5mm and fibrous plaque detected by OCT. One might hypothesise that the inflammatory state of lipid-rich plaque and the endothelial dysfunction caused by low WSS mutually influence each other, thereby accelerating the process of plaque progression.

Another important finding of this chapter was significant WSS-related wall thickness progression in plaque-free wall regions, confirming the often described role of low WSS in plaque initiation<sup>36,37</sup>. Even though no plaque was visible at baseline, the regions exposed to low WSS had minimal but significant plaque progression, in contrast to plaque-free wall sectors exposed to mid or high WSS in which no significant increase in wall thickness was observed. Unfortunately, with our current methodology, the plaque characteristics and composition of the sectors adjacent to those classified as plaque-free are not considered when analysing these plaque-free sectors' plaque progression and might warrant further research on the topic. To correct for any correlation and random effects between sectors, the individual vessel was added to the statistical model as a random factor using an unstructured covariance and correlation matrix for the sectors in the vessel. This is a conservative method to avoid any potential correlation effect between the sectors within a vessel. However, based on the literature, we know that these regions distal from a plaque are often exposed to low WSS and oscillatory flow<sup>38</sup>. It would be interesting to study if plaque-free wall sectors adjacent to the plaque exhibit differential growth compared to plaque-free wall sectors more distant from a plaque. Future analysis and studies might provide more insight into the influence of the position of a sector related to the composition and location of an adjacent sector.

Thus, lipid-rich sectors exposed to low WSS showed the most plaque progression in our study. However, not all lipid-rich sectors are exposed to low WSS. In **Chapter 5**, an observational study was included in which atherosclerotic plaques containing lipids as detected by NIRS were evaluated for their exposure to low and high WSS compared to plaques that do not have NIRS-detected lipids. The observation that lipid-rich plaques were most often exposed to high WSS might have consequences for the pathophysiology of these plaques. From large clinical trials in the last

decade, we know that a high lipid burden is related to future events<sup>31,32</sup>. Exposure to high WSS is one of the pathological factors that might play a role in the evolution from a lipid-rich plaque to a ruptured plaque leading to myocardial infarction. High WSS was previously related to fibrous cap thinning<sup>39–41</sup>. In the process of cap thinning, as soon as the structural stresses in the cap exceed the strength of the cap, a rupture will occur<sup>42</sup>. Showing colocalisation of high WSS and lipid-rich plaques might be the first step, from a biomechanical point of view, in understanding why lipid-rich plaques as detected by NIRS are associated with future cardiac events.

Inflammatory cells in the atherosclerotic plaque secrete matrix metalloproteinases, and these MMPs break down the extracellular matrix of the fibrous cap, affecting the structure and the strength of the cap<sup>43</sup>. Variations in blood pressure can directly lead to high structural stress leading to a plaque rupture and thus to an event.

These differences between low and high WSS described in these two chapters potentially describe two separate pathophysiological mechanisms<sup>40,44</sup>. Although most lipid-rich plaques are exposed to high shear stress (**Chapter 5**), these regions are prone to plaque progression whenever NIRS positive regions are exposed to low WSS (**Chapter 6**). A combined process of lipid-induced inflammation and endothelial dysfunction caused by low WSS might further amplify the atherosclerotic processes of inflammation and lipid accumulation. From a methodical point of view, in these non-culprit arteries with one-third exposed to low WSS, we can assume that regions exposed to low WSS are not lumen intruding plaques. Eventually, when these plaques grow, the compensatory vessel remodelling cannot maintain lumen size, and atherosclerotic plaque enters the lumen, causing the lumen to narrow<sup>45</sup>. Because the smallest lumen narrowing already influences WSS, these regions that first were exposed to low WSS later become exposed to high WSS due to narrowing.

### Vulnerable plaque and plaque components

The majority of atherosclerotic plaques are stable and rarely cause a cardiovascular event. In treating asymptomatic lesions, the number of patients needed to treat to prevent one event versus the number of patients needed to harm plays a crucial role in clinical decision-making. The ultimate imaging biomarker that identifies the one specific plaque or lesion that will eventually lead to a cardiovascular event has not yet been found<sup>46</sup>. However, some plaque features have already been associated with plaque vulnerability. For example, patients with a higher lipid core burden index, a marker for the extent of lipid content derived from a NIRS pullback, are more at risk for future events<sup>31,32</sup>. A high lipid core and plaques with a large plaque

burden (>70%) and minimal lumen area <4.0mm have been considered vulnerable features<sup>28</sup>.

Another plaque feature is the calcification of the plaque. Calcium is well-known in non-invasive coronary computed tomography and is incorporated in a quantitative risk score<sup>47,48</sup>. The CT-based calcium score is a generalised measure of the overall atherosclerosis burden for all three coronary arteries<sup>49</sup>. Calcifications are easily visible and thus detectable on intravascular ultrasound (IVUS), and extensive calcifications are associated with local plaque stability<sup>50–52</sup>. Using the multimodality NIRS-IVUS imaging catheter, lipid-rich and calcified plaques can be visualised simultaneously<sup>53</sup>. **Chapter 9** describes the colocalisation of NIRS positive signal, representing lipid-rich plaques with calcifications as detected by IVUS on three levels: cross-sectional, 4 mm segment, and vessel level. A remarkable colocalisation of lipid-rich and calcified plaque was found. Our observational study identified high segmental LCBI associated with high segmental IVUS-derived calcium scores. This suggests that these plaque characteristics should not be seen as separate entities. Combining both plaque features could enhance the prediction of future adverse events. With the newly developed automated segmentation of IVUS-derived calcium score and the combined NIRS-IVUS catheter, there is potential for an extensive retrospective analysis of studies using the NIRS-IVUS catheter<sup>54</sup>. Recent studies have already demonstrated that an increased IVUS-based calcium score is strongly associated with the long-term risk of POCE (all-cause mortality, stroke, myocardial infarction and revascularisation)<sup>55</sup>. Therefore, similar to the CT-based calcium score, it might be a generalised score for the atherosclerosis burden. It opens new opportunities for investigating calcified and lipid-rich plaque simultaneously on a large scale, potentially searching for a combined score and relating them to future events.

### Clinical applicability of WSS and future perspective

Since the analysis of intravascular imaging and the fusion with the CTA-derived 3D-centerline is a labour-intensive process, more and more studies are trying to capture the shear stress distribution and shear stress-related plaque progression based on a single imaging modality. Previously, 3D geometries based on biplane angiography or computed tomography angiography imaging have been used to investigate the shear stress distribution in the coronary arteries<sup>56–59</sup>. Although the imaging resolution of the 3D lumen using CTA and biplane angiography is lower than in research in which intravascular imaging was used, these methodologies allow the availability and applicability of shear stress in clinical practice. In **Chapter 10**, the WSS distribution of two reconstructions, one based solely on CTA and one on the fusion of IVUS and CTA, of the same coronary arteries was compared to validate the CTA-based geometries to the IVUS-CTA based



geometries. The absolute WSS values in the CTA-based geometries were higher than in the IVUS-CTA-based geometry. However, as discussed in **Chapter 2**, using the distribution of WSS and a relative measure for low WSS is more important than the absolute WSS value for predicting the location of plaque progression. Therefore, CTA-based geometries, having comparable results in WSS distribution, could be the next step to make shear stress analysis more applicable for larger datasets and contribute to clinical availability.

A first approach would be using retrospective study data with available clinical outcomes for this type of research. However, research not initially designed for WSS analysis will present several challenges. First, the datasets must be critically assessed for quality. For example, only CTAs with high image quality and sufficient contrast delivery in the coronary arteries should be used. Furthermore, two orthogonal views are needed to create a correct 3D centreline when applying intravascular imaging with an angiography-based centreline. However, one major benefit of retrospective analysis would be the direct availability of clinical follow-up to relate the calculated parameters to clinical events.

After conducting the research in this thesis, some questions have been answered, but multiple new questions have arisen. We focussed on the relationship between WSS and plaque progression. However, implementing this multimodality approach in routine clinical practice is still far away. So far, WSS has been used in research to understand the pathophysiology of atherosclerosis. One previous study, a sub-analysis of the FAME II trial, showed that proximal higher WSS predicts myocardial infarction<sup>56</sup>. However, it is essential to recall that all vessels studied in the FAME II sub-study had a fractional flow reserve (FFR)-based hemodynamically significant stenosis. In current guidelines, intermediate but hemodynamically significant stenosis based on FFR has a class 1A recommendation for treatment in European guidelines<sup>60</sup>. Therefore, the added value of high WSS in this specific subgroup has become redundant. However, in future research, it would be interesting to investigate the added predictive value of WSS in a subgroup with borderline FFR values.

Based on the currently available evidence, WSS is a predictor of atherosclerotic plaque development. In future in-silico trials, implementing WSS computations could further strengthen predictors models for atherosclerotic disease progression and adverse clinical events. However, in order to do so, shear stress calculation should be simplified to make shear stress more easily available. However, with Moore's law in mind, we know that computers will become faster and more capable of calculating CFD models in a shorter period over the coming years<sup>61,62</sup>. One illustrative example of the use of WSS in cardiovascular research and development is in the development and improvement of new coronary stents. The stent design

has an important influence on the local hemodynamics and low WSS<sup>63</sup>. Since low WSS distal behind the stent struts has been related to in-stent hyperplasia<sup>64</sup>, an optimal design to minimise exposure to low WSS might prove beneficial<sup>65,66</sup>.

Within this thesis, we aimed to enhance insights into the complexity of the atherosclerotic disease progression by focusing on the interaction of WSS and atherosclerotic plaque components at a local level. We could confirm the pivotal role of low WSS on initiation and progression. Furthermore, we showed that the local distribution of WSS in a vessel seems more critical than the absolute WSS value for the predictive value on plaque progression. Different imaging techniques were used to gain knowledge on interaction and plaque progression in coronary arteries. This thesis reconfirms the complexity of the pathophysiology of atherosclerosis, with both biomechanical forces, inflammation and lipid accumulation all contributing to plaque progression.

Although we were able to confirm previous findings using more comprehensive methods and where we could connect the dots between several items in the complex cascade of plaque initiation and plaque progression, new research arose. We believe the data we collected could be used to study further the role of biomechanical forces within the vessel wall, such as structural stresses in the plaque leading up to plaque rupture. Hopefully, this thesis is only the start of exploring the IMPACT data, and it will support and stimulate the multidisciplinary approach to investigating atherosclerosis and keep on combining the knowledge and different views of medical doctors, biologists, and engineers in the future.

## References

- Roth GA, Mensah GA, Johnson CO, Addolorato G, Ammirati E, Baddour LM, et al. Global Burden of Cardiovascular Diseases and Risk Factors, 1990-2019: Update From the GBD 2019 Study. *J Am Coll Cardiol* 2020;76:2982-3021.
- Stone PH, Coskun AU, Kinlay S, Clark ME, Sonka M, Wahle A, et al. Effect of Endothelial Shear Stress on the Progression of Coronary Artery Disease, Vascular Remodeling, and In-Stent Restenosis in Humans. *Circulation* 2003;108:438-44.
- Wentzel JJ, van der Giessen AG, Garg S, Schultz C, Mastik F, Gijzen FJH, et al. In vivo 3D distribution of lipid-core plaque in human coronary artery as assessed by fusion of near infrared spectroscopy-intravascular ultrasound and multislice computed tomography scan. *Circ Cardiovasc Imaging* 2010;3:e6-7.
- Bourantas CV, Zanchin T, Sakellarios A, Karagiannis A, Ramasamy A, Yamaji K, et al. Implications of the local haemodynamic forces on the phenotype of coronary plaques. *Heart* 2019;105:1078-86.
- Samady H, Eshtehardi P, McDaniel MC, Suo J, Dhawan SS, Maynard C, et al. Coronary Artery Wall Shear Stress Is Associated With Progression and Transformation of Atherosclerotic Plaque and Arterial Remodeling in Patients With Coronary Artery Disease. *Circulation* 2011;124:779-88.
- Giannopoulos AA, Chatzizisis YS, Maurovich-Horvat P, Antoniadis AP, Hoffmann U, Steigner ML, et al. Quantifying the effect of side branches in endothelial shear stress estimates. *Atherosclerosis* 2016;251:213-8.
- Stone PH, Saito S, Takahashi S, Makita Y, Nakamura SS, Kawasaki T, et al. Prediction of progression of coronary artery disease and clinical outcomes using vascular profiling of endothelial shear stress and arterial plaque characteristics: the PREDICTION Study. *Circulation* 2012;126:172-81.
- Chatzizisis YS, Toutouzas K, Giannopoulos AA, Riga M, Antoniadis AP, Fujinomi Y, et al. Association of global and local low endothelial shear stress with high-risk plaque using intracoronary 3D optical coherence tomography: Introduction of "shear stress score." *Eur Heart Journal-Cardiovascular Imaging* 2017;18:888-97.
- Eshtehardi P, McDaniel MC, Suo J, Dhawan SS, Timmins LH, Binongo JNG, et al. Association of Coronary Wall Shear Stress With Atherosclerotic Plaque Burden, Composition, and Distribution in Patients With Coronary Artery Disease. *J Am Heart Assoc* 2012;1.
- Caro GG. Discovery of the role of wall shear in atherosclerosis. *Arterioscler Thromb Vasc Biol* 2009;29:158-61.
- Molony DS, Timmins LH, Hung OY, Rasoul-Arzrumly E, Samady H, Giddens DP. An assessment of intra-patient variability on observed relationships between wall shear stress and plaque progression in coronary arteries. 2015.
- Timmins LH, Molony DS, Eshtehardi P, McDaniel MC, Oshinski JN, Samady H, et al. Focal Association Between Wall Shear Stress and Clinical Coronary Artery Disease Progression. *Ann Biomed Eng* 2014;43:94-106.
- Stone PH, Maehara A, Coskun AU, Maynard CC, Zaromytidou M, Siasos G, et al. Role of Low Endothelial Shear Stress and Plaque Characteristics in the Prediction of Nonculprit Major Adverse Cardiac Events. *JACC Cardiovasc Imaging* 2018;11:462-71.
- Chatzizisis YS, Giannoglou GD, Parcharidis GE, Louridas GE. Is left coronary system more susceptible to atherosclerosis than right? *Int J Cardiol* 2007;116:7-13.
- Peiffer V, Sherwin SJ, Weinberg PD. SPOTLIGHT REVIEW Does low and oscillatory wall shear stress correlate spatially with early atherosclerosis? A systematic review. *Cardiovasc Res* 2013;99:242-50.
- Rikhtegar F, Knight JA, Olgac U, Saur SC, Poulikakos D, Marshall WC, et al. Choosing the optimal wall shear parameter for the prediction of plaque location-A patient-specific computational study in human left coronary arteries. *Atherosclerosis* 2012;221:432-7.
- Van der Heiden K, Hoogendoorn A, Daemen MJ, Gijzen FJH. Animal models for plaque rupture: A biomechanical assessment. *Thromb Haemost* 2016;115:501-8.
- Mach F, Baigent C, Catapano AL, Koskinas KC, Casula M, Badimon L, et al. 2019 ESC/EAS Guidelines for the management of dyslipidaemias: lipid modification to reduce cardiovascular risk. *Eur Heart J* 2020;41:111-88.
- Collet J-P, Thiele H, Barbato E, Barthélémy O, Bauersachs J, Bhatt DL, et al. 2020 ESC Guidelines for the management of acute coronary syndromes in patients presenting without persistent ST-segment elevation. *Eur Heart J* 2021;42:1289-367.
- Roleder T, Karimi Galougahi K, Chin CY, Bhatti NK, Brilakis E, Nazif TM, et al. Utility of near-infrared spectroscopy for detection of thin-cap neoatherosclerosis. *Eur Heart J - Cardiovasc Imaging* 2016;8:jew198.
- Kilic ID, Caiazzo G, Fabris E, Serdoz R, Abou-Sherif S, Madden S, et al. Near-infrared spectroscopy-intravascular ultrasound: scientific basis and clinical applications. *Eur Heart J - Cardiovasc Imaging* 2015;16:jev208.
- Bec J, Ma DM, Yankelevich DR, Liu J, Ferrier WT, Southard J, et al. Multispectral fluorescence lifetime imaging system for intravascular diagnostics with ultrasound guidance: In vivo validation in swine arteries. *J Biophotonics* 2014;7:281-5.
- Iskander-Rizk S, Wu M, Springeling G, van Beusekom HMM, Mastik F, te Lintel Hekkert M, et al. In vivo intravascular photoacoustic imaging of plaque lipid in coronary atherosclerosis. *EuroIntervention* 2019;15:452-6.
- Cecchetti L, Wang T, Hoogendoorn A, Witberg KT, Ligthart JMR, Daemen J, et al. In-vitro and in-vivo imaging of coronary artery stents with Heartbeat OCT. *Int J Cardiovasc Imaging* 2020;36:1021-9.
- Cecchi E, Giglioli C, Valente S, Lazzeri C, Gensini GF, Abbate R, et al. Role of hemodynamic shear stress in cardiovascular disease. *Atherosclerosis* 2011;214:249-56.
- Wentzel JJ, Janssen E, Vos J, Schuurbijs JCH, Krams R, Serruys PW, et al. Extension of increased atherosclerotic wall thickness into high shear stress regions is associated with loss of compensatory remodeling. *Circulation* 2003;108:17-23.
- Virmani R, Burke AP, Farb A, Kolodgie FD. Pathology of the Vulnerable Plaque. *J Am Coll Cardiol* 2006;47:C13-8.
- Stone GW, Maehara A, Lansky AJ, de Bruyne B, Cristea E, Mintz GS, et al. A Prospective Natural-History Study of Coronary Atherosclerosis. *N Engl J Med* 2011;364:226-35.
- Cheng JM, Garcia-Garcia HM, De Boer SPM, Kardys I, Heo JH, Akkerhuis KM, et al. In vivo detection of high-risk coronary plaques by radiofrequency intravascular ultrasound and cardiovascular outcome: Results of the ATHEROREMO-IVUS study. *Eur Heart J* 2014;35:639-47.
- Shin ES, Garcia-Garcia HM, Ligthart JMR, Witberg K, Schultz C, Van Der Steen AFW, et al. In vivo findings of tissue characteristics using iMap™ IVUS and virtual histology™ IVUS. *EuroIntervention* 2011;6:1017-9.
- Schuurman A-S, Vroegindewey M, Kardys I, Oemrawsingh RM, Cheng JM, de Boer S, et al. Near-infrared spectroscopy-derived lipid core burden index predicts adverse cardiovascular outcome in patients with coronary artery disease during long-term follow-up. *Eur Heart J* 2018;39:295-302.
- Waksman R, Di Mario C, Torguson R, Ali ZA, Singh V, Skinner WH, et al. Identification of patients and plaques vulnerable to future coronary events with near-infrared spectroscopy intravascular ultrasound imaging: a prospective, cohort study. *Lancet* 2019;394:1629-37.
- Schultz CJ, Serruys PW, van der Ent M, Ligthart J, Mastik F, Garg S, et al. First-in-man clinical use of combined near-infrared spectroscopy and intravascular ultrasound: a potential key to predict distal embolization and no-reflow? *J Am Coll Cardiol* 2010;56:314.
- Tearney GJ, Regar E, Akasaka T, Adriaenssens T, Barlis P, Bezerra HG, et al. Consensus standards for acquisition, measurement, and reporting of intravascular optical coherence tomography studies: A report from the International Working Group for Intravascular Optical Coherence Tomography Standardization and Validation. *J Am Coll Cardiol* 2012;59:1058-72.

35. Libby P, Hansson GK. From Focal Lipid Storage to Systemic Inflammation: JACC Review Topic of the Week. *J Am Coll Cardiol* 2019;74:1594–607.
36. Chiu JJ, Chien S. Effects of disturbed flow on vascular endothelium: Pathophysiological basis and clinical perspectives. *Physiol Rev* 2011;91:327–87.
37. Koskinas KC, Chatzizisis YS, Baker AB, Edelman ER, Stone PH, Feldman CL. The role of low endothelial shear stress in the conversion of atherosclerotic lesions from stable to unstable plaque. *Curr Opin Cardiol* 2009;24:580–90.
38. Gijzen F, van der Giessen A, van der Steen A, Wentzel J. Shear stress and advanced atherosclerosis in human coronary arteries. *J Biomech* 2013;46:240–7.
39. Fitzgerald TN, Shepherd BR, Asada H, Teso D, Muto A, Fancher T, et al. Laminar shear stress stimulates vascular smooth muscle cell apoptosis via the Akt pathway. *J Cell Physiol* 2008;216:389–95.
40. Slager C, Wentzel J, Gijzen F, Thury A, van der Wal A, Schaar J, et al. The role of shear stress in the destabilization of vulnerable plaques and related therapeutic implications. *Nat Clin Pract Cardiovasc Med* 2005;2:456–64.
41. Chatzizisis YS, Baker AB, Sukhova GK, Koskinas KC, Papafakis MI, Beigel R, et al. Augmented expression and activity of extracellular matrix-degrading enzymes in regions of low endothelial shear stress colocalize with coronary atheromata with thin fibrous caps in pigs. *Circulation* 2011;123:621–30.
42. Ohayon J, Finet G, Gharib AM, Herzka DA, Tracqui P, Heroux J, et al. Necrotic core thickness and positive arterial remodeling index: emergent biomechanical factors for evaluating the risk of plaque rupture. *Am J Physiol Heart Circ Physiol* 2008;295:H717–27.
43. Bench TJ, Jeremias A, Brown DL. Matrix metalloproteinase inhibition with tetracyclines for the treatment of coronary artery disease. *Pharmacol Res* 2011;64:561–6.
44. Slager C, Wentzel J, Gijzen F, Schuurbijs J, van der Wal A, van der Steen A, et al. The role of shear stress in the generation of rupture-prone vulnerable plaques. *Nat Clin Pract Cardiovasc Med* 2005;2:401–7.
45. Glagov S, Weisenberg E, Zarins CK, Stankunavicius R, Kolettis GJ. Compensatory Enlargement of Human Atherosclerotic Coronary Arteries. *N Engl J Med* 1987;316:1371–5.
46. Di Mario C, Moreno PR. Invasive coronary imaging: Any role in primary and secondary prevention? *Eur Heart J* 2016;37:1883–90.
47. Greenland P, Blaha MJ, Budoff MJ, Erbel R, Watson KE. Coronary Calcium Score and Cardiovascular Risk. *J Am Coll Cardiol* 2018;72:434–47.
48. Silverman MG, Harkness JR, Blankstein R, Budoff MJ, Agatston AS, Carr JJ, et al. Baseline subclinical atherosclerosis burden and distribution are associated with frequency and mode of future coronary revascularization: Multi-ethnic study of atherosclerosis. *JACC Cardiovasc Imaging* 2014;7:476–86.
49. Villines TC. Coronary artery calcium score, distribution, and future revascularization. *JACC Cardiovasc Imaging* 2014;7:487–9.
50. Mori H, Torii S, Kutyna M, Sakamoto A, Finn A V., Virmani R. Coronary Artery Calcification and its Progression: What Does it Really Mean? *JACC Cardiovasc Imaging* 2018;11:127–42.
51. Barrett HE, Van der Heiden K, Farrell E, Gijzen FJH, Akyildiz AC. Calcifications in atherosclerotic plaques and impact on plaque biomechanics. *J Biomech* 2019;87:1–12.
52. Beckman JA, Ganz J, Creager MA, Ganz P, Kinlay S. Relationship of clinical presentation and calcification of culprit coronary artery stenoses. *Arterioscler Thromb Vasc Biol* 2001;21:1618–22.
53. Roleder T, Kovacic JC, Ali Z, Sharma R, Cristea E, Moreno P, et al. Combined NIRS and IVUS imaging detects vulnerable plaque using a single catheter system: A head-to-head comparison with OCT. *EuroIntervention* 2014;10:303–11.
54. Liu S, Neleman T, Hartman EMJ, Ligthart JMR, Witberg KT, van der Steen AFW, et al. Automated Quantitative Assessment of Coronary Calcification Using Intravascular Ultrasound. *Ultrasound Med Biol* 2020;46:2801–9.
55. Neleman T, Liu S, Tovar Forero MN, Hartman EMJ, Ligthart JMR, Witberg KT, et al. The Prognostic Value of a Validated and Automated Intravascular Ultrasound-Derived Calcium Score. *J Cardiovasc Transl Res* 2021;14:992–1000.
56. Kumar A, Thompson EW, Lefieux A, Molony DS, Davis EL, Chand N, et al. High Coronary Shear Stress in Patients With Coronary Artery Disease Predicts Myocardial Infarction. *J Am Coll Cardiol* 2018;72:1926–35.
57. Hetterich H, Jaber A, Gehring M, Curta A, Bamberg F, Filipovic N, et al. Coronary Computed Tomography Angiography Based Assessment of Endothelial Shear Stress and Its Association with Atherosclerotic Plaque Distribution In-Vivo. *PLoS One* 2015;10:e0115408.
58. Huang D, Muramatsu T, Li Y, Yang W, Nagahara Y, Chu M, et al. Assessment of endothelial shear stress in patients with mild or intermediate coronary stenoses using coronary computed tomography angiography: comparison with invasive coronary angiography. *Int J Cardiovasc Imaging* 2016;0:1–10.
59. Timmins LH, Suo J, Eshtehardi P, Molony DS, McDaniel MC, Oshinski JN, et al. Comparison of angiographic and IVUS derived coronary geometric reconstructions for evaluation of the association of hemodynamics with coronary artery disease progression. *Int J Cardiovasc Imaging* 2016;32:1327–36.
60. Neumann F-J, Sousa-Uva M, Ahlsson A, Alfonso F, Banning AP, Benedetto U, et al. 2018 ESC/EACTS Guidelines on myocardial revascularization. *Eur Heart J* 2019;40:87–165.
61. Leiserson CE, Thompson NC, Emer JS, Kuszmaul BC, Lampson BW, Sanchez D, et al. There's plenty of room at the Top: What will drive computer performance after Moore's law? *Science (80- )* 2020;368:eaam9744.
62. Shalf J. The future of computing beyond Moore's Law. *Philos Trans R Soc A Math Phys Eng Sci* 2020;378.
63. Tarrahi I, Colombo M, Hartman EMJ, Tovar Forero MN, Torii R, Chiastra C, et al. Impact of bioresorbable scaffold design characteristics on local haemodynamic forces: an ex vivo assessment with computational fluid dynamics simulations. *EuroIntervention* 2020;16:e930–7.
64. Shishido K, Antoniadis AP, Takahashi S, Tsuda M, Mizuno S, Andreou I, et al. Effects of Low Endothelial Shear Stress After Stent Implantation on Subsequent Neointimal Hyperplasia and Clinical Outcomes in Humans. *J Am Heart Assoc* 2016;5.
65. Katagiri Y, Torii R, Takahashi K, Tenekecioglu E, Asano T, Chichareon P, et al. Preclinical evaluation of a thin-strut bioresorbable scaffold (ArterioSorb): acute-phase invasive imaging assessment and hemodynamic implication. *EuroIntervention* 2020;16:e141–6.
66. Tenekecioglu E, Torii R, Katagiri Y, Chichareon P, Asano T, Miyazaki Y, et al. Post-implantation shear stress assessment: an emerging tool for differentiation of bioresorbable scaffolds. *Int J Cardiovasc Imaging* 2019;35:409–18.



# A

## Appendices

Summary  
Nederlandse samenvatting  
List of publications  
PhD-Portfolio  
Acknowledgements / Dankwoord  
About the author



## Summary

### Chapter 1

Atherosclerotic plaque development starts with endothelial cell dysfunction, lipid influx into the vessel wall, and local inflammation. Several biomechanical parameters, including wall shear stress (WSS), are involved in early plaque development and related to plaque progression. Intravascular imaging techniques allow studying atherosclerosis development in vivo. We used clinically available imaging techniques, including near-infrared spectroscopy intravascular ultrasound (NIRS-IVUS), optical coherence tomography (OCT) and cardiac computed tomographic angiography (CCTA). By combining these techniques and creating 3D reconstructions, information on the plaque volume and composition was available. Furthermore, by applying computational fluid dynamics in these 3D coronary reconstructions, WSS can be computed. With the colocalisation of both plaque and WSS, the relation between WSS and plaque progression was further investigated. This thesis aimed to investigate the relationship between WSS, plaque composition and plaque progression using invasive and non-invasive imaging techniques.

### Chapter 2

In previous research, low WSS has been related to the initiation and development of atherosclerosis. Different studies used different approaches to define low WSS. In Chapter 2, we studied the four most used definitions of low WSS. These were compared for their predictive power of plaque progression in one dataset of human coronary arteries. Both absolute thresholds based on previous data in the literature and relative thresholds based on vessel-specific tertiles were used to define low WSS. We concluded that sectors exposed to low WSS showed significant plaque progression irrespective of the specific definition used. However, on an individual basis, the WSS values in human coronary arteries vary too widely between the patients to use absolute thresholds. So, in individual arteries, a relative threshold based on vessel-specific tertiles should be used when determining regions at risk of plaque progression.

### Chapter 3

Animal models are used to study the initial process and development of atherosclerosis. This chapter introduces a new porcine model with a homozygous LDLR R84C mutation. The mini-pigs were of adult age when put on a high-fat diet. Using clinically available imaging techniques such as NIRS-IVUS and OCT, atherosclerosis development was monitored at three different time points during a one-year high-fat diet. Half of the animals developed advanced atherosclerotic plaques with both stable and unstable characteristics. The imaging data was related to histopathological analysis to assess plaque composition showing

vulnerable features such as large necrotic cores, intra-plaque haemorrhage and calcifications. Hence, making this animal model suitable for testing and validating pathophysiology, new interventions and imaging techniques.

#### Chapter 4

WSS, the mechanical force of the blood flow on the vessel wall, has been related to atherosclerotic plaque development. The pulsatility of the blood flow causes variation in the magnitude and direction of the WSS. The multidirectional WSS metrics capture the multidirectional behaviour of blood flow induced during the cardiac cycle and are a descriptor of disturbed blood flow. Multidirectional WSS have been related to plaque progression. This chapter describes a comprehensive study comparing five WSS metrics and their influence on plaque progression in a single data set generated in the porcine model described in Chapter 3. By fusing IVUS and CCTA, a 3D reconstruction of the coronary artery was created. Invasive flow measurements were used in the computational fluid dynamics (CFD) analysis to obtain (multidirectional) WSS. The most crucial finding was that both low time-averaged WSS and high multidirectional WSS were related to plaque growth and progression. However, none of the multidirectional WSS parameters outperformed the time-averaged WSS for plaque progression prediction.

#### Chapter 5

Recently published data linked the presence of lipid-rich plaques as detected by NIRS-IVUS to future adverse cardiac events. An underlying mechanism causing these events might be the rupture of a fibrous cap that overlies these lipid-rich plaques. From a biomechanical point of view, the cap ruptures if the structural stresses within the cap exceed the cap's strength. High WSS has been linked to fibrous cap thinning, weakening the cap and making it prone to rupture. Currently, data on colocalisation of high WSS exposure and lipid-rich plaques is lacking. Chapter 5 includes a hypothesis-generating observational study investigates the differences in WSS exposure of lipid-rich plaque vs non-lipid-rich plaques as detected by NIRS. A colocalisation of high WSS and lipid-rich plaques was found. This colocalisation might be a first step in understanding why lipid-rich plaques are associated with future events from a biomechanical point of view.

#### Chapter 6

Both low WSS and endothelial dysfunction have been individually correlated to plaque initiation and progression. Nonetheless, the interaction between WSS and plaque composition on the effect of plaque growth is an unexplored field. Chapter 6 studies the interplay between WSS and plaque composition and its effect on plaque progression. Plaques presenting with a lipid-rich plaque composition were compared for their WSS-related plaque progression to non-lipid-rich plaques and regions free of plaque at baseline (plaque-free wall). Lipid-rich plaque showed

most plaque progression after a one-year follow-up and demonstrated that the relationship between low WSS and plaque progression was still apparent in these already developed atherosclerotic regions. Interestingly, there was an interaction effect between low WSS and lipid-rich plaques, suggesting a potential synergistic effect of the presence of lipids and low WSS on plaque progression. We found a significant plaque progression in plaque-free regions exposed to low WSS at baseline. This relation was not found in plaque-free regions exposed to mid or high WSS at baseline, confirming the role of low WSS in plaque initiation

#### Chapter 7

The current gold standard for generating 3D reconstructions of coronary arteries used in WSS analysis is based on the fusion of intravascular ultrasound with 3D information from CTA. Chapter 7 studies the differences between the above mentioned gold standard and a simplified methodology using only CTA to generate the 3D reconstruction of the coronary artery. The WSS distribution observed in two reconstructions of the same vessel was compared, one solely based on CTA and one based on the fusion of IVUS and CTA. Although the WSS in CTA-based 3D reconstructions of coronary arteries was significantly higher than the golden standard, the distribution of the WSS over the vascular tree was very similar. Since we found similarities in the WSS distribution, the sole use of CT might make WSS analysis more applicable for studying larger clinical datasets, investigating and relating biomechanics to atherosclerosis and potential adverse events.

#### Chapter 8

In our studies on atherosclerosis in both the atherosclerotic porcine model and the patients, the same methodology was used for the 3D reconstruction of the coronary arteries and vessel specific boundary conditions for the computational fluid dynamics. Therefore, a comprehensive comparison could be performed between the hemodynamics, WSS, and anatomical features of porcine and human coronary arteries. Interestingly, no clinically relevant differences were found, showing that porcine and human coronary arteries demonstrate the same near wall and intravascular hemodynamics.

#### Chapter 9

In coronary atherosclerosis research, there is an ongoing debate on biomarkers of plaque stability and plaque vulnerability to identify the plaques at risk of plaque rupture and thus are precursors of myocardial infarctions. In previous studies, calcifications were associated with plaque stability. As detected by NIRS, lipids have been noticed as a relevant imaging marker for plaque vulnerability. This chapter presented a detailed analysis of the colocalisation of calcium and lipid-rich regions using data acquired with the NIRS-IVUS catheter. Calcium and lipid scores were calculated for the whole vessel, segmental level(4mm) and frame-level

(1mm). Remarkably, high lipid scores are associated with high local calcium scores at segmental and frame levels, suggesting that these plaque characteristics should not be seen as separate entities. Both plaque components should be considered when estimating the potential plaque vulnerability.

#### **Chapter 10**

When analysing NIRS-IVUS, regions without any visible intima thickening showed NIRS positive signal and thus lipid-rich regions. These thin lipid-rich regions might be wrongly dismissed as an artefact. This chapter describes the differences in plaque progression between these thin lipid-positive regions and thin regions without positive lipid detection. Thin regions with lipid-rich signals demonstrated increased plaque progression comparable to lipid-rich regions with already intima thickening. Thin regions with a NIRS negative signal did not show significant plaque progression. These thin lipid-rich regions could be explained by a very early phase in plaque development where there is already lipids and inflammation process in the vessel wall, but no thickening of the vessel wall has yet occurred.

#### **Chapter 11**

Finally, the main findings of this thesis were discussed in this last chapter. Cross-chapter connections were made, as well as the clinical relevance and future perspectives were discussed. Based on this thesis, we confirmed the relationship between low WSS and plaque progression. Furthermore, the synergistic effect of lipid-rich plaques and low WSS on plaque progression was recognised. The clinical applicability of WSS might be too ambitious for now, but the role in pathophysiological research has been established and confirmed in this thesis.

## Nederlandse samenvatting

### Hoofdstuk 1

Het ontstaan van aderverkalking, ook wel atherosclerose genoemd, begint met de disfunctie van endotheelcellen in de bloedvaatwand. Wall shear stress (WSS), de wandschuifspanning van het bloed op de endotheel cellen, heeft effect op de functie van de endotheelcellen. Endotheelcellen die blootgesteld worden aan lage WSS laten makkelijker vetten (Lipiden) de vaatwand in. Hierdoor ontstaat er een lokale ontstekingsreactie die uiteindelijk het begin vormt van aderverkalking en zal leiden tot het vormen van atherosclerotische plaques in de vaatwand. In dit proefschrift was het doel de relatie tussen WSS, plaquesamenstelling en plaqueprogressie van kransslagaderen die rondom het hart liggen verder te onderzoeken met behulp van invasieve en niet-invasieve beeldvormingstechnieken. Sinds de introductie van verschillende beeldvormingstechnieken, kunnen we de ontwikkeling van atherosclerose in mensen en dieren in beeld brengen en bestuderen. In dit proefschrift maakten we gebruik van klinisch beschikbare beeldvormingstechnieken. Invasieve technieken zoals infraroodspectroscopie en intravasculaire ultrageluid (NIRS-IVUS) en optische coherentie tomografie (OCT) kunnen van binnen uit in de bloedvaten de grootte en de samenstelling van de atherosclerotische plaques in kaart brengen. Door de beelden en verzamelde gegevens te combineren met de 3D informatie van de kransslagaderen van een computer tomografie scan (CT-scan) konden we hoge resolutie 3D-reconstructies van de kransslagaderen maken. Door het gebruik van numerieke stromingsleer (CFD), kan WSS worden uitgerekend in deze 3D reconstructies van de kransslagaderen. Alle data, zowel de informatie over plaque samenstelling, dikte, locatie en de WSS werd geprojecteerd op de 3D-reconstructie zodat de verbanden tussen deze parameters konden worden onderzocht.

### Hoofdstuk 2

In eerder onderzoek is lage WSS in verband gebracht met de vroege fase van de ontwikkeling van atherosclerose. Verschillende studies gebruiken verschillende manieren om lage WSS te definiëren. Door verschillende definities te gebruiken zou dit effect kunnen hebben op de voorspellende waarde van lage WSS op plaque groei. In Hoofdstuk 2 hebben we in één dataset met kransslagaderen de vier meest toegepaste definities van lage WSS vergeleken. Absolute afkapwaarden worden in literatuur beschreven en veel toegepast. Relatieve waarden, waarbij de beschikbare data van een studie of bloedvat wordt opgedeeld in drie gelijke groepen (tertielen) kunnen ook gebruikt worden om lage WSS te definiëren. We concludeerden dat sectoren blootgesteld aan lage WSS significante plaque-progressie vertoonden, ongeacht welke definitie voor lage WSS gebruikt werd. Echter, op individuele basis variëren de absolute WSS-waarden in menselijke kransslagaders te sterk tussen de patiënten om absolute afkapwaarden te gebruiken. Dus bij in individuele casussen



zou een relatieve afkapwaarde op basis van bloedvat specifieke tertielen kunnen worden gebruikt bij het bepalen van regio's met risico op plaqueprogressie.

### Hoofdstuk 3

Diermodellen worden gebruikt om de beginfase en de ontwikkeling van atherosclerose te bestuderen. Dit hoofdstuk introduceert een nieuw varkensmodel met een homozygote LDLR R84C-mutatie. De minivarkens waren al volwassen, en niet meer onderhevig aan groei, toen ze op een vetrijk dieet werden gezet. Met behulp van klinisch beschikbare beeldvormende technieken zoals NIRS-IVUS en OCT, werd de ontwikkeling van atherosclerose gevolgd op drie verschillende tijdstippen in een periode van 1 jaar waarbij de varkens op een vetrijk dieet stonden. De helft van de dieren ontwikkelde vergevorderde en uitgebreide atherosclerotische plaques met zowel stabiele als onstabiele kenmerken. De invasieve beeldvorming werd vergeleken met de histologie van kransslagaders om de samenstelling te beoordelen op kwetsbare kenmerken van de plaque zoals necrose, bloedingen en calcificaties. Dit soort plaques worden bijna nooit aangetroffen in andere diermodellen, wat dit model geschikt maakt voor het testen en valideren van pathofysiologie, nieuwe interventies en beeldvormende technieken.

### Hoofdstuk 4

WSS, de wandschuifspanning van de bloedstroom op de vaatwand, wordt in verband gebracht met de ontwikkeling van atherosclerotische plaques. Het bloed stroomt niet in een continue stroom, maar er zijn pulsaties die worden veroorzaakt door de pomp werking van het hart. Dit zorgt voor variatie in de bloedstroom tijdens de een hart cyclus, in zowel de grootte als de richting, de multidirectioneiteit van de WSS. Dit hoofdstuk beschrijft een uitgebreide studie waarin vijf verschillende WSS parameters (zowel een tijdsgemiddelde WSS, als multidirectionele WSS) en de relatie met plaque progressie worden vergeleken binnen een enkele dataset. De dataset met 3D reconstructies van de kransslagaderen is afkomstig van de studie van het varkensmodel zoals beschreven in hoofdstuk 3. Door de beelden van IVUS en CT-scan te fuseren, werd een 3D-reconstructie van de kransslagader gemaakt. Invasieve stromingsmetingen werden gebruikt in de numerieke stromingsleer (CFD) sommen om (multidirectionele) WSS te verkrijgen van deze kransslagaders. De verschillende multidirectionele WSS parameters leggen het multidirectionele gedrag van de bloedstroom vast tijdens de hartcyclus, en zijn een maat voor de verstoorde bloedstroom. De meest cruciale bevinding was dat zowel lage tijdsgemiddelde WSS als hoge multidirectionele WSS is gerelateerd aan plaquegroei als plaque. Echter, geen van de multidirectionele WSS-parameters presteerde beter dan de tijdsgemiddelde WSS als voorspeller van plaqueprogressie.

### Hoofdstuk 5

Recent gepubliceerde studies koppelde de aanwezigheid van door NIRS gedetecteerde lipidenrijke plaques aan cardiovasculaire events zoals hartinfarcten. Het scheuren van de fibreuze kap die over de lipidenrijke plaque heen ligt, zou een van de oorzaken van zo een event kunnen zijn. Vanuit mechanistisch oogpunt scheurt de kap als de spanning die op zo een kap werkt groter is dan de kap kan weerstaan. Hoge WSS wordt in verband gebracht met het dunner worden van deze fibreuze kap, de kap verzwakt en is vatbaarder voor het scheuren. Momenteel ontbreken gegevens over of de lipidenrijke regio's worden blootgesteld aan hoge of lage WSS. Hoofdstuk 5 omvat een hypothese-genererende observationele studie waarin de verschillen in WSS-blootstelling van lipidenrijke plaques versus niet-lipide-rijke plaques worden vergeleken. In deze studie worden lipiden gedetecteerd door NIRS. Op lipidenrijke plaque was er vooral sprake van blootstelling aan hoge WSS. Vanuit mechanistisch oogpunt zou het samen voorkomen van zowel lipiden als de hoge WSS mogelijke verklaring kunnen zijn waarom NIRS-lipiden rijke plaque worden geassocieerd met cardiovasculaire events.

### Hoofdstuk 6

Zowel lage WSS als de disfunctie van endotheel zijn individueel geassocieerd met het ontstaan van atherosclerose. Desalniettemin is het vooralsnog onduidelijk wat de interactie is tussen WSS en de samenstelling van de plaque en of dit een effect heeft op de plaquegroei. Hoofdstuk 6 bestudeert dit samenspel. Lipidenrijke plaques werden vergeleken met niet-lipidenrijke plaque op basis van hun WSS-gerelateerde plaque-groei. Lipidenrijke plaque vertoonde de meeste plaque-progressie na een follow-up van een jaar. Daarnaast was de relatie tussen lage WSS en plaque-groei nog steeds duidelijk aanwezig in deze gebieden waar al plaque zichtbaar was op het 1<sup>e</sup> meetpunt. Interessant genoeg was er een interactie-effect tussen lage WSS en lipidenrijke plaques, wat een mogelijk synergetisch effect suggereert van de aanwezigheid van lipiden en lage WSS op plaque groei. Ook werd WSS effect op plaque groei bekeken in regio's waar nog geen plaque zichtbaar was op het 1<sup>e</sup> meetpunt (de plaque-vrije vaatwand). We vonden een significante plaque-progressie in plaquevrije regio's van het 1<sup>e</sup> meetpunt die zijn blootgesteld aan een lage WSS. Deze relatie werd niet gevonden in plaquevrije regio's die waren blootgesteld aan gemiddelde of hoge WSS bij baseline, wat de rol van lage WSS bij het ontstaan van plaque bevestigt.

### Hoofdstuk 7

De huidige gouden standaard voor het maken van 3D-reconstructies van kransslagaders die worden gebruikt in WSS-analyse, is gebaseerd op de fusie van intravasculaire beeldvorming (IVUS/OCT) met de 3D-informatie van CT-scan. Hoofdstuk 7 bestudeert de verschillen tussen de bovengenoemde gouden standaard en een vereenvoudigde methodologie waarbij alleen CT-scan wordt

gebruikt om de 3D-reconstructie van de kransslagader te genereren. Voor deze studie werd gebruik gemaakt van een dataset met bloedvaten waarvan zowel één reconstructie uitsluitend gebaseerd op CT-scan en één reconstructie gebaseerd op de fusie van IVUS en CTA beschikbaar was. De WSS-verdeling twee verschillende methodes van reconstructie werd vergeleken. Hoewel de absolute WSS waarde in op CT-scan gebaseerde 3D-reconstructies significant hoger was dan de gouden standaard, was de verdeling van de WSS over de vasculaire boom erg vergelijkbaar. Aangezien er een overeenkomst is in de WSS-distributie, zou het gebruik van CT-scans in WSS-analyse meer toepasbaar kunnen maken voor het bestuderen van grotere al bestaande klinische datasets, het onderzoeken en relateren van biomechanica aan atherosclerose en cardiovasculaire events.

### Hoofdstuk 8

In onze studies van atherosclerose in zowel het varkensmodel als in de patiënten studie, werd dezelfde methodologie gebruikt voor de 3D-reconstructie van de kransslagaders en specifieke randvoorwaarden voor de numeriek vloeistof leer. Daarom werd er een uitgebreide vergelijking gemaakt tussen de hemodynamica, WSS en anatomische kenmerken van varkens- en menselijke kransslagaders. Interessant genoeg werden er geen relevante verschillen gevonden, wat aantoont dat varkens- en menselijke kransslagaders dezelfde nabije wand- en intravasculaire hemodynamiek vertonen.

### Hoofdstuk 9

In het onderzoek naar coronaire atherosclerose is er een voortdurende zoektocht naar een marker die de kwetsbaarheid van plaques voorspeld en daarmee plaque identificeert die het risico loopt tot een scheur in de kap en daarmee op het ontstaan van een hartinfarct. In eerdere studies waren lokale calcificaties geassocieerd met plaquestabiliteit. Daarentegen zijn lipiden gedetecteerd door NIRS gerelateerd met de kwetsbaarheid van een plaque. Dit hoofdstuk presenteert een gedetailleerde analyse van de het tegelijkertijd voorkomen van calcium- en lipidenrijke gebieden op dezelfde locatie. Dit werd gedaan met behulp de NIRS-IVUS-katheter, die zowel lipiden als calcium tegelijkertijd lokaliseert. Calcium- en lipiden scores werden berekend voor het hele vat, op segmentniveau (4 mm) en op frameniveau (1 mm). Opmerkelijk is dat hoge lokale lipiden scores geassocieerd is met hoge lokale calcium scores op segment- en frameniveau, wat suggereert dat deze plaquekenmerken niet als afzonderlijke entiteiten moeten worden gezien. Beide plaquecomponenten zullen moeten worden meegewogen bij het inschatten van de potentiële plaquekwetsbaarheid.

### Hoofdstuk 10

Tijdens het analyseren van NIRS-IVUS beelden, vertoonden regio's zonder enige zichtbare wandverdikking toch een NIRS-positief signaal en werden daarmee dus geclassificeerd als lipidenrijke regio's. Deze dunne wand lipidenrijke gebieden zouden ten onrechte kunnen worden afgedaan als een artefact. Dit hoofdstuk beschrijft de verschillen in plaqueprogressie tussen deze dunne wand lipiden positieve regio's en dunne wand regio's zonder positieve lipiden-detectie. Dunne wand regio's met lipidenrijke signalen vertoonden meer plaquegroei dan dunne wand regio's zonder lipidenrijk signaal. De groei was vergelijkbaar met lipidenrijke regio's waarbij de vaatwand al wel verdikt was. Dunne wand gebieden met een lipiden-negatief signaal vertoonden geen significante plaquegroei. De dunne lipidenrijke regio's zijn mogelijk de detectie van de zeer vroege fase in de ontwikkeling van atherosclerose waar er wel al lipiden en een ontstekingsproces in de vaatwand zijn, maar waar nog geen verdikking van de vaatwand heeft plaatsgevonden.

### Hoofdstuk 11

Ten slotte werden in dit laatste hoofdstuk de belangrijkste bevindingen van dit proefschrift besproken. Er werden hoofdstuk overschrijdende verbanden gelegd, evenals de klinische relevantie en toekomstperspectieven werden besproken.

## List of publications

- Tomaniak M, **Hartman EMJ**, Tovar Forero MN, Wilschut J, Zijlstra F, Van Mieghem NM, et al. Near-infrared spectroscopy to predict plaque progression in plaque-free artery regions. *EuroIntervention* 2022;18:253–61.
- Neleman T, Liu S, Tovar Forero MN, **Hartman EMJ**, Ligthart JMR, Witberg KT, et al. The Prognostic Value of a Validated and Automated Intravascular Ultrasound-Derived Calcium Score. *J Cardiovasc Transl Res* 2021;14:992–1000.
- Hartman EMJ**, De Nisco G, Gijzen FJH, Korteland S-A, van der Steen AFW, Daemen J, et al. The definition of low wall shear stress and its effect on plaque progression estimation in human coronary arteries. *Sci Rep* 2021;11:22086.
- Eslami P, **Hartman EMJ**, Albaghadaï M, Karady J, Jin Z, Thondapu V, et al. Validation of Wall Shear Stress Assessment in Non-invasive Coronary CTA versus Invasive Imaging: A Patient-Specific Computational Study. *Ann Biomed Eng* 2021;49:1151–68.
- De Nisco G, Chiastra C, **Hartman EMJ**, Hoogendoorn A, Daemen J, Calò K, et al. Comparison of Swine and Human Computational Hemodynamics Models for the Study of Coronary Atherosclerosis. *Front Bioeng Biotechnol* 2021;9:731924.
- Tarrahi I, Colombo M, **Hartman EMJ**, Tovar Forero MN, Torii R, Chiastra C, et al. Impact of bioresorbable scaffold design characteristics on local haemodynamic forces: an ex vivo assessment with computational fluid dynamics simulations. *EuroIntervention* 2020;16:e930–7.
- Majeed K, **Hartman EMJ**, Mori TA, Alcock R, Spiro J, Ligthart J, et al. The Effect of Stent Artefact on Quantification of Plaque Features Using Optical Coherence Tomography (OCT): A Feasibility and Clinical Utility Study. *Hear Lung Circ* 2020;29.
- Liu S, Neleman T, **Hartman EMJ**, Ligthart JMR, Witberg KT, van der Steen AFW, et al. Automated Quantitative Assessment of Coronary Calcification Using Intravascular Ultrasound. *Ultrasound Med Biol* 2020;46:2801–9.
- Hoogendoorn A, Kok AM, **Hartman EMJ**, de Nisco G, Casadonte L, Chiastra C, et al. Multidirectional wall shear stress promotes advanced coronary plaque development: comparing five shear stress metrics. *Cardiovasc Res* 2020;116:1136–46.
- Hartman EMJ**, Hoogendoorn A, Akyildiz AC, Schuurman A-S, van der Steen AFW, Boersma E, et al. Colocalization of Intracoronary Lipid-Rich Plaques and Calcifications: An Integrated NIRS-IVUS Analysis. *JACC Cardiovasc Imaging* 2020;13:1627–8.
- Hartman EMJ**, De Nisco G, Kok AM, Hoogendoorn A, Coenen A, Mastik F, et al. Lipid-rich Plaques Detected by Near-infrared Spectroscopy Are More Frequently Exposed to High Shear Stress. *J Cardiovasc Transl Res* 2020.
- Eslami P, **Hartman EMJ**, Albaghadaï M, Karady J, Jin Z, Thondapu V, et al. Validation of Wall Shear Stress Assessment in Non-invasive Coronary CTA versus Invasive Imaging: A Patient-Specific Computational Study. *Ann Biomed Eng* 2020.
- Hoogendoorn A, den Hoedt S, **Hartman EMJ**, Krabbendam-Peters I, Te Lintel Hekkert M, van der Zee L, et al. Variation in Coronary Atherosclerosis Severity Related to a Distinct LDL (Low-Density Lipoprotein) Profile: Findings From a Familial Hypercholesterolemia Pig Model. *Arterioscler Thromb Vasc Biol* 2019;39.

- van den Berge JC, Dulfer K, Utens EMWJ, **Hartman EMJ**, Daemen J, van Geuns RJ, et al. Predictors of subjective health status 10 years post-PCI. *IJC Hear Vasc* 2016;11.
- van den Berge JC, Utens EMWJ, Dulfer K, **Hartman EMJ**, van Geuns R-J, Daemen J, et al. Can anxiety and depression, separately or in combination predict subjective health status 10 years post-PCI? *Int J Cardiol* 2015;186:57–9.
- Karanasos A, Van Mieghem N, Bergmann MW, **Hartman EMJ**, Ligthart J, Van Der Heide E, et al. Multimodality intra-Arterial imaging assessment of the vascular trauma induced by balloon-based and nonballoon-based renal denervation systems. *Circ Cardiovasc Interv* 2015;8.
- Hartman EMJ**, Groenendijk IM, Heuvelman HM, Roos-Hesselink JW, Takkenberg JJM, Witsenburg M. The effectiveness of stenting of coarctation of the aorta: A systematic review. *EuroIntervention* 2015;11.
- Hartman EMJ**, Dulfer K, Utens EMWJ, Van Den Berge JC, Daemen J, Van Domburg RT. Gender differences in quality of life after PCI attenuate after a 10 year follow-up. *Int J Cardiol* 2014;176.

## Accepted

- Hartman EMJ**, De Nisco G, Kok AM, Tomaniak M, Nous FMA, Korteland SA, et al. Wall shear stress related plaque growth of lipid-rich plaques in human coronary arteries: a NIRS and OCT study, Cardiovascular Research

**PhD-Portfolio****General Courses**

	<b>Year</b>
BROK course	2017
Scientific integrity	2019
Biomedical English writing and communication course	2019

**Scientific courses**

Imaging for ischemic heart and brain disease (COEUR)  
 Pathophysiology of Ischemic Heart disease part 1 ( COEUR)  
 Pathophysiology of Ischemic Heart disease part 2 ( COEUR)  
 Cardiovascular imaging and diagnostics part 1 ( COEUR)  
 Cardiovascular imaging and diagnostics part 3 ( COEUR)  
 Congenital Heart Disease part 1 ( COEUR)  
 Sex and Gender differences in Cardiovascular research

**Scientific seminars (Erasmus MC)**

Dilemma's in orgaan donatie	2019
BME-lab lab meetings (4 presentations)	2016-2020

**Scientific seminars (other)**

Dutch society for medical ultrasound spring meeting	2016
Infraredx course	2017
2 <sup>nd</sup> translational research meeting, Netherlands heart institute	2018
ESC working group atherosclerosis and vascular biology: imaging of vulnerable plaque	2019
Young@heart talent day, Netherlands heart institute	2017

**National and international conferences**

	<b>Year</b>
Biomechanics in Vascular Biology and Cardiovascular Disease symposium 2017, Rotterdam	2017
Optics in cardiology, 2017, Rotterdam	2017
Optics in cardiology, 2018, Zurich ( 2x poster presentation)	2018
ESC 2018, Munich (poster + oral presentation)	2018
ESC 2019, Paris (poster presentation)	2019
EuroPCR 2019, Paris (poster presentation)	2019

Biomechanics in Vascular Biology and Cardiovascular Disease symposium 2019, London (Oral presentation) 2019

**Supervision of students**

Supervision of medical students writing a systematic literature review

Supervision of Master student Technical University Delft.

Supervision of Bachelor student VU Medisch Centrum

**Others**

COEUR excursion: Medical development department Philips	2017
COEUR excursion: General medical council	2018
COEUR PhD day	2018
Infraredx course presenter	2019



## About the author

Eline Hartman was born on May 9<sup>th</sup>, 1991, in Haarlem, the Netherlands. She visited secondary school in Heemstede, the Netherlands, where she graduated in 2009. The same year Eline started studying Medicine at the Erasmus University Rotterdam. During her bachelor's, she performed her first research project at the Department of Congenital Cardiology with dr. Witsenburg. After obtaining her Bachelor degree in Medicine, she continued in studying for her master's degree in Rotterdam. During that time, she performed a scientific internship under the supervision of dr. van Domburg in the Cardiology Department. After obtaining her master's degree in Medicine in 2016, Eline continued performing research as a full-time PhD-candidate at the Biomedical Engineering Department part of the Cardiology Department, Erasmus Medical Centre under the supervision of prof. van der Steen, dr. Wentzel and dr. Daemen. Her research project focused on coronary atherosclerosis, biomechanics and imaging. Eline conducted a prospective patient study in collaboration with the cath lab of the Erasmus Medical Centre. During this research project she worked alongside clinicians, engineers and biologists in the overlapping field of clinical research and engineering. This work has led to the results presented in this thesis. After 4 years as a PhD-student, Eline started working as a resident (not in training), first at the Albert Schweitzer Hospital in Dordrecht and later in the Erasmus Medical Centre at the Cardiology Department. Currently, Eline is working as a cardiologist in training at the Maastad Hospital, Rotterdam.

